Synthesis, Characterization, and Anticancer Activity of Arene Mono-Ruthenium and Heteroleptic Mixed-Valent Diruthenium Complexes

THATO TSHWARO MEDUPE

Student No.: MDPTHA004

SUBMITTED TO THE UNIVERSITY OF CAPE TOWN

In fulfilment of the requirements for the degree of Doctor of Philosophy

Department of Chemistry

Faculty Of Science

Supervisor: Dr Siyabonga Ngubane

Co-supervisor: Professor Sharon Prince

Date of Submission: 25 July 2023

DECLARATION

I, Thato Tshwaro Medupe, declare that this work titled "**Synthesis, Characterization, and Anticancer Activity of Arene Mono-Ruthenium and Heteroleptic Mixed-Valent Diruthenium Complexes**" which is submitted in fulfilment of the requirements for the Degree of Doctor of Philosophy (PhD) at the University of Cape Town has not been previously submitted for a degree at this University or any other University.

The following research project was compiled, collated, and written by me, Thato Tshwaro Medupe. All the quotations are indicated by appropriate punctuation marks. All sources of information used are acknowledged, cited and listed on the reference pages found at the end of every chapter.

Signed by candidate

Thato T. Medupe Date

25 July 2023

…… ……..

ACKNOWLEDGEMENTS

I, Thato Tshwaro Medupe, wish to express my sincere gratitude and appreciation to my supervisor, Dr Siyabonga Ngubane for his consistent supervision, enormous contributions, and assistance in moulding this project to be a success. Thank you for your training and skill set in many aspects, assistance in writing reports, funding proposals, abstracts for conferences and this thesis. It would not have all been possible if it were not for your participation and interest in this scientific body of work. To my co-supervisor, Professor Sharon Prince, thank you kindly, for your tremendous contributions and input, vast knowledge, and expertise in breast cancer research and motivation to always believe in my research data. Thank you for extending your motherly tender love, patience, and kindness to me when I needed it the most till the very end of this challenging journey.

Many thanks to Associate Professor Burget Blom and colleagues (Inorganic Chemistry, Maastricht University), for offering me the opportunity to collaborate and pre-screen organometallic ruthenium(II) arene compounds synthesized from your lab and include this collaborative work as a thesis chapter (Chapter 2).

Special appreciation to Associate Professor Gregory Smith, for your knowledge input, suggestions and contributions during my lab meeting progress presentations. Dr Shepherd Siangwata, Dr Marwaan Rylands, Dr Preshendren Govender, Athi Welsh, and Sinethemba Mkhize- thank you kindly for your insightful inputs and for proofreading this work.

To the former (from 2017) and present cohort members of the SN, GS, and SP research groups, scientific officers, and laboratory technicians, thank you all for your friendship, love and support, guidance, and assistance throughout my research project. To the late Mr Andre De Jagger, chemistry department glassblower, thank you for your tremendous work in amending my broken glassware and for your friendship. May your soul continue to rest in peace. To the department's central administrative office (CAO), thank you all for your administrative support.

I would like to express my sincere appreciation to Dr Annick van Niekerk (BioInorganic Chemist, Stellenbosch University), for your assistance with the DNA binding titration and

horizontal agarose gel electrophoresis experimental work and analysis. To Karabo Mashiloane, thank you for your guidance and advice on the synthesis of my compounds in the early stages of my synthesis laboratory work. Many thanks to Nirvashi Autar and Sinethemba Mkhize, for your assistance with the paramagnetic susceptibility and cyclic voltammetry electrochemical measurements and analysis.

Special thanks to Dr Alexis Joy Mufweba, Dr Hapiloe Maranyane and Claire Bellis for your guidance, training, and assistance with the *in vitro* biological assays, and data analysis. To my colleagues and friends, Dr Anna Casimiro, Athi Welsh, Sinethemba Mkhize, Nozuko Motimane, Stephanie Ncube, Lihle Mokhaye, and Thulisa Mkatazo, thank you for your support throughout this journey.

I recognize that this research project would not have been possible without the financial assistance of the National Research Foundation (NRF), the Faculty of Science Equity Scholarship from the University of Cape Town, and the South African Medical Research Council (SAMRC). Thank you, a million times more.

To my siblings, Mpho Abegail and Aobakwe Alloycious Medupe, and my nephew Kgosi Molapisi. Thank you for your patience, unwavering love, and support throughout this journey. My late parents, Maggy Keikantsemang and Earnest Smuts Medupe, and my late grandmother Kebuileng Gabanakgosi, I know you are constantly watching over me. Thank you for being my shadow and walking by my side in the early hours of the morning as I returned home after a long day of lab work and writing sessions. Your presence was deeply felt.

To my friends Mapaseka Setlhodi, Mogomotsi Mokobane, Malebogo Lephalo, Mzikasi Ntintelo, Ronald Oatlhotse, Shaun Siphesihle Cele, Bokamoso Seameco, Njabulo Dube, Mfundo Khumalo, Mfundo Thwala, Tshepang Kgositau, Banele Mazibuko, the late Sephekana Samuel Mohapi, Josiah Sikundla, Lindani Maqetuka and finally, David Stevens. It does take a village to raise a child. Thank you all for your undying love and for actively being present throughout my darkest hours, most especially when I didn't believe in myself. I do recognise that it would not have been possible for me to reach the finish line without you and the great support structure you formed.

The UCT postgraduate Shut Up and Write (SUW) community, Busisiwe Radebe, Mikateko Ndhambi, and Dr Tebogo Lefifi, thank you kindly for holding my hand through it all.

To my therapist, Ms Sadia Edross, I cannot thank you enough for being present in my life from the moment I walked into your office at the Student Wellness Services to this day. Thank you for allowing me to speak my thoughts in your presence and constantly reassuring and validating my voice and presence at the University of Cape Town.

To you, Thato Tshwaro Medupe, this body of work is dedicated.

Through all the hardships and storms that you've encountered, let this be a reminder that you are more than capable to wither the storm and reach that peak of a mountain.

Congratulations kiddo, you did it.

ABSTRACT

To contribute towards the good health and well-being sustainable development goal, this project aims to synthesize and characterize organometallic arene mono-ruthenium and diruthenium complexes that have anti-neoplastic properties against the oestrogen receptor-positive MCF-7, and the triple negative aggressive and invasive MDA-MB-231 human breast adenocarcinoma and mammary non-malignant MCF-12A epithelial cell lines. The preparation of diruthenium complexes led to the formation of paddlewheel-type complexes having a general chemical formula $[Ru_2(O_2CCH_3)_3(R\text{-}ap)Cl]$ (**C1 - C8**). On the other hand, the preparation of mono-ruthenium complexes led to the formation of the complexes $[RuCl_2(\eta^6\text{-}C_6H_5OCH_2CH_2OH)(R)]$ (**C10 - C12**), and the novel $[RuCl(\eta^6\text{-}C_6H_5OCH_2CH_2OH)(P(OPh)_3)(SnCl_3)]$ (**C13** and **C14**). All complexes were characterized using spectroscopic techniques such as IR, UV-visible, 1-D and 2-D NMR. The connectivity of atoms through space as well as the solid-state structures was confirmed using X-ray crystallography. The purity of all synthesized compounds was confirmed by high-resolution mass spectrometry (HRMS), hyphenated chromatographic techniques (LCMS) as well as melting points. Magnetic susceptibility studies were conducted to determine and confirm the number of unpaired electrons of the paramagnetic bimetallic complexes. Due to their mixed-valent Ru_2(II, III) metalcore, cyclic voltammetry measurements were recorded to study the electrochemical behaviour of complexes of interest. The cytotoxic experiments performed against MCF-7 and MDA-MB-231 cancer cells suggest that all free anilinopyridinate (R-ap) ligands do not inhibit the proliferation of both cell viable lines significantly, whereas coordination of these ligands to a Ru_2^{5+} metal core to form $[Ru_2(O_2CCH_3)_3(R\text{-}ap)Cl]$ complexes (where R = CH_3 or F) improves the anticancer activity against the afore-mentioned human breast cancer cells.

Anilinopyridinate-type ligands were prepared via a facile nucleophilic aromatic substitution reaction between 2-bromopyridine and the corresponding substituted anilines. The generated R-ap ligands are such that the substituent R is varied with electron-withdrawing fluorine (F) and donating methyl (CH_3) substituents (**L1 - L8**) at different positions of the aniline ring. Synthesis of the organometallic ruthenium arene complexes was achieved via cleavage of the known ruthenium dimer $[RuCl_2(\eta^6\text{-}C_6H_5OCH_2CH_2OH)]_2$ with phosphine ligands. This synthetic method yielded organometallic $[RuCl_2(\eta^6\text{-}C_6H_5OCH_2CH_2OH)(R)]$ complexes,

where R = triphenyl phosphine (**C10**), triphenyl phosphite (**C11**), trimethyl phosphite (**C12**). Furthermore, the reactions of **C10** and **C11** with $SnCl_2$ led to the formation of the novel complexes $[RuCl(\eta^6\text{-}C_6H_5OCH_2CH_2OH)(PPh_3)(SnCl_3)]$ (**C13**) and $[RuCl(\eta^6\text{-}C_6H_5OCH_2CH_2OH)(P(OPh)_3)(SnCl_3)]$, respectively. The desired diruthenium complexes were achieved via a metathesis displacement of an acetate ligand from the precursor tetraacetate complex $[Ru_2(O_2CCH_3)_4Cl]$ by one substituted ap ligand. This afforded stable mixed-valent diruthenium(II, III) paddlewheel complexes with a general chemical formula $[Ru_2(O_2CCH_3)_3(R\text{-}ap)Cl]$.

Complexes $[Ru_2(O_2CCH_3)_3(4\text{-}CH_3ap)Cl]$ (**C3)** and $[Ru_2(O_2CCH_3)_3(4\text{-}Fap)Cl]$ (**C8**) show promising anticancer effects against MCF-7 cells, having an IC_{50} value of 39.0 µM and 49.1 µM, respectively with favourable selectivity towards the human breast MCF-7 cells. Clonogenic assay experiments showed that **C3** inhibited the growth and regeneration of MCF-7 cells after 7 days of monitoring cell colony formation. Western blotting analysis suggests that **C3** induces double-stranded DNA breaks, observed by the increase in protein expression levels of key DNA damage response marker, ɣ-H2AX. Furthermore, **C3** activates the intrinsic apoptotic signalling molecular markers, particularly caspase-9 and its downstream substrate, PARP.

The stability of **C3** in DMSO and RPMI media solution (used in biological assays) was confirmed by ultraviolet-visible spectroscopy. The results obtained suggest that $[Ru_2(O_2CCH_3)_3(R\text{-}ap)Cl]$ complexes are stable in DMSO for over 7 days and react rapidly with the RPMI-1640 culture media. Preliminary mechanistic studies investigating the biological molecular targets of **C3** were performed by following the interactions of **C3** with salmon-sperm DNA, blue-script plasmid DNA and glutathione (GSH). Experiments were probed using UV-visible spectroscopic and agarose gel electrophoresis techniques.

Altogether, the results obtained and presented herein in this work substantiate that the potential use of ruthenium coordination compounds and organometallic complexes in cancer therapy continues to remain a vital approach in the discovery of potent metal-based anticancer therapeutic drug leads.

CONFERENCES/SYMPOSIA CONTRIBUTIONS

- Oral presentation: Thato Medupe, Sharon Prince, and Siyabonga Ngubane., Towards the development of monosubstituted paddlewheel [$Ru_2(O_2CCH_3)_3$(R-ap)Cl] complexes for the treatment of Human Breast Cancer subtypes: Preparation, characterisation, and preclinical in vitro evaluation. Presented at the Science Faculty Postgraduate Research Symposium, 27th November, 2023.

- Flash Talk presentation: Thato Medupe, Sharon Prince, and Siyabonga Ngubane., Mono-substituted anilinopyridinate-triacetatochlorodiruthenium(II, III) complexes: Synthesis, characterization and anticarcinoma properties against human breast adenocarcinoma subtypes. Presented at the 2nd PG CRI 3-Minute Thesis competition, Virtual Competition, 13th Oct 2021.

- Poster presentation: Thato Medupe, Sharon Prince, and Siyabonga Ngubane., Synthesis, characterization, and antineoplastic activity of Redox-Active Diruthenium(II, III) complexes. Presented virtually on Twitter (@SACI_Chemistry), Royal Society of Chemistry/South African Chemical Institute Young Chemists, Virtual Symposium, 30 Sep - 01 Oct 2020.

- Poster Presentation: Thato Medupe, Sharon Prince, and Siyabonga Ngubane., Synthesis, characterization, and antineoplastic activity of Redox-Active Diruthenium(II, III) complexes. Presented at the 12th Annual Science Postgraduate Symposium at Stellenbosch University, South Africa, 2019.

- Poster Presentation: Thato Medupe, Sharon Prince, and Siyabonga Ngubane., Synthesis, characterization, and antineoplastic activity of Redox-Active Diruthenium(II, III) complexes. Presented at the Cape Organometallic Symposium (COS) at the University of Cape Town, South Africa, July 2019.

- Flash Talk + presentation: Thato Medupe, Sharon Prince, and Siyabonga Ngubane., Synthesis, characterization, and antineoplastic activity of Redox-Active Diruthenium(II, III) complexes. Presented at BMIC/LABIC XIX Brazilian Meeting on

Biological Inorganic Chemistry, VI Latin American Meeting on Biological Inorganic Chemistry, VII Brazillian Meeting on Rare Earth Metals, Fortaleza - CE, Brazil, 24 - 09 Sep 2018.

PUBLICATIONS

- C. Berg, S. Chari, K. Jurgaityte, A. Laurora, M. Naldony, F. Pope, D. Romano, T. Medupe, S. Prince, S. Ngubane, J. Baumgartner, B. Blom, Modulation of the solubility properties of arene ruthenium complexes bearing stannyl ligands as potential anti-cancer agents, Journal of Organometallic Chemistry (2019), doi: https://doi.org/10.1016/j.jorganchem.2019.04.002

- Medupe, T., Bellis, C., Autar, N., Siangwata, S., Mutomb, J-L., Prince, S., Ngubane, S. Anilinopyridinate-based Diruthenium(II, III) Paddlewheel Complexes: Synthesis, Characterization, and *In vitro* Cytotoxicity Studies against Human Breast Cancer Cell Lines. (*Manuscript in preparation*).

- Medupe, T., Bellis, C., Mkhize. S., Autar, N., Prince, S., Ngubane, S. Mono-substituted anilinopyridinate-triacetatoochlorodiruthenium(II, III) complexes: Preparation, characterization and anticarcinoma properties against human breast adenocarcinoma subtypes. (*Manuscript in preparation*).

LIST OF FIGURES

Chapter 3 Figures

LIST OF SCHEMES

LIST OF TABLES

LIST OF ABBREVIATIONS

%	Percentage
$[Ru_2(O_2CCH_3)_4Cl]$	Tetraacetatochlorodiruthenium(II, III)
°	Degrees
°C	Degrees Celsius
µA	Microamperes
μ_{eff}	Effective Magnetic Moment
^{13}C NMR	Carbon-13 Nuclear Magnetic Resonance
^{1}H NMR	Proton Nuclear Magnetic Resonance
Å	Angstrom
Ar	Aromatic
ATR	Attenuated Total Reflectance
br	broad
Calcd.	Calculated
$CDCl_3$	Deuterated Chloroform
CE	Counter Electrode
$CHCl_3$	Chloroform
cm^{-1}	Reciprocal Centimetres
d	doublet
DCM	Dichloromethane
ddd	doublet of doublets of doublets
DMSO	Dimethyl sulfoxide
$E_{1/2}$	Half-wave Potential
ER+ve	Oestrogen receptor positive
FTIR	Fourier Transform Infrared Spectroscopy
HOMO	Highest Occupied Molecular Orbital
HR(ESI)-MS	High Resolution (Electron Spray Ionization) Mass Spectrometry
HSQC	Heteronuclear Single Quantum Coherence Spectroscopy
Hz	Hertz
IC_{50}	Half-maximal inhibitory concentration
i_{pa}	Anodic Potential
i_{pc}	Cathodic Potential

IR	Infrared
J	Coupling constant
L	Ligand
LMCT	Ligand-to-Metal Charge Transfer
LUMO	Lowest Unoccupied Molecular Orbital
m	multiplet
M.P	Melting Point
m/z	Mass-to-charge ratio
MeCN	Acetonitrile
MeOH	Methanol
MLCT	Metal-to-Ligand Charge Transfer
mmol	Millimoles
mol	Moles
n	number of unpaired electrons
nm	nanometres
mL	millilitre
NMR	Nuclear Magnetic Resonance
PARP	Poly (ADP-ribose) polymerase
ppm	Parts per million
PTA	1,3,5-Triaza-7-phosphaadamantane
qt	quartet
R-ap	Electron withdrawing or donating substituted anilinopyridinate
RE	Reference Electrode
ROS	Reactive Oxygen Species
s	Singlet
SCE	Saturated Calomel Electrode
t	Triplet
TBACl	Tetrabutylammonium chloride
TBAP/TBAClO$_4$	Tetrabutylammonium perchlorate
UV-vis	Ultraviolet-visible
V	Voltz
WE	Working Electrode
X_m	Magnetic Susceptibility
γ-H2AX	Gamma-H2AX

δ	Chemical shift
λ_{nm}	Wavelength
ν	Wavenumber
ν_s	Vibrational stretching frequency

SIMILARITY INDEX REPORT

mdptha004:Thato_Medupe_-_Abstract,_Thesis_Synopsis,_and_PhD_Thesis_(Chapter_1_-_5)_Draft_3.pdf

ORIGINALITY REPORT

22%	16%	16%	4%
SIMILARITY INDEX	INTERNET SOURCES	PUBLICATIONS	STUDENT PAPERS

mdptha004:Thato_Medupe_-_Abstract,_Thesis_Synopsis,_and_PhD_Thesis_(Chapter_1_-_5)_Draft_3.pdf

by Thato Medupe

Submission date: 20-Jul-2023 06:20PM (UTC+0200)
Submission ID: 2134106493
File name: act,_Thesis_Synopsis,_and_PhD_Thesis__Chapter_1_-_5__Draft_3.pdf (6.67M)
Word count: 48458
Character count: 258522

TABLE OF CONTENTS

THESIS SYNOPSIS

This thesis titled "**Synthesis, Characterization, and Anticancer Activity of Arene Mono-Ruthenium and Heteroleptic Mixed-Valent Diruthenium Complexes**" addresses the development of metallodrugs as alternatives to the chemotherapeutic treatment of human breast MCF-7 and MDA-MB-231 adenocarcinoma cell lines. In a thesis format, this work is collated into individual chapters as follows:

Chapter 1 is an introductory and literature review chapter highlighting the prevalence, history, treatment regimen and management of cancer. In addition, this chapter sheds light on the use of transition metal complexes, particularly the platinum group metals (PGMs) class of compounds and their possible use as anticancer chemotherapeutic agents. The rationale, motivation, specific aims, and objectives of this research project are herein stated in detail.

By way of comparison, ***Chapter 2*** focuses on the synthesis, characterization, and cell viability preliminary screen of monoruthenium(II) arene organometallic complexes against oestrogen receptor-positive (ER+ve) human breast MCF-7 adenocarcinoma cells.

Chapter 3 discusses the synthesis of anilinopyridinate (ap) ligands, as well as the metal precursor tetraacetatechlorodiruthenium(II, III) complex $[Ru_2(O_2CCH_3)_4Cl]$, used in the preparation of the eight (8) complexes of the type $[Ru_2(O_2CCH_3)_3(R\text{-}ap)Cl]$ (where R is either an electron-withdrawing or donating group on the ap ligand). The synthesis, spectroscopy, electrochemistry, and X-Ray crystallography of these complexes of interest are discussed as well.

Chapter 4 addresses the short- and long-term cytotoxic properties of the synthesized $[Ru_2(O_2CCH_3)_3(R\text{-}ap)Cl]$ complexes against human breast adenocarcinoma and mammary non-malignant epithelial cell lines of choice. Mechanisms responsible for cell death that were probed via a combination of spectroscopic, analytical, and molecular cell biology techniques and discussed herein presented in this chapter.

In ***Chapter 5***, the experimental findings and future work insights involving structural modifications to enhance the anticancer properties of the proposed paddlewheel Ru_2^{5+} compounds are summarized and proposed in this chapter.

All supplementary spectroscopic, and cell biological data and protocols are presented in ***Chapter 6***.

CHAPTER 1

Metal Complexes as Anticancer Agents

1.1 Introduction: History and prevalence of cancer

Cancer, as defined by the National Cancer Institute (NCI), is characterized by a large group of abnormal cells dividing uncontrollably at a rapid rate and metastasising to nearby bodily tissues.[1] Cancers can be broadly classified as sarcoma, carcinoma, lymphoma, melanoma, and leukaemia. In this ever-changing society, cancer remains one of the crucial public health complications and one of the primary leading causes of mortality and morbidity. In 2008, the International Agency for Research on Cancer (IARC) identified 12.7 million cancer cases and 7.6 million deaths.[2] Additionally, about 56% of new cancer cases and 63% of deaths occurred in less developed countries. This number of deaths is anticipated to increase to 13.1 million by the year 2030. In 2020, 18.1 million new cases were reported, accounting for approximately 9.6 million deaths of both sexes and all ages globally.[3,4,5] However, these numbers in mortality reported in 2020 account for all cancer-related cases excluding non-melanoma skin cancer cases, as shown in Figure 1.1.

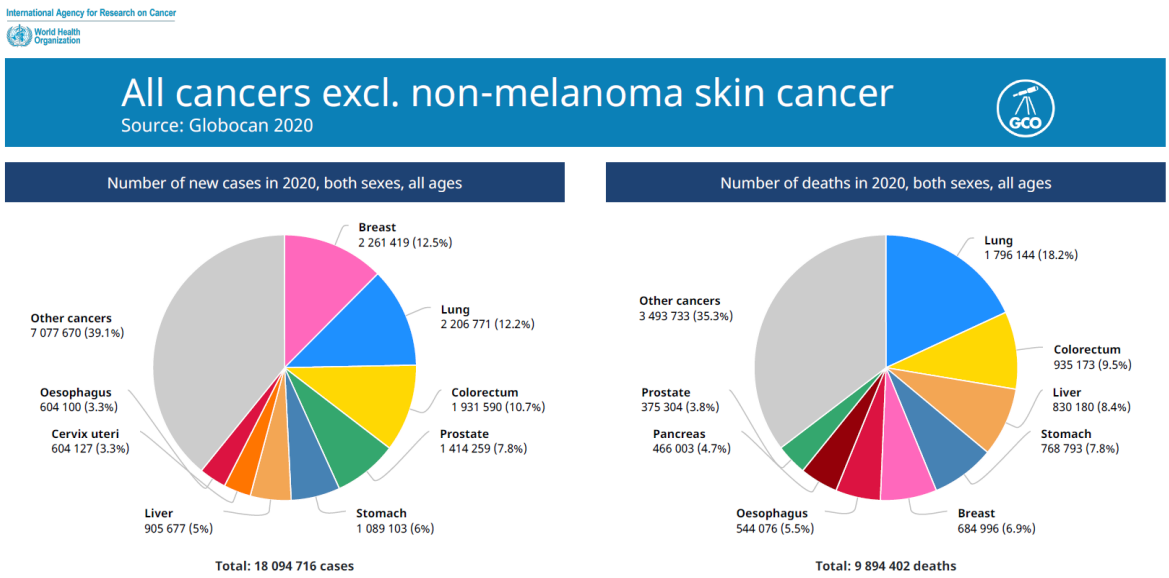

Figure 1.1 Cancer mortality statistics reported in 2020, excluding non-melanoma skin cancer.[5] Pie charts figure is obtained from The Global Cancer Observatory depository website: Globocan 2020.[6]

This approximation in cancer mortality surpasses the death toll statistics from HIV/Aids, tuberculosis and malaria combined reported in the same year.[7] According to the mortality rate estimates reported in 2019 by the World Health Organisation (WHO), cancer and coronary cardiovascular-related diseases are the leading causes of mortality in 127 of the 183 countries sampled for data collection. In 50 countries, which include most sub-Saharan countries, cancer

and cardiovascular diseases were among the top 3 causes of premature death, as illustrated in Figure 1.2.[5,8] The provision and availability of the appropriate healthcare treatment vary significantly from one country or nation to another. This is of great concern as less than 15% of low-income countries receive very little attention, while an extensive treatment regimen plan is readily available to most high-income-generating countries.

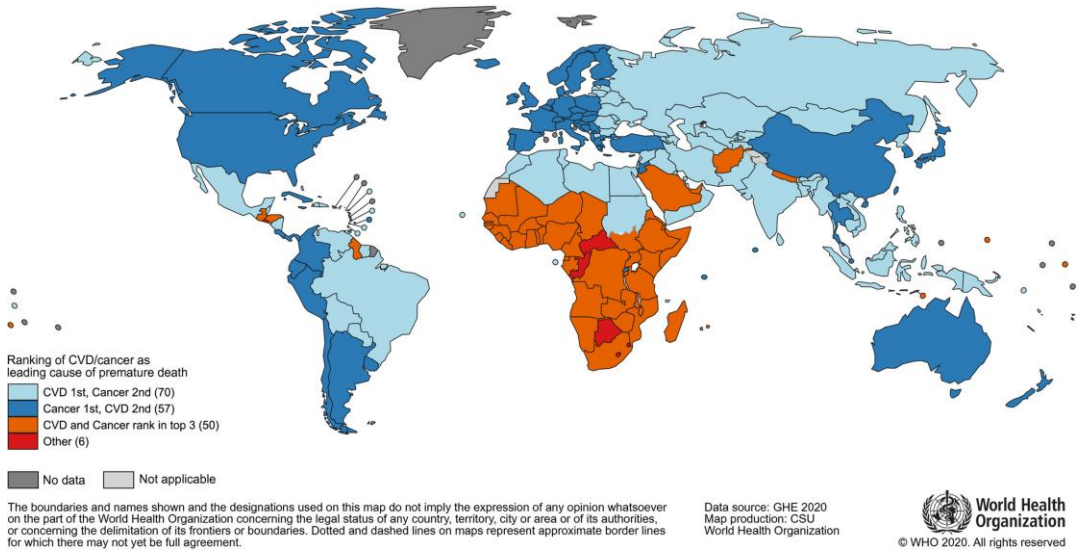

Figure 1.2 Global map highlighting the mortality rankings from 183 countries caused by cancer and cardiovascular-related diseases, reported in 2020. The graphical map figure is obtained from The World Health Organization (WHO) depository website.[5]

In South Africa, the GLOBOCAN 2020 report highlights a total of approximately 108 thousand cancer cases and a total number of 56 thousand death cases, as indicated in Figure 1.3.[5,9] Furthermore, the reported new cases of cancer were due to unclassified cancers followed by breast cancers.

There are various methods of treatment aimed at improving both primitive and advanced cancer stages. These include radiotherapy, surgical implementation, and systemic therapy such as chemotherapy, hormonal treatments, and biologically targeted therapies. It is worth noting that every cancer is peculiar to its type of treatment regimen and the patient. Therefore, an accurate diagnosis is of great importance and crucial for the determination and proper selection of an effective treatment regimen.

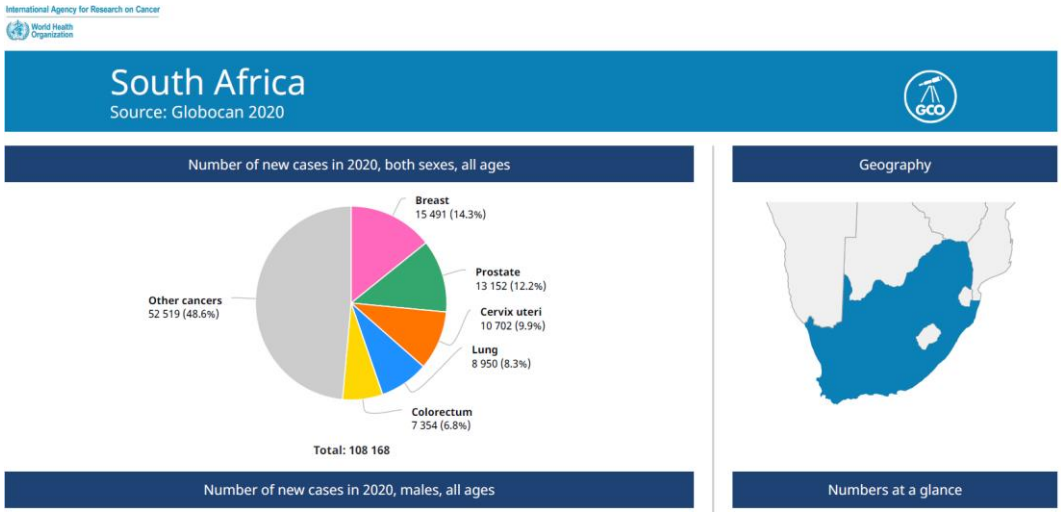

Figure 1.3 The total number of cancer new cases in South Africa, as reported by GLOBOCAN in 2020. Both figures are obtained from The Global Cancer Observatory depository website: Globocan 2020.[5,9]

1.2 Current treatment regimens and management of cancer

Before considering a type of treatment plan or regimen, it is important to determine the achievable goals of a particular treatment plan that can lead to better outcomes directed towards curing cancer, increasing the lifespan and the quality of life of the patient. This can be achieved by considering a holistic approach including the provision of physical, psychosocial and spiritual well-being, and palliative care/support, especially in the late stages of cancer.[10]

While the primal methods of treatment previously mentioned such as chemotherapy, radiotherapy and surgery are implemented to treat tumours, cancer remains a problematic disease with high mortality rates.[5,11] Metastasis, the spread of cancerous cells to different areas of the body often *via* the lymphatic system,[12] accounts for high mortality rates with a low probability of recovery once metastasis has occurred.[13]

Chemotherapy as a treatment regimen is the most common and widely utilized treatment to cater for malignant tumours.[14] However, chemotherapy is associated with numerous debilitating and expeditious side effects which can affect vital organs such as the heart, lungs, and brain.[15] The immediate ramifications of toxicity are noticeable through implications such as alterations of the skin and hair loss, vomiting, depletion of bone marrow and low blood pressure, and infection of the gastrointestinal tract, and kidneys. Furthermore, chronic ramifications include carcinogenicity, infertility, and drug resistance.[15] Of the 132 cancer

chemotherapeutic drugs approved by the United States Food and Drug Administration (US FDA), a total of 56 drugs are known to induce oxidative stress with examples including cisplatin, anthracyclines, cyclophosphamide, busulfan, mitomycin, fluorouracil, cytarabine, and bleomycin (Figure 1.4).[16]

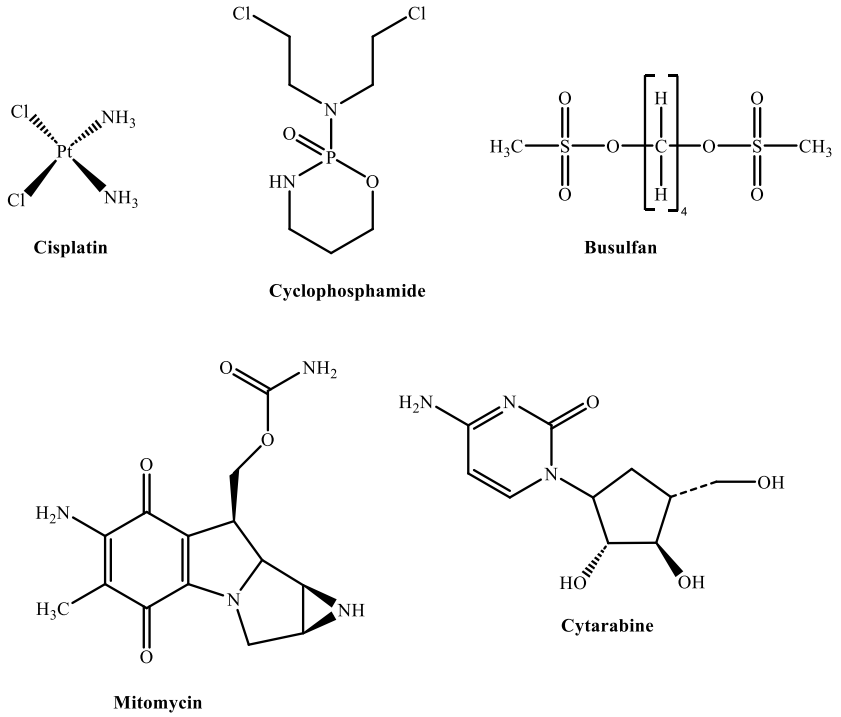

Figure 1.4 Examples of chemotherapeutics drugs approved by the US FDA responsible for inducing oxidative stress.[16]

Due to the highlighted complications and challenges associated with chemotherapeutic anticancer drugs approved by the US FDA, extensive research in the design synthesis and development of chemotherapeutic anticancer agents incorporating metal centres through coordination to organic scaffolds or ligands (metallodrugs) has received much attention. Metallodrugs are unique and advantageous as they offer the possibility of forming diverse classes of compounds, due to their rich redox chemical properties (ability to access various oxidation states), the range of coordination numbers and geometries, and due to the ability to fine-tune the thermodynamic and kinetic properties of ligand substitution.[17] It is against this backdrop that metallodrugs are explored and applied in biological research work.

1.3 Transition metal complexes used as anticancer agents

Many metal-based compounds with coordinated organic molecules have played a crucial role in the medicinal drug discovery research field, with research efforts directed towards the development and applications in clinical practices treating several pathogens causing bacterial infections and potential use as anticancer activity.[18,19] Transition metal coordination complexes offer endless chemical synthetic possibilities for the drug design and development of anticancer chemotherapeutic agents. The existence of the metal complexes in various oxidation states, geometry, their interchangeable hard and soft properties, thermodynamic and kinetic characteristics, and the ability to modify the structures of their coordinated ligands and fine-tune their electronic properties make them unique and offer the possibility to explore their reactivities with biological molecular targets. These metal complexes are often termed "pro-drugs" as they undergo chemical transformations/modifications and are activated while making their way or upon arrival and interaction with the biological target site.[20] The chemical transformations/modifications referred to often involve a change in oxidation state, the displacement of one or several coordinated labile ligands, and the ring opening of a coordinated chelate ligand. The metal-organic prodrug can be selectively activated upon exposure to external sources such as a light source or radiation, sound, or heat once they reach the target site. Their reactivities with their biological molecular targets can further be exploited to understand the mode of action suitable for the desired biological activity.[21] The diverse nature of the transition metal complexes may also be the key to fighting issues related to drug resistance, which remains one of the major research challenges towards the treatment of cancer.

1.3.1 Platinum-based metal complexes as anticancer agents

The use of transition metal complexes in biological applications led to the serendipitous discovery of a class of platinum(II) metal-based chemotherapeutic agents administered intravenously to cancer patients and used in chemotherapeutic treatment regimens. Cisplatin, *cis*-diamminedichloridoplatinum(II) (Figure 1.5), is one of the first metal inorganic complexes to be studied for its antiproliferative effects against bacterial growth and generation, and later approved for cancer therapy.[22] Cisplatin was initially synthesized by Michele Peyrone and later discovered by Barnett Rosenberg in the late 1960s for its cytostatic properties against bacterial proliferation.[22] Further onwards, clinical trials were conducted in 1971[23] with the outcome obtained leading to the approval for use alone or in combination for the treatment of testicular and ovarian cancers by the US Food and Drug Administration and several European countries

in 1979.[24] Later onwards, cisplatin second- and third-generation derivates have been approved regionally in Japan, South Korea and China for the treatment of various cancers (Figure 1.5).[25]

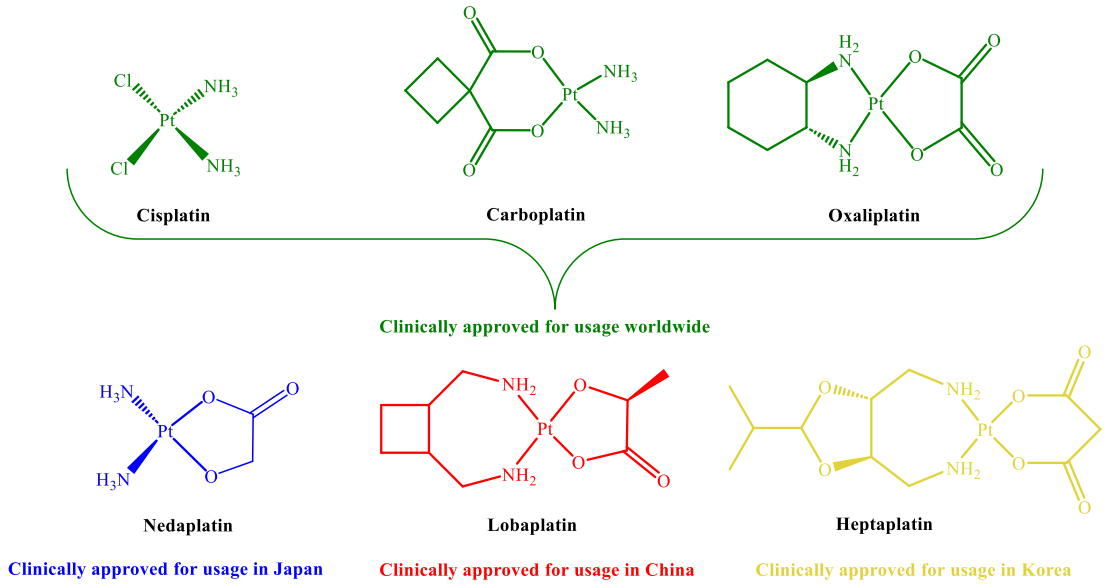

Figure 1.5 Chemical structures of platinum(II) metallodrugs used as anticancer chemotherapeutic regimens.[22,25]

Its treatment usage is inclusive of, but not limited to a wide range of solid neoplastic cancers of the bladder, head and neck, lymphoma, prostate, lung, cervix, and in some paediatric cancers.[24] The usage of platinum(II) drugs can be coupled with other modes of treatment methods such as radiotherapy, used as singular or in combination with other cytotoxic/cytostatic agents.

1.3.2 Mechanism of action of platinum-based metal complexes

The common classical mechanism of the cisplatin metallodrug is governed by its controlled aquation, migration of the complex to the cellular target and binding to the genomic DNA nucleotide bases.[26] The metal complex was initially thought to enter the cellular environment through a passive diffusion process, as its uptake and accumulation within the cell are concentration-dependent and non-saturable. However, cellular entry and uptake of the cisplatin drug is facilitated by the copper transporter 1 (CTR1) transmembrane protein, a protein involved in copper homeostasis.[27] Once found on the cytoplasm of the cell, due to its inert nature, the metal complex is intracellularly activated by aquation reactions which involve the chloride ligands undergoing either mono- (yielding $[Pt(NH_3)_2Cl(OH_2)]^+$ product) or bi-

(yielding $[Pt(NH_3)_2Cl(OH_2)]^+$ species) chloride-water ligand substitution reaction (Scheme 1.1).[25]

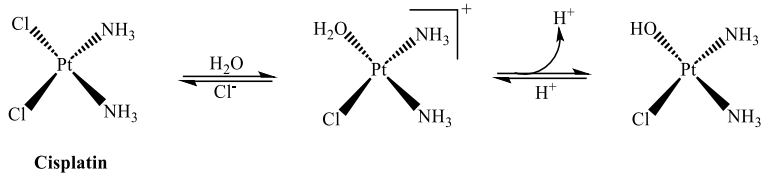

Cisplatin

Scheme 1.1 Hydrolysis reaction of cisplatin yielding the aqua-platinated species.[25]

The hydrolysis reaction that occurs upon intracellular migration of dichlorodiammineplatinum(II) complex (cisplatin) is thought to be a crucial step in the activation of the complex before binding to the DNA nucleotide bases.[28] This reaction occurs with great ease intracellularly in the cytoplasm, resulting in a decrease in chloride ion concentration ([**Cl**$^-$] = 4 - 20 mM when compared with [**Cl**$^-$] ≈ 100 mM in the extracellular environment) and thus the formation of highly reactive hydrolysed mono- and bi-aqua cisplatin adducts, as described previously. However, *in vitro* experimental work investigating the rate of aquation reactions of cisplatin in the presence of oligonucleotide 5′-d(AATT**GG**TACCAATT)-3, consisting of the GpG intra-strand binding site, suggests that the mono-aquaplatinum(II) complex is more reactive and binds to the intra-strand over the di-aquaplatinum(II) complex.[29] This is closely followed by an electrophilic attack on the nucleophilic N7-reactive positions of the guanosine and adenosine purine nucleotide base of the DNA (Scheme 1.2).

The two reactive sites on the platinum(II) metal centre allow for the generation of a cross-link between two adjacent guanines. Additionally, platinum(II) can form covalent coordination bonds with guanine bases of different double-stranded DNA, resulting in the generation of DNA–DNA inter- and intra-strand or protein–DNA platinum(II) complex adducts. The 1,2-intrastrand guanine and guanine d(GpG) and the neighbouring adenine and guanine d(ApG) crosslinks adducts are the most eminent platinated-DNA adducts present within the nucleus of the cell. The cytotoxic properties of cisplatin are reported to originate from the 1,2-intrastrand *d*(GpG) crosslinks which induce a significant distortion of the DNA helical structure and inhibits the unwinding of the helical double-stranded DNA, which in turn halts DNA replication and transcription processes and thus initiating apoptotic cell death.[30,31]

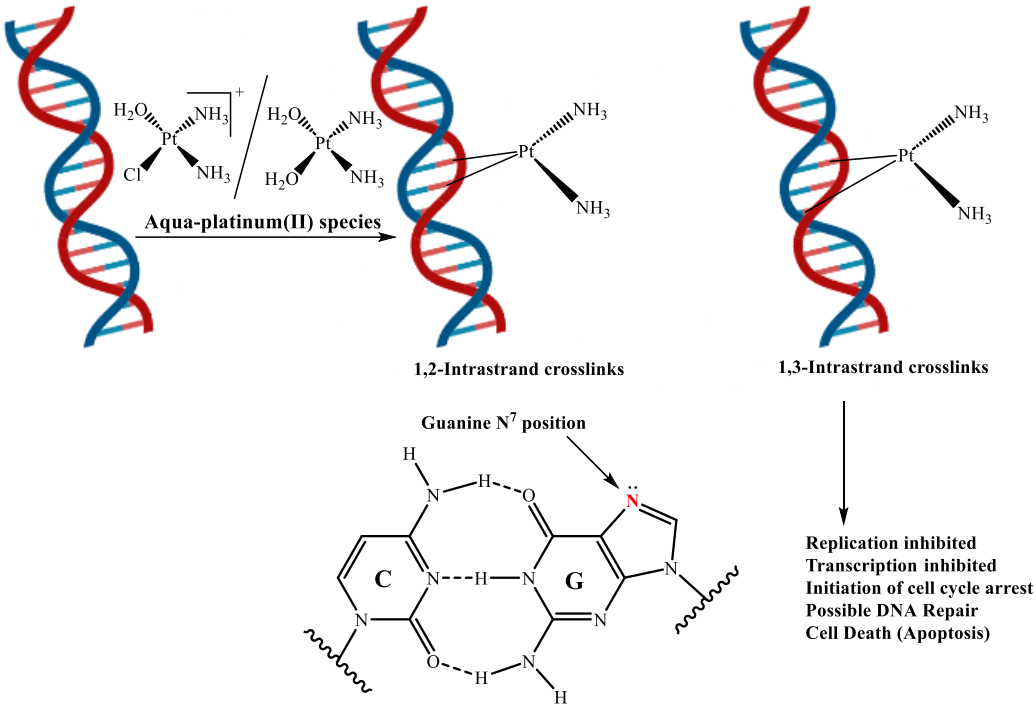

Scheme 1.2 Schematic representation of the covalent binding mode of cisplatin to the N^7-position site of purines, forming 1,2- or 1,3-intrastrand crosslinks. The platinum-DNA adducts cause an array of cellular responses including inhibition of replication and transcription, induction of p53 tumour suppressor protein, cell cycle arrest, DNA repair and apoptosis as a mechanism of cell death.[32] The diagram was redrawn and created using BioRender.com online software.

Several protein families can detect and recognise platinum-DNA adducts such as nucleotide excision repair (NER) and mismatch repair (MMR) proteins.[33] MMR proteins are often mistaken for being responsible for repairing cisplatin-DNA adducts. This is not the case as this class of proteins functions to repair DNA damage. However, failure to repair DNA lesions often results in the activation of the signal transduction molecular pathway, initiating cell death *via* apoptosis.[33] Besides the "traditionally" reported platinum(II)-DNA binding, there are a few other mechanisms of cell death induced by the cisplatin listed as follows, as depicted in Figure 1.6.[34]

Cisplatin induces cell cycle arrest (G1, S and G2 phase) through activation of checkpoint kinases (Chk1 and Chk2, responsible for G and S phase arrest). Retraction of the mentioned G and S phase arrests may result in cellular apoptosis by forcing cells to impulsively undergo cell

cycle arrest in the unrepaired DNA damage phase. Thus, enabling cell apoptosis through the NER mechanism.

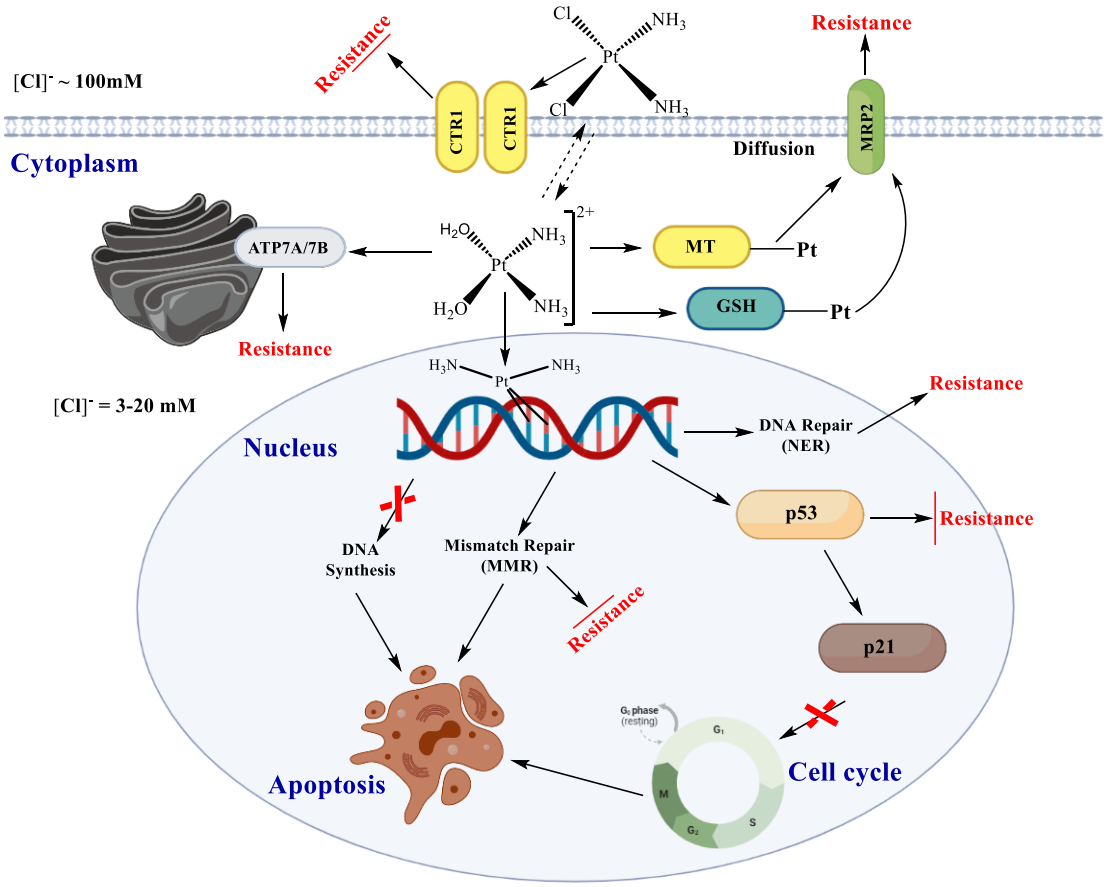

Figure 1.6 Mechanism of action of cisplatin: Schematic representation of the chemotherapeutic drug and drug resistance pathways in a tumourigenic cell.[35] The diagram was redrawn and created using BioRender.com online software.

Oxidative stress, induced by the production of reactive oxygen species (ROS) intracellularly contributes to an increase in lipid peroxidation. This results in modifications of structural proteins, enzymes, and signal molecular transduction pathways and ultimately leads to cellular apoptosis.[36] Cisplatin promotes an increase in superoxide production, leading to the generation of hydrogen peroxide molecules that can, in turn, form hydroxyl free radicals. These newly formed hydroxyl free radicals are unstable, extremely reactive and can interact with polyunsaturated fatty acids in the cell membrane. To regulate the overexpression of ROS, glutathione, and antioxidant enzymes (glutathione peroxidase and glutathione reductase) are released to minimize the overload of these ROS intracellularly. However, sometimes the production of antioxidants does not occur at the optimal level as needed, leading to an overload

and the presence of H_2O_2 and toxic lipid peroxides. These chemical processes result in Ca^{2+} influx and lead to apoptosis.[36]

Concerning the mitochondrion, the formation of ROS tends to drastically alter the mitochondrial respiratory function and can cause cellular dysfunction. When coupled with Bax (Bcl2 in association with X) and Ca^{2+}, causes mitochondrial DNA damage and a drop in mitochondrial permeability transition. This ultimately leads to a mitochondrial rupture and thus initiates cellular apoptosis which is ATP (adenosine triphosphate) dependent.

1.3.3 Drug resistance issues associated with platinum-based metal complexes

Despite the above-mentioned benefits of cisplatin chemotherapy, drug resistance remains a great challenge and a hurdle in achieving a successful orally administered chemotherapeutic drug that eradicates cancer cells effectively with no adverse side effects having an impact on the lives of patients. This is attributed to the fact that many cancer malignancies are resistant to cisplatin and develop resistance gradually after initial intravenous administration and response.[37] Unfortunately, a proportion (approximately 1%) of intravenously administered cisplatin reaches its pharmacological target, the genomic nuclear double-stranded DNA.[38] As discussed previously, there are several factors contributing to cisplatin resistance. Cellular uptake and accumulation of the aqua-platinated species in the cell *via* transportation through the copper exporters ATP7A/B across the cell membrane is associated with a good prognosis and therapeutic response. The depletion and deletion of CTR1 would result in cisplatin uptake and accumulation, thus increasing cisplatin drug resistance.[27] The aqua-platinum(II) drug adducts become deactivated by reacting rapidly with various cytoplasmic substrates such as nucleophilic thiol-containing sulfhydryl groups (reduced glutathione, methionine, metallothioneins and other cysteine-rich proteins) and nitrogen donor atoms on nucleic acids.[39] Some DNA lesions such as protein-Pt(II)-DNA and cisplatin-DNA adducts may become reorganized by several cellular proteins and enzymes (DNA polymerase) resulting in DNA damage repair.

The clinically prepared platinum(II) drug agents are among the most effective and efficient antineoplastic drugs used to treat various human malignancies. The cytotoxic properties of the platinum metal-centred drugs are attributed to their ability to target multiple intracellular sites to trigger tumour cell death. Nevertheless, due to the intracellular drug resistance previously detailed extensively, other platinum derivatives complexes were investigated and reported to

possess anticancer therapeutic activities.[40] These included platinum metal-centred complexes such as oxaliplatin, carboplatin, nedaplatin and lobaplatin (Figure 1.5). Platinum-based complexes not only target tumour cells but also target normal functioning cells required to carry out metabolic processes. These complexes have been indicated to display undesirable complications such as gastrointestinal, and haematological toxicity, nausea, deficiency in blood cell count and production of blood platelet in bone marrow, the inefficacy of the immune system (immunosuppression), and hearing loss. More distinct side effects include nephrotoxicity, neurotoxicity and hearing loss in patients undergoing chemotherapy.[41] Inevitably, these shortcomings have led to the applicability of cisplatin being limited to a range of malignant tumours due to issues associated with selectivity.[42,43] Furthermore, such shortcomings have fuelled the search towards the development of more effective and selective novel non-platinum group transition metal complexes in pursuit of combating the disadvantages associated with clinical platinum-based chemotherapy.

1.3.4 Ruthenium-based metal complexes as anticancer agents

Ruthenium (Ru) is a platinum group metal (PGM), amongst other transition metals, and is of enormous interest in the generation of metallopharmaceutical chemotherapeutic agents in cancer research due to its ability to exist in various stable oxidation states (namely, Ru(II), Ru(III) and Ru(IV)), all can easily undergo redox chemical processes due to the low energy barriers between these oxidation states.[19,44] When a metal centre is coordinated to organic molecules or a ligand to form a metal complex, the coordination geometry, stability, as well as their associated thermodynamic, kinetic and electronic properties can be altered to allow for selective binding to biological targets.[44] Ruthenium compounds have various potential pharmacological advantages as anticancer agents, with antimetastatic properties and low systemic toxicity profiles.[45] Additionally, they tend to accumulate in neoplastic solid tumours, with their anti-cancer properties attributed to their ability to mimic iron-binding to biomolecules such as serum plasma proteins (human serum albumin and transferrin), all responsible for solubilizing and transportation of iron in plasma.[21] Ru(III) complexes remain inactive in their +3 oxidation state until they reach their target tumour site. Upon arrival at their biological target site, they become reduced to their reactive Ru(II) oxidation state by biological reducing agents such as ascorbate and glutathione. This “activation by reduction” process is responsible for the efficacy of the drug in the hypoxic tumour environment, with tumours known to be resistant to chemotherapy and/or radiotherapy.[46] Additionally, ruthenium complexes possessing octahedral geometries, are best suitable for biological evaluation and

applications due to the slow ligand exchange rates resembling cellular processes.[47] Research studies[48] conducted on ruthenium complexes have revealed that complexes are expected to have good sensitivity for tumours and are less toxic. This is attributed to the ruthenium metal being able to mimic the action of iron by binding to the biological molecules, leading to a new mode of action and thus, the potential to overcome resistance experienced by other platinum drugs.[48,49]

1.3.5 Ruthenium(III)-based metal complexes as anticancer agents

The search for alternative non-platinum anticancer agents has led to the discovery of ruthenium(III) complexes of the formula $HL[RuCl_4L_2]$, where the inner sphere coordinated ligand (L) is a heterocyclic ligand bonded to ruthenium metal through the nitrogen atom while HL is the protonated ligand. These ruthenium(III) complexes show astounding activity against various tumour models *in vitro* and *in vivo* experiments, more so against autochthonous colorectal tumours in rats.[50] Their antiproliferative effects were significant when exposed to two human colon cancer cell lines, SW707 and SW948, respectively.[51] Ruthenium red or *fac*-$[Ru(Cl)_3(NH_3)_3]$, is among the first ruthenium metal-centred compounds to be evaluated for their biological activity.[52] When tested against EMT-6 sarcoma *in vivo* mice models, *fac*-$[Ru(Cl)_3(NH_3)_3]$ was reported to selectively localize in tumours with no appreciable chemotherapeutic activity. Due to its poor solubility in aqueous media, the metal complex was prohibited for its usage in clinical trials. This has led to further intensive research work which led to the successful discovery of Ru(III)/(II)-chloride-N-heterocyclic complexes such as NAMI-A, KP1019, and NKP1339. The mentioned complexes are currently in phase I and early phase II clinical evaluation (Figure 1.7).[53,54,55]

Generally, ruthenium complexes having an overall charge of +3 are more inert toward ligand exchange/substitution chemical reactions compared to complexes existing in a lower oxidation state of +2. Ruthenium(III) complexes are often administered in their “inactive” state and are considered prodrugs, implying that they undergo bio-transformations in the extracellular environment. Like some of the platinum complexes, ruthenium(III) complexes undergo a rapid halide-aqua substitution reaction (replacement of the axial chloride ligands by aqua ligands), resulting in an intermediate active species with higher reactivity and affinity toward biomolecules found in the intracellular matrix.[56]

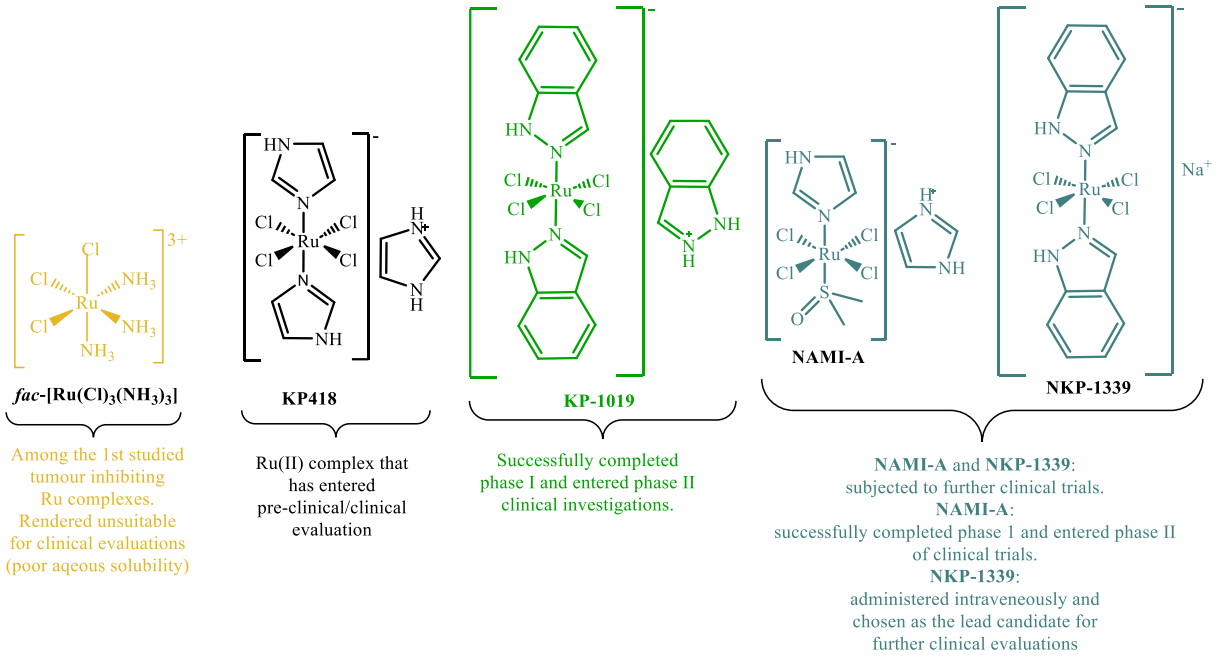

Figure 1.7 Structures of ruthenium(III) complexes namely; *fac*-[Ru(Cl)$_3$(NH$_3$)$_3$], NAMI-A, KP418, KP1019, and NKP1339.[52,53,54,55,57]

This facile redox cellular process decreases the π-acceptor ability of the ruthenium metal centre, enhancing the lability of the coordinated π-donor ligands. Due to their strong affinity and reactivity within the cytoplasm, complexes can be converted into the active ruthenium(II) species in the cytoplasm by biological reducing agents such as GSH, ascorbate or NADH.

1.3.5.1 Imidazolium-trans-DMSO-imidazole-tetrachlororuthenium(III), or NAMI-A

The imidazolium-trans-DMSO-imidazole-tetrachlororuthenium(III), or NAMI-A, is a ruthenium(III) based metal centred complex, reported and discovered by Enzo Alessio, Giovanni Mestroni and Gianni Sava in Trieste.[53] The chemical structure of NAMI-A consists of a distorted octahedral geometry and the ruthenium(III) metal ion coordinated to four equatorial chloride ligands, with imidazole and dimethylsulfoxide ligands *trans*- to one another. Compared to its parent molecule NAMI, NAMI-A consists of an Imidazole-H$^+$ (ImH$^+$) cation which replaced the sodium cation (Na$^+$). It is one of the first ruthenium metallodrugs derived from NAMI to have entered clinical evaluation, with great stability in the solid state and with appreciable solubility in water.[58]

Although the prodrug possesses very little intrinsic cytotoxic properties compared to cisplatin when tested on several cancer cell lines,[59,60] it shows significant appreciable selectivity and

affinity for tumours, possesses anti-metastatic/anti-migration properties (prevents the formation of metastatic tumours) and inhibits secondary metastatic tumour formation. In contrast, a study undertaken to investigate the cytotoxic properties of NAMI-A against an array of leukaemia cell lines suggested that the drug prohibits their proliferation at a faster rate than cisplatin.[60] Furthermore, the induction of cell death occurred *via* an apoptotic pathway as the operative mechanism, with the cytotoxic properties arising from the selective blockade of KCA 3.1 channels, thus, making the metallodrug suitable for clinical evaluation in oncology.[61] Phase I studies of NAMI-A have been completed successfully and have progressed to Phase II clinical trials that are currently ongoing.[58] Preclinical pharmacological research work suggests that NAMI-A decreases lung metastasis significantly compared to its parent molecule, and is selective for lung metastasis of murine tumours.[61] This favourable activity was also observed in experimental *in vivo* mice models with Lewis lung carcinoma. Overall, the metastatic activity of NAMI-A is likely to be independent of the primary tumour type and stage of metastatic tumour growth.[62,63]

Despite the extensive *in vitro* and *in vivo* investigations performed, the operative biological and pharmacological molecular mode of action of NAMI-A remains largely unclear and debatable.[64] However, it is well understood that the biological properties of octahedral ruthenium(III) complexes mainly arise from interactions of NAMI-A with extracellular biomolecules such as blood serum proteins and collagen proteins, and cytoplasmic enzymes. The evaluation of serum protein and albumin binding (which affects the biodistribution, bioavailability and pharmacokinetics) is marked as a prerequisite in the development process of a drug by the FDA, since the binding of a drug to the mentioned biomolecular proteins may form part of an effective strategy to achieving an efficient mode of transport.[64] Additionally, human serum albumin drug binding aids tumour mass targeting due to its accumulation in malignancies and inflamed tissues due to the enhanced permeability and retention (EPR) effect.[65]

In the human endothelial cell line ECV304, NAMI-A was observed to induce apoptosis as a mechanism of cell death, through the hindrance of the MEK/ERK signalling pathway.[66] Additionally, NAMI-A interacts with cell cycle regulation, leading to a temporal accumulation of cancerous cells in the G_2-M phase.[63,67] Upon NAMI-A drug exposure to myelogenous K562 leukaemia cells, a G_2-M cell cycle block was induced. Furthermore, an appreciable accumulation of K562 leukaemia cells was observed in the G_2-M phase cell cycle upon 24

hours of drug treatment at concentrations above 5 μM, leading to the activation of specific apoptotic pathways resulting in cell death.[60] Furthermore, upon exposure to lung metastasis, the capsule thickness surrounding the primary tumour along with the extracellular matrix surrounding the tumour blood vessels are greatly enhanced. As a result, the tumour cells cease to invade the surrounding blood vessels and tissues.[62]

1.3.5.2 Sodium trans-[tetrachlorobis(1H-indazole)ruthenium(III)], or NKP-1339

NKP-1339,[51] or sodium trans-[tetrachlorobis(1H-indazole)ruthenium(III)], is the sodium salt analogue of KP1019 that shares similar structural motifs as the NAMI-A, owing to its octahedral geometry and the coordination of the chloride ligands in an equatorial plane. The complex is one of the synthesized ruthenium(III) complexes to have undergone intensive biological and clinical evaluations. The selection of the complex as a drug lead for further clinical evaluation was attributed to its enhanced water solubility properties, compared to the previously synthesized complex, KP1019. NKP-1339 is categorized as a prodrug, with aquation reactions occurring at a steady rate compared to KP1019 and was previously synthesized as a precursor complex used in the formulation of KP1019 in clinical evaluations.[51,55] Owing to its enhanced solubility, this metallodrug was incorporated into clinical trials. Thus, combating the dose limitations by the high infusion volume motivates for clinical administration of larger drug molecules at higher doses. Phase I clinical evaluations involving the NKP1339 administration were deemed successful as evidenced by the clinical anticancer effects of the metallodrug when 34 patients with several types of solid tumours were subjected to 30 - 90-minute infusions on days 1, 8 and 15 of a 28-day cycle with 9 different drug-dosage (20, 40, 80, 160, 320, 420, 500, 625 and 780 mg/m^{-2} body weight).[55] However, treatment of NKP-1339 at high doses ($\approx > 625$ mg/m^{-2}) led to the discolouration of plasma to a transient green colour, with no noticeable symptoms. Additionally, patients with gastrointestinal neuroendocrine tumours (NET) have either experienced a partial response or disease stabilization. Disease stabilization was observed in patients with various solid tumours including non-small cell lung cancer, sarcoma, colorectal cancer, and an unknown primary tumour. NKP1339 administration is also associated with undesirable ramifications which are often manageable, with common side effects including mild to moderate nausea, vomiting and fatigue.

NKP-1339, along with NAMI-A and KP1019, is administered intravenously and forms non-covalent bonds with proteins, particularly to albumin and transferrin in the bloodstream.[68] The

chemical reaction of NKP-1339 with the transferrin is reported to occur rapidly within only a few minutes, compared to the imidazole analogue KP418 (Figure 1.7) which takes several hours. This was demonstrated by the preclinical *in vitro* experiments[43] (ICP-MS measurements) which suggests that the degree of uptake of NKP-1339 by the epithelial human colorectal cancer cells HCT116 and SW480, occurs within 2 hours and is significantly dependent on the serum concentration in biological media.

The formation of NKP-1339-transferrin adducts is said to be kinetically preferred, while stable NKP-1339-serum albumin adducts are thermodynamically preferred and favoured.[68] Additionally, the formation of the NKP1339-serum albumin adduct may result in selective accumulation in malignant tumour cells and inflamed tissues, due to the oozing of blood capillaries combined with the defect of lymphatic drainage *via* the exploitation of the enhanced permeability and retention (EPR) effect.[69] This is a strategy noted to be utilised by the nature of octahedral heterocyclic ruthenium(III) complexes. The EPR effect aids the accumulation of macromolecules (> 40 kDa) such as human serum albumin in solid tumours, which are retained for longer duration periods because of the inefficient lymphatic drainage.[69] In *in vitro* preclinical studies (cell culture), the anticancer effects of NKP-1339 are minimal upon a decrease in intracellular serum concentration. This suggests that the formation of NKP-1339-serum albumin adducts leads to a decrease in activity *in vitro* cell cultures, as evidenced by the absence of any EPR effect. Additionally, conditions *in vitro* cell cultures may be less favourable for protein-assisted uptake into cancer cells. Furthermore, a high accumulation of NKP-1339 in SW480 colorectal cells was observed with no dependency or coordination with serum albumin. Ultimately, these *in vitro* preclinical studies are in accord with the notion that ruthenium(III) complexes act as prodrugs and bind to serum proteins for transport and delivery purposes, and are not reduced effectively once bonded to serum proteins. Thus, activation by reduction occurs intracellularly upon detachment from protein and arrival at the targeted site.[70]

1.3.5.3 Mechanism of action of Ru(III)-chloro-N-heterocyclic complexes, KP1019 and NKP-1339

The proposed mode of action of NKP-1339, owing to its anticancer properties, is strongly linked with their redox properties and involves the reduction of ruthenium(III) to active species ruthenium(II) by biological reducing agents (as shown in Figure 1.8).[71] This is shortly followed by the reaction of ruthenium(II) active species with numerous diverse biological molecules.[72] NKP-1399, like other reported chloride-N-heterocyclic ruthenium(II) and platinum(II)

complexes, involves binding to the guanine nucleotide base to form metal ion complex-DNA adducts. However, the binding to the guanine nucleotide base, which halts replication and DNA synthesis, is not only the primary mechanism of cell death.[49] Ruthenium(III) complexes are well capable of interfering with the redox chemical balance of a cell, either *via* direct or indirect chemical processes or mechanisms.[38] This includes the inhibition of DNA synthesis, induction of G2/M phase cell cycle arrest,[73] initiations of both intrinsic[55] and extrinsic apoptosis.[74]

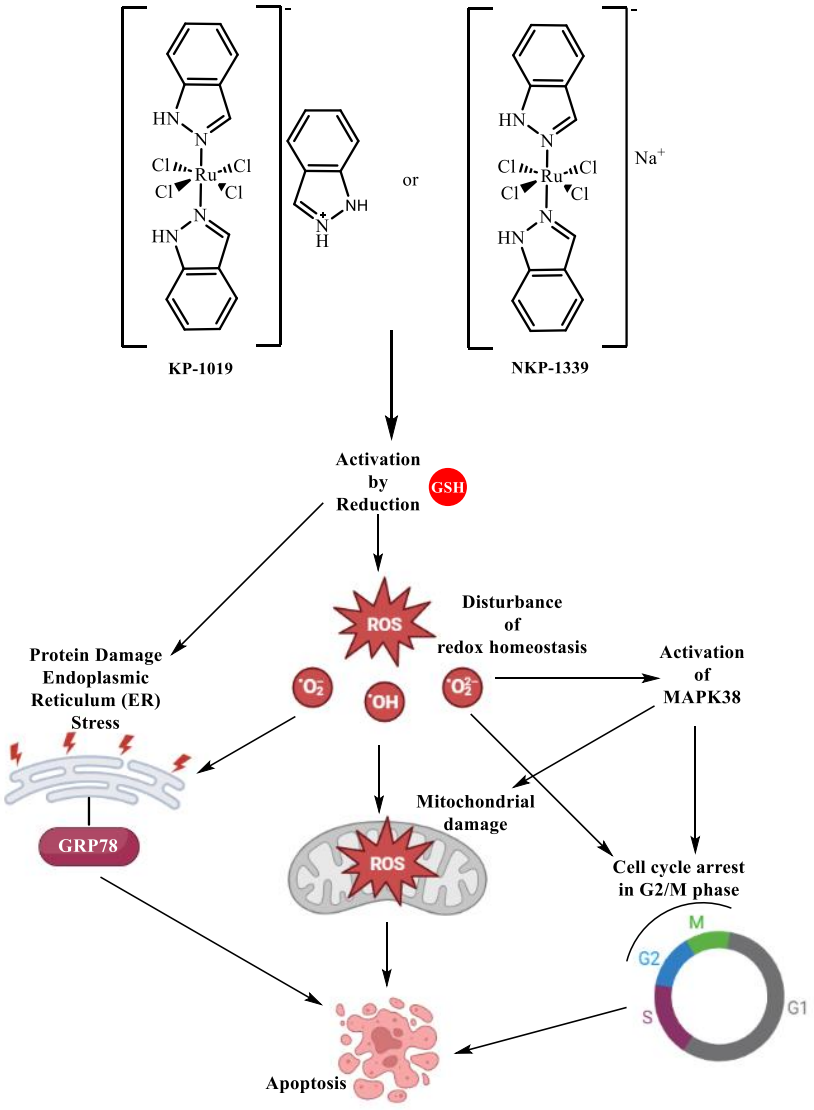

Figure 1.8 Multiple mechanisms of action responsible for the anticancer activity of KP1019 and NKP-1339.[55,71] The diagram was redrawn and created using BioRender.com online software.

Ruthenium(III) prodrugs can participate in chemical reactions resembling the Fenton-like reactions[75,76] presented below:

$Fe(II) + H_2O_2 \rightarrow Fe(III) + {}^{\cdot}OH + OH^{-}$ (Fenton reaction)

The following reactions are noted to involve free radicals presented in equations (1) – (3) as follows[76]:

$\cdot OH + H_2O_2 \rightarrow H_2O_2 + H^{+} + O_2$ (1)

$\cdot OH + Fe(II) \rightarrow Fe(III) + OH^{-}$ (2)

$ROOH + Fe(II) \rightarrow Fe(III) + RO^{-} + \cdot OH$ (3)

where ROOH = lipid hydroperoxides.

These reactions enable the formation of reactive oxygen species (ROS) molecules. On the contrary, the formation of ruthenium(II)-glutathione conjugates (*via* reactions of intracellular GSH with ruthenium(III) prodrugs) may result in a depletion of GSH. The lack of abundant GSH may render cancer cells more prone to endo- and exogenous oxidative stress. This was evidenced by the accumulation of ROS molecules when colorectal tumour cells SW480 and HT29 were subjected to KP1019 treatment, thus suggesting the involvement of the generation of ROS in the mode of action accountable for the anticancer activity of NKP-1339.[77]

NAMI-A and NKP-1339, are well-known nitric oxide ($NO^{\cdot}$) scavengers (forming of Ru(II)-NO^{+} species).[78] The presence of $NO^{\cdot}$ signals a diverse range of physiological processes, primarily in vascular homeostasis, neurotransmission, inflammatory/immune response and tumour progressions. This leads to a negative impact on endothelial cell migration and angiogenesis induced by KP1019 and NKP-1339. Nonetheless, due to this high redox chemical imbalance (overproduction of ROS species) that leads to cell stress, the induction of cancer cellular apoptosis by NKP-1339 and KP1019 exposure was noted to occur *via* the extrinsic mitochondrial pathway.[74] Despite the mitochondria being a biological organelle target of NKP-1339, its interaction results in minimal to no activity as apoptosis often occurs *via* the regulation of death receptors on the cell surface or involves other extrinsic molecular pathways. However, NKP-1339 along with the coordinated benzimidazole ligands, do not influence the expression of cell death receptors. Therefore, implying that ruthenium(III) complexes induce apoptosis *via* the extrinsic endoplasmic reticulum (ER) homeostasis pathway.[74]

The endoplasmic reticulum (ER) is another intracellular biological target of NKP-1339, with its anticancer properties being attributed to the mediation of disturbances in redox homeostasis.

The ER organelle functions to regulate the maturation, folding, and release of essential proteins, inaugurating the unfolded protein response (UPR), causing a delay in the cell cycle temporarily until the restoration of proteins or, permanently and thus initiating apoptosis.[43] The glucose-regulated protein of size 78 kDa (GRP78), is an ER stress-sensing chaperone and a cytosolic "heat-shock" protein targeted by NKP-1339. NKP-1339 inhibits GRP78 by preventing its activation effectively. GRP78 is responsible for activating "pro-survival" pathways and can transmit signals involved in the advancement of high tumour proliferation, survival, anti-death initiation and resistance to cell stress such as exposure to treatment regimens.[79,80] In addition, GRP78 plays a significant role in the unfolded protein response (UPR) regulation and maintenance to restore the ER to its normal functioning conditions. Cancer cells are highly dependent on the preservation of the ER folding capacity. Therefore, inhibition or downregulation of ER chaperones and UPR proteins is likely to result in uncontrollable protein folding capacity and accumulation of damaged proteins, leading to ER cell stress. Furthermore, the disturbances of redox homeostasis by NKP-1339 (promotes an increase in ROS levels) lead to the downregulation of UPR target genes and proteins *in vitro* in human colorectal cancer cell lines, HCT116 and SW480.[43] Thus, the deactivation of ER chaperone, GRP78 protein by NKP-1399 serves as evidence that targeting UPR is a promising new strategy for cancer treatment.[55]

As shown in Figure 1.8, treatment with NKP-1339 results in the disturbances of the chemical redox homeostasis and promotes the elevation of ROS levels.[55] This, in turn, promotes the upregulation of the p38 pro-apoptotic mitogen-activated protein kinase (MAPK) stress response pathway which further leads to the induction of G2/M phase cell cycle arrest.[81] This cascading results in cellular apoptosis as a mechanism of cell death.

In general, patients undergoing chemotherapy of ruthenium-based metallopharmaceuticals experience fewer undesirable drawbacks as compared to when undergoing chemotherapy of platinum-based metallopharmaceutical agents.[82] Due to such reasons, organometallic half-sandwich ruthenium(II) complexes were discovered and are an emerging class of metal-based compounds with intensive applications in cancer research. Their biological applications include but are not limited to evaluations of their anti-bacterial, anti-inflammatory, anti-fungal, anti-plasmodial, and anti-viral properties. Unlike the octahedral N-heterocyclic-ruthenium(III) chloride complexes which are often less stable in the extracellular matrix due to extensive transformations and rapid aquation, piano-stool organoruthenium(II) complexes like RAPTA-

C tend to be more stable in the extracellular matrix and are hypothesized to undergo a similar activation mechanism as cisplatin, intracellularly.

1.3.6 Ruthenium(II) polypyridyl photosensitizer complexes

Ruthenium(II) polypyridyl complexes and their use in cancer research qualify them as exceptional candidates due to their attractive photophysical and chemical properties i.e. appreciable water solubility, large two-photon absorption (TPA) cross-section, greater production of singlet oxygen species ($^1O_2$), prolonged luminescence lifetime, large Stokes shift and admirable photostability.[83] TLD1433[84] (Figure 1.9) is an octahedral photosensitizer (PS) that belongs to a class of metal-organic dyads.[85] The structure of TLD1433 contains an expansive π organic chromophores attached to the 2,2′-bipyridine (bpy), 1,10-phenanthroline (phen), or imidazo-[4,5-*f*][1,10]phenanthroline (IP) chelating ligands to give the chemical formula, $[Ru(dmb)_2(LL')]^{2+}$, where dmb = 4,4′-dimethyl-2,2′-bipyridine and LL′ = 2-((2′,2″:5″,2‴-terthiophene)-imidazo(4,5-*f*)(1,10-phenanothroline)).[86] TLD1433 is a well-known organoruthenium(II) photodynamic therapeutic (PDT) agent that takes advantage of the potent photophysical and chemical properties of Ru(II) metal-ion. The ruthenium(II) polypyridyl complex is currently undergoing phase 1 and phase 2a clinical evaluations, with treatment administered to patients suffering from non-muscle invasive bladder cancer *via* photodynamic therapy (PDT) strategy.[87]

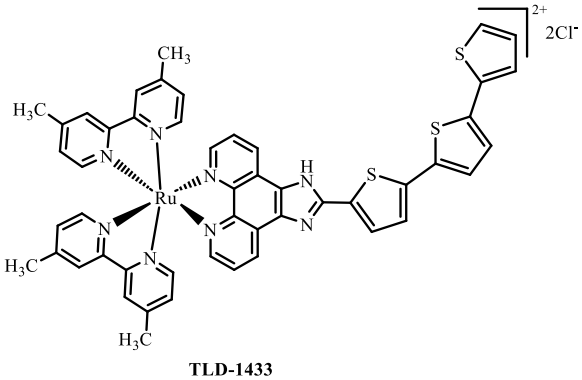

Figure 1.9 The structure of organoruthenium(II) polypyridyl complex, TLD1433, in clinical evaluations[84]

Though in phases 1 and 2a of clinical evaluations, the mechanism of action of TLD1443 has not been fully elucidated and established. However, a duplex mode of action is hypothesized for TLD1433, which is noted to induce or generate ROS when irradiated with light. It was

further established that the complex is capable of causing DNA photodamage in hypoxic conditions and amid ROS scavengers.[85]

1.3.7 Organometallic ruthenium-based metal complexes as anticancer agents

Apart from the N-heterocyclic ruthenium(III) complexes and ruthenium(II) photodynamic therapy (PDT) agents, many ruthenium complexes possess anti-proliferative activity when tested against human ovarian tumours. Particularly, η^6-arene ruthenium(II) organometallic complexes have been evaluated for their potential anticancer properties.[88] Although piano-stool organometallic ruthenium(II) complexes have not yet been applied in clinical trials, the development of half-sandwich η^6-arene-Ru(II) complexes has led to intensive studies and investigations of their anticancer and antimetastatic properties against a wide variety of cancerous cell lines.[88,89] These organometallic ruthenium complexes are deemed suitable for such investigations because of their low toxicity properties compared to cisplatin, and their ability to mimic iron-binding to plasma and extracellular proteins.[90] Organometallic ruthenium(II) arene complexes present greater antiproliferative, greater anti-tumour properties and low toxicity in comparison to platinum anticancer agents.[91] Complexes generally consist of the general chemical formula [(η^6-arene moeity)Ru(XY)(Z)], where X, Y, and Z are coordination sites often occupied by monodentate, bidentate, or tridentate chelating ligands and/or leaving groups (Figure 1.10).[90,92]

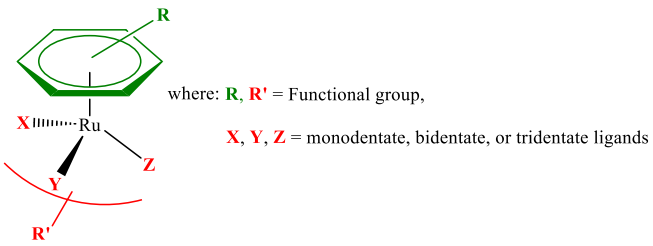

Figure 1.10 The general structure of half sandwich organometallic ruthenium(II) arene complexes with "piano-stool" configuration.[90,92]

The hydrophobic η^6 coordinated arene moiety stabilizes the +2 oxidation state of the complex and can be varied by introducing various forms of substituents.[92] Governed by the coordination mode of the ligands to the ruthenium metal centre, a variety of neutral and charged complexes can be prepared. Furthermore, these ligands can be fine-tuned by introducing biological active substituents to the inner coordination sphere around the metal centre to achieve the desired biological activity, modulating their pharmacological and kinetic pharmacokinetic properties,

and thus resulting in multifunctional ruthenium metal-ligand drug complexes with increased synergistic effects.[90,93,94] The ruthenium(II) arene complex, $[Ru(\eta^6\text{-}C_6H_6)(DMSO)Cl_2]$, is among one of the first organometallic piano-stool complexes with promising antitumour properties. The complex is reported to halt the primal function of topoisomerase II, responsible for the organisation of mitotic chromosomal structure during cellular replication.[95]

Further studies of organoruthenium(II)-arene compounds led to the discovery of two sub-families namely, the RAPTA and RAED families (Figure 1.11), respectively.[96]

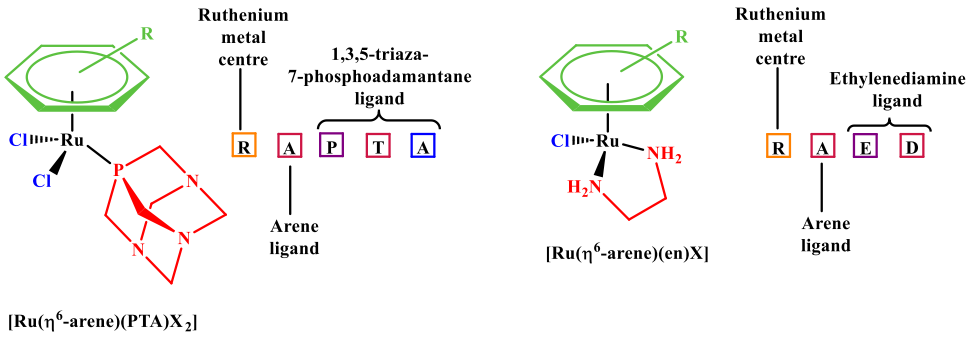

Figure 1.11 Generic structural motif of RAPTA and RAED complexes as potential anticancer agents.[96]

The substitution of DMSO ligands with a monodentate PTA (1,3,5-triaza-7-phosphaadamantane) ligand and the replacement of η^6-arene ancillary ligand with *p*-cymene ligand led to the formation of ruthenium(II)-arene-PTA complex, RAPTA-C[84] (Figure 1.12), which has a structural motif similar to the $[Ru(\eta^6\text{-}C_6H_6)(DMSO)Cl_2]$ complex.

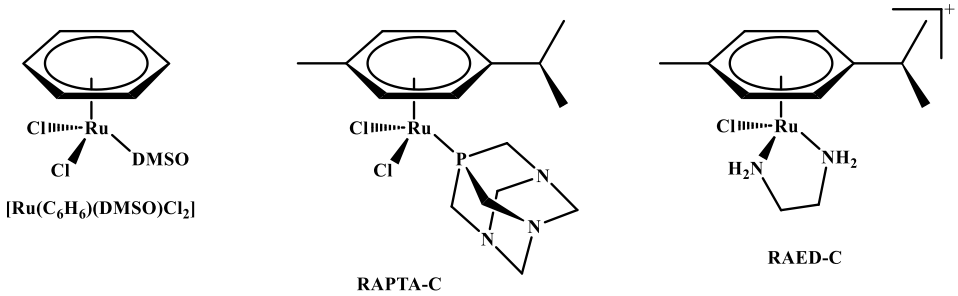

Figure 1.12 Organometallic ruthenium(II) arene complexes with promising anticancer properties.[95,84]

The operative mechanism of action of the RAPTA-C complex is not well understood but is reported to involve both intra- and extra-cellular biological processes. Like any other pro-drug, RAPTA-C undergoes aquation reactions and is activated upon entry into the cellular environment consisting of low chloride concentration (Scheme 1.3).[97]

The replacement of the previously mentioned ligands resulted in enhanced aqueous solubility properties of the complex. As a result, the complex showed promising antimetastatic effects, enhanced selectivity, and low toxicity profiles.[98,44]

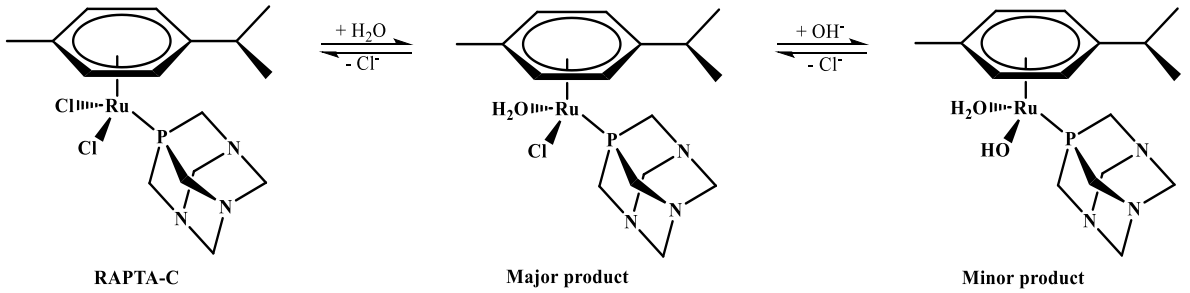

Scheme 1.3 Aquation reaction of RAPTA-C in a low-concentration cellular environment.[97]

RAPTA-C exhibits moderate *in vitro* cytotoxic properties when tested against TS/A adenocarcinoma (IC_{50} > 300 μM after 72-hour treatment) and A2780 ovarian cancer cell lines. Additionally, no appreciable selectivity towards the TS/A adenocarcinoma cell line was observed when the complex was tested against the non-tumourigenic HBL-100 epithelial cell line (IC_{50} > 300 μM after 72-hour treatment).[98] This moderate cytotoxic property was reported for all complexes with a PTA structural motif. RAPTA-C halts the growth, number and weight of solid lung metastases that originate from the primary tumour with reduced side effects *in vivo* compared to the platinum-based drugs in CBA mice bearing the Mca mammary breast carcinoma. Such observations were correlated with strong intrinsic antiangiogenic properties, similar to the small drug molecule that is in clinical usage, sorafenib when evaluated on primal tumours.[84] The effect is attributed to the preferential binding to the histone core of a chromatin molecule, as compared to binding to the initially hypothesized primal target, double-stranded DNA.[99] Thus, making the RAPTA-C complex attractive for pre-clinical evaluation and development as an antimetastatic agent.

In vivo experimental studies centred around the evaluation of the efficacy of RAPTA-C on the germination of primary tumours in preclinical models were performed.[84] This involved the

usage of various standard dosing procedures which were compared to those utilised in previous studies. RAPTA-C was found to inhibit approximately 75% of tumour growth and formation of human A2780 ovarian carcinoma which were transplanted onto the chicken chorioallantoic membrane (CAM) model. This inhibition was observed when a dosage of 0.2 $mg.kg^{-1}$/day of RAPTA-C was administered for 5 days (commenced 4 days after tumour inoculation of the CAM). Furthermore, *in vivo* experimental studies involving the antitumour evaluation of RAPTA-C in athymic mice bearing an LS174T colorectal adenocarcinoma were performed.[100] The obtained experimental data suggests that RAPTA-C inhibits 50% of tumour growth and germination significantly when 100 $mg.kg^{-1}$ of the drug was administered per day for approximately 2 weeks relative to controls. Additionally, further observations of the treated tumorigenic tissue suggest that RAPTA-C exhibits strong anti-angiogenic properties, as evidenced by the decrease in micro-vessel density. This observation correlates well with earlier reports highlighting the antiangiogenic effects of RAPTA-C in a in a series of cell-based assays and in the CAM model. Thus, it is worth noting that the *in vitro* and *in vivo* experimental data collected suggests that RAPTA-C possess no cytotoxic properties against the previously mentioned cancerous cell lines but is an efficacious drug towards reducing primary tumour weight and size than the highly cytotoxic compound doxorubicin, possibly attributed to the highlighted antiangiogenic properties.[96]

The RAED class of organoruthenium(II) complexes (Figure 1.11) are a series of compounds that exhibit promising cytotoxic properties towards a variety of cancer cell lines, including the cisplatin-resistant and MCA mammary carcinoma *in vitro*.[101] The RAED series, like other organoruthenium(II) complexes, are notorious for forming guanine monofunctional adducts through the coordination to the N7-site of the nucleotide base. The derivatization of the η^6-arene ligand by incorporating extended π-conjugated ligands such as biphenyl, dihydroanthracene, and tetrahydroanthracene may encourage DNA intercalation.[96] The biphenyl ethylenediamine chloride complex (RM175), is one complex that has gained traction in preclinical evaluations due to its appealing *in vitro* anticancer properties.[96] The complex possesses similar or greater *in vitro* cytotoxic properties than the carboplatin platinum complex. Furthermore, the complex does not have similar modes of action in common with other platinum drugs such as cisplatin (i.e. cross-resistance mechanisms).[102] The cytotoxicity of RM175 is attributed to the presence of the coordinated η^6-arene ligand, the chelating ethylenediamine and the chloride as the leaving group. In short-term Sulphorhodamine B assay experiments, the compound shows significant ($p < 0.05$) cytotoxic properties and inhibits the

survival of HCT116 colorectal cancer cells, with an IC_{50} value of 16 µM (p-53 suppressed cell line) and 8 µM (p53 wild-type cells), after 96-hour treatment. A dose-dependent increase in p53 and the cell cycle inhibitor p21/WAF1 accumulation was observed from 24- to 48 hours of treatment while the accumulation of Bax, the proapoptotic Bcl2 family member was observed at a 48-hour time interval. RM175 induces apoptosis in a p53 and Bax-dependent manner, suggesting that the expression of these proteins after RM175 treatment is related to the apoptotic pathway as a mechanistic of cell death.[103] Upon exposure to the A2780 human ovarian cancer cell line, RM175 is reported to induce G1 and G2 phases of the cell cycle arrest thus leading to apoptosis.[102] RM175 halts solid tumour growth significantly and the likelihood of the development of secondary lung metastasis.[101]

Based on recent literature, RAPTA and RAED series of organometallic ruthenium(II) complexes have shown promise as anticancer agents and offer the versatility of controlling by tuning the kinetic and thermodynamic properties of biologically important chemical reactions. A study investigating the structure-activity relationship for monofunctional Ru(II) complexes $[Ru(\eta^6\text{-arene})(chelate)Cl]^+$ demonstrates that tunning the electronic properties of the complexes by choosing the appropriate arene and chelating ligands, as well as the coordination of the appropriate leaving group can result in a dramatic effect on the chemical and biological activity of the investigated piano-stool complexes.[104]

In addition to the unearthed pharmacological anticancer therapeutic properties of ruthenium(III) and ruthenium(II) mononuclear complexes, the synthesis and development of binuclear ruthenium paddlewheel structured complexes is another strategy used to enhance the potent activity and achieve desirable pharmacological therapeutic properties. The strategy serves to incorporate two ruthenium metals to enhance the anticancer properties of ruthenium metallodrugs, to promote cellular uptake, active transportation, stability in the biological milieu and drug delivery to the biological molecular target. The coordination of two ruthenium metal centres is advantageous due to the ability to coordinate mono and bidentate pharmacological ligands to the metal centres. Thus, offering a variety of possibilities to form novel therapeutic agents with a broad spectrum of biological activity.

1.3.8 Diruthenium(II, III)-based complexes as anticancer agents

The discovery and recognition of the quadruple metal-metal bonded $Re_2Cl_8^{2-}$ ion[105] has ignited a growing interest in the chemistry of bimetallic complexes bearing other transition metal ions with applications in catalysis, supramolecular chemistry under the construction of Metal-Organic Frameworks (MOFs), formation of nanoparticles as dimers, and medicinal bioinorganic application.[106] The diruthenium cores exist in various overall oxidation states of IV [Ru_2(II, II)], V [Ru_2(II, III)] and VI [Ru_2(III, III)], with the most stable to air and moisture being the [Ru_2(II, III)] class of compounds and the most studied of the family. These d^5-d^6 class of paddlewheel complexes are characterized by strong multiple metal-metal bonds, with a spin state of 3/2 for each ruthenium metal. Complexes possess three unpaired electrons in the π- and δ-antibonding orbitals, yielding peculiar magnetic features with high effective magnetic moments of 3.8 – 4.4 B.M per diruthenium metal core. The electrochemical properties consist of reduction potentials ranging from 0.30 to 0.50 V (versus normal hydrogen electrode), thus implying that these compounds can be easily accessible under physiological conditions. Furthermore, this implies that the Ru_2^{5+}core undergoes activation by reduction to yield Ru_2^{4+} adducts in the biological environment, which makes them suitable candidates for biological applications.[107] The tetracarboxylatodiruthenium(II, III) complexes usually show a polymeric structure with ionic or neutral ligands that link the $[Ru_2(O_2CR)_4]^+$ metal scaffolds. The most common equatorial bridging ligands are the *O,O*-donors (i.e carboxylates), *N,O*-donors (i.e amidates or hydroxipyridinates) and *N,N*-donor (i.e aminopyridinates, triazenates, benzamidinates or formamidinates).[108]

1.3.8.1 Diruthenium(II, III) complexes incorporating O,O-donor bridging ligands for anticancer therapy evaluation

The bimetallic Ru_2^{5+} paddlewheel structured complexes of the type $[Ru_2(O_2CR)_4]^+$ (Figure 1.13) bearing four mono-negative three-atom carboxylate ligands (O_2C-R) have attracted much attention in the discovery of novel anticancer agents.[109,110]

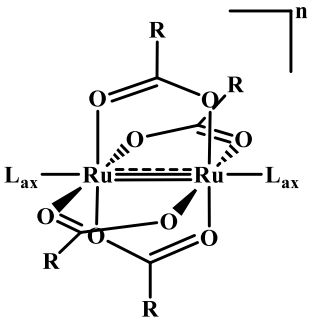

Figure 1.13 General structure of the lantern-type diruthenium(II, III) complexes, $[Ru_2(O_2CR)_4L_{ax}]^{q+}$. R-$COO^-$ are equatorial carboxylate ligands (where R can be an alkyl, aryl, alkoxy, or a metallocene moiety), n is the overall charge (n = 0 - 2), and L_{ax} are axial anionic or neutral ligands (often consists of halides or a Lewis base and L_{ax} = 1 or 2).

The tetraacetate diruthenium(II, III) paddlewheel complexes, $[Ru_2(\mu\text{-}O_2CCH_3)_4Cl]$[109] and $[Ru_2(\mu\text{-}O_2CCH_2CH_2CH_3)_4Cl]$,[111] were among the first paddlewheel complexes to be successfully prepared and structurally characterized using spectroscopic techniques. Their synthesis led to the subsequent preparation of diruthenium(II, III) tetraacetates consisting of the general chemical formula $[Ru_2(\mu\text{-}O_2CR)_3Cl]$, where R = an aliphatic chain, aryl, alkoxy, or a metallocene moiety. These complexes were evaluated for their *in vivo* antitumour properties against P388 leukaemia tumours.[112] The experimental data obtained show that complexes possess appreciable antitumour effects, reaching T/C values of 125% and 133% for $[Ru_2(\mu\text{-}O_2CCH_3)_4Cl]$ and $[Ru_2(\mu\text{-}O_2CCH_2CH_2CH_3)_4Cl]$, respectively. T/C values are representative of the median survival time/tumour weight of treated (T) animals *versus* the median survival time/tumour weight of control (C) animals x 100. However, speculations about their poor solubility in water led to the conclusion that the antitumour effects of the complexes were hindered. In this light, advancements towards improving their solubility properties led to a myriad of a unique class of tetraacetatodiruthenium(II, III) complexes. The coordination of the appropriate choice of equatorial ligands bearing the biologically active carboxylate moiety, along with the axial coordination of an excellent choice of an anionic or neutral ligand to the metal cores offers the versatility of designing a unique class of anticancer agents with improved toxicity profiles compared to platinum-based complexes.[113] Furthermore, this allows for fine-tuning of their electronic properties and thus the modulation of the pharmacokinetic and pharmacodynamic properties to achieve the desired therapeutic efficacy. The attraction towards the use of carboxylate ligands is associated with the stabilization of the diruthenium(II, III) cores, which serve to protect and transport the bimetallic core to the biological molecular

targets. Additionally, they exert their biological properties while the axial ligands influence the modulation of target selectivity.[114]

A dual strategy which exploits the anticancer properties of diruthenium(II, III) metal cores and incorporates the pharmacological properties of the Non-Steroidal Anti-Inflammatory Drugs (NSAID) with a carboxylic acid moiety, was developed to prepare a class of $[Ru_2(NSAID)_4]^+$ compounds.[114,115,116] Examples of the NSAID compounds coordinated to the Ru_2^{5+} metal cores are herein presented in Figure 1.14.

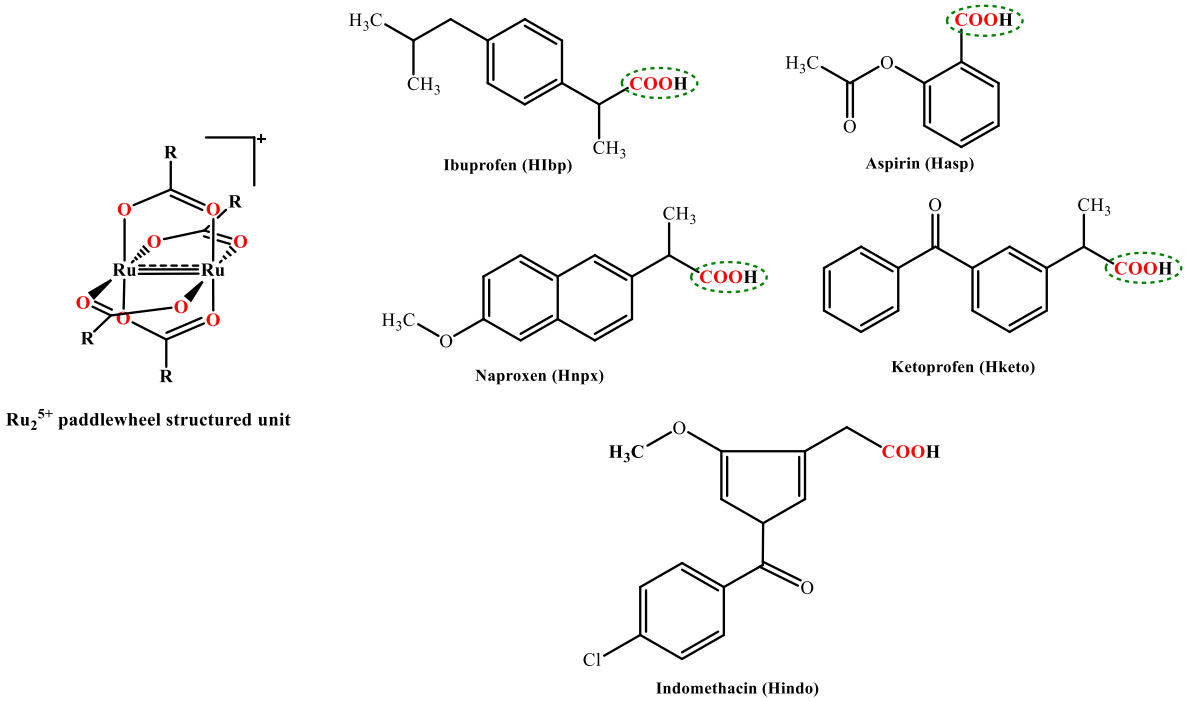

Figure 1.14 Chemical structures of typical examples of Non-Steroidal Anti-Inflammatory (NSAID) drugs that are coordinated to the diruthenium(II, III) core *via* the oxygen atoms of the carboxylate anions (highlighted in red).[114,115,116]

NSAIDs are approved worldwide as the first line of treatment against inflammation, pain, and fever. However, their use as anti-inflammatory drugs has also provoked substantial attention as chemotherapeutic precautionary measures against the risk of developing malignant tumours such as colorectal, gastric, breast, prostate, lung and skin cancers.[114,117] For example, the prolonged usage of aspirin resulted in a significant decrease in the likelihood of forming gastric and colon malignancies. Additionally, the treatment of aspirin along with other NSAIDs, can inhibit cell proliferation, induce apoptosis, and halt tumorigenesis in several cancer types. In

in vivo mice models, the long-term administration of NSAIDs such as aspirin, ibuprofen, indomethacin, and sulindac caused a significant decrease in gastric tumours that were chemically induced. Furthermore, the prolonged usage of NSAIDs was correlated with a 30 to 50% reduction in the development of colorectal cancer or adenomatous polyps or loss of life from colorectal cancer.[118] However, the discontinuation of NSAID administration resulted in tumour recurrence. Although the mechanism of action responsible for the anticancer properties of NSAIDs is not well understood, several reports highlight their involvement in the inhibition of cyclooxygenase, COX-1 and COX-2 isoforms.[119] Their anticancer efficacy may correlate with the inhibition of COX-2 coenzyme, which is overexpressed in numerous cancer types and is related to tumour progression.[120] Furthermore, despite their potential to inhibit tumour progression, the high doses required to induce apoptosis and inhibit carcinogenesis deter their use in the treatment of cancer.

The coordination of NSAID carboxylate moiety with the Ru_2^{5+} cores led to the discovery of interesting biological properties. This ideology served as motivation directed towards enhancing the biological properties of NSAIDs and ameliorating the lived experiences of patients undergoing the organic NSAID by reducing or eradicating undesirable treatment limitations and shortcomings. This led to the successful preparation and characterization of the first four Ru_2-NSAID class of complexes, $[Ru_2(d\text{-NSAID})_4Cl]$ where *d*-NSAID is deprotonated ibuprofenate (ibp) and aspirin (asp) and $[Ru_2(d\text{-NSAID})_4(H_2O)]\cdot PF_6$, where *d*-NSAID is the deprotonated naproxen (npx) and indomethacin (ind) (Figure 1.14).[121] The *in vitro* antiproliferative effects of the complexes were evaluated against C6 rat glioma cells. In malignant gliomas, COX-2 is overexpressed and upregulated and is correlated with poor patient prognosis.[122] Thus, the motivation to evaluate their anticancer effects against glioma models. In comparison to the free NSAID ligands, the $[Ru_2(Ibp)_4Cl]$ and $[Ru_2(Npx)_4(H_2O)]\cdot PF_6$ complexes exhibited greater antiproliferative properties against the C6 rat glioma cell line *in vitro*. The obtained biological data suggest that the coordination of the *d*-NSAID to the Ru_2^{5+} metal cores is important as it enhances and results in synergistic biological properties. Upon exposure to the C6 rat glioma cells, $[Ru_2(Ibp)_4Cl]$ caused alterations in mRNA expression by inducing an increase in p21 and p27 cyclin-dependent kinase inhibitors and their protein expression. Additionally, the complex induced a substantial decline in mitochondrial membrane potential and expressed anti-apoptotic Bcl2 in the same manner. The complex further caused a modest increase in apoptosis and expressed a decrease in pro-apoptotic Bax. The decrease in the production of prostaglandin E2 (PGE2), is caused by a pronounced incline

in augmented COX-1 protein expression. Ultimately, it can be deduced that the antiproliferative properties of $[Ru_2(Ibp)_4Cl]$ against the C6 rat glioma tumour cells are strongly influenced by modifications in the mitochondrial membrane potential, alterations in mRNA and protein expression of p21, p27 and Bax/Bcl2 ratio.[123] These findings support the hypothesis of possible decomposition of the complex within the cytoplasm, releasing the organic ibuprofen ligands to induce inhibition of cyclooxygenase enzyme, COX-1.[123] Further *in vivo* studies involving direct intraperitoneal injections (*i.p*) of $[Ru_2(Ibp)_4Cl]$ complex resulted in 45% impediment of tumour progression in C6 rat glioma models with no undesirable drawbacks. Moreover, $[Ru_2(Ibp)_4Cl]$ caused a 41% decrease in tumour area in rat animal models with no noticeable toxic effects, and caused an appreciable reduction in the production of blood lymphocytes and an incline in blood monocytes and neutrophils.[124]

The anti-inhibitory effects of $[Ru_2(Ibp)_4]^+$ scaffold were further evaluated against the human glioma cell lines, U87MG, U138MG, T98G and A172.[124] The paddlewheel diruthenium(II, III) scaffold was modified through the coordination of variations axial ligands to form complexes $[Ru_2(Ibp)_4(CF_3SO_3)]$ and $[Ru_2(Ibp)_4(EtOH)_2]^+$. The complexes exhibited promising cytotoxic properties against the A172 and U87MG, characterized by expression of the p53 wild type. The parent $[Ru_2(Ibp)_4Cl]$ complex showed greater cytotoxic properties in comparison to the $[Ru_2(Ibp)_4(CF_3SO_3)]$ and $[Ru_2(Ibp)_4(EtOH)_2]^+$ derivatives, showing significant impact in cell proliferation, apoptosis, mitosis and cell migration *in vitro*. It is noteworthy that after exposure to glioma cell lines, the investigated complexes showed great cell permeability, causing an appreciable decrease in the number of apoptotic and mitotic cells.[124] In conclusion, $[Ru_2(Ibp)_4]^+$ scaffold exhibits potent and promising anti-inhibitory properties against the previously mentioned high-graded human glioma cell lines with potent effects on cellular mitosis and migration.

1.4 Closing remarks

Owing to their fewer toxicity profiles compared to the platinum metal-centred complexes due to the incorporation of the ruthenium metal centre, organometallic ruthenium(II) arene and paddlewheel diruthenium(II, III) complexes continue to show promise as anticancer chemotherapeutic agents. This is advantageous and is an effective dual strategy to overcome toxicity, solubility issues and drug resistance issues. Furthermore, ruthenium metal-based complexes discussed extensively in this chapter seek to[125]:

- To enhance the solubility properties and stability of complexes under investigation in aqueous solution,
- To enhance the cellular uptake and improve the drug delivery to the active biological drug target,
- For complexes to possess various mechanisms of action inducing cell death and have several interactions with small biological molecules.

Research contributions directed towards the discovery and identification of the antitumour properties of organometallic mononuclear ruthenium complexes, with great promise to serve as the next generation of cancer chemotherapeutic agents, motivate the investigation of bimetallic ruthenium derivatives as a way of comparison for metal-additivity and bioavailability effect. Whilst there is exponential growth in the design synthesis and development of water-soluble paddlewheel Ru_2^{5+} structured complexes with applications in cancer research, there is a need to identify their biological molecular targets. Furthermore, there is a need to address, understand and evaluate the mechanism of action responsible for their anticancer activity and selectivity for tumour models.

1.5 Research rationale and motivation

In light of the past and recent investigations and discovery of the anticancer properties of the organometallic arene monoruthenium(II) complexes bearing stannyl ligands and paddlewheel diruthenium(II, III) complexes, there is precedence for the development of ruthenium(II) arene and bimetallic diruthenium(II, III) paddlewheel complexes with prominent anticancer properties against a wide spectrum of carcinomas and significantly selective for tumours. This research project aimed to synthesize stable, effective, and water-soluble ruthenium(II) arene complexes bearing stannyl and various phosphine ligands, and diruthenium mixed ligand complexes that serve as potential candidates as anticancer pharmaceutical agents with fewer side effects to halt cancer cells or growth development proliferation. To the best of our knowledge, the medicinal anticancer activity of the diruthenium(II, III) paddlewheel complexes of the type $[Ru_2(O_2CCH_3)_3(R\text{-}ap)Cl]$ complexes have not been studied extensively, while organometallic ruthenium arene complexes bearing stannyl ligands have been investigated for their potential cytotoxic properties against a variety of cancer cell lines. Furthermore, the operative mechanisms of these compounds were investigated by studying their interaction with potential biological molecular targets.

1.6 Aims and Objectives

1.6.1 General aims of this research project

The synthesis and chemistry of the organometallic arene monoruthenium(II) complexes bearing stannyl ligands and mixed valent paddlewheel structured diruthenium(II, III) complexes comprising of the chemical formula $[Ru_2(O_2CCH_3)_3(R\text{-}ap)Cl]$, where ap = anilinopyridinate bridging ligand, have been well investigated and documented in published reports. However, there exist few research prospects focused on the anticancer biological impact and the mode of action responsible for their anticancer activity. Thus, there is precedence in discovering their biological impact on various cancer cell lines and evaluating their possible mode of action. Therefore, the aims of the project were:

- To synthesize and characterize novel organometallic ruthenium(II) arene complexes bearing stannyl ligands and various π-acceptor phosphine ligands.
- To evaluate the cytotoxic properties of the synthesised ruthenium(II) arene complexes against human breast cancer subtypes.
- To improve on the synthetic route of $[Ru_2(O_2CCH_3)_3(R\text{-}ap)Cl]$ complexes and obtain the synthesized complexes in greater yields.
- To evaluate the synthesized $[Ru_2(O_2CCH_3)_3(R\text{-}ap)Cl]$ complexes for their anticancer activity against human breast cancer cell lines as therapeutic agents.

1.6.2 The specific objectives of the research project

1.6.2.1 Preparation/synthetic objectives:

- To prepare various organometallic ruthenium(II) arene complexes bearing stannyl ligands and various π-acceptor phosphorylated ligands.

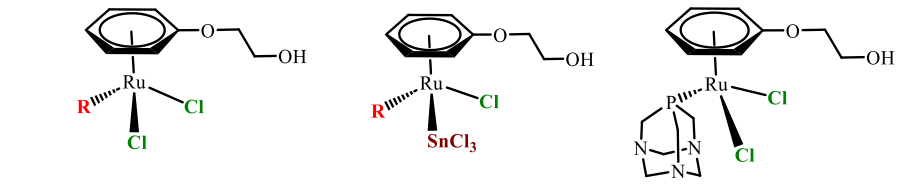

R = PPh_3, $P(OPh)_3$, $P(OMe)_3$. **R** = PPh_3, $P(OPh)_3$

Figure 1.15 Structures of the desired organometallic ruthenium(II) arene complexes bearing various π-acceptor phosphine and stannyl ligands.

The prepared ruthenium dimer, $[RuCl_2(\eta^6\text{-}C_6H_6OCH_2CH_2OH)]$,[126] enables facile entry to form piano stool complexes bearing the desired π-acceptor phosphine ligands, *via* bridge splitting

reaction with the appropriate phosphine ligand. The reaction of $SnCl_2$ with one equivalence of the synthesized piano stool complexes leads to the formation of the novel complexes $[RuCl(\eta^6\text{-}C_6H_5OCH_2CH_2OH)(Ph_3)(SnCl_3)]$ and $[RuCl(\eta^6\text{-}C_6H_5OCH_2CH_2OH)\{P(OPh_3)\}(SnCl_3)]$. The phosphine π-acceptor ligands are postulated to enhance the solubility properties of the complexes and thus enhance the efficacy of the investigated compounds.

- To prepare various nitrogen-nitrogen-based bidentate equatorial bridging anilinopyridinate (R-ap) ligands (Figure 1.15).

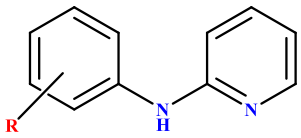

anilinopyridinate (R-ap) ligand

R = H (**L1**), 2-CH_3 (**L2**), 4-CH_3 (**L3**), 2,4-$(CH_3)_2$ (**L4**), 2,6-$(CH_3)_2$ (**L5**), 2,4,6-$(CH_3)_3$ (**L6**), 2-F (**L7**), 4-F (**L8**)

Figure 1.16 Prepared anilinopyridinate (R-ap) substituted ligands (**L1 - L8**).

The synthesis of nitrogen-nitrogen-based bidentate equatorial bridging anilinopyridinate (R-ap) ligands was achieved by an addition-elimination reaction of 2-bromopyridine and the respective aniline, with the electronic properties varied by incorporating methyl electron-donating and fluorine withdrawing substituents on the *ortho*- and *para*- positions of the aniline phenyl ring. Substituents were chosen based on the Craig Plot (Figure 1.17); a plot used in medicinal chemistry to design analogues of bioactive molecules to enhance the efficacy of the desired bioactive compound.[127] Furthermore, the plot is utilized in the rational drug design of bioactive compounds and classifies substituents based on their hydrophobic properties (π) and electron donating/withdrawing nature (σ) to achieve the desired characteristic traits.

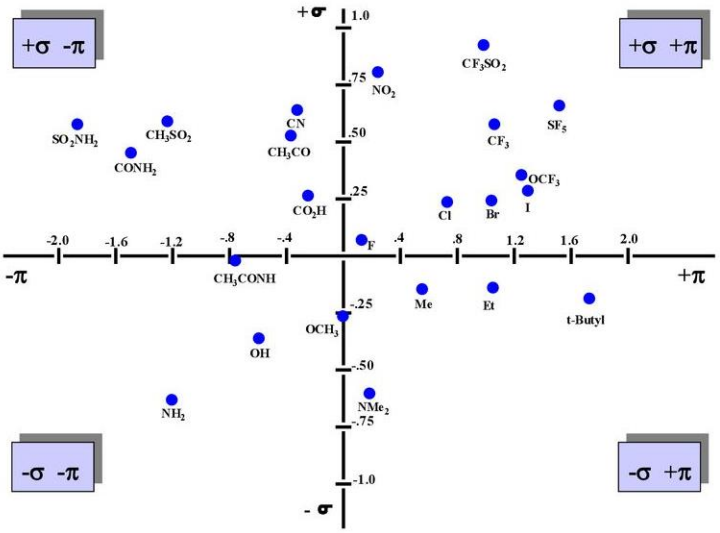

Figure 1.17 Craig plot, a plot used in medicinal chemistry to rationalize drug design and development of bioactive compounds.[127] The plot classifies substituents based on their hydrophobic properties (π) and electron donating/withdrawing nature (σ) to achieve the desired characteristic traits.

- To prepare the desired mixed ligand mono-substituted anilinopyridinate triacetatechlorodiruthenium(II, III) complexes, $[Ru_2(O_2CCH_3)_3(R\text{-ap})Cl]$ complexes (Figure 1.18).

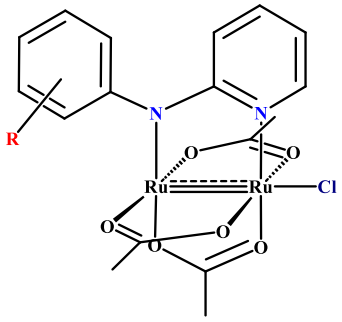

where **R** = H (**C1**), 2-CH_3 (**C2**), 4-CH_3 (**C3**), 2,4-$(CH_3)_2$ (**C4**), 2,6-$(CH_3)_2$ (**C5**), 2,4,6-$(CH_3)_3$ (**C6**), 2-F(**C7**),and 4-F (**C8**)

Figure 1.18 The desired water-soluble mixed ligand monosubstituted anilinopyridinate triacetatechlorodiruthenium(II, III) complexes, $[Ru_2(O_2CCH_3)_3(R\text{-ap})Cl]$ complexes.

The respective anilinopyridinate (R-ap) ligands were complexed with the $[Ru_2(O_2CCH_3)_4Cl]$ precursor to afford a library of mixed ligand monosubstituted anilinopyridinate triacetatechlorodiruthenium(II, III) complexes, $[Ru_2(O_2CCH_3)_3(R\text{-ap})Cl]$ complexes. The synthesis was achieved by a metathesis displacement of the bridging acetate ligand (one

moiety) of the $[Ru_2(O_2CCH_3)_4Cl]$ precursor complex and replaced with one equivalence of the R-ap ligand to achieve the desired complexes.

1.6.2.2 Characterization

To ascertain the purity and structures of the synthesised compounds, the proposed compounds were purified *via* recrystallization and chromatography techniques. Furthermore, compounds were characterized using an array of spectroscopic and analytical techniques. These included Nuclear Magnetic Resonance (NMR) spectroscopy, Fourier Transform Infrared (FT-IR) spectroscopy, liquid chromatography (LC) or High Resolution (HR) Mass spectrometry, and Elemental Analysis (EA) techniques, cyclic voltammetry to ascertain their electronic measurements. Single crystal X-Ray diffraction (XRD) was performed for structure elucidation purposes.

1.6.2.3 Evaluation of the potential anticancer properties of the piano stool arene ruthenium(II) and paddlewheel $[Ru_2(O_2CCH_3)_3(R\text{-}ap)Cl]$ complexes.

To investigate and evaluate the cytotoxic properties of the prepared piano stool ruthenium(II) arene, R-ap ligands, and $[Ru_2(O_2CCH_3)_3(R\text{-}ap)Cl]$ complexes against human breast cancer subtypes and mammary non-malignant MCF-12A epithelial cell lines using MTT and colony formation assays.

1.6.2.4 Mechanistic studies

- To investigate the mechanism of action responsible for the cytotoxic properties of the proposed complexes and their stability in solution.
- To characterize and determine the mode of cell death of human breast cancer cells induced by the treatment with the most cytotoxic compound, western blotting technique was utilized with antibodies to ɣH2Ax, p53, caspase-9 and PARP. P38 was used as the loading control.
- Investigation of the interaction of the synthesized lead compound with small biological molecules including glutathione (reduced), *p*Bluescript plasmid and salmon sperm DNA was performed by conducting ultraviolet-visible titration experiments.

1.7 REFERENCES

1 National Cancer Institution at the National Institutes of Health, What Is Cancer?, https://www.cancer.gov/about-cancer/understanding/what-is-cancer.

2 J. Ferlay, H.-R. Shin, F. Bray, D. Forman, C. Mathers and D. M. Parkin, *Int. J. Cancer*, 2010, **127**, 2893–2917.

3 M. Roser and Hannah Ritchie, Cancer, https://ourworldindata.org/cancer.

4 M. Naghavi, A. A. Abajobir, C. Abbafati, K. M. Abbas, F. Abd-Allah, S. F. Abera and V. Aboyans, *Lancet*, 2017, **390**, 1151–1210.

5 H. Sung, J. Ferlay, R. L. Siegel, M. Laversanne, I. Soerjomataram, A. Jemal and F. Bray, *CA. Cancer J. Clin.*, 2021, **71**, 209–249.

6 Globocan, *Glob. Obs. Cancer*, 2020, **419**, 5–6.

7 G. W. Prager, S. Braga, B. Bystricky, C. Qvortrup, C. Criscitiello, E. Esin, G. S. Sonke, G. Martínez, J.-S. Frenel, M. Karamouzis, M. Strijbos, O. Yazici, P. Bossi, S. Banerjee, T. Troiani, A. Eniu, F. Ciardiello, J. Tabernero, C. C. Zielinski, P. G. Casali, F. Cardoso, J.-Y. Douillard, S. Jezdic, K. McGregor, G. Bricalli, M. Vyas and A. Ilbawi, *ESMO Open*, 2018, **3**, e000285.

8 F. Bray, M. Laversanne, E. Weiderpass and I. Soerjomataram, *Cancer*, 2021, **127**, 3029–3030.

9 J. Ferlay, M. Colombet, I. Soerjomataram, C. Mathers, D. M. Parkin, M. Piñeros, A. Znaor and F. Bray, *Int. J. Cancer*, 2019, **144**, 1941–1953.

10 World Health Organization: International Agency for Research on Cancer, *Cancer*, Geneva, 2022.

11 J. Ferlay, M. Colombet, I. Soerjomataram, D. M. Parkin, M. Piñeros, A. Znaor and F. Bray, *Int. J. Cancer*, 2021, **149**, 778–789.

12 T. N. Seyfried and L. C. Huysentruyt, *Crit. Rev. Oncog.*, 2013, **18**, 43–73.

13 X. Guan, *Acta Pharm. Sin. B*, 2015, **5**, 402–418.

14 B. A. Chabner and T. G. Roberts, *Nat. Rev. Cancer*, 2005, **5**, 65–72.

15 V. Schirrmacher, *Int. J. Oncol.*, 2018, **54**, 407–419.

16 Y. Chen, P. Jungsuwadee, M. Vore, D. A. Butterfield and D. K. St. Clair, *Mol. Interv.*, 2007, **7**, 147–156.

17 I. Yousuf, M. Bashir, F. Arjmand and S. Tabassum, *Coord. Chem. Rev.*, 2021, **445**, 1–30.

18 G. Sava, G. Jaouen, E. A. Hillard and A. Bergamo, *Dalt. Trans.*, 2012, **41**, 8226–8234.

19 C. S. Allardyce and P. J. Dyson, *Platin. Met. Rev.*, 2001, **45**, 62–69.

20 E. J. Anthony, E. M. Bolitho, H. E. Bridgewater, O. W. L. Carter, J. M. Donnelly, C. Imberti, E. C. Lant, F. Lermyte, R. J. Needham, M. Palau, P. J. Sadler, H. Shi, F.-X. Wang, W.-Y. Zhang and Z. Zhang, *Chem. Sci.*, 2020, **11**, 12888–12917.

21 I. Ott and R. Gust, *Arch. Pharm. (Weinheim).*, 2007, **340**, 117–126.

22 B. ROSENBERG, L. VAN CAMP and T. KRIGAS, *Nature*, 1965, **205**, 698–699.

23 H. Kay, *J. Clin. Pathol.*, 1982, **35**, 1298–1299.

24 D. Lebwohl and R. Canetta, *Eur. J. Cancer*, 1998, **34**, 1522–1534.

25 N. J. Wheate, S. Walker, G. E. Craig and R. Oun, *Dalt. Trans.*, 2010, **39**, 8113–8127.

26 A. Bergamo and G. Sava, *Chem. Soc. Rev.*, 2015, **44**, 8818–8835.

27 G. V. Kalayda, C. H. Wagner and U. Jaehde, *J. Inorg. Biochem.*, 2012, **116**, 1–10.

28 Hanif-Ur-Rehman, T. E. Freitas, R. N. Gomes, A. Colquhoun and D. de Oliveira Silva, *J. Inorg. Biochem.*, 2016, **165**, 181–191.

29 M. S. Davies, S. J. Berners-Price and T. W. Hambley, *Inorg. Chem.*, 2000, **39**, 5603–5613.

30 L. R. Kelland, G. Abel, M. J. McKeage, M. Jones, P. M. Goddard, M. Valenti, B. A. Murrer and K. R. Harrap, *Cancer Res.*, 1993, **53**, 2581–2586.

31 P. M. Takahara, A. C. Rosenzweig, C. A. Frederick and S. J. Lippard, *Nature*, 1995, **377**, 649–652.

32 S. G. K. R, B. B. Mathew, C. N. Sudhamani and H. S. B. Naik, *Biomed. Biotechnol.*, 2013, **2**, 1–9.

33 A. Vaisman, M. Varchenko, A. Umar, T. A. Kunkel, J. I. Risinger, J. C. Barrett, T. C. Hamilton and S. G. Chaney, *Cancer Res.*, 1998, **58**, 3579–85.

34 S. Ghosh, *Bioorg. Chem.*, 2019, 88, 1–20.

35 S. Dilruba and G. V. Kalayda, *Cancer Chemother. Pharmacol.*, 2016, **77**, 1103–1124.

36 C. Casares, R. Ramírez-Camacho, A. Trinidad, A. Roldán, E. Jorge and J. R. García-Berrocal, *Eur. Arch. Oto-Rhino-Laryngology*, 2012, **269**, 2455–2459.

37 L. Galluzzi, L. Senovilla, I. Vitale, J. Michels, I. Martins, O. Kepp, M. Castedo and G. Kroemer, *Oncogene*, 2012, **31**, 1869–1883.

38 U. Jungwirth, C. R. Kowol, B. K. Keppler, C. G. Hartinger, W. Berger and P. Heffeter, *Antioxid. Redox Signal.*, 2011, **15**, 1085–1127.

39 A. R. Timerbaev, C. G. Hartinger, S. S. Aleksenko and B. K. Keppler, *Chem. Rev.*, 2006, **106**, 2224–2248.

40 R. Wai-Yin Sun, A. Lok-Fung Chow, X.-H. Li, J. J. Yan, S. Sin-Yin Chui and C.-M. Che, *Chem. Sci.*, 2011, **2**, 728–736.

41 A.-M. Florea and D. Büsselberg, *Cancers (Basel).*, 2011, **3**, 1351–1371.

42 J. Reedijk, *Proc. Natl. Acad. Sci.*, 2003, **100**, 3611–3616.

43 L. S. Flocke, R. Trondl, M. A. Jakupec and B. K. Keppler, *Invest. New Drugs*, 2016, **34**, 261–268.

44 W. M. Motswainyana and P. A. Ajibade, *Adv. Chem.*, 2015, **2015**, 1–21.

45 S. Y. Lee, C. Y. Kim and T.-G. Nam, *Drug Des. Devel. Ther.*, 2020, **Volume 14**, 5375–5392.

46 G. Sava and A. Bergamo, *Int. J. Oncol.*, 2000, **17**, 353–365.

47 V. V Ranade, *Platin. Met. Rev.*, 2008, **52**, 1–62.

48 T. S. Morais, F. Santos, L. Côrte-Real, F. Marques, M. P. Robalo, P. J. A. Madeira and M. H. Garcia, *J. Inorg. Biochem.*, 2013, **122**, 8–17.

49 M. J. Clarke, *Coord. Chem. Rev.*, 2002, **232**, 69–93.

50 M. Hartmann and B. K. Keppler, *Comments Inorg. Chem.*, 1995, **16**, 339–372.

51 W. Peti, T. Pieper, M. Sommer, B. K. Keppler and G. Giester, *Eur. J. Inorg. Chem.*, 1999, **1999**, 1551–1555.

52 M. J. Clarke, S. Bitler, D. Rennert, M. Buchbinder and A. D. Kelman, *J. Inorg. Biochem.*, 1980, **12**, 79–87.

53 Enzo Alessio, Giovanni Mestroni, Alberta Bergamo and Gianni Sava, *Curr. Top. Med. Chem.*, 2004, **4**, 1525–1535.

54 C. G. Hartinger, S. Zorbas-Seifried, M. A. Jakupec, B. Kynast, H. Zorbas and B. K. Keppler, *J. Inorg. Biochem.*, 2006, **100**, 891–904.

55 R. Trondl, P. Heffeter, C. R. Kowol, M. A. Jakupec, W. Berger and B. K. Keppler, *Chem. Sci.*, 2014, **5**, 2925–2932.

56 A. Casini, G. Mastrobuoni, M. Terenghi, C. Gabbiani, E. Monzani, G. Moneti, L. Casella and L. Messori, *JBIC J. Biol. Inorg. Chem.*, 2007, **12**, 1107–1117.

57 M. J. Clarke, *Ruthenium Chemistry Pertaining to the Design of Anticancer Agents*, 1989, vol. 10.

58 J. M. Rademaker-Lakhai, D. van den Bongard, D. Pluim, J. H. Beijnen and J. H. M. Schellens, *Clin. Cancer Res.*, 2004, **10**, 3717–3727.

59 G. Sava, S. Zorzet, C. Turrin, F. Vita, M. Soranzo, G. Zabucchi, M. Cocchietto, A. Bergamo, S. DiGiovine, G. Pezzoni, L. Sartor and S. Garbisa, *Clin. Cancer Res.*, 2003, **9**, 1898–905.

60 S. Pillozzi, L. Gasparoli, M. Stefanini, M. Ristori, M. D'Amico, E. Alessio, F. Scaletti, A. Becchetti, A. Arcangeli and L. Messori, *Dalt. Trans.*, 2014, **43**, 12150–12155.

61 G. Sava, S. Pacor, G. Mestroni and E. Alessio, *Clin. Exp. Metastasis*, 1992, **10**, 273–280.

62 G. Sava, I. Capozzi, K. Clerici, G. Gagliardi, E. Alessio and G. Mestroni, *Clin. Exp. Metastasis*, 1998, **16**, 371–379.

63 A. Bergamo, R. Gagliardi, V. Scarcia, A. Furlani, E. Alessio, G. Mestroni and G. Sava, *J. Pharmacol. Exp. Ther.*, 1999, **289**, 559–564.

64 F. Frausin, V. Scarcia, M. Cocchietto, A. Furlani, B. Serli, E. Alessio and G. Sava, *J. Pharmacol. Exp. Ther.*, 2005, **313**, 227–233.

65 F. Kratz, *J. Control. Release*, 2008, **132**, 171–183.

66 M. Debidda, B. Sanna, A. Cossu, A. Posadino, B. Tadolini, C. Ventura and G. Pintus, *Int. J. Oncol.*, 2003, **23**, 477–482.

67 G. Sava, K. Clerici, I. Capozzi, M. Cocchietto, R. Gagliardi, E. Alessio, G. Mestroni and A. Perbellini, *Anticancer. Drugs*, 1999, **10**, 129–138.

68 M. Sulyok, S. Hann, C. G. Hartinger, B. K. Keppler, G. Stingeder and G. Koellensperger, *J. Anal. At. Spectrom.*, 2005, **20**, 856–863.

69 H. Maeda, J. Wu, T. Sawa, Y. Matsumura and K. Hori, 2000, **65**, 271–284.

70 A. R. Timerbaev, L. S. Foteeva, A. V. Rudnev, J. K. Abramski, K. Połeć-Pawlak, C. G. Hartinger, M. Jarosz and B. K. Keppler, *Electrophoresis*, 2007, **28**, 2235–2240.

71 J. Coverdale, T. Laroiya-McCarron and I. Romero-Canelón, *Inorganics*, 2019, **7**, 1–15.

72 M. Groessl, Y. O. Tsybin, C. G. Hartinger, B. K. Keppler and P. J. Dyson, *JBIC J. Biol. Inorg. Chem.*, 2010, **15**, 677–688.

73 T. M. Thornton and M. Rincon, *Int. J. Biol. Sci.*, 2009, **5**, 44–52.

74 B. Schoenhacker-Alte, T. Mohr, C. Pirker, K. Kryeziu, P.-S. Kuhn, A. Buck, T. Hofmann, C. Gerner, G. Hermann, G. Koellensperger, B. K. Keppler, W. Berger and P. Heffeter, *Cancer Lett.*, 2017, **404**, 79–88.

75 A. Chumakov, V. Batalova and Y. Slizhov, in *AIP Conference Proceedings*, 2016, vol. 1772, pp. 0400041–0400046.

76 K. Jomova, S. Baros and M. Valko, *Transit. Met. Chem.*, 2012, **37**, 127–134.

77 S. Kapitza, M. A. Jakupec, M. Uhl, B. K. Keppler and B. Marian, *Cancer Lett.*, 2005, **226**, 115–121.

78 L. Morbidelli, S. Donnini, S. Filippi, L. Messori, F. Piccioli, P. Orioli, G. Sava and M. Ziche, *Br. J. Cancer*, 2003, **88**, 1484–1491.

79 J. B. Gifford, W. Huang, A. E. Zeleniak, A. Hindoyan, H. Wu, T. R. Donahue and R. Hill, *Mol. Cancer Ther.*, 2016, **15**, 1043–1052.

80 C. Roller and D. Maddalo, *Front. Pharmacol.*, 2013, **4**, 1–5.

81 P. Heffeter, B. Atil, K. Kryeziu, D. Groza, G. Koellensperger, W. Körner, U. Jungwirth, T. Mohr, B. K. Keppler and W. Berger, *Eur. J. Cancer*, 2013, **49**, 3366–3375.

82 H. A. O'Riley, A. Levina, J. B. Aitken and P. A. Lay, *Inorganica Chim. Acta*, 2017, **454**, 128–138.

83 Y. Chen, R. Guan, C. Zhang, J. Huang, L. Ji and H. Chao, *Coord. Chem. Rev.*, 2016, **310**, 16–40.

84 A. Weiss, R. H. Berndsen, M. Dubois, C. Müller, R. Schibli, A. W. Griffioen, P. J. Dyson and P. Nowak-Sliwinska, *Chem. Sci.*, 2014, **5**, 4742–4748.

85 G. Shi, S. Monro, R. Hennigar, J. Colpitts, J. Fong, K. Kasimova, H. Yin, R. DeCoste, C. Spencer, L. Chamberlain, A. Mandel, L. Lilge and S. A. McFarland, *Coord. Chem. Rev.*, 2015, **282**–**283**, 127–138.

86 D. A. Smithen, H. Yin, M. H. R. Beh, M. Hetu, T. S. Cameron, S. A. McFarland and A. Thompson, *Inorg. Chem.*, 2017, **56**, 4121–4132.

87 L. Zeng, P. Gupta, Y. Chen, E. Wang, L. Ji, H. Chao and Z. S. Chen, *Chem. Soc. Rev.*, 2017, **46**, 5771–5804.

88 T. S. Prathima, B. Choudhury, M. G. Ahmad, K. Chanda and M. M. Balamurali, *Coord. Chem. Rev.*, 2023, **490**, 1–38.

89 C. S. Allardyce, P. J. Dyson, D. J. Ellis and S. L. Heath, 2001, **2**, 1396–1397.

90 G. S. Smith and B. Therrien, *Dalt. Trans.*, 2011, **40**, 10793–10800.

91 F. Wang, A. Habtemariam, E. P. L. van der Geer, R. Fernández, M. Melchart, R. J. Deeth, R. Aird, S. Guichard, F. P. A. Fabbiani, P. Lozano-Casal, I. D. H. Oswald, D. I. Jodrell, S. Parsons and P. J. Sadler, *Proc. Natl. Acad. Sci.*, 2005, **102**, 18269–18274.

92 B. Therrien, *Coord. Chem. Rev.*, 2009, **253**, 493–519.

93 Y. Wang, J. Jin, L. Shu, T. Li, S. Lu, M. K. M. Subarkhan, C. Chen and H. Wang, *Chem. – A Eur. J.*, 2020, **26**, 15170–15182.

94 A. Mondal, U. Sen, N. Roy, V. Muthukumar, S. K. Sahoo, B. Bose and P. Paira, *Dalt. Trans.*, 2021, **50**, 979–997.

95 Y. N. V. Gopal, D. Jayaraju and A. K. Kondapi, *Biochemistry*, 1999, **38**, 4382–4388.

96 B. S. Murray, M. V. Babak, C. G. Hartinger and P. J. Dyson, *Coord. Chem. Rev.*, 2016, **306**, 86–114.

97 C. Scolaro, C. G. Hartinger, C. S. Allardyce, B. K. Keppler and P. J. Dyson, *J. Inorg. Biochem.*, 2008, **102**, 1743–1748.

98 C. Scolaro, A. Bergamo, L. Brescacin, R. Delfino, M. Cocchietto, G. Laurenczy, T. J. Geldbach, G. Sava and P. J. Dyson, *J. Med. Chem.*, 2005, **48**, 4161–4171.

99 Z. Adhireksan, G. E. Davey, P. Campomanes, M. Groessl, C. M. Clavel, H. Yu, A. A. Nazarov, C. H. F. Yeo, W. H. Ang, P. Dröge, U. Rothlisberger, P. J. Dyson and C. A. Davey, *Nat. Commun.*, 2014, **5**, 1–13.

100 P. Nowak-Sliwinska, J. R. van Beijnum, A. Casini, A. A. Nazarov, G. Wagnières, H. van den Bergh, P. J. Dyson and A. W. Griffioen, *J. Med. Chem.*, 2011, **54**, 3895–3902.

101 A. Bergamo, A. Masi, A. F. A. Peacock, A. Habtemariam, P. J. Sadler and G. Sava, *J. Inorg. Biochem.*, 2010, **104**, 79–86.

102 R. E. Aird, J. Cummings, A. A. Ritchie, M. Muir, R. E. Morris, H. Chen, P. J. Sadler and D. I. Jodrell, *Br. J. Cancer*, 2002, **86**, 1652–1657.

103 R. L. Hayward, Q. C. Schornagel, R. Tente, J. S. Macpherson, R. E. Aird, S. Guichard, A. Habtemariam, P. Sadler and D. I. Jodrell, *Cancer Chemother. Pharmacol.*, 2005, **55**, 577–583.

104 A. Habtemariam, M. Melchart, R. Fernández, S. Parsons, I. D. H. Oswald, A. Parkin, F. P. A. Fabbiani, J. E. Davidson, A. Dawson, R. E. Aird, D. I. Jodrell and P. J. Sadler, *J. Med. Chem.*, 2006, **49**, 6858–6868.

105 F. A. Cotton, *Inorg. Chem.*, 1965, **4**, 334–336.

106 M. A. S. Aquino, *Coord. Chem. Rev.*, 1998, **170**, 141–202.

107 M. A. S. Aquino, *Coord. Chem. Rev.*, 2004, **248**, 1025–1045.

108 A. C. Murillo, F. A. Cotton and A. R. Walton, *Multiple Bonds Between Metal Atoms*, Springer Science and Business media, New York, Boston, Dordrecht, London, Moscow, 3rd edn., 2005.

109 T. A. Stephenson and G. Wilkinson, *J. Inorg. Nucl. Chem.*, 1966, **28**, 2285–2291.

110 I. Tolbatov, E. Barresi, S. Taliani, D. La Mendola, T. Marzo and A. Marrone, *Inorg. Chem. Front.*, 2023, **10**, 2226–2238.

111 M. J. Bennett, K. G. Caulton and F. A. Cotton, *Inorg. Chem.*, 1969, **8**, 1–6.

112 B. K. Keppler, M. Henn, U. M. Juhl, M. R. Berger, R. Niebl and F. E. Wagner, 1989, vol. 10, pp. 41–69.

113 R. Janicki, A. Mondry and P. Starynowicz, *Coord. Chem. Rev.*, 2017, **340**, 98–133.

114 M. J. Thun, S. J. Henley and C. Patrono, *JNCI J. Natl. Cancer Inst.*, 2002, **94**, 252–266.

115 D. de Oliveira Silva, *Anticancer. Agents Med. Chem.*, 2010, **10**, 312–323.

116 D. de Oliveira Silva, in *Frontiers in Anti-Cancer Drug Discovery, Volume 4*, eds. Atta-

ur-Rahman; and M. I. Choudhary, BENTHAM SCIENCE PUBLISHERS, Sharjah, 2014, vol. 4, pp. 88–156.

117 D. PEREG and M. LISHNER, *J. Intern. Med.*, 2005, **258**, 115–123.

118 L. A. García, C. Huerta-alvarez, L. A. G. Rodriguez and C. Huerta-alvarez, *Epidemiology*, 2000, **11**, 376–381.

119 G. A. FitzGerald, *Nat. Rev. Drug Discov.*, 2003, **2**, 879–890.

120 P. Rao and E. E. Knaus, *J. Pharm. Pharm. Sci.*, 2008, **11**, 81–110.

121 G. Ribeiro, M. Benadiba, A. Colquhoun and D. de Oliveira Silva, *Polyhedron*, 2008, **27**, 1131–1137.

122 K. Xu, L. Wang and H.-K. G. Shu, *Oncotarget*, 2014, **5**, 1241–1252.

123 M. Benadiba, R. R. P. dos Santos, D. de O. Silva and A. Colquhoun, *J. Inorg. Biochem.*, 2010, **104**, 928–935.

124 M. Benadiba, I. De M. Costa, R. L. S. R. Santos, F. O. Serachi, D. De Oliveira Silva and A. Colquhoun, *J. Biol. Inorg. Chem.*, 2014, **19**, 1025–1035.

125 C. Sumithaa and M. Ganeshpandian, *Mol. Pharm.*, 2023, **20**, 1453–1479.

126 B. Lastra-Barreira, J. Díez and P. Crochet, *Green Chem.*, 2009, **11**, 1681.

127 P. Ertl, *J. Cheminform.*, 2020, **12**, 1–6.

CHAPTER 2

Synthesis, characterization, and in vitro cytotoxic screening of organometallic ruthenium(II) arene complexes bearing trichloro stannyl ligands against human breast MCF-7 cancer cell line

2.1 INTRODUCTION

Research directed towards ruthenium complexes has shown that they possess good selectivity, low toxicity, and high sensitivity for tumours both *in vitro* and *in vivo.*[1] Early investigations of ruthenium complexes and the evaluation of their anticancer properties began in the 1970s, with the discovery that ruthenium red exhibits cytotoxic anticancer activity.[2] Further investigations led to the discovery of the cytotoxic properties of compounds *fac*-$[RuCl_3(NH_3)_3]$ and cis-$[RuCl_2(NH_3)_4]Cl$.[3] However, *fac*-$[RuCl_3(NH_3)_3]$ was declared unsuitable for further evaluation due to its poor solubility in aqueous solutions.

RAPTA-C, an organometallic complex bearing an arene ligand, has anticancer properties comparable to the abovementioned antimetastatic clinical drugs and is currently being employed in advanced preclinical studies.[4] The organometallic complex inhibits primary tumour growths in preclinical models of colorectal and ovarian cancers through an antiangiogenic mode of action.[5] The presence of the Ru–Cl bond within the inner coordination sphere of the three-legged piano stool or pseudo-octahedral type of complex has been reported to impart high susceptibility of the complex to hydrolysis. The hydrolysis of this metal-chloride bond is of great importance as the resultant aqua species are the activated form of the drug, with capabilities of binding to biological molecular drug targets such as proteins and DNA sequences/nucleotides (through electrostatic forces, weak Van der Waals forces or hydrogen bonding). The choice of a ligand is of great importance, with arene moieties known to increase bioavailability, cellular uptake and accumulation.[6] Overall, organometallic ruthenium arene-bearing complexes have shown promising potential as anticancer therapeutic agents.

Organotin complexes have been studied and investigated for their cytotoxic properties against malignant tumours, with a particular class of interesting compounds involving the facile insertion of $SnCl_2$ within the coordination sphere of ruthenium arene complexes. The insertion of $SnCl_2$ on the metal centre is expected to enhance the solubility properties of these complexes, as reported previously.[7] The reaction of Ru(II) arene complexes, $[RuCl_2(\eta^6\text{-}C_6H_6)(PR_3)]$, where R = aryl or alkyl with anhydrous $SnCl_2$ leads to the formation of a Ru(II) complex with a strong covalent Ru–Sn bond.[8] The reaction of SnX_2 with other metal centres such as palladium and platinum has received far more attention, while those involving ruthenium derivatives have not been investigated extensively.[9] The neutral complexes based on $[RuCl(\eta^6\text{-}C_6H_6)(PR_3)(SnCl_3)]$, where the R substituent was varied between the σ – donor OCH_3 and the two π - acceptor ligands (OPh, Ph) reported to exhibit very mild to negligible

anticancer properties, while the ionic complex $[RuCl(\eta^6 - C_6H_6)(PPh_3)(SnCl_3)(DMAP)]^+BF_4^-$ (Figure 2.1) was reported to be selective for the human ovarian A2780 cancer cell line.

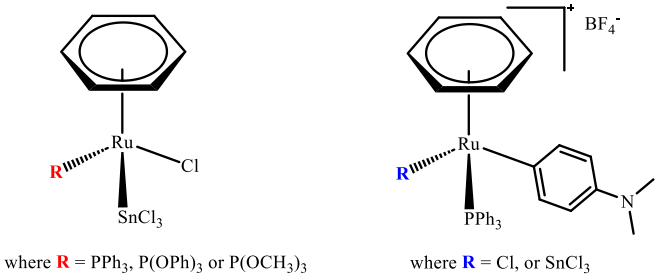

Figure 2.1 Ruthenium arene complexes with promising cytotoxic properties against the human ovarian A2780 cancer and the cisplatin-resistant cell lines.[7]

The moderate cytotoxic properties of the neutral complexes are observed to be a result of the insolubility of $[RuCl(\eta^6\text{-}C_6H_6)(PR_3)(SnCl_3)]$ complexes in aqueous media. This was despite the incorporation of $SnCl_3$ ligands within the inner coordination sphere shell, which is expected to enhance the cytotoxic properties of the complexes. Encouraged by these findings, research directed towards improving the solubility, cytotoxicity, and selectivity of organometallic ruthenium arene complexes bearing trichlorostannyl ligands against carcinoma cell lines has been of great interest. In this chapter, the synthesis, characterization and cytotoxic properties of the complexes **C10 - C15** evaluated against the estrogen receptor-positive human breast MCF-7 adenocarcinoma cell line are described and discussed.[10]

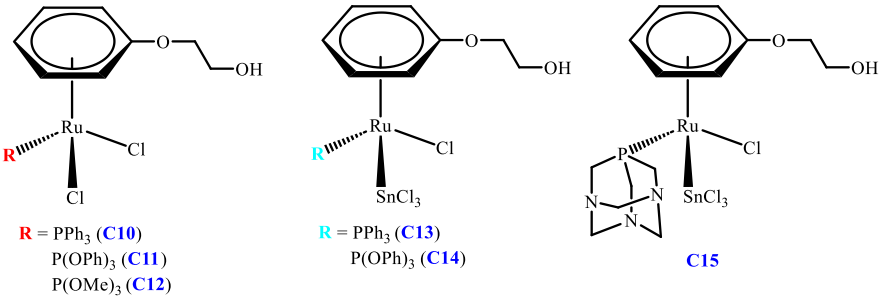

Figure 2.2 Organometallic Ru(II) arene piano stool complexes bearing trichlorostannyl ligands screened for cytotoxic effects against human breast oestrogen receptor-positive (ER+) MCF-7 adenocarcinoma cell line.[10]

2.2 RESULTS AND DISCUSSION

2.2.1 Synthesis of complexes, **C10 - C15**.

The ruthenium dimer, $[RuCl_2(\eta^6\text{-}C_6H_6OCH_2CH_2OH)]$ (**C9**), was synthesized following previously published literature methods.[11] The precursor complex enables facile entry to form the piano stool complexes **C10** - **C12** *via* bridge splitting reaction with the appropriate phosphine ligand, as shown in Scheme 2.1.[11,12] Complexes **C10** and **C11**, were also synthesized following modified previously published literature procedures.[11] In the modification of the procedure, the reaction mixture was allowed to stir for an extended period for the reaction to reach completion, which enabled a facile product isolation procedure without the need for column chromatography techniques. The reaction of $SnCl_2$ with one equivalence of the synthesized complexes, **C10** or **C11** led to the formation of the novel complexes $[RuCl(\eta^6\text{-}C_6H_5OCH_2CH_2OH)(Ph_3)(SnCl_3)]$ (**C13**) and $[RuCl(\eta^6\text{-}C_6H_5OCH_2CH_2OH)\{P(OPh_3)\}(SnCl_3)]$ (**C14**), respectively. Complex **C15** is a well-known complex[12,13] and is an analogue to RAPTA-C. The complex was successfully synthesized by reacting the ruthenium dimer **C9,** with 1,3,5-triaza-7-phosphaadamantane (PTA) ligand.

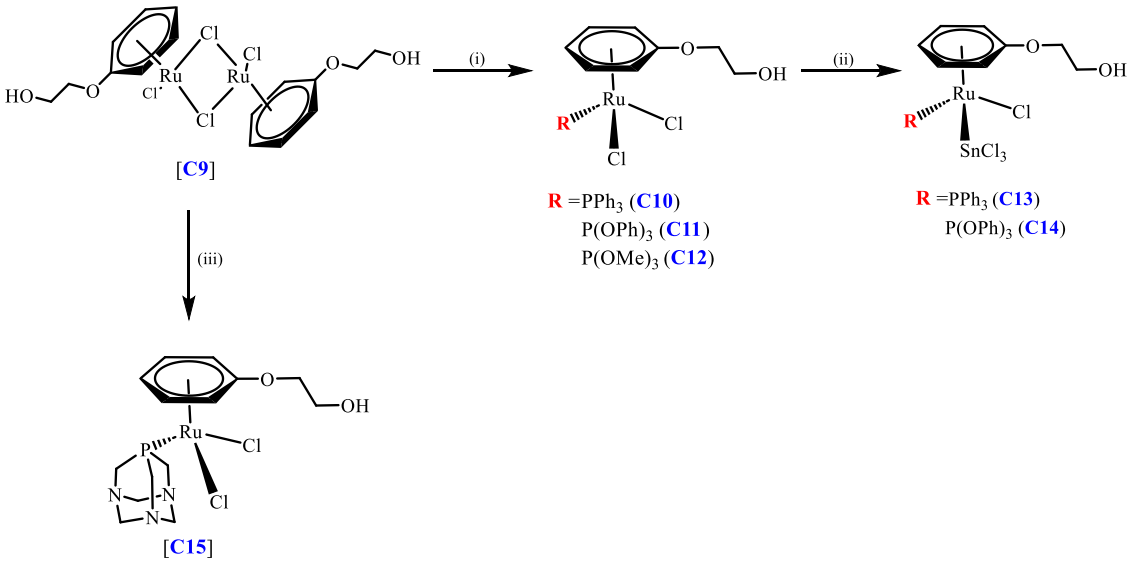

Scheme 2.1 Synthetic procedure of organometallic ruthenium(II) arene complexes bearing trichlorostannyl ligands. (i) 2 equiv. of PPh_3/$P(OPh)_3$/$P(OMe)_3$ in DCM, r.t., 17 h; (ii) 1 equiv. $SnCl_2$ in DCM, reflux, 4.5 h; (iii) 2 equiv. PTA in DCM:Methanol (1:1), 50 °C, 30 min.[10]

2.2.2 Spectroscopic and solid state characterization of complexes **C10** - **C15**.

The novel organometallic ruthenium(II) arene complexes bearing trichloro stannyl ligands were characterized using various spectroscopic and analytical techniques which included Nuclear Magnetic Resonance (^{1}H and ^{31}P{^{1}H}) spectroscopy, infrared spectroscopy (IR), thermogravimetric analysis (TGA), high-resolution mass spectrometry (HRMS), and ultraviolet-visible spectroscopy (UV-Vis). Single crystals suitable for X-ray analysis were collected for **C14** only through slow evaporation from dichloromethane solvent. Attempts to grown crystals for all other complesxes discussed in this chapter were not successful.

2.2.2.1 Nuclear Magnetic Resonance (NMR) Spectroscopy

The ^{1}H-NMR spectra of complexes **C10** - **C12** were recorded in DMSO-d_6 and were in agreement with the proposed structures and are comparable with those reported in the literature.[7] The ^{1}H-NMR spectrum of **C10** - **C12** are all documented in Chapter 6 (Figures 6.1 - 6.3).

For **C10** (Figure 6.1), the most de-shielded protons in the downfield region (7.39 - 7.68 ppm) resonate as a multiplet that integrates for fifteen protons in total, indicative of the coordinated triphenylphosphine ligand. The spectra of the triphenylphosphite complex (**C11**, Figure 6.2) resulted in an up-field shift of the spectrum, with the signals for the triphenylphosphite moiety observed between 7.16 - 7.45 ppm. This up-field shift is indicative of strong π-backbonding in the presence of triphenylphosphite compared to the triphenylphosphine, shielding the aromatic protons. The replacement of a triphenylphosphine with a trimethylphosphite in **C12** results in the appearance of a doublet signal observed in the up-field region between 3.62 and 3.65 ppm, corresponding to the $P(OCH_3)_3$ protons coupling to the phosphorous atom as observed ^{1}H NMR spectrum of **C12** (Figure 6.3). Furthermore, for **C10**, the -CH_2CH_2- proton signals of the hydrophilic tail are observed at 3.73 and 4.14 ppm, each represented by a triplet and integrating for the two protons (**H$_e$** and **H$_f$**). The signal for the methylene protons **H$_e$** appears further downfield at 4.14 ppm, ascribed to the mesomeric of the oxygen atom, which donates its electrons onto the η^6-coordinated arene ring and at the same time withdraws electrons from the adjacent CH_2 of the hydrophilic tail. On the other hand, the signal for the protons **H$_f$** is observed further up-field, suggesting that these protons are more shielded. A similar observation was made in the ^{1}H-NMR spectra of complexes **C11** and **C12**. The ^{1}H-NMR spectrum of **C12** indicates a doublet observed in the up-field region between 3.62 and 3.65 ppm, corresponding to the $P(OCH_3)_3$ protons coupling to the phosphorous atom. A triplet assigned to the OH group

of the hydrophilic tail was observed at 4.91 ppm. In most cases, the hydroxyl group is indicated by a broad signal. However, in this case upon complexation, the hydroxyl group proton couples with the aliphatic -CH_2CH_2- protons.

The η^6-coordinated arene protons observed in the ^{1}H-NMR spectrum of **C10** are labelled **b**, **c** and **d** and are characterized by a multiplet (integrating for 2H, observed between 5.62 - 5.57 ppm), a doublet (integrating for 2 protons, observed between 5.27 - 5.26 ppm) and a triplet (integrating the proton located in the para position of the ring, 4.23 ppm), respectively. The protons located in the ortho-positions of the arene ring and adjacent to the hydrophilic tail (labelled **c**) are in the same chemical environment. Similarly, the same is true for the protons located in the meta-positions (labelled **b**) of the arene ring. In the spectrum of **C11**, the protons located in the *meta*- (labelled **b**) and *para*- (labelled **d**) positions of the η^6-arene ring overlap with one another, a broad singlet observed between 5.77 - 5.68 ppm and integrating for 3 protons. The 2 protons located in the *ortho*-positions of the arene ring, adjacent to the attached hydrophilic tail (labelled **c**) appear as a doublet between (4.90 - 4.82 ppm) as anticipated. The spectrum of **C12** is shifted further up-field due to the electron donating coordinated trimethyl phosphite ligand. The η^6-arene ring protons labelled **b**, **c** and **d** are characterized by a multiplet (integrating for 2 protons), a doublet (integrating for 2 protons) and a triplet (integrating for one 1 proton) observed in the aromatic region. Surprisingly, the hydroxyl group of the hydrophilic tail has a proton signal appearing as a triplet (observed between 4.18 ppm). This may be attributed to the fact that the hydroxyl proton may be overlapping with the -CH_2 adjacent protons (labelled **f** in the structure of the **C12**).

The ^{1}H NMR spectra of the novel complexes **C13 - C14** were recorded in DMSO-d_6 and $CDCl_3$ respectively, with all assignments in agreement and consistent with the proposed structures. The spectra of the complexes are represented in Figure 6.4 (**C13**) and Figure 6.6 (**C14**) and are all documented in Chapter 6.

For both novel complexes **C13** and **C14**, the η^6 coordinated arene ring loses its symmetrical nature and the substitution of the Ru–Cl with the Ru–Sn results in the aromatic protons being in different chemical environments. This analogy was also observed and correlates to earlier reports of similar work.[7,13] The ^{31}P{^{1}H} NMR spectra of **C13** and **C14** were recorded in

DMSO-d_6 and $CDCl_3$ respectively and are represented in Figure 6.5 and Figure 6.7 documented in Chapter 6

In the ^1H NMR spectrum of **C13** (Figure 6.4), the resonance η^6- arene ring protons (labelled **b-f**) are all in different chemical environments due to the asymmetrical nature of the ligand. This analogy was also observed and correlates to earlier reports of similar work[7,13]. The proton located in the para position to the hydrophilic tail (labelled **b**) is characterized by a triplet observed between 6.38 - 6.42 ppm. The two doublets of proton signals labelled **e** (5.93 - 5.95 ppm) and **f** (6.08 - 6.10 ppm) are observed further downfield in comparison to the two multiplets proton signals **c** (5.02 ppm) and **d** (5.54 - 5.59 ppm). This implies that the arm attached to the ring is more electron withdrawing (ie. increased inductive effect of the oxygen). Furthermore, protons **e** and **f** as well as **c** and **d** are all in different chemical environments. Under normal conditions, protons **e** and **f** would be in the same chemical environment. This is also true for protons **c** and **d**. However, according to the spectrum, all η^6-coordinated arene protons appear in different chemical environments. From this, we can postulate that all these protons recognise different electronegative groups coordinated to the ruthenium metal centre ($SnCl_3^-$ and Cl^-) from their locked positions (the bond between the ruthenium metal centre and arene ring is not freely rotating). In addition, each of these protons in each pair (pair **c**/**d** and pair **e**/**f**) will have different chemical shifts. The triphenylphosphine proton signals are located further downfield and are labelled **a** (7.41 - 7.66 ppm), though the integration number is slightly overboard but the protons of the bulky triphenylphosphine ligand are observed in their respective region. The proton signal **c** appears to be broad surprisingly. Ideally, this proton signal should be represented by a triplet multiplicity. However, due to the nuclear magnetic resonance frequency of the instrument used to acquire and record the spectrum being 300 MHz, the signal proton appears to be broad and not well-defined. The hydrophilic tail protons (-CH_2CH_2-) labelled **g** (4.17 ppm) and **h** (3.71 ppm) are observed in the up-field region, each integrating for the two protons as expected.

For **C14** (Figure 6.6), the structure of the complex was confirmed by the presence of a multiplet assigned to the electron donating triphenylphosphite protons labelled **a** (7.38 pm) integrated along with the solvent signal, chloroform. Similarly, for **C14**, the η^6 arene ring has proton signals labelled **b-f** all in chemically different environments and were assigned accordingly. The proton signals **e** and **f** are in chemically different environments, with **f** appearing as doublet observed further downfield between 5.74 - 5.76 ppm. This may be attributed to the proximity

of the proton to the chloride and tin trichloride ligands as they are in the same environment, in this locked position. The same concept applies to the protons labelled **c** (observed at 4.51 and 4.53 ppm) and **d** (4.16 ppm). The latter aromatic protons are observed outside the aromatic region due to the presence of the sterically hindered electron-donating triphenyl phosphite ligand existing in the same chemical environment as the protons labelled **c** and **d**. Proton **c** is observed as a multiplet in the spectrum as it couples to the other η^6 arene protons *via* long-range coupling.

*2.2.2.2 Single X-ray crystallography of **C14***

Crystals suitable for analysis of complex **C14** were obtained by slow evaporation of a dilute sample of **C14** in dichloromethane at 7°C (Ortep diagram represented in Figure 2.3). Additionally, the CheckCIF report and packing diagram (Figure 6.8) of **C14** are documented in Chapter 6.

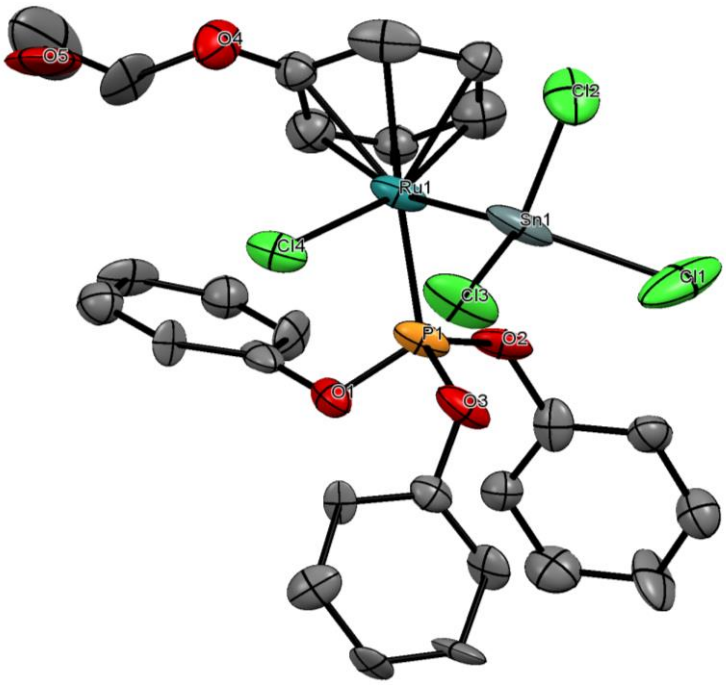

Figure 2.3 ORTEP representation of the X-ray structure of complex **C14**. The diagram was drawn with 30% probability thermal ellipsoids and all hydrogen atoms were omitted for clarity. A disorder is noticeable at one Cl^- atom (Cl3 and Cl33), consisting of sites of occupancy of 0.55 and 0.45, respectively.

This was conducted to confirm whether the Ru–Cl was replaced with the Ru–Sn bond. The complex **C14** crystallizes in the orthorhombic Pca21 space group with molecules in the unit

cell. The crystal data and structure refinement are summarized in Table 2.4 and documented in the experimental section. The complex has typical features of a piano-stool organometallic Ru(II) arene complexes. Additionally, the complex has a Ru–Sn bond length of 2.5627 (19) Å comparable to the complex $[(\eta^6\text{-}C_6H_6)RuCl(SnCl_3)(P(OPh)_3)]$ (2.5686 Å) reported in published literature.[7] The geometry around the Ru metal centre can be described as a distorted tetrahedral because the complex constitutes a slightly distorted tetrahedral geometry about the Sn centre, as observed by the slight deviations to form a perfect tetrahedral geometry: Cl(1)–Sn(1)–Ru(1) 120.30, Cl(3)–Sn(1)–Ru(1) 118.9, Cl(2)–Sn(1)–Ru(1) 115.34 °. The selected bond lengths and angles are summarized in Table 2.1.

Table 2.1 Selected bond lengths (Å) and angles (°) of **C14**.

Bond	Bond lengths [Å]	Angle	Bond angles [°]
Sn1 – Cl1	2.377	Ru1 – Sn1 – Cl4	85.46
Sn1 – Cl2	2.351	Ru1 – Sn1 – Cl2	86.56
Sn1 – Cl3	2.409	Cl1 – Sn1 – Cl2	96.30
Sn1 – Ru1	2.563	Cl1 – Sn1 – Cl3	108.00
Ru1 – Cl4	2.379	Cl2 – Sn1 – Cl3	92.50
Ru1 – P1	2.246		

2.2.2.3 Thermogravimetric analysis

Thermogravimetric analysis (TGA) thermal curve of **C13** and **C14** was performed on TGA Q500 V20.13 Build 39, and the analysis curves are depicted in Figure 6.9 (Chapter 6).

For **C14**, the first mass lost weighs 26.50 g/mol (3.2 %) at 177.74°C. This significant loss in mass can be roughly attributed to the detachment of the combination of the tin trichloride and the chloride ligands coordinated to the ruthenium metal centre from the parent complex molecule. The largest mass decrease weighs 149.00 g/mol (18.40%) and was lost at temperatures ranging from 225.24 - 339.11°C. This decomposition step can tentatively be traced to the loss of the η^6 -phenyl ring coordinated ligand, having a hydrophilic $-OCH_2CH_2OH$ tail.

2.2.3 Water solubility tests

The addition of a hydrophilic substituent on the arene ligand was intended to induce and improve the solubility of the novel investigated complexes. Dilution tests were conducted to assess the relative water solubilities of the complexes. Complexes **C13** and **C15** were found to be partially water-soluble at 20°C (0.0300 mg/mL and 10 mg/mL, respectively). On the other hand, complexes **C11** and **C14** were found to be insoluble.

2.2.4 *In vitro* cell viability assays

The short-term cytotoxicity of the organometallic Ru(II) arene complexes bearing stannyl trichloride ligands **C10 - C15** was investigated against the human breast MCF-7 adenocarcinoma cell line. Cell viability assays were performed using the MTT colourimetric assay. Mycoplasma infection tests were performed to ensure the healthy conditions of MCF-7 cells and only mycoplasma-negative cells were seeded for experiments. Mycoplasma-free cells when stained with Hoechst staining, exhibit bright nuclear staining with no cytoplasmic or membrane staining and were photographed and represented in Figure 2.4.

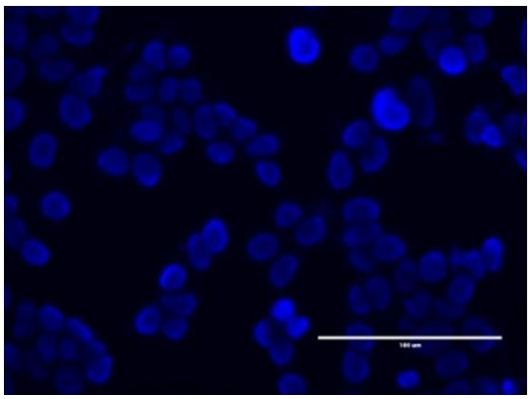

Figure 2.4 Fluorescent microscope images of mycoplasma-free human breast MCF-7 cancer cells used in the study.

*2.2.4.1 Preliminary cytotoxic screen of Ru(II) arene complexes, **C10 - C15**.*

To evaluate the anticancer properties of the prepared Ru(II) arene complexes, **C10 - C15** were prescreened for cytotoxic properties at 5.0 µM and 10 µM. Cell viability of MCF-7 cancer cells was determined using the MTT colourimetric assay. In all experiments, DMSO was used as the vehicle and the clinically prepared cisplatin drug was used as the positive control. The percentage cell viability of MCF-7 cells after 24 hours of drug exposure is shown in Table 2.2 and as a bar graph in Figure 2.5.

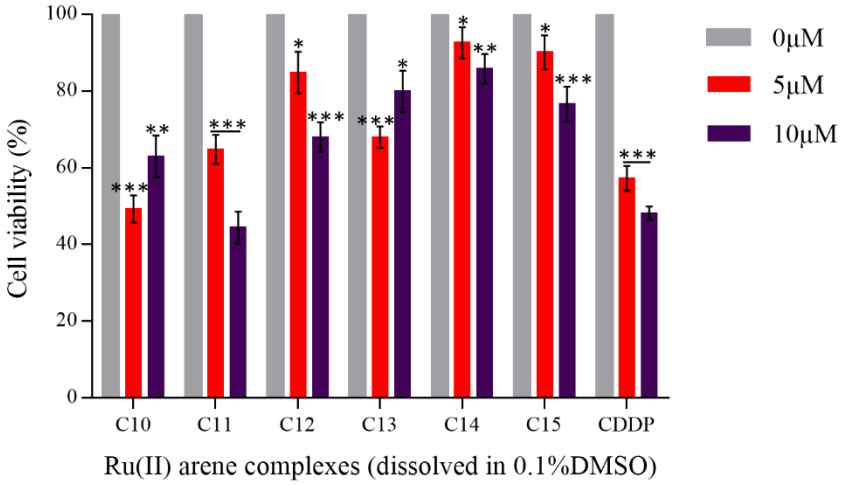

Figure 2.5 Percentage cell viability screen test of complexes **C10 - C15** against the human breast MCF-7 adenocarcinoma cell line after 24 hours of 5 µM and 10 µM dose treatment. The clinically prepared cisplatin drug (CDDP) was used as a positive control. GraphPad Prism 7.0 was used to analyse the data and a parametric unpaired t-test was performed, where *p<0.05, **P<0.01 and ***p<0.001 were accepted and considered to be significant.

Table 2.2 Percentage cell viability (µM ± SEM) screen test for ruthenium(II) arene trichloride stannyl complexes **C10 - C15** against the oestrogen receptor-positive (ER +ve) human breast MCF-7 adenocarcinoma cell line.

Ru(II) arene organometallic complexes	Single-dose treatments	
	5.0 µM	10 µM
	(% cell viability ± SEM)	
C10	49.3 ± 0.125	62.9 ± 0.180
C11	64.8 ± 0.102	44.4 ± 0.132
C12	84.9 ± 0.160	68.0 ± 0.121
C13	68.0 ± 0.094	79.9 ± 0.170
C14	92.6 ± 0.146	82.5 ± 0.281
C15	90.2 ± 0.126	76.6 ± 0.152
CDDP[a]	57.3 ± 0.114	48.2 ± 0.175

[a]*Clinically prepared cisplatin drug, used as a positive control for 24-hour single dose-response treatments.*

The results show that all complexes at both 5.0 µM and 10 µM after 24 hours of drug exposure cause a decrease in MCF-7 cell viability. The four complexes, **C11**, **C12**, **C14** and **C15** cause a dose-dependent significant decrease in cell viability. At 10 µM, **C11** exhibits the greatest cytotoxicity of all complexes and compared to **C10** and **C12**, caused 55.6% of MCF-7 cell death. This provides evidence that the coordination of the sterically hindered triphenyl phosphite ligand, possessing greater electron-donating effects compared to the coordinated triphenylphosphine (**C10**) and trimethyl phosphite (**C12**), enhances the cytotoxic properties of **C11**. Importantly, **C11** inhibited MCF-7 cell viability comparable to that of cisplatin (CDDP).

2.2.4.2 Multidose *in vitro* screen of the novel complexes, **C13** and **C14**.

To further evaluate the short-term cytotoxic properties of the novel complexes **C13** and **C14,** MCF-7 breast cancer cells were treated for 24 hours with 5 doses of these complexes (2 - 10 µM). MTT assays were performed, and the half-maximal inhibitory concentrations (IC_{50}) were determined. CDDP was included as a positive control and all experiments were performed in

triplicate with each of the complexes tested in quadruplicate. Dose-response curves were fitted using GraphPad prism v7.0 (Chapter 6, Figure 6.10 - 6.12). Results show that **C13** and **C14** exhibit minimal to moderate cytotoxicity (represented in Figure 2.6) and therefore their relative IC_{50} values had to be predicted (shown in Table 2.3). Cell density images of wells consisting of the treated cells were photographed before and after a 24-hour treatment with complexes **C13** and **C14** at 10 µM, as represented in Figure 2.7.

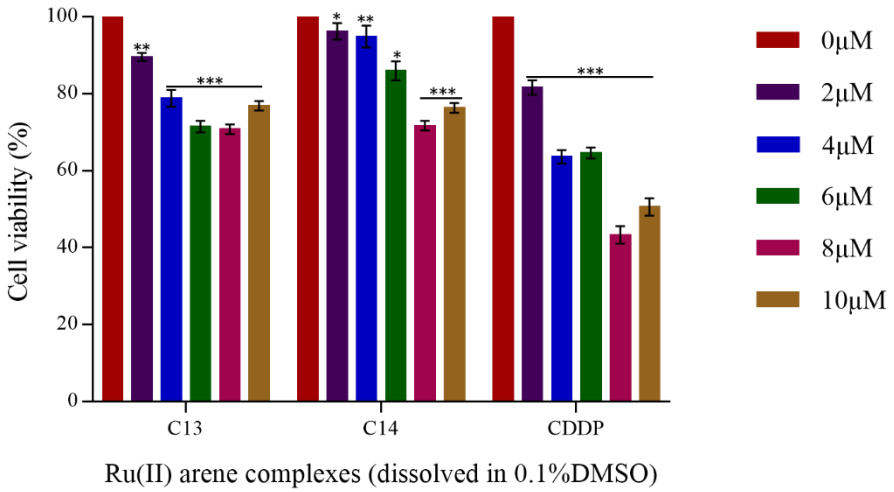

Figure 2.6 Cytotoxic properties of complexes C13 and C14 after multidose 24-hour treatment (2 - 10 µM). The clinically prepared cisplatin drug (CDDP) was used as a positive control. GraphPad Prism 7.0 was used to analyse the data and a parametric unpaired t-test was performed, where *p<0.05, **P<0.01 and ***p<0.001 were accepted and considered to be significant.

Table 2.3 Predicted IC_{50} values (µM ± SEM) of the Ru(II) arene complexes bearing trichlorostannyl ligands, **C13** and **C14** against human breast MCF-7 adenocarcinoma cell line.

Ru(II) arene complexes	IC_{50} value (µM ± SEM)
C13	31.3 ± 0.27
C14	16.7 ± 0.14
CDDP[a]	8.02 ± 0.05

[a]Clinically prepared cisplatin drug, used as a positive control for 24 hours of complex exposure.

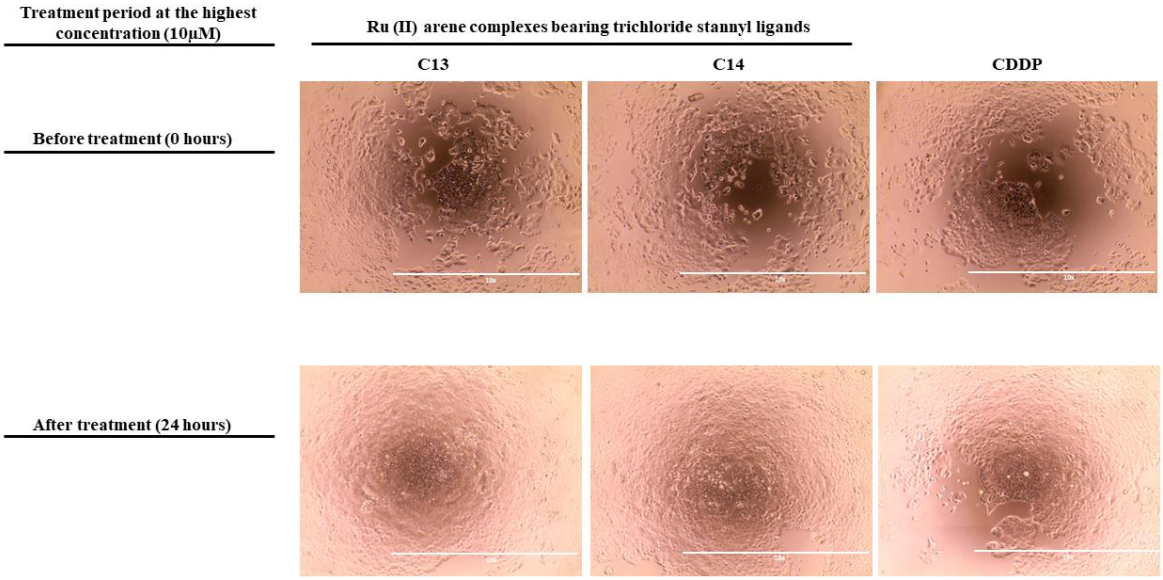

Figure 2.7 Cell density images before and after 24-hour treatment with ruthenium(II) arene bearing trichloride stannyl ligands (10 µM).

The photographed images indicate MCF-7 cells surviving treatment and are proliferating, thus implying that the cellular mechanisms required for the normal functioning and carrying out of metabolic activities were unaffected or had undergone damage repairs under such tested conditions. Interestingly, at 10 µM, both complexes and CDDP were less effective than at 8 µM (as observed in Figure 6.11). The IC_{50} value determined for CDDP was 8.02 µM which is comparable to the relative IC_{50} value reported in the literature (IC_{50} = 8.60 µM) for MCF-7 cells.[14,15] Compared to **C13** which has a predicted IC_{50} of 31.3 µM, **C14** was more cytotoxic against the MCF-7 cell line with a predicted IC_{50} value of 16.7 µM. These results were not entirely unexpected, because the presence of a triphenyl phosphite was expected to enhance the cytotoxic properties of **C14**, as was observed for **C11** at 10 µM. The insertion of tin dichloride ($SnCl_2$) on ruthenium organometallic arene complexes **C13** and **C14**, is efficacious in improving the solubility and thus increasing the likelihood of impacting the cytotoxicity of complexes against MCF-7 cells. However, these complexes exhibited moderate cytotoxic properties at the tested concentrations. Thus, suggesting that the insertion of the tin congener causes less impact on the growth rate or survival of MCF-7 cells or that the cytotoxic properties are likely to induce short-term cytotoxicity against MCF-7 cells. Earlier reports[7] highlight that complexes of the type $[RuCl(\eta^6\text{-}C_6H_6)(PR_3)(SnCl_3)]$ exhibited considerable cytotoxicity when tested against human ovarian A2780 and the A2780cisR variant (with acquired CDDP resistance) cancer cells, though cells were exposed to drug compounds for 72-hours. However, the partial solubility properties of these types of complexes rendered them ineffective in

biological solvents used to prepare the drug complexes. The tin congener complexes, **C13** and **C14** were also expected to contribute to the insolubility of compounds when dissolved in aqueous solvents used for biological testing. However, the attachment of the hydrophilic tail on the arene moiety was advantageous in enhancing the solubility properties of these complexes, as presented in this work.

2.3 SUMMARY

The novel half-sandwich organometallic Ru(II) arene complexes bearing trichlorostannyl ligands, [RuCl(η^6-$C_6H_5OCH_2CH_2OH$)(PPh_3)($SnCl_3$)] (**C13**) and [RuCl(η^6-$C_6H_5OCH_2CH_2OH$){$P(OPh)_3$}($SnCl_3$)] (**C14**), were successfully synthesized and investigated for their cytotoxic properties against the estrogen receptor-positive MCF-7 adenocarcinoma cell line. The synthesized complexes were fully characterized using various spectroscopic and analytical techniques. **C14** complex has an octahedra geometry which displays typical features of a piano-stool organometallic Ru(II) arene complex, as indicated by single X-ray crystallography. The cytotoxic properties of complexes **C10** - **C15** were investigated against the MCF-7 cell line for 24 hours of drug exposure using the MTT cell viability assay. The screening tests performed reveal that complexes **C10** and **C11** possess greater cytotoxic properties against the MCF-7 cell line significantly compared to the Ru(II) arene complexes bearing trichlorostannyl ligands, **C13** and **C14**. On a structure-activity relationship basis, the bioavailability of complexes was promoted by the attachment of the aliphatic tail - OCH_2CH_2OH to the arene moiety, thus increasing their hydrophilic nature. This was gauged by conducting preliminary water solubility tests which highlighted that complexes **C13**, and **C15** were found to be water-soluble, while **C14** was partially soluble. From the cell viability screening tests performed, complexes **C11**, **C12**, **C14** and **C15** showed moderate to good cytotoxic properties against the MCF-7 cancer cells after 24 hours of drug exposure at the tested concentrations. Compared to **C13**, **C14** show greater cytotoxic properties when treated with a range of complex concentration (2 - 10 µM), as indicated by the predicted IC_{50} value (16.7 µM) determined using the GraphPad Prism v7.0. It would be beneficial to incubate these complexes for longer incubation periods to assess their short-term cytotoxic properties. An investigation directed towards the solubility of these complexes in a synthetic buffer such as the human serum albumin (HSA), the most abundant protein in the circulatory human body, may provide insights about the solubility, stability, and ability to bind to biological molecules for transportation to the targeted sites. These experimental studies may reveal information about the mechanistic insights of these types of organometallic ruthenium(II) arene complexes, concerning their pharmacodynamic and pharmacokinetic properties.

2.4 EXPERIMENTAL

2.4.1 Chemicals and Reagents

All chemical reactions were carried under nitrogen atmospheric pressure, with all the complexes isolated being fully characterized as the complexes were moisture and air-stable. All chemical reagents were obtained and purchased from Sigma-Aldrich and were used without any further purification process. Complex **C15** was synthesized usig published literature procedures.[12,13]

2.4.2 General methods and physical instrumentation

All the spectroscopic data were obtained and performed at the University of Maastricht, Brightlands Chemelot Campus, Netherlands. Nuclear Magnetic Resonance (NMR) spectroscopic data were recorded on a Bruker Ultrashield 300. For ^{119}Sn NMR (111.8MHz), a Varian Unity INOVA 300 spectrometer, using a Bruker Bio-spin GmbH casing and sample injector. Chemical shifts are reported δ (ppm) relative to their solvent residual signals (7.26 ppm for $CDCl_3$ and 2.50 ppm for DMSO-d_6). H_3PO_3 was used as an internal standard for ^{31}P NMR. Coupling constants are reported in Hz. Attenuated total reflectance (ATR) infrared spectra of all compounds reported in this work were recorded on a Shimadzu MIRacle spectrophotometer. The infrared (IR) peaks are reported according to their relative intensities: s: strong; w: weak; m: medium; vs: very strong; vw: very weak. Electronic absorption spectra were recorded on a Shimadzu UV 3600. Thermal gravimetric analysis (TGA) curves were recorded on a TGA Q-500.

2.4.3 X-ray crystallography

Single crystal X-ray diffraction data collection was performed with a BRUKER-AXS SMART APEX CCD diffractometer using graphite-monochromated Mo Kα radiation (0.71073 Å). The data were reduced to F^2_0 and corrected for absorption effects with SAINT and SANDBAS[16] software applications. All non-hydrogen atoms were refined with anisotropic displacement parameters. Hydrogen atoms were placed in calculated positions to correspond to standard bond lengths and angles. All diagrams were drawn with 30% probability thermal ellipsoids and all hydrogen atoms were omitted for clarity. The crystal structure of the complex was solved by direct methods refined by full-matrix least-squares method, SHELXL97[17] and SHELX2013[18], respectively. The refinement data of the crystal structure is given in Table 2.4.

Table 2.4 Crystal data and structure refinement for complex **C14**.

Empirical formula	C_{26} H_{25} Cl_4O_5PRuSn
Formula weight	809.99
Temperature/K	100(2)
Crystal system	Orthorhombic
Space group	Pca2(1)
Unit cell dimensions	a = 14.599(3) Å α = 90°
	b = 10.723(2) Å β = 90°
	c = 18.291(4) Å γ = 90°
Volume/A^3	2863.5(10)
Z, Calculated density	4, 1.879 Mg/m^3
θ range for data collection	1.90 to 25.00°
Reflections collected / unique	19443 / 5042 [R(int) = 0.0701]
Goodness-of-fit on F^2	1.271
Final R indices	
[I > 2σ (I)]	R1 = 0.0988, wR2 = 0.1894
Final R indices (all data)	R1 = 0.1057, wR2 = 0.1926

2.4.4 Preparation of the novel organometallic ruthenium(II) arene, **C13** and **C14**.

*Synthesis of [RuCl(η^6-$C_6H_5OCH_2CH_2OH$)(PPh_3)($SnCl_3$)] (**C13**)*

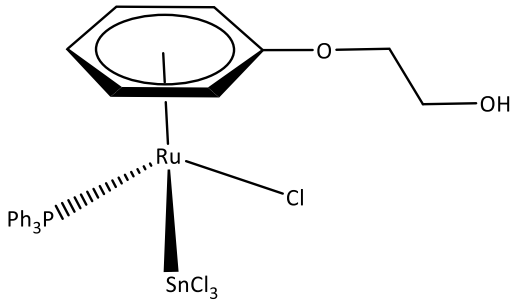

C13. Anhydrous tin dichloride (0.109 g, 0.576 mmol) was added to a dissolved solution of compound **C10** (0.300 g, 0.524 mmol) in DCM (35 mL). The mixture was refluxed for 4.5 hours under nitrogen. After cooling to room temperature, the solution was filtered *via* suction followed by the removal of the solvent on a rotary evaporator, affording a dark red solid. **Yield**: 80.0% (0.32 g, 0.42 mmol). **Melting point**: 205 °C. **^{1}H NMR (300.1 MHz, DMSO-d_6)**: (δ, ppm) 7.66 - 7.41 (m, 15H, P*Ph*$_3$), 6.40 (t, $^3J_{H,H}$ = 5.9,1H, C_6H_5), 6.09 (d, $^3J_{H-H}$ = 5.9, 1H,

C_6H_5), 5.94 (d, $^3J_{H\text{-}H}$ = 6.3, 1H, C_6H_5), 5.59 - 5.54 (ps. q, 1H, C_6H_5), 5.02 (broad s, 1H , OH), 4.24 - 4.17 (m, 1H, C_6H_5), 4.12 - 4.05 (m, 2H, CH_2O), 3.71 (broad s, 2H, CH_2OH). **^{31}P {^{1}H} NMR (121.5 MHz, DMSO-*d*$_6$,)** (δ, ppm) 33.2 (s). **TGA: (Weight % decrease)** 80 °C - 128.17 °C (3.847 %), 128.17 °C - 237.71 (6.69 %), 237.71 °C - 283.11°C (6.52 %), 283.11 °C - 321.01 °C (11.13 %), 321.01 °C - 342.26 °C (14.22 %), 342.26 °C - 375.16 °C (7.55 %), 375.16 °C - 493.45 °C (5.70 %). **$S_{20\,°C}$ (H_2O)** soluble, 0.03 mg/mL.

*Synthesis of [RuCl(η^6-$C_6H_5OCH_2CH_2OH$){$P(OPh_3)$}($SnCl_3$)] (**C14**)*

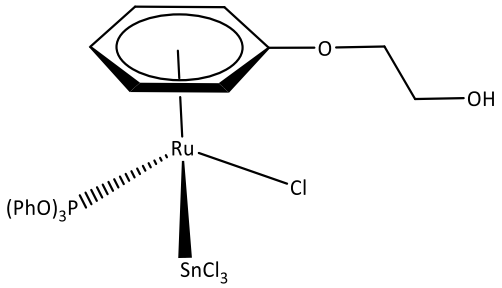

C14. Anhydrous tin dichloride (0.100 g, 0.532 mmol) was added to a dissolved solution of compound **C11** (0.300 g, 0.484 mmol) in DCM (35 mL). The mixture was refluxed for 4 ½ h under N_2 atmosphere. After cooling to room temperature, the orange solution that had formed was filtered *via* suction followed by the removal of the solvent on a rotary evaporator, affording a viscous red oil. The crude product was left to crystallize from a mixture of diethyl ether and DCM at 25 °C, affording bright red crystals. **Yield**: 54.0% (0.26 mmol, 0.21 g). **Melting point**: 169 °C. **^{1}H - NMR (300.1 MHz, $CDCl_3$)**: (δ, ppm) 7.38 -7.25 (m, 15 H, P(O*Ph*)$_3$), 6.33 (t, $^xJ_{H,H}$ = 5.4 Hz, 1H, C_6H_5), 5.76 - 5.74 (m, 1H, C_6H_5), 5.60 -5.55 (1H, m, C_6H_5), 4.52 (dd, $^3J_{H\text{-}H}$ = 2.03, $^3J_{H\text{-}H}$ = 3.35, 1H, O*H*), 4.16 - 4.10 (m, 1H, C_6H_5), 4.04 - 3.99 (m, 1H, C_6H_5), 3.93 - 3.86 (m, 2H, OCH_2), 3.71 (ps t, $^3J_{H\text{-}H}$ = 6.0, 1H, CH_2OH), 2.45 (t, 1H, CH_2OH). **^{31}P{^{1}H} NMR (121.5 MHz, $CDCl_3$):** (δ, ppm) 123.7 (s). **TGA (Weight % decrease)** 150 - 177.74 °C (3.27 %), 177.74 °C - 225.24 (8.59 %), 225.24 °C - 339.11 °C (18.40 %), 399.11 °C - 404.81 °C (12.89 %), 404.81 °C - 485.32 °C (14.81 %). **$S_{20\,°C}$ (H_2O)** insoluble.

2.4.5 Cell culture

Roswell Park Memorial Institute-1640 (RPMI-1640) medium (RPMI, Gibco®, Life Technologies, New York) was used to maintain estrogen receptor-positive (ER +) human breast MCF-7 adenocarcinoma cell line. Culture media was supplemented with heat-inactivated foetal bovine serum (FBS, 10%) and penicillin (100 U/mL) and streptomycin (100 µg/mL). Cells were adherent in monolayers and maintained in T75 cm flasks or 10 cm dishes. The dishes were handled under sterile conditions to prevent any bacterial contamination or infections and maintained in a 95% air-humidified incubator at 37°C and 5% CO_2. When confluent, cell adhesion was weakened with trypsin-EDTA (Gibco®), and the resultant cells were sub-cultivated at a ratio of 1:9. Media was replaced every 2 - 3 days.

2.4.5.1 Light microscopy

Culture plates subjected to treatment with **C13** and **C14** were monitored, and images of the wells were captured before and after 24 hours of treatment using the EVOS^{TM} M5 000 microscope (ThermoFisher Scientific, Massachusetts, USA). Cells were visualized at 40X magnification.

2.4.5.2 Mycoplasma Infection Test

Cells were seeded on sterilized coverslips in culture plates (35 mm) and incubated overnight in an antibiotic-free medium. After an incubation period, cells were fixed with a fixative solution (1 mL) in a 1:3 glacial acetic acid: methanol mixture for 10 seconds. After 10 seconds, cells were rinsed with distilled water 3 times and the coverslips were air-dried at room temperature for a few minutes. Once dried, DNA was stained with Hoechst (1 mL, 0.5 µg/mL, Sigma St Louis, MO, USA) for 30 seconds. The excess stain was washed off with distilled water and the coverslips were mounted on a slide with mounting fluid (Chapter 6). Cells were viewed under fluorescence microscopy (EVOS^{TM} M5000, ThermoFisher Scientific, Massachusetts, USA) using the DAPI filter and viewed at 40X magnification. Mycoplasma-free cells stained positive with Hoechst only in the nucleus, while cells infected with mycoplasma showed staining in both the nucleus and the cytoplasm.

2.4.6 Drug Preparation for cell culture treatment

Organometallic ruthenium(II) arene complexes were synthesized accordingly as reported in published material.[10] Complexes were dissolved in DMSO (Sigma Aldrich, Missouri, USA) to give a drug stock solution (10 mM) and further diluted in cell culture RPMI medium to achieve

the desired final concentrations. For the screen tests, cells were treated with complexes (5.0 and 10 µM), CDDP (5.0 and 10 µM) as a positive control, and the vehicle DMSO (10 µM) control. For multidose response treatment, complexes **C13** and **C14** were treated at 2 µM, 4 µM, 6 µM, 8 µM and 10 µM concentrations. The vehicle DMSO was prepared at 0.1% and CDDP was prepared simultaneously at the same concentrations of the Ru(II) organometallic complexes. Complex solutions were prepared on the same day of treatment.

2.4.7 *In vitro* cell viability assay screen test using MTT (3(4,5-dimethylthioazol-2-yl)-2,5-diphenyl tetrazolium)

Cell viability assays were performed on MCF-7 cells using the 3-(4,5-dimethylthiazol-2-yl)-2,5-diphenyl tetrazolium (MTT) cell proliferation kit (M218, Sigma Aldrich, Missouri, USA).[19] The assay kit was performed as advised by the manufacturer's instructions.[20] The principle of the assay is based on the ability of viable cells to metabolize the yellow tetrazolium salt (MTT) to purple formazan crystals by the mitochondrial succinate dehydrogenase (represented in Scheme 2.2).[20]

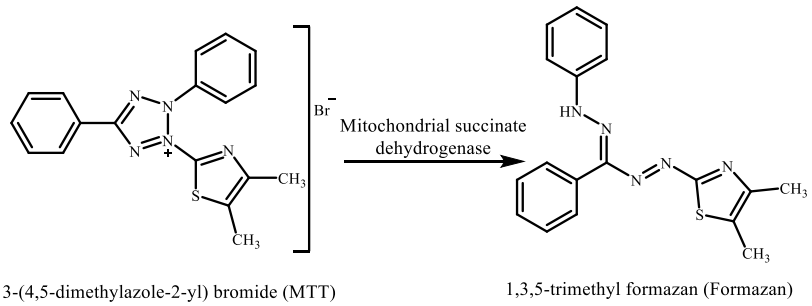

3-(4,5-dimethylazole-2-yl) bromide (MTT) 1,3,5-trimethyl formazan (Formazan)

Scheme 2.2 The conversion of MTT (Yellow) to formazan (purple).

The solubilizing reagent was prepared according to a protocol provided by the Sharon Prince Lab (Chapter 6). MCF-7 cells were seeded at 4 500 cells/well in 96 well plates. Plates were incubated for 48 hours to reach 50 - 60% cell confluency. After 24 - hours of treatment with drug complexes or vehicle and positive control, the MTT labelling reagent (10 µL) was added to each well. This promotes the formation and accumulation of the purple formazan crystals intracellularly. After 4 - hours of incubation at 37°C, solubilizer solution (100 µL) was added to dissolve the formazan crystals and incubated overnight. Plates were read using an RT-2100C (China) microplate spectrophotometer. The spectrophotometric absorbance of samples was determined at 585 nm wavelength. Wells of the 96-well plate containing medium and complex, or vehicle were utilized as blanks to account for any inherent absorbance. Three independent

biological experiments were performed with each drug tested in quadruplicate per concentration. The cytotoxic effects of drugs were quantified with cell viability expressed as a percentage of the mean vehicle control ± standard error of the means. Percentage cell viability was calculated as follows:

$$\% \text{ Cell viability} = \left(\frac{\text{absorbance value of the tested sample utilised in treatment}}{\text{absorbance value of the uncontrol treated cell}} \right) \times 100$$

2.4.8 Determination of half maximal inhibitory concentration (IC_{50})

Half maximal inhibitory concentrations (IC_{50}) were determined using data from cell viability assays after 24 hours of complex or vehicle treatment. Values were predicted based on non-linear regression analysis of the dose-response curves data (reported using GraphPad Prism version 7.0, California, USA).

2.4.9 Statistical analysis

Statistical analysis was conducted with the acquisition of the data represented as mean values and SEM (standard error of the means) of three independent experiments. The *t-test* (a student's statistical hypothesis test) was used to compare the two experimental frames and a value of *$p<0.05$, **$P<0.001$ and ***$p<0.0001$ were accepted as statistically significant.

2.5 REFERENCES

1 S. Thota, D. A. Rodrigues, D. C. Crans and E. J. Barreiro, *J. Med. Chem.*, 2018, **61**, 5805–5821.

2 L. J. Anghileri, *Zeitschrift Krebsforsch*, 1975, **83**, 213–217.

3 C. G. Hartinger, S. Zorbas-Seifried, M. A. Jakupec, B. Kynast, H. Zorbas and B. K. Keppler, *J. Inorg. Biochem.*, 2006, **100**, 891–904.

4 P. J. Dyson, *Chimia (Aarau).*, 2007, **61**, 698–703.

5 C. S. Allardyce, P. J. Dyson, D. J. Ellis and S. L. Heath, *Chem. Commun.*, 2001, **2**, 1396–1397.

6 S. K. Singh and D. S. Pandey, *RSC Adv.*, 2014, **4**, 1819–1840.

7 O. Renier, C. Deacon-Price, J. Peters, K. Nurekeyeva, C. Russon, S. Dyson, S. Ngubane, J. Baumgartner, P. Dyson, T. Riedel, H. Chiririwa and B. Blom, *Inorganics*, 2017, **5**, 1–13.

8 B. Therrien, T. T. Thai, J. Freudenreich, G. Süss-Fink, S. S. Shapovalov, A. A. Pasynskii and L. Plasseraud, *J. Organomet. Chem.*, 2010, **695**, 409–414.

9 S. H. L. Thoonen, M. Lutz, A. L. Spek, B.-J. Deelman and G. van Koten, *Organometallics*, 2003, **22**, 1156–1159.

10 C. Berg, S. Chari, K. Jurgaityte, A. Laurora, M. Naldony, F. Pope, D. Romano, T. Medupe, S. Prince, S. Ngubane, J. Baumgartner and B. Blom, *J. Organomet. Chem.*, 2019, **891**, 12–19.

11 B. Lastra-Barreira, J. Díez and P. Crochet, *Green Chem.*, 2009, **11**, 1681.

12 L. C. Matsinha, P. Malatji, A. T. Hutton, G. A. Venter, S. F. Mapolie and G. S. Smith, *Eur. J. Inorg. Chem.*, 2013, **2013**, 4318–4328.

13 C. Deacon-Price, D. Romano, T. Riedel, P. J. Dyson and B. Blom, *Inorganica Chim. Acta*, 2019, **484**, 513–520.

14 J. O. Suberu, I. Romero-Canelón, N. Sullivan, A. A. Lapkin and G. C. Barker, *ChemMedChem*, 2014, **9**, 2791–2797.

15 İ. Işıkdağ, Y. Özkay, Z. İncesu and G. Akalın, *Zeitschrift für Naturforsch. C*, 2011, **66**, 465–470.

16 R. H. Blessing, *Acta Crystallogr. Sect. A Found. Crystallogr.*, 1995, **51**, 33–38.

17 G. M. Sheldrick, *Acta Crystallogr. Sect. C Struct. Chem.*, 2015, **71**, 3–8.

18 G. M. Sheldrick, *Acta Crystallogr. Sect. A Found. Crystallogr.*, 2008, **64**, 112–122.

19 T. L. Riss, R. A. Moravec, A. L. Niles, S. Duellman, H. A. Benink, T. J. Worzella and L. Minor, *Cell Viability Assays*, 2004.

20 Roche Diagnostics GmbH, *Protocol*, 2016, 6–9.

CHAPTER 3

Synthesis and characterization of R-substituted anilinopyridinate (R-ap) ligands and mixed ligand mono-substituted anilinopyridinate triacetatechlorodiruthenium(II, III) complexes

3.1 INTRODUCTION

The mixed valent diruthenium(II, III) lantern-type/paddlewheel structured complexes equatorially bridged by four monoanionic, three atom donor and axial ligands, are among the most commonly studied compounds in the family of Ru_2^{5+} complexes. Since the discovery of the lantern-type tetraacetatechlorodiruthenium(II, III) complex ($[Ru_2(O_2CCH_3)_4Cl]$)[1], further investigations included the generation of a class of Ru_2^{5+} complexes which were extensively characterized using theoretical methods, structural, magnetic, and electrochemical properties to better understand their metal-metal bond and reactivity.[2,3,4] Ru_2^{5+} complexes can be equatorially bridged by oxygen-oxygen, nitrogen-oxygen, and nitrogen-nitrogen donor atoms (Figure 3.1). As an added advantage, complexes offer the versatility of incorporating electron-donating and withdrawing substituents to alter the electronic environment of complexes through axial and equatorial coordination. Thus, leading to the generation of a myriad of Ru_2^{5+} complexes.

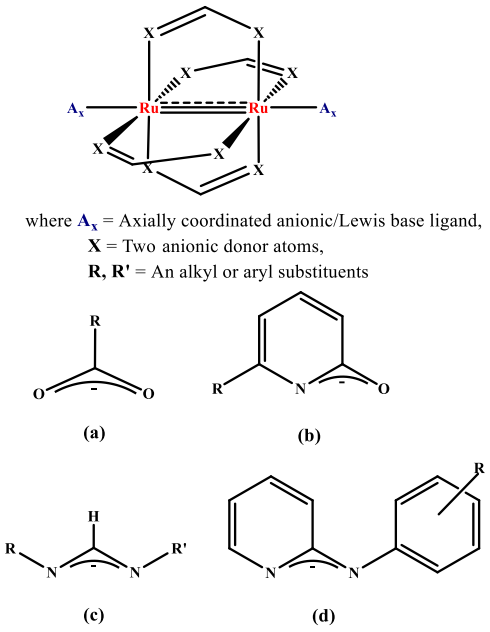

Figure 3.1 Ru_2^{5+} paddlewheel structure with examples of *O,O′* (a), *N,O* (b), and *N,N′* (c and d) equatorial bridging ligands.[4]

Ru_2^{5+} complexes are the most common and structurally stable complexes studied[5], with the oxidation state of the complexes being stabilized by the half-filled two highest-lying occupied molecular orbitals (HOMO), with 3 unpaired electrons occupying the near degenerate π* and δ* antibonding orbitals to give an electronic configuration $\sigma^2\pi^4\delta^2(\pi^*\delta^*)$.[3,6] Owing to their rich

redox chemistry, it is for this reason that complexes have attracted much attention in academic research.

The first paddlewheel $[Ru_2(O_2CCH_3)_4Cl]$ complex synthesized and structurally characterized by Stephenson and Wilkinson,[1] is often used as a precursor in the synthesis of mixed ligand diruthenium(II, III) complexes containing a mixture of *N,N′*-donor and labile acetate equatorial bridging ligands. The habitual synthetic procedures often involve the refluxing of stoichiometric amounts of the $[Ru(O_2CCH_3)_4Cl]$ with the respective *N,N′*-donor ligand in polar solvents (methanol or THF).[7,8] Examples include complexes with the general formula $[Ru_2(O_2CCH_3)_x(L)_{4-x}Cl]$, where x = 2, 1, or 0 and L = anilinopyridinate (ap) or diphenylformamidinate (dpf) donor ligands (Scheme 3.1).

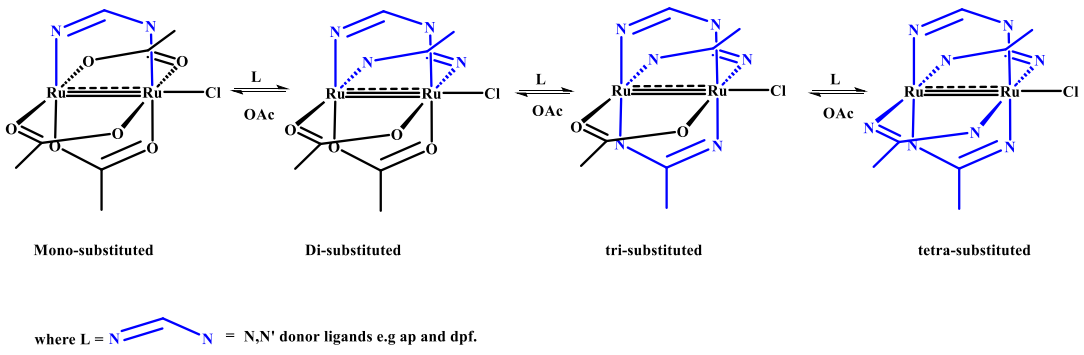

Scheme 3.1 Metathesis displacement and replacement of acetate ligands with the *N,N′*-donor ligands.

There exist few published materials reporting on the synthesis, structural and spectroscopic studies of paddlewheel diruthenium(II, III) complexes containing a single *N,N′*-donor and three equatorial bridged acetate ligands.[9] However, the synthetic procedures often used in the preparation of these complexes tend to favour complexes with more than one equatorially substituted *N,N′*-donor bridging ligands, with further challenges associated with the isolation and purification of the mono-substituted complexes in greater yields.

A reaction carried out using two formamidines, HDXyl^{2,6}F = N,N′-di(2,6-xylyl)formamidine or HDAnif = *N,N′*-di-*p*-anisylformamidine, under reflux with $[Ru_2(O_2CCH_3)_4Cl]$ precursor in THF, led to the formation of various derivatives of the Ru_2^{5+} complexes with the general chemical formula $[Ru_2(O_2CCH_3)_{4-n}(DArF)_nCl]$ where DarF anion = N,N′-diarylformamidine.[10] It is noteworthy to highlight that the degree of selectivity for greater substituted *N,N′*-donor

ligated complexes is driven by the choice of reaction conditions used such as the type of solvent, temperature and the nature of the *N,N′*-donor bridging ligand.

In the preparation of $[Ru_2(O_2CCH_3)x(L)_{4-x}Cl]$ complexes, where L is a 2-anilinopyridinate (ap) or aminopyridinate (amp) anionic bridging ligands and x = 0 - 3, different synthetic procedures have been explored resulting in a greater degree of substitution of the respective bridging ligands.[11,12] For instance, at room temperature, the reaction with $[Ru_2(O_2CCH_3)_4Cl]$ and 2-amino- 4,6-dimethylpyridine [H(admp)] bridging ligand in methanol under inert conditions led to the formation of greater substituted complexes.[11] Under refluxing conditions, a one-pot synthesis involving the reaction of $[Ru_2(O_2CCH_3)_4Cl]$ precursor with [H(2-Fap)] ligand in excess methanol led to the formation of a library of compounds with the general chemical formula, $[Ru_2(O_2CCH_3)_x(2\text{-Fap})_{4-x}Cl]$, where x = 0 - 3.[12]

Due to the shortage of refined synthetic methods to yield the desired mono-substituted $[Ru_2(O_2CCH_3)_3(R\text{-ap})Cl]$ complexes, the modified synthetic procedure is herein established and highlighted in this work. The spectroscopic, structural, and electrochemical characterization of mono-substituted ap triacetatochlorodiruthenium(II, III) complexes with the general chemical formula $[Ru_2(O_2CCH_3)_3(R\text{-ap})Cl]$ (Figure 3.2).

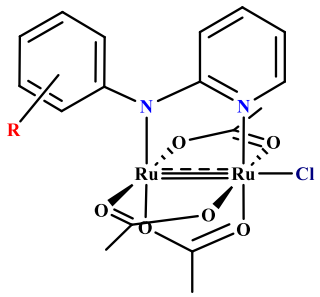

where **R** = H (**C1**), 2-CH_3 (**C2**), 4-CH_3 (**C3**), 2,4-$(CH_3)_2$ (**C4**), 2,6-$(CH_3)_2$ (**C5**), 2,4,6-$(CH_3)_3$ (**C6**), 2-F(**C7**), and 4-F (**C8**)

Figure 3.2 Generic structure of $[Ru_2(O_2CCH_3)_3(R\text{-ap})Cl]$ complexes.

Furthermore, complexes were synthesized to enhance the solubility and stability of the lantern-type diruthenium complexes in aqueous solvents for the evaluation against human breast MCF-7 and MDA-MB-231 cancer cells. Owing to their rich redox chemistry, these Ru_2^{5+}complexes are of great interest due to the proposed correlation between the anticancer properties and the ability of cellular redox processes to reduce and/or oxidize the ruthenium metal centres which in turn is highly dependent on the coordination sphere of the ruthenium complex.[13,14] The

proposed reduction of the metal centres to ruthenium(III) or ruthenium(II) active species may lead to interactions with potential biological molecular targets, and possible production of ROS which interferes with the redox chemical balance of a cell, either *via* direct or indirect chemical processes or mechanisms.[14]

To confirm their structural identity, the obtained spectroscopic data are compared relative to those reported in the literature.[9] The spectral data of the complexes $[Ru_2(O_2CCH_3)_3(Hap)Cl]$ (**C1**), $[Ru_2(O_2CCH_3)_3(4\text{-}CH_3ap)Cl]$ (**C3**), and $[Ru_2(O_2CCH_3)_3(4\text{-}CH_3ap)Cl]$ (**C8**) are herein discussed as the show promise as potential anticancer agents (Chapter 4), while those of the remaining complexes were referred to- and documented in Chapter 6. Indeed, there exists literature published material reporting on the synthesis of mono-substituted *N,N′*-anilinopyridinate triacetatechlorodiruthenium(II, III) complexes.[9] Thus, complexes were synthesized for the sole purpose of evaluating their anticancer properties against oestrogen receptor-positive (ER +ve) MCF-7 and triple-negative aggressive and invasive MDA-MB-231 human breast cancer cell lines.

3.2 RESULTS AND DISCUSSION

3.2.1 Preparation of anilinopyridinate (R-ap) ligands

All nitrogen-nitrogen anilinopyridinate (R-ap) ligands (**L1 - L8**) were synthesized according to reported methods,[15,16,17] with fluorine and methyl substituents localized on the *ortho*- or *para*-positions of the aniline ring. It is important to note that the synthesis and characterization of the substituted anilinopyridinate (R-ap) ligands (**L1**, **L2** and **L7**) incorporated in this chapter is an extension of the work performed by Ms Karabo Mashiloane,[18] a former MSc student (Univerisity of the Witwatersrand, https://hdl.handle.net/10539/24928) from the SN research lab. All synthetic experimental work was obtained from published literature and referenced accordingly with fewer modifications as discussed.

The synthesis of the R-ap ligands involved stirring 2-bromopyridine (1 equiv.) with the respective aniline (2 equiv.) The starting materials were heated overnight at temperatures above 100°C to yield the desired products (Scheme 3.2), with the reaction proposed to follow a general nucleophilic aromatic substitution (SN_{Ar}) reaction to yield the desired products (**L1 - L8**).

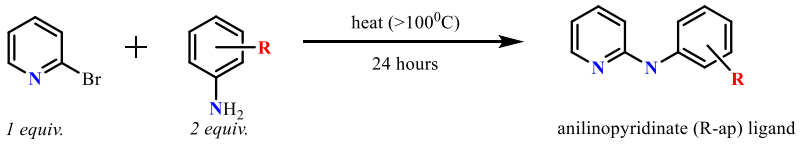

R = H (**L1**), 2-CH_3 (**L2**), 4-CH_3 (**L3**), 2,4-$(CH_3)_2$ (**L4**), 2,6-$(CH_3)_2$ (**L5**), 2,4,6-$(CH_3)_3$ (**L6**), 2-F (**L7**), 4-F (**L8**)

Scheme 3.2 Synthesis of the anilinopyridinate (R-ap) ligands (**L1 - L8**).

The reaction was monitored by thin layer chromatography (TLC), with the analysis confirming the near complete formation of the more non-polar desired product. The prepared R-ap ligands were purified by recrystallizing the dark brown crude products several times with hot hexane. The compounds were obtained as pure cream to white crystalline solid materials in moderate to excellent yields. To confirm the purity and structural identity of the synthesized R-ap ligands, all ligands were characterized *via* various spectroscopic and analytical techniques including infrared, ^{1}H-NMR, ^{13}C-NMR and LCMS. All the obtained spectroscopic data is documented in Chapter 6 (Figures 6.13 - 6.52) and agrees with the data published in the literature.[15,16,17]

3.2.2 Preparation of the precursor complex, $[Ru_2(O_2CCH_3)_4Cl]$.

The synthesis of the precursor complex, tetraacetatechlorodiruthenium(II, III) was achieved by following published literature procedures.[1,19,20] In short, the reaction involved stirring refluxing of ruthenium trichloride ($RuCl_3 \cdot 3H_2O$) and anhydrous LiCl in a mixture of glacial acetic acid and acetic anhydride (Scheme 3.3). The resulting product was filtered, washed with a minimal amount of diethyl ether to remove the unreacted ruthenium trichloride starting material, and obtained as a brown solid material.

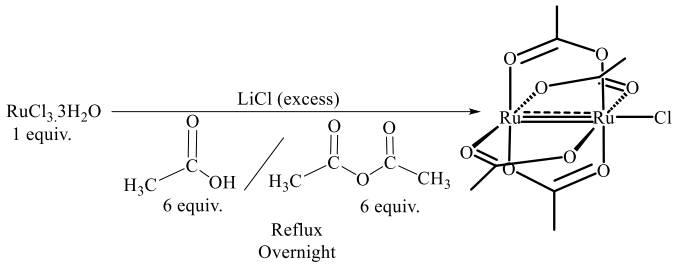

Scheme 3.3 Schematic representation of the preparation of the precursor complex, $[Ru_2(O_2CCH_3)_4Cl]$.[1,19,20]

The formation of the paddlewheel $[Ru_2(O_2CCH_3)_4Cl]$ structure occurs *via* the coordination of the acetate oxygen atoms to the ruthenium(III) metal centre *via* carboxyl oxygens. The $[Ru_2(O_2CCH_3)_4Cl]$ precursor was isolated as a brown precipitate and obtained moderate yields (69%). Of particular interest, the yields obtained are moderate. This is possibly attributed to the presence of water molecules from the acquired hydrated ruthenium trichloride ($RuCl_3.3H_2O$), and the absence of oxygen (O_2) gas required to favour the forward reaction since the preparation of $[Ru_2(O_2CCH_3)_4Cl]$ is often carried out under oxygen.[19,1,20] The prepared $[Ru_2(O_2CCH_3)_4Cl]$ precursor was characterized *via* UV-vis, Fourier Transform Infrared (FT-IR) spectroscopy, Elemental Analysis (CHNS), and High-Resolution Mass spectrometry. The obtained spectroscopic data is documented in Chapter 6 (Figures 6.52 - 6.55) and agrees with the data published in the literature.

3.2.3 Preparation of $[Ru_2(O_2CCH_3)_3(R\text{-}ap)Cl]$ (**C1 - C8**) complexes.

The synthetic methods employed to obtain the titled complexes (**C1 - C8)** were similar to those described in published materials,[9] with a few modifications. In particular, the synthetic chemistry and characterization of complexes **C1**, **C2**, **C5** and **C7** are extensively documented and discussed in this report.[9] In addition, It is worth noting that the synthesis and chemistry of

the substituted paddlewheel $[Ru_2(O_2CCH_3)_3(R\text{-ap})Cl]$ structured complexes, particularly **C1**, **C2** and **C7** incorporated in this chapter is an extension of the work performed by Ms Karabo Mashiloane,[18] a former MSc student (Univerisity of the Witwatersrand, https://hdl.handle.net/10539/24928) from the SN research lab.

Two synthetic procedures were explored to improve the yields obtained of the desired mono-substituted complexes. Both methods undergo a metathesis displacement of a single moiety of an acetate group followed by the replacement with an equivalence of the nitrogen-nitrogen R-ap bridging ligand. The first method is a generic synthetic literature procedure[15,12,19] and follows the stoichiometric reaction of the starting materials placed in a round bottom flask and dissolved in anhydrous methanol. The resulting mixture was stirred and refluxed at 60°C under N_2 for 4 hours (Scheme 3.4), and the reaction was carefully followed on TLC silica plates with ethyl acetate/hexane solvent mixture (v/v 7:3). The solution mixture changed colour from light brown to a dark blue colour after the first 2 hours and further allowed time to react for the next 2 hours.

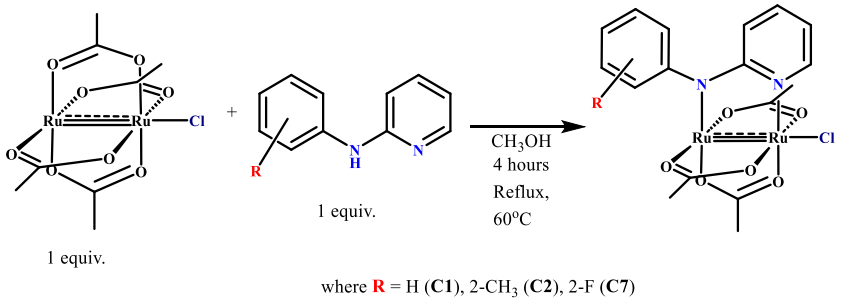

Scheme 3.4 Synthesis of the mixed ligand $[Ru_2(O_2CCH_3)_3(R\text{-ap})Cl]$ (**C1**, **C2**, **C7**) complexes.

The residue was spotted on TLC silica plates and four bands were observed. One light brown band on the baseline ($[Ru_2(O_2CCH_3)_4Cl]$ complex), one dark blue/purple spot (Rf value = 0.14), one emerald-green spot (Rf value = 0.53), and one band (Rf value = 0.81) observed closer to the mobile phase of the TLC plate and only visible under the UV lamp. This synthetic procedure was used to prepare 3 complexes (**C1**, **C2** and **C7**) with varying electron-withdrawing or donating substituents to investigate the influence of these substituents on the yields obtained. The yields obtained were relatively low (**C1** > **C2** < **C7**). This may be attributed to the favoured mesomeric effects induced by the nature of the substituents located on the *para*-positions of the aniline ring. Furthermore, altering the reaction conditions of this

type of metathesis displacement reaction strongly influences the formation of the desired products. W. Ryan Osterloh et al[9] mentioned that an implementation such as a change in solvent from methanol to methanol/THF (1:1) solvent mixture had improved the yields obtained for the desired products, $[Ru_2(O_2CCH_3)_3(R\text{-}ap)Cl]$, where R-ap = $[(2,6\text{-}CH_3)_2ap]$ or $[(2,4,6\text{-}CH_3)_3ap]$ and ultimately inhibiting the formation of side reactions and thus the possibility of yielding other unwanted side products. Such findings fuelled our investigations to further troubleshoot the synthetic procedure to improve the yields initially obtained for complexes **C1**, **C2** and **C7**. The synthetic procedure previously described was implemented and modified by deprotonating the R-ap ligands using a weak base (triethylamine, added *in excess*). Furthermore, LiCl salt was added to the reaction mixture to ensure axial coordination of the chloride ligand on the Ru_2(II, III) metal cores, as represented in Scheme 3.5.

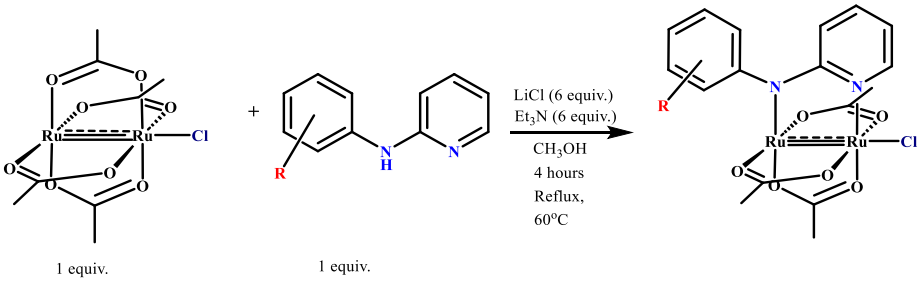

Scheme 3.5 Synthesis of the mixed ligand $[Ru_2(O_2CCH_3)_3(R\text{-}ap)Cl]$ (**C1 - C8**) complexes; application of the deprotonation method.

This method was adopted from published synthetic procedures, reporting on the synthesis of mixed ligand complexes of the type $[Ru_2(O_2CCH_3)_3(L)Cl]$, where L = two formamidine ligands of the type HDXyl[2,6]F = N,N´-di(2,6-xylyl)formamidine and HDAniF = N,N´-di(*p*-anisyl)formamidine.[10] TLC analysis showed an intense blue spot observed closer to the stationary phase owing to the more polar properties of the desired product, with the unreacted materials observed on the baseline of the TLC silica plate ($[Ru_2(O_2CCH_3)_4Cl]$ precursor complex) and closer to the solvent front line of the silica plate (non-polar R-ap ligands). Although the unreacted materials were present in the reaction mixture as proven by TLC analysis, the yields obtained were significantly greater in comparison to the yields obtained when the first synthetic procedure was utilized and ranged from 65.3% and above with complex **C1** having the greatest yield (82.5%). All 8 complexes were obtained as dark blue/purple microcrystalline solids after recrystallization from dichloromethane/pentane. The electron

configuration of the reported Ru_2^{5+} complexes indicate the presence of the three unpaired electrons in the antibonding orbitals (σ* and δ*) of ruthenium metal centres and thus the paramagnetic characteristics of the complexes. The resulting paramagnetic character excludes all NMR characterization. To confirm their structural identity, complexes were characterized using spectroscopic techniques such as infrared spectroscopy, high-resolution (ESI) mass spectrometry, and UV-visible spectroscopy with spectra obtained in coordinating and non-coordinating solvents and the electronic transitions compared to those reported in published methods. Single crystal XRD analysis confirmed the structural identity of complexes **C1**, **C3** and **C8** (Figures 3.3 - 3.5). The structural characteristics of the complex **C1** obtained from the crystallographic data are compared with those obtained and reported in published methods.[9]

3.2.4 Characterization of $[Ru_2(O_2CCH_3)_3(R\text{-}ap)Cl]$ (**C1** - **C8**) complexes.

*3.2.4.1 Molecular crystal structures of (**C1**·OH)·OH_2, [(**C3**·OH_2)]·OH_2·$(CHCl_3)_3$ and [(**C8**·OH_2)]·OH_2·$(CHCl_3)_3$.*

Molecular crystal structures of complexes (**C1**·OH_2)·OH_2, (**C3**·OH_2)·OH_2·$(CHCl_3)_3$ and (**C8**·H_2O)·H_2O·$(CHCl_3)_3$ were obtained by slow diffusion of concentrated solutions of **C1** in anhydrous dichloromethane, **C3** and **C8** in anhydrous chloroform and were layered with pentane at room temperature. Figures 3.3 - 3.5 represent ORTEP diagrams of the above-mentioned complexes, with all hydrogen atoms omitted for clarification purposes and better representation. Selected bond lengths and angles are all shown in Table 3.1. Additionally, the single X-ray crystallographic data collected such as CheckCIF reports and packing diagrams of complexes **C1** (Figure 6.57), **C3** (Figure 6.58) and **C8** (Figure 6.59) are included in Chapter 6.

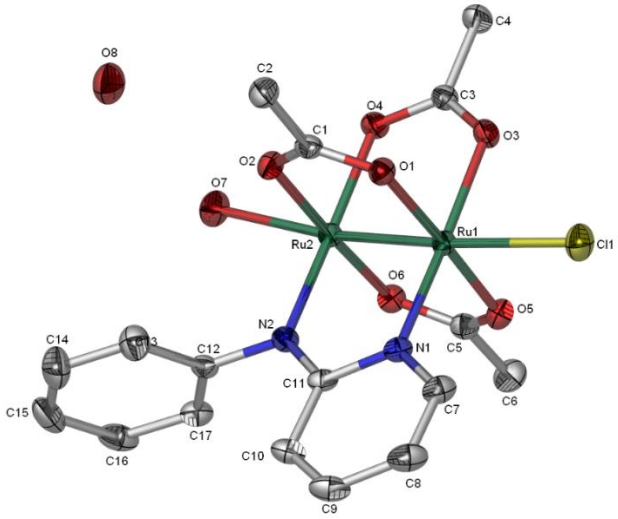

Figure 3.3 ORTEP diagram of complex [**C1**·OH_2]·OH_2. The ellipsoidal model was drawn at the probability level of 50%. Hydrogen atoms have been omitted for clarity.

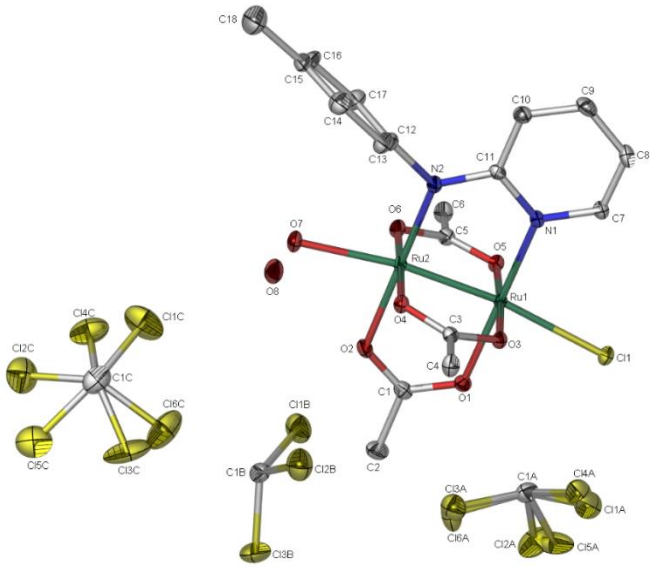

Figure 3.4 ORTEP diagram of complex [**C3**·OH_2]·OH_2·$(CHCl_3)_3$. The ellipsoidal model was drawn at the probability level of 30%. Hydrogen atoms have been omitted for clarity. Two chloroform solvent molecules are disordered. C1A consists of Cl2A and Cl5A, with sites of occupancy of 0.649 and 0.351. Cl3A and Cl6A consist of sites of occupancy of 0.649 and 0.351. Cl4A and Cl1A consist of sites of occupancy of 0.649 and 0.351. C1C consists of Cl2C and Cl5C, with sites of occupancy of 0.625 and 0.375. Cl3C and Cl6C consist of sites of occupancy of 0.625 and 0.375. Cl4C and Cl1C consist of sites of occupancy of 0.625 and 0.375.

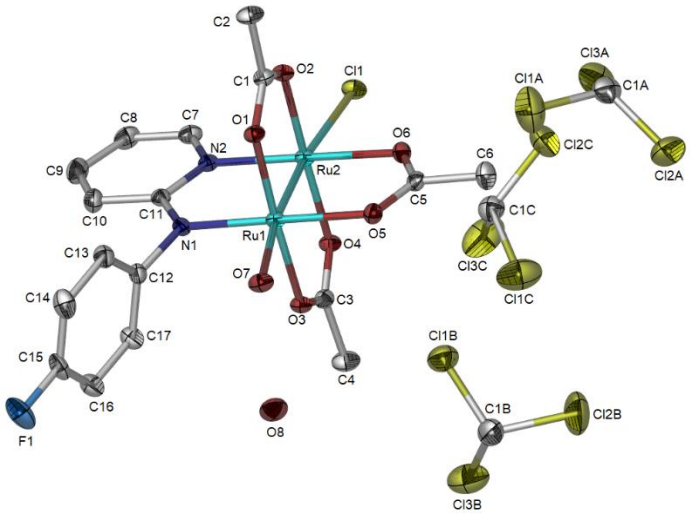

Figure 3.5 ORTEP diagram of complex [**C8**·OH_2]·OH_2·$(CHCl_3)_3$. The ellipsoidal model was drawn at the probability level of 40%. Hydrogen atoms have been omitted for clarity.

Table 3.1 Selected bond lengths (Å) and angles (deg) for complexes ([**C1**·OH_2]·OH_2, [**C3**·OH_2]·OH_2·$(CHCl_3)_3$ and [**C8**·OH_2]·OH_2·$(CHCl_3)_3$.

Bond	[**C1**·OH_2]·OH_2	**1**·OH_2[9]	**2**·$OHCH_3$[9]	[**C3**·OH_2]·OH_2·$(CHCl_3)_3$	**7**·$OC(CH_3)_2$[9]	[**C8**·OH_2]·OH_2·$(CHCl_3)_3$
			Bond Lengths (Å)			
Ru1 – Ru2	2.286 (2)	2.284 (9)	2.288 (3)	2.2834 (5)	2.286 (4)	2.2814 (4)
Ru1 – Cl1	2.536 (6)	2.544 (17)	2.484 (9)	2.5636 (9)	2.485 (10)	2.5459 (10)
Ru1 – N1	2.046 (18)[a]	1.988 (5)[a]	1.990 (2)[a]	2.039 (3)[a]	1.996 (3)[b]	1.981 (3)
Ru2 – N2	1.985 (17)[p]	2.052 (5)[p]	2.046 (2)[p]	1.981 (3)[p]	2.056 (3)[p]	2.048 (3)
Ru1 – O7	2.2859 (15)	2.315 (18)	2.326 (3)	2.299 (2)	2.326 (3)	2.293 (3)
Ru1 – O1	2.0561(14)	2.017 (4)	2.032 (17)	2.061 (3)	2.036 (3)	2.041 (2)
Ru2 – O2	2.0292 (14)	2.036 (4)	2.046 (17)	2.068 (3)	2.045 (3)	2.039 (3)
Ru1 – O3	2.0677 (15)	2.017 (4)	2.032 (17)	2.043 (2)	2.036 (3)	2.039 (3)
Ru2 – O4	2.0700 (15)	2.036 (4)	2.046 (17)	2.038 (2)	2.045 (3)	2.037 (2)
Ru1 – O5	2.0445 (14)	2.064 (4)	2.069 (17)	2.051 (2)	2.049 (3)	2.062 (3)
Ru2 – O6	2.0440 (14)	2.056 (4)	2.069 (17)	2.045 (2)	2.072 (3)	2.065 (3)
			Bond Angles (°)			
Ru1 – Ru2 – Cl1	173.379 (16)	173.51 (4)	174.46(16)	172.51 (3)	173.48 (3)	172.19 (3)
N1 – Ru2 – Ru1	90.59 (5)	90.02 (13)	90.16 (6)	90.46 (8)	89.86 (10)	90.71 (9)
N2 – Ru2 – Ru1	90.19 (5)	90.17 (14)	90.60 (6)	90.51 (3)	91.00 (10)	90.16 (9)
O7 – Ru2 – Ru1	172.00 (5)	174.5(11)	173.59 (5)	171.77 (8)	174.83 (8)	172.27 (8)

[a]Ru1 – N1 (anilino nitrogen) bond length

[b]Ru2 – N2 (pyridyl nitrogen) bond length

1·H_2O = [$Ru_2(O_2CCH_3)_3$(ap)Cl·H_2O] (see ref 36)

2·OCH_3 = [$Ru_2(O_2CCH_3)_3$(2-CH_3ap)Cl] (see ref 36)

7·$OC(CH_3)_2$ = [$Ru_2(O_2CCH_3)_3$(2-Fap)Cl] (see ref 36)

All complexes crystallize in the triclinic space group, P-1. The coordination geometry around each ruthenium metal centre is octahedral, with Ru_2-cores equatorially bridged by 3 acetates and one nitrogen-nitrogen anilinopyridinate ligand. For all complexes, Ru1 is axially coordinated to a chloride ligand while Ru2 is coordinated to a water molecule. The presence of the axially coordinated water molecule on Ru2 is most likely to be obtained from solvents utilized during crystallization, as would be expected because of the sterically unhindered axial site in the inner coordination sphere. Both the axially coordinated chloride and water molecules are slightly distorted towards the quadrant containing the less bulky equatorially bridging acetate ligands and away from the unsymmetrical bulky R-ap ligands to release strain, as observed by the Ru1 – Ru2 – O7 and Ru1 – Ru2 – Cl bond angles, which all range between 171.77° – 174.83° bond angles.

Molecular structures of similarly reported mono-substituted R-ap triacetatechlorodiruthenium(II, III) paddlewheel complexes have been extensively discussed concerning their bond lengths and angles, by Osterloh, Ryan. W et al[9]. and were compared to similar complexes of the type $[Ru_2(L_4)Cl]$, where L is the ap bridging ligand.[21] **C1**, **C3** and **C8** are compared to those reported by the same authors, particularly complexes $[Ru_2(O_2CCH_3)_3(ap)Cl{\cdot}H_2O]$ represented as **1**$\cdot H_2O$, $[Ru_2(O_2CCH_3)_3(2\text{-}CH_3ap)Cl{\cdot}OCH_3]$ as **2**$\cdot OCH_3$ and lastly, $[Ru_2(O_2CCH_3)_3(2\text{-}Fap)Cl{\cdot}OC(CH_3)_2]$ as **7**$\cdot OC(CH_3)_2$. These complexes are chosen for comparison purposes solely because of the nature of the electron-donating- and withdrawing- substituents (the fluorine and methyl groups) and their localized position (*para*-) on the aniline ring, making it easier to investigate the influence and effect of changing the varying the electronic effects on the lability of the chloride ligand that is axially coordinated to Ru1. The Ru1—Cl1 bond length of complexes **C1**, **C3** and **C8** are 2.536Å, 2.564Å, 2.546Å, respectively, with substituents located on the *para* positions of the aniline ring. The bond length is slightly elongated for complex **C3**, suggesting a weaker Ru1—Cl1 bond and shortened for complex **C8**, suggesting a stronger Ru1—Cl1 bond. The slight differences in bond lengths are attributed to the mesomeric electronic effects, which are the major contributing factor and thus strongly influence the lability of the Cl^- ion, regardless of the presence of the coordinated solvent molecule on Ru2 axial site. The Ru1—Cl1 bond of the reported complexes **1**$\cdot OH_2$, **2**$\cdot OHCH_3$ and **7**$\cdot OC(CH_3)_2$ are 2.544 Å, 2.484 Å and 2.485Å, respectively, with substituents located on the *ortho*-positions of the aniline ring.[9] Surprisingly, the Ru1—Cl1 bond is relatively unchanged between all three complexes, with no correlation regarding the shifting of the substituents which are located on the ortho positions being observed in this case, simply

because of the different solvents coordinating on the Ru2 axial site. These bond distances are all slightly shorter than that reported for the $[Ru_2(O_2CCH_3)_4Cl]$ complex (2.577Å). In all complexes, the Ru1—N1 (Ru1 coordinated to aniline nitrogen) bong lengths are significantly shorter than the Ru2—N2 (Ru2 coordinated to the pyridyl nitrogen) bond lengths, as can be observed from Table 1. Furthermore, for complexes **C1**, **C3** and **C8**, the Ru1—N1 bond lengths shorten significantly with varying substituents on the para positions of the aniline ring, with the **C8** complex having the shortest Ru1—N1 (1.981Å) bond length. On the other hand, the bond length of Ru2—N2 is shortened for **C3** and is elongated significantly for complex **C8**, all in comparison to **C1**. This phenomenon is also observed for the published crystal structures reported in Table 3.1 and is attributed to the negative charge being primarily situated on the nitrogen of the aniline ring on the R-ap type anionic ligands.[9,17,22]

One more observation worth noting, the bond lengths (Å) of the Ru – O (equatorially acetate ligands) are slightly longer than the Ru – N bond lengths. These observations suggest that the R-ap bridging ligands are strongly bound and coordinated to the ruthenium metal cores since they stabilize the charge. Additionally, there is more π-back bonding from the Ru1 due to the increased electron density by the presence of the axially coordinated water molecule and thus a decrease in the bond length of the Ru – N bonds.

*3.2.5.2 Infrared spectroscopy of $[Ru_2(O_2CCH_3)_3(R\text{-}ap)Cl]$ (**C1** - **C8**).*

To identify the characteristic functional groups present in the desired synthesized complexes, the infrared spectra of $[Ru_2(O_2CCH_3)_3(R\text{-}ap)Cl]$ complexes (**C1** - **C8**) in the solid state were recorded at room temperature using an FTIR (ATR) spectrophotometer. The characteristic absorption bands of all complexes are shown in Table 3.2 while the spectra of complexes **C1**, **C3,** and **C8** are represented in Figure 3.6 for variation and comparison purposes. The infrared spectra of **C2**, **C4** - **C7** are included in Figures 6.60 - 6.64 (Chapter 6).

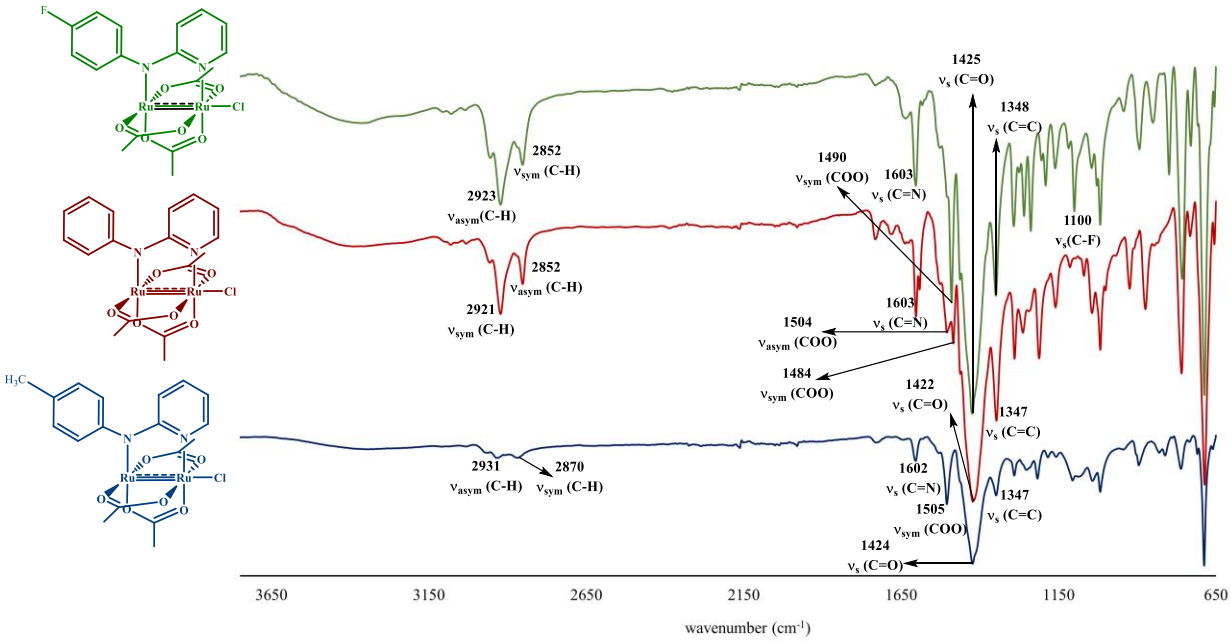

Figure 3.6 Infrared (IR-ATR) spectra of $[Ru_2(O_2CCH_3)_3(R\text{-ap})Cl]$ (**C1**, **C3**, and **C8**) complexes.

Table 3.2 Characteristic infrared spectroscopic assignments of $[Ru_2(O_2CCH_3)_3(R\text{-ap})Cl]$ (**C1 - C8**) complexes.

Complex	ν_{asym} (C-H)	ν_{sym} (C-H)	ν_s (C=N)	ν_{asym} (COO)	ν_{sym} (COO)	ν_s (C=O)	ν_m (C=C)
C1	2921	2852	1603	1504	1484	1422	1347
C2	2962	2924	1603	1506	1486	1421	1346
C3	2931	2870	1602	1517 (sh)	1505	1424	1349
C4	2922	2852	1603	-	1493	1424	1349
C5	2921	2852	1603	-	1493	1424	1349
C6	2921	2856	1603	-	1508	1424	1346
C7	2958	2928	1603	-	1490	1426	1350
C8	2923	2852	1603	-	1490	1425	1348

ν_{asym} – asymmetrical vibration stretching mode

ν_{sym} – symmetrical vibrational stretching mode

ν_s – strong vibrational stretching mode

ν_m – medium vibrational stretching mode

The spectra of complexes **C1 - C8** display broad absorption bands observed between 3107 - 3660 cm^{-1}. In the free ligands, the resolute absorption peaks observed in this region are assigned to the asymmetrical and symmetrical vibrational stretching frequencies of the secondary amine

(N-H). In the infrared spectra of the complexes **C1 - C8**, broad bands are observed in this region, thus suggesting the successful deprotonation and coordination of the free equatorial bridging nitrogen-based R-ap ligands to the precursor complex $[Ru_2(O_2CCH_3)_4Cl]$ to yield the desired complexes, respectively. The broad absorption bands observed in this region are assigned to the presence of the hydrogen O-H bond, due to axially coordinated water molecules trans to the chloride (Cl^-) ligand and possibly obtained from the solvents used during the work-up reaction. The presence of the hydrogen bonds is confirmed by X-ray crystallography (as previously discussed), where the Ortep diagrams of complexes **C1**, **C3** and **C8** show the presence of the axially coordinated water molecules through the oxygen atom. The hydrogen atoms of the coordinated water molecule are further bonded to the other floating water molecules present within the crystal lattice of a unit cell. A similar infrared spectral feature was observed and noted in literature for complexes of the type, $[Ru_2(hp)_4(Hhp)Cl]$, where hp is a 2-hydroxypyridine ligand.[22]

Furthermore, a more distinct characteristic to confirm the successful synthesis of the desired complexes is the presence of one distinct imine $\nu_s(C=N)_{pyridyl}$ absorption peak observed between 1603 - 1602 cm^{-1}. This peak is accompanied by a weak shoulder peak that was initially resolute and distinct in the infrared spectra of the free R-ap ligands and attributed to the imine $\nu_s(C=N)_{aniline}$ stretching frequency (Figure 3.7). This phenomenon is attributed to the coordination of the asymmetric nature of the R-ap ligand to the diruthenium(II, III) metal cores. Thus, the appearance of one distinguishable absorption imine peak is observed in the spectra of all $[Ru_2(O_2CCH_3)_3(R\text{-}ap)Cl]$ complexes.

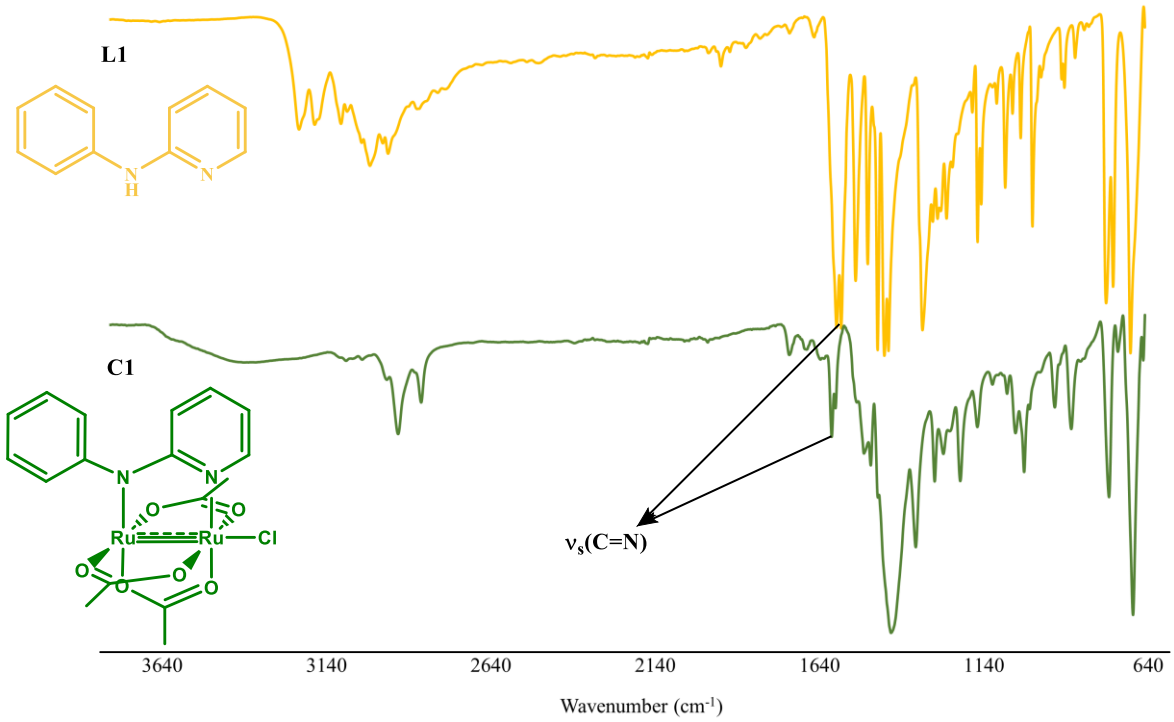

Figure 3.7 Stacked infrared spectra of **L1** and the corresponding complex, **C1**.

Additionally, in the infrared spectra of the free R-ap ligands, the imine (C=N) vibrational stretching frequencies are observed at slightly higher wavenumbers, 1657 - 1589 cm^{-1} while in the spectra of the complexes, the imine stretches are observed at lower wavenumbers (1602 - 1603 cm^{-1}). Upon coordination with the diruthenium(II, III) cores, a shift towards lower wavenumbers upon is expected as this shift is attributed to the π-back bonding of the ruthenium metals to the π*-antibonding orbitals of the R-ap ligands.

For complexes with methyl substituents located on the ortho- and para-positions of the R-ap ligands (**C2 - C6**), the presence of the methyl groups is expected to cause a significant shift of the ν_s (C=N) imine stretching frequencies to lower wavenumbers. The methylated ligands are expected to withdraw electrons onto the π*-antibonding orbitals, resulting in the elongation of the C=N bond due to the increase in electron density around the R-ap coordinated ligands. However, such a shift of the ν_s (C=N) imine peaks to lower wavenumbers were not observed. The infrared spectra of complexes **C7** and **C8** consist of ν_s(C-F) stretching frequencies observed at 1101 and 1100 cm^{-1}, similar to their respective ligands **L7** and **L8**. The equatorially bridged carboxylate (COO) asymmetrical and symmetrical stretching frequencies in the

infrared spectrum of all $[Ru_2(O_2CCH_3)_3(R\text{-}ap)Cl]$ complexes were observed between 1508 - 1484 cm^{-1}, and appear in the similar region as the $[Ru_2(O_2CCH_3)_4Cl]$ precursor complex.

*3.2.5.3 UV-visible spectra of $[Ru_2(O_2CCH_3)_3(R\text{-}ap)Cl]$ (**C1 - C8**).*

To characterize and study the electronic properties of the synthesized **C1 - C8** complexes, ultraviolet-visible solution studies were performed on an Agilent Cary 5454 UV-Visible and a Shimadzu 1800 UV-Vis series scanning spectrophotometers. All complexes were prepared in neat dichloromethane (5 x 10^{-4} M) and spectra were recorded at room temperature. Dichloromethane was the solvent of choice because it is a non-coordinating solvent and thus its less interference with complexes is negligible. All spectra were collected and represented in Figures 6.74 - 6.81 (Chapter 6) while the spectral data is shown in Table 3.3. Molar absorptivity coefficients were calculated by following the Beer-Lambert law.

Table 3.3 UV-visible absorption bands of **C1 - C8** complexes in DCM (5 x 10^{-4} M).

		λ_{max}, nm (ε x 10^{-4} M^{-1} cm^{-1})				
Solvent	Complex	Band I	Band II	Band III		Band IV
MeOH	$[Ru_2(O_2CCH_3)_4Cl]$	338 (0.03)	424 (0.02)	-		-
DCM	**C1**	306 (0.02)	412 (0.003)	582 (0.008)	654 (0.008)	-
	C2	307 (0.37)	422 (0.06)	602 (0.13)	653 (0.11)	-
	C3	304 (0.10)	418 (0.02)	578 (0.03)	660 (0.03)	-
	C4	-	424 (0.10)	590 (0.09)	668 (0.07)	962 (0.03)
	C5	-	423 (0.04)	597 (0.06)	647 (0.06)	946 (0.01)
	C6	-	423 (0.07)	591 (0.07)	668 (0.06)	956 (0.02)
	C7	302 (0.13)	416 (0.02)	576 (0.04)	656 (0.04)	-
	C8	304 (0.30)	420 (0.04)	587 (0.08)	653 (0.07)	-

The spectra of complexes **C1 - C8** recorded in DCM (5 x 10^{-4} $mol.dm^{-3}$) display identical spectral features characteristic of the mixed-ligand Ru_2(II, III) R-ap type complexes, $[Ru_2(ap)_4Cl]$, extensively discussed in the literature.[9,23,24,22,25] The oxidation states of each ruthenium metal centres are +2 ($4d^6$) and +3 ($4d^5$), with strong ruthenium-ruthenium metal bond resulting in the nearly degenerate two π^* and δ^* antibonding orbitals. All complexes are paramagnetic and characterized by 3 unpaired electrons in the nearly degenerate antibonding orbitals, thus giving rise to the electronic configuration of $(\sigma^2)(\pi^4)(\delta)^2(\pi^*)^2(\delta^*)^1$. Most Ru_2^{5+} and the generated Ru_2^{4+}complexes are of D_4h symmetry, with a bond order of 2.5 and magnetic moments ranging from 3.88 to 4.05 μ_B. The UV-visible spectra of these types of complexes are

notorious for exhibiting 3 - 4 absorption bands (280 – 1100 λ_{nm}), with shoulder bands observed at high energies (influenced by the nature of the axially coordinated ligand/solvent). The spectral changes and absorption maxima of all synthesized $[Ru_2(O_2CCH_3)_3(R\text{-ap})Cl]$ complexes are strongly influenced by the number of *N,N′* equatorial bridging and the type of axially coordinated ligands. Similarly, all spectra recorded in CH_2Cl_2 at room temperature show similar spectral features. Diruthenium(II, III) complexes equatorially bridged by R-ap type ligands with an axially bound Cl- anion to give the chemical formulae $[Ru_2(R\text{-ap})_4Cl]$ are essentially characterized by two intense absorption bands. One absorption band is split into two bands at 410 - 430 and 460 - 480 nm region, while the other is essentially a single band observed at lower energies ranging from 750 – 950 nm region.[25,26]

In the spectrum of the investigated $[Ru_2(O_2CCH_3)_3(R\text{-ap})Cl]$ complexes, the absorption bands II observed at approximately 412 - 423 nm are assigned to the ligand-to-metal charge transfer transitions [π(Ru–O, Ru_2) → $\pi^*(Ru_2)$] electronic transitions, as was reported for similar diruthenium(II, III) complexes.[9,23,27,28] The absorption bands observed at higher energies (276 – 307 λ_{nm}, pronounced for complexes **C1** - **C3**, **C7** and **C8**), are assigned to the ligand-to-metal charge transfer [π(Cl) → π^*/ $\delta^*(Ru_2)$] electronic transitions.

Additionally, the low energy weak absorption bands (shoulder bands) observed ≈ at 418 – 470 λ_{nm} (more prominent for complexes **C4** - **C6**) in the visible region are assigned to the d – d [$\pi/\sigma/\delta(Ru_2)$ → $\delta^*(Ru_2)$] excitation transitions, as was observed for similar diruthenium(II, III) complexes.[23] In the visible region (band III), broad low energy absorption bands observed between 578 λ_{nm} - 668 λ_{nm} are assigned to the [π(Ru – N, Ru_2) → $\pi^*/\delta^*(Ru_2)$] electronic transitions. It was tentatively proposed[9] that for $[Ru_2(O_2CCH_3)_3(R\text{-ap})Cl]$ complexes, the broad low energy absorption bands be assigned to the [π(N), π(axial) → π^* (Ru_2)] electronic transitions. Initially, the shoulder bands observed at ≈ 630 – 668 λ_{nm} region were assigned to the [δ (Ru_2) → π^* (Ru_2)] electronic transitions and are characteristic of Ru_2^{5+} tetracarboxylate complexes.[29] This absorption band in the visible region of the Ru_2^{5+} complexes has been reported to be sensitive to the type and number of the *N,N′* equatorial bridging ligand, as well as the mode of binding of the bridging ligand to the ruthenium metal cores.[25,26] In fact, the major visible band of the diruthenium(II, III) R-ap compounds shifts to higher energies upon an increase in the number of the R-ap equatorially bridging ligands around the diruthenium(II, III) cores from $[Ru_2(O_2CCH_3)_3(R\text{-ap})Cl]$ to $[Ru_2(R\text{-ap})_4Cl]$.[12,25]

The weak absorption bands (band IV) observed in the near-infrared region (946 - 962 λ_{nm}) are assigned to the [$\delta(Ru_2) \rightarrow \pi^*(Ru_2)$] or [$\delta(Ru_2) \rightarrow \delta^*(Ru_2)$] electronic transitions, and are sensitive to the donor strength of the axially coordinated ligand.[23,30] These bands resemble the near-infrared band of the spectrum of the $[Ru_2(O_2CPr)_4Cl]$ recorded in methanol, where Pr is a propyl linear chain and assigned to the [$\delta(Ru_2) \rightarrow \pi^*/\delta^*(Ru_2)$] electronic transition. [12,29] The electronic transitions assigned to bands observed in this region are reported to be sensitive to the donor strength of the axial ligand.

In neat CH_2Cl_2, the broad absorption band in the visible region is sensitive to the coordinated R-ap ligands and has a slightly significant impact on the spectral changes of the $[Ru_2(O_2CCH_3)_3(R\text{-ap})Cl]$, as observed by the spectral changes of **C4** - **C6**. The *N*,*N*-donor strength of the R-ap ligands along with the electron-withdrawing or donating nature of the substituents of the R-ap ligands increases the electron density on the metal cores. Thus, influencing the lability of the axially coordinated chloride ligand, as observed by the differences in the Ru – Cl bond lengths (Å). It is for this reason, that Ru_2^{5+} complexes are known to exist as a mixture of 2 analogues, the neutral $[Ru_2(O_2CCH_3)_3(R\text{-ap})Cl]$ and cationic $[Ru_2(O_2CCH_3)_3(R\text{-ap})]^+$ species in a chemical equilibrium (Scheme 3.6). This chemical equilibrium involves the association and dissociation of the axially coordinated Cl- ion on $[Ru_2(O_2CCH_3)_3(R\text{-ap})Cl]$ neutral species, as was observed for the reported $[Ru_2(O_2CCH_3)_3(2\text{-Fap})Cl]$ complex.[12]

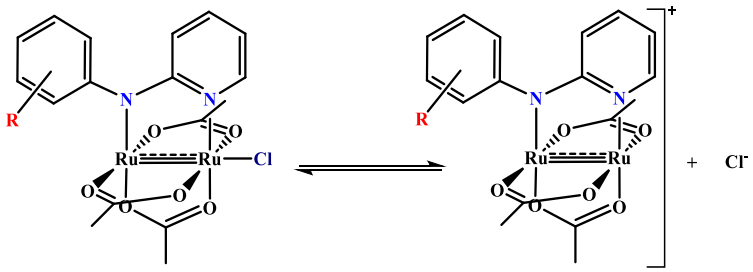

Scheme 3.6 Two diruthenium(II, III) species existing equilibrium in neat CH_2Cl_2.

This UV-visible spectral feature was also observed for diruthenium(II, III) species of the form $[Ru_2(dpb)_4Cl]$ complexes in neat CH_2Cl_2 and explains the broadness of the absorption band in the visible region (≈ 500 – 680 λ_{nm}).[31] The existence of two analogues of the form $[Ru_2(dpb)_4Cl]$ and $[Ru_2(dpb)_4]^+$, were confirmed by monitoring the spectral changes of the Ru_2^{5+} complex at various concentrations. Thus, to ascertain and establish the presence of an

equilibrium between Ru_2^{5+} analogues ($[Ru_2(O_2CCH_3)_3(R\text{-}ap)Cl]$ and $[Ru_2(O_2CCH_3)_3(R\text{-}ap)]^+$ species), UV-visible spectra of $[Ru_2(O_2CCH_3)_3(4\text{-}CH_3ap)Cl]$ (**C3)** in neat CH_2Cl_2 solutions containing 0.1 M quaternary salts in excess TBAX, where X = ClO_4^- and Cl^- were recorded at room temperature and displayed in Figure 3.8. Table 3.4 highlights the spectral data of **C3** (5 x 10^{-4} M) in CH_2Cl_2, in the absence and presence of 0.1 M quaternary salts ($TBAClO_4$/TBACl) dissolved in CH_2Cl_2 solution.

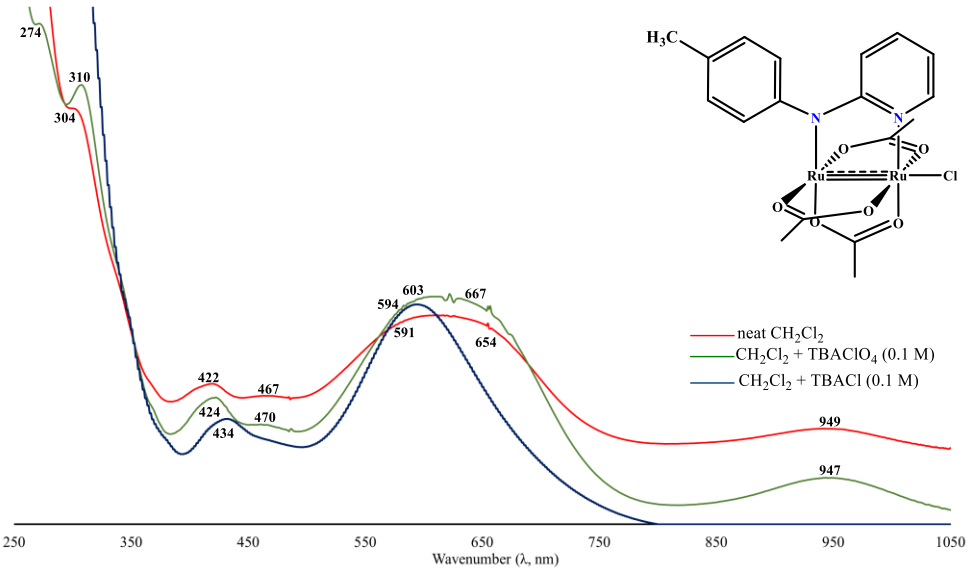

Figure 3.8 Ultraviolet-visible spectra of **C3** (5 x 10^{-4} M) recorded at room temperature. All spectra were recorded in neat CH_2Cl_2 (**red** solid line) and after additions of 0.1M quaternary salts [$TBAClO_4$ (**green** solid line) and TBACl (**blue** solid line)] dissolved in CH_2Cl_2.

Table 3.4 Ultraviolet-visible spectral data of **C3** (5 x 10^{-4} M) in CH_2Cl_2, in the absence and presence of 0.10 M quaternary salts ($TBAClO_4$ and TBACl).

Complex	Quaternary salt (0.1 M)	λ_{max}, nm (ε x 10^{-4} M^{-1} cm^{-1})				
		Band I	Band II	Band III		Band IV
C3	Neat CH_2Cl_2	304 (0.13)	422 (0.04)	591 (0.06)	654 (0.06)	947 (0.03)
	$TBAClO_4$	310 (0.14)	424 (0.04)	603 (0.07)	667 (0.06)	949 (0.01)
	TBACl	-	434 (0.03)	594 (0.07)	-	-

The UV-visible spectra of **C3** in neat CH_2Cl_2 (indicated by a **red**-lined spectrum) and a solution containing 0.1 M $TBAClO_4$ (**green**-lined spectrum) display similar spectra features with no significant spectral changes. The shoulder bands appearing at higher energies (304 and 310

λ_{nm}, respectively) are assigned to the ligand-to-metal charge transfer electronic transition [π (Cl) $\rightarrow$ π^*/ $\delta^*(Ru_2)$]. Surprisingly, this higher energy band is not observed in the UV-visible spectrum of **C3** recorded in CH_2Cl_2 solution containing 0.1M TBACl (**blue**-lined spectrum). The UV instrument (Shimadzu 1800 UV-Vis series scanning spectrophotometer) was used to record the spectrum of **C3** in excess 0.1 M TBACl dichloromethane solution consisting of a limited uv-range (280 - 800 λ_{nm}). Thus, absorption bands in this UV range below 280 λ_{nm} cannot be recorded under such limits.

In the near-infrared region, no new spectral features were observed for both **C3** spectra recorded in CH_2Cl_2 and the presence of excess $TBAClO_4$ solutions. The weak absorption bands and the electronic transitions are altered and susceptible to solvent coordination. No bands were observed for the spectrum with excess TBACl quaternary salt as the spectrum was recorded in the UV-visible region limits.

The broad low-energy absorption bands in the visible region become more resolute and intense to yield an absorption band at 594 λ_{nm}, in the presence of excess Cl^- ions. All these spectral changes suggest that there are two species of **C3** existing in a chemical equilibrium (as depicted in Scheme 3.7), the neutral $[Ru_2(O_2CCH_3)_3(R\text{-}ap)Cl]$ and the chemically generated cationic $[Ru_2(O_2CCH_3)_3(R\text{-}ap)]^+$ species. In the presence of excess Cl^- ions, the neutral $[Ru_2(O_2CCH_3)_3(R\text{-}ap)Cl]$ species is likely to be favoured as the major product present in the solution, according to LeChatelier's principles.[32]

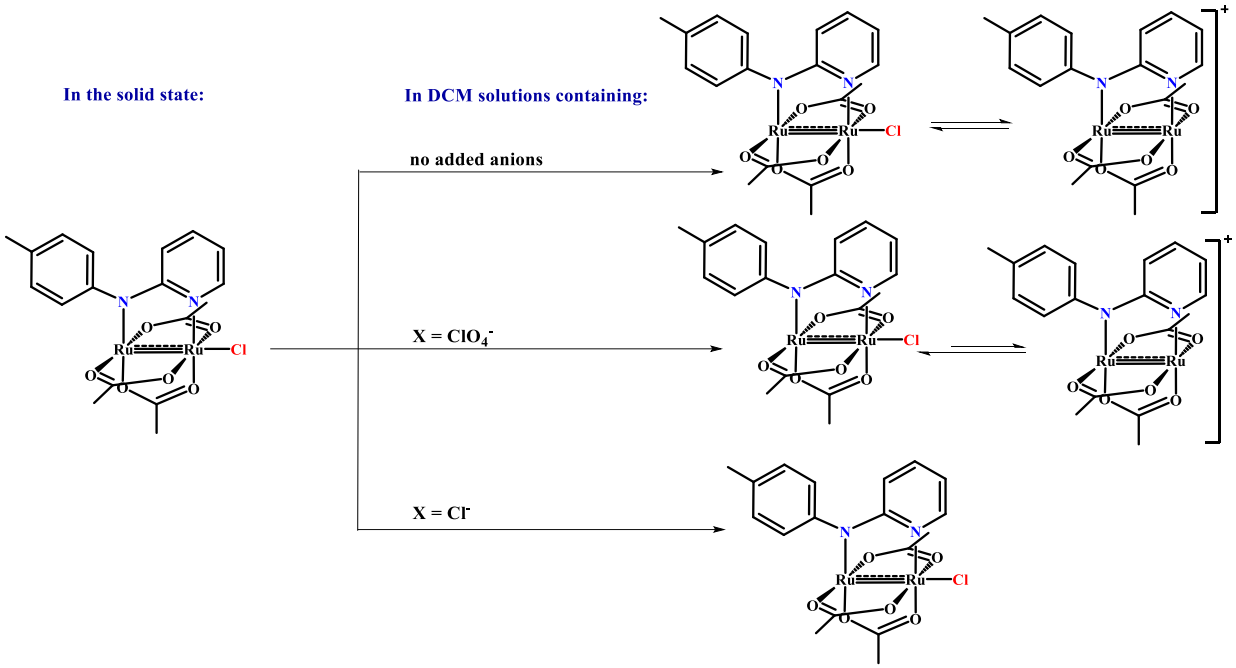

Scheme 3.7 Proposed mixed-ligand diruthenium(II, III) species formed from **C3** complex in DCM solutions containing 0.1M of quaternary salts ($TBAClO_4^-$, TBACl). The scheme was redrawn from examples depicted in literature.[33]

Thus, the spectrum of **C3** dissolved in CH_2Cl_2 with excess TBACl (0.1M) suggests that the neutral Ru_2^{5+} analogue $[Ru_2(O_2CCH_3)_3(R\text{-}ap)Cl]$ is the chemically favoured species in solution. Additionally, similar diruthenium(II, III) complexes have been reported to be susceptible to axial coordination of the second Cl^- to yield an anionic reduced form of the Ru_2^{5+} neutral species, Ru_2^{4+} species ($[Ru_2(O_2CCH_3)_3(Cl_2)]^-$). This may be attributed to the less steric hindered structures of the complexes, as was observed for the $[Ru_2(F_3ap)_4Cl]$ complex, where F_3ap = 2,4,6-trifluoroanilinopyridinate anion.[34]

The UV-visible spectra of the **C1**, **C3** and **C8** complexes, recorded in non-coordinating (DCM) coordinating (MeOH, MeCN, and DMSO) solvents were all conducted at room temperature and represented in Figures 3.9 - 3.11, respectively over a spectral region 250 - 800 λ_{nm}. There are five possible species of diruthenium(II, III) species that might be obtained upon dissolving the neutral species in coordinating solvents (S), as represented in Scheme 3.8 and redrawn from published reports.[26]

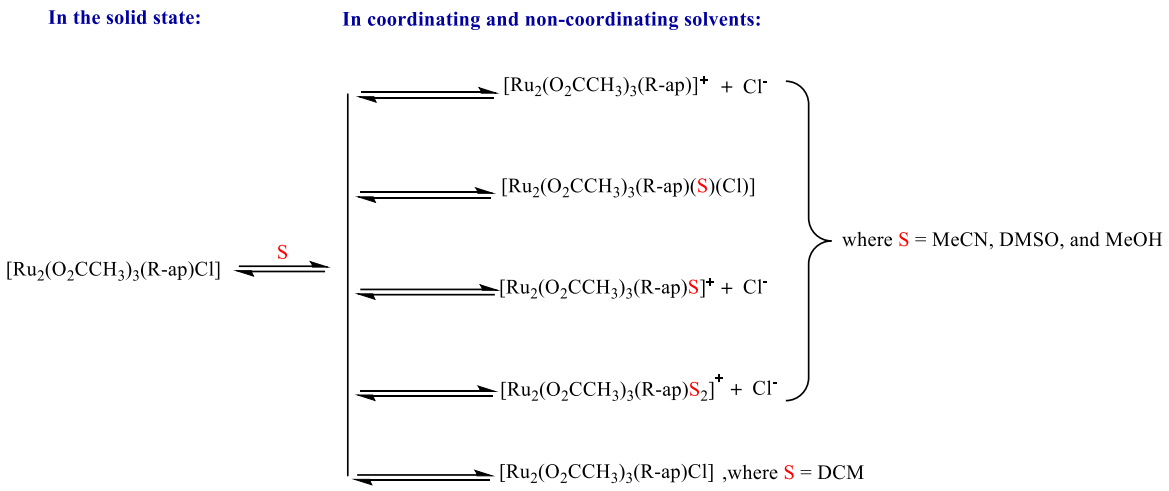

Scheme 3.8 A schematic representation of possible mixed ligand diruthenium(II, III) species formed when dissolved in coordinating and non-coordinating solvents (S). The schematic diagram was redrawn from diruthenium(II, III) analogues depicted in literature.[26]

Three chemically generated diruthenium(II, III) species with a dissociated Cl^- anion exist in solution and thus become positively charged on the $[Ru_2(O_2CCH_3)_3(R\text{-}ap)]^+$ unit while the other two species remain neutral in solution with Cl^- ion remaining axially bound to the diruthenium(II, III) metal cores. From figures 3.9 - 3.11, the UV-visible spectral features of **C1**, **C3**, and **C8** complexes change slightly, suggesting that the coordinating solvents bind weakly to the vacant axial site and do not dissociate the axially coordinated chloride ligand to form $[Ru_2(O_2CCH_3)_3(R\text{-}ap)(Cl)(S)]$ species in solution. The UV-visible spectral data of **C1**, **C3**, and **C8** complexes in the presence of coordinating and non-coordinating solvents are summarized in Table 3.5.

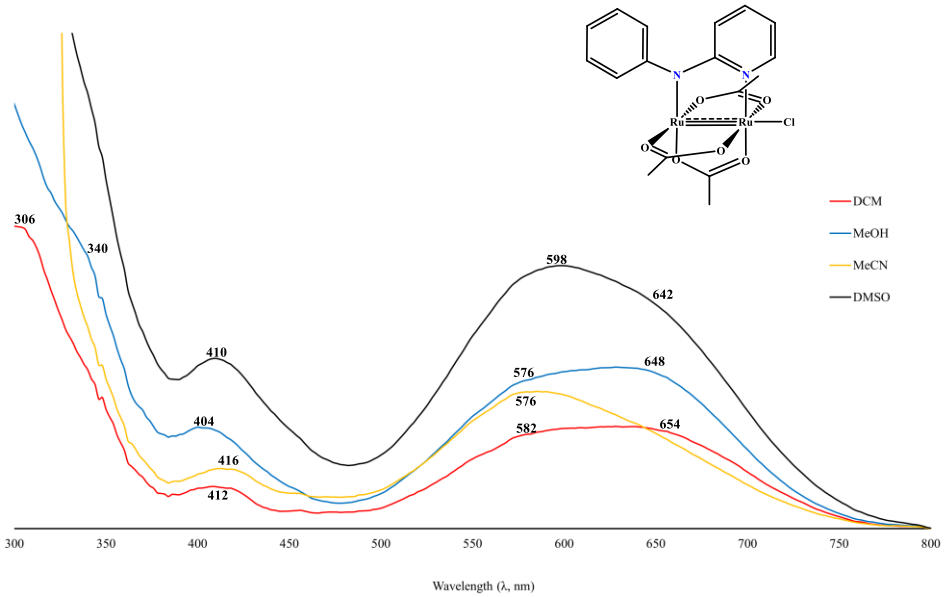

Figure 3.9 Ultraviolet-visible spectra of **C1** (5 x 10^{-4} M) in coordinating and non-coordinating solvents (DCM, MeOH, MeCN, and MeOH).

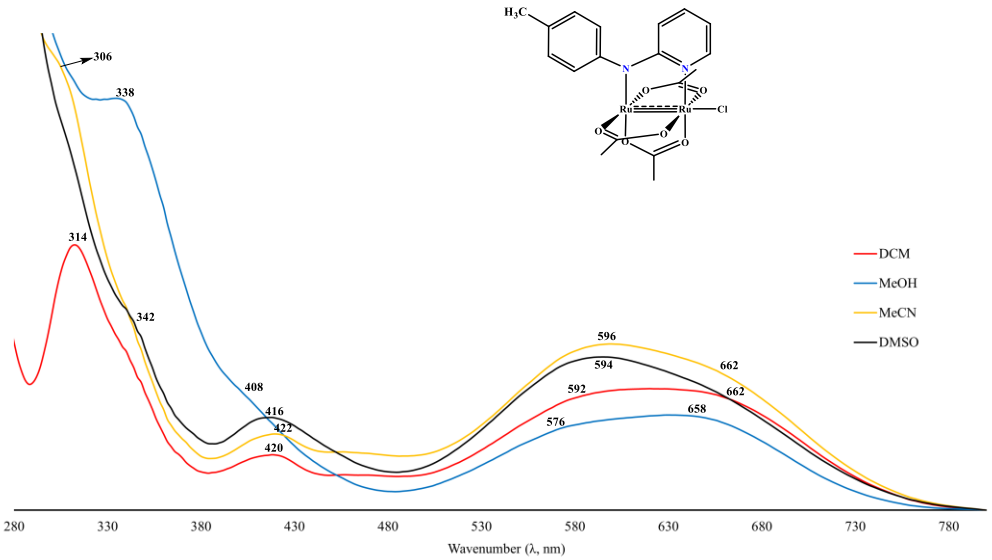

Figure 3.10 Ultraviolet-visible spectra of **C3** (5 x 10^{-4} M) in coordinating and non-coordinating solvents (DCM, MeOH, MeCN, and MeOH).

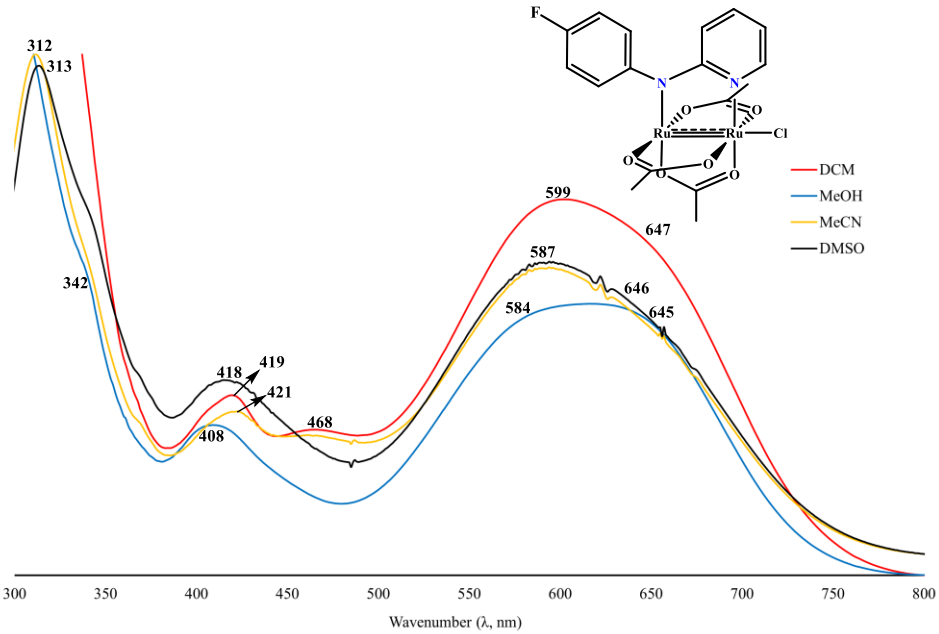

Figure 3.11 Ultraviolet-visible spectra of **C8** (5 x 10^{-4} M) in coordinating and non-coordinating solvents (DCM, MeOH, MeCN, and MeOH).

Table 3.5 Ultraviolet-visible spectral data of **C1**, **C3** and **C8** complexes in coordinating (MeOH, MeCN, and DMSO) and non-coordinating (DCM) solvents.

		λ_{max}, nm (ε x 10^{-4} M^{-1} cm^{-1})			
Solvent	**Complex**	**Band I**	**Band II**	**Band III**	**Band IV**
DCM	**C1**	306 (0.02)	412 (0.003)	582 (0.01) 654 (0.01)	-
	C3	304 (0.10)	418 (0.02)	578 (0.03) 660 (0.03)	-
	C8	304 (0.30)	420 (0.04)	587 (0.08) 653 (0.07)	-
MeOH	**C1**	340 (0.02)	404 (0.008)	576 (0.01) 648 (0.01)	-
	C3	338 (0.01)	408 (0.03)	576 (0.02) 658 (0.02)	-
	C8	342 (0.07)	408 (0.03)	584 (0.06) 645 (0.06)	-
MeCN	**C1**	310 (0.04)	416 (0.01)	576 (0.02) 674 (0.01)	-
	C3	306 (0.11)	422 (0.02)	596 (0.04) 662 (0.04)	-
	C8	313 (6.24)	425 (0.04) 467 (0.03)	592 (0.07) 646 (0.06)	989 (0.01)
DMSO	**C1**	-	412 (0.01)	598 (0.02) 642 (0.02)	-
	C3	342 (0.05)	416 (0.02)	596 (0.04) 670 (0.03)	-
	C8	313 (0.12)	425 (0.04) 467 (0.03)	592 (0.07) 646 (0.06)	989 (0.01)

As observed from the UV-visible spectra of all complexes, all spectra consist of 3 absorption bands characteristic of Ru_2^{5+} complexes in solution observed in the UV-visible region. The broad absorption bands observed in the visible region slightly differ due to the different coordinating solvents and the type or nature of the R-ap bridging ligands (H-ap, 4-CH_3ap, and 4-Fap). The spectral features of **C8** in coordinating and non-coordinating solvents are significantly different from the spectral features of **C1** and **C3**. For example, the low energy absorption bands (599, 587, and 587 λ_{nm}) in the spectra of **C8** recorded in DCM, MeCN, and DMSO (Figure 3.11) are slightly more resolute compared to the spectra of **C1** (Figure 3.9) and **C3** (Figure 3.10), having more broader absorption bands in the same solvent systems. The spectral features of the discussed diruthenium(II, III) complexes would differ should the axially coordinated chloride anion be displaced to form the Ru_2^{5+} species of the formula $[Ru_2(O_2CCH_3)_3(R\text{-}ap)]^+$, $[Ru_2(O_2CCH_3)_3(R\text{-}ap)S]^+$ or $[Ru_2(O_2CCH_3)_3(R\text{-}ap)S_2]^+$, as was observed for $[Ru_2(ap)_4Cl]$ complexes in coordinating and non-coordinating solvents.[26]

Bands near the infrared region were not recorded as the UV instrument (Shimadzu 1800 UV-vis series scanning spectrophotometer) used to record the spectra of complexes **C1**, **C3** and **C8**

in coordinating and non-coordinating solvents consist of a limited uv-visible range (280 – 800 λ_{nm}).

In summary, all recorded spectra in coordinating (MeCN, DMSO, and MeOH) and non-coordinating (DCM) solvents suggest that solvents bind weakly to the axially vacant site of the Ru_2^{5+} cores trans to the axially coordinating Cl^- anion. Thus, forming the neutral species $[Ru_2(O_2CCH_3)_3(R\text{-ap})Cl]$ and the cationic $[Ru_2(O_2CCH_3)_3(R\text{-ap})]^+$ species in solution (indicated in Scheme 3.8)

*3.2.5.4 Magnetic susceptibility of $[Ru_2(O_2CCH_3)_3(R\text{-ap})Cl]$ (**C1**, **C3** - **C8**).*

To determine magnetic effective moments (μ_{eff}) and confirm the paramagnetic properties of the synthesized mono-substituted $[Ru_2(O_2CCH_3)_3(R\text{-ap})Cl]$ (**C1**, **C3**, and **C8**) complexes, the magnetic susceptibility measurements of the mentioned complexes were determined by following D.F Evans[35,36] method. The ^{1}H-NMR spectra of complexes were recorded at room temperature, with the spectrum of **C1**, **C3** and **C8** presented in Figures 3.12 - 3.14 while the spectrum of **C4** - **C7** is presented in Figures 6.65 - 6.68 (Chapter 6).

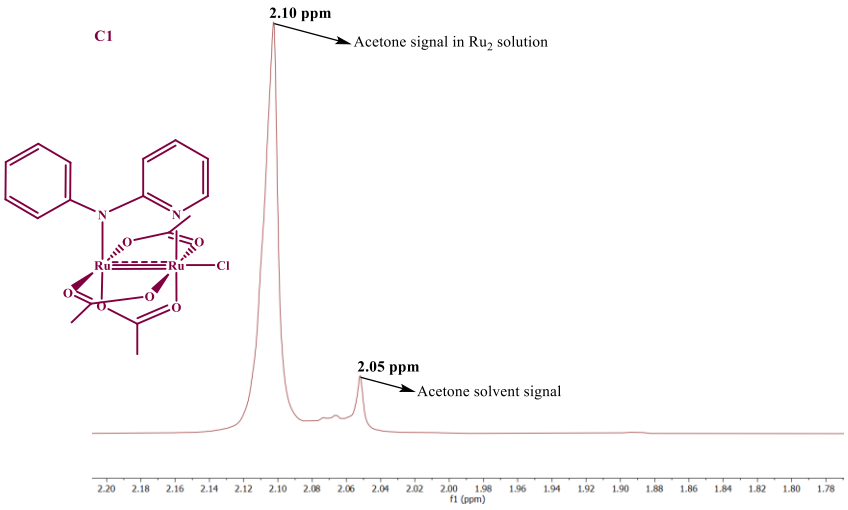

Figure 3.12 The paramagnetic susceptibility of **C1** in 50:1 (v/v) $(CD_3)_2CO$ and $(CH_3)_2CO$ solvent, recorded at room temperature (298K) using NMR (300 Hz) spectrometer.

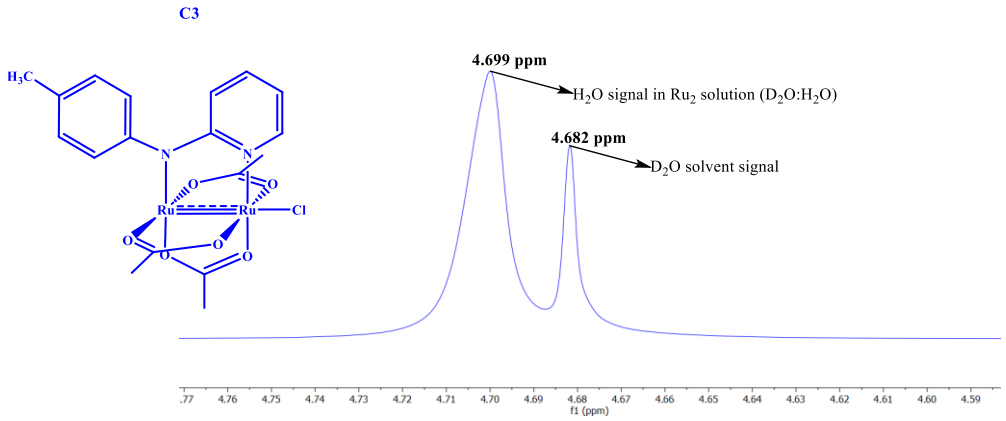

Figure 3.13 The paramagnetic susceptibility ^{1}H NMR spectrum of **C3** in 50:1 (v/v) D_2O and H_2O, recorded at room temperature (298K) using NMR (300 Hz) spectrometer.

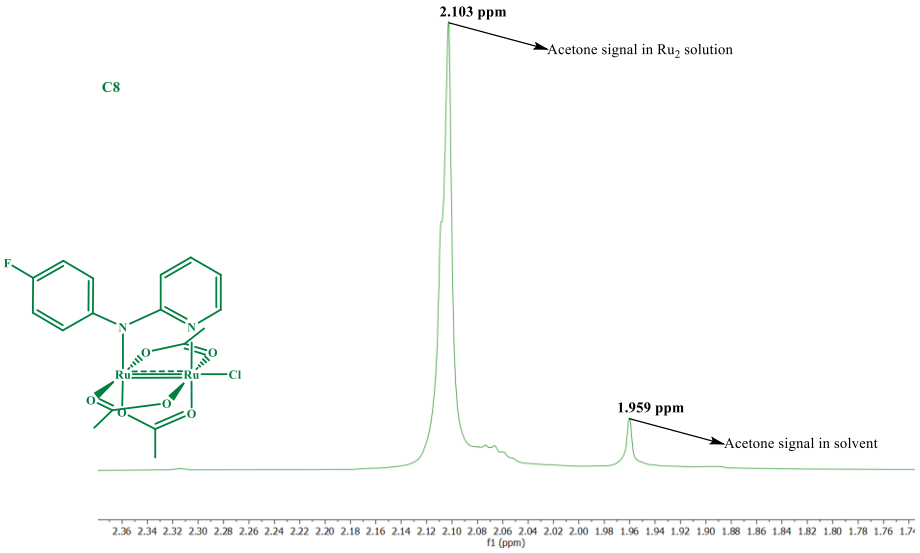

Figure 3.14 The paramagnetic susceptibility of **C8** in 50:1 (v/v) $(CD_3)_2CO$ and $(CH_3)_2CO$ solvent, recorded at room temperature (298K) using NMR (300 Hz) spectrometer.

According to Evan's[35] method, the number of unpaired electrons (n) in a paramagnetic material is determined from its effective magnetic moment (μ_{eff}) using equation (1), which in turn is related to the magnetic susceptibility (X_m) of the paramagnetic material according to equations (2) and (3), respectively.

$$n = \sqrt{\mu + 1} - 1 \qquad (1)$$

$$\mu_{eff} = \sqrt{8 \times X_M \times T} \qquad (2)$$

$$X_M = \frac{3 \times \Delta f}{4\pi \times F \times C} \qquad (3)$$

Where F = 300 x 10^6 Hz (frequency of instrument),

C = concentration of the paramagnetic solution,

T = 293.0 K (temperature of the ^{1}H NMR spectrometer),

Δf = change/shift in frequency of proton signal in Hz

The magnetic moments (μ_{eff}) of all mixed-valent paddlewheel Ru_2^{5+} complexes measured at room temperature have been reported to range between 3.6 to 4.4 B.M, all in alignment with the spin ground-state of 3/2, with the electronic configuration $\sigma^2\pi^4\delta^2(\delta^*\pi^*)^3$ (Figure 3.15), with 3 unpaired electrons occupying the nearly degenerate antibonding molecular orbitals (π* and δ*).[37,38]

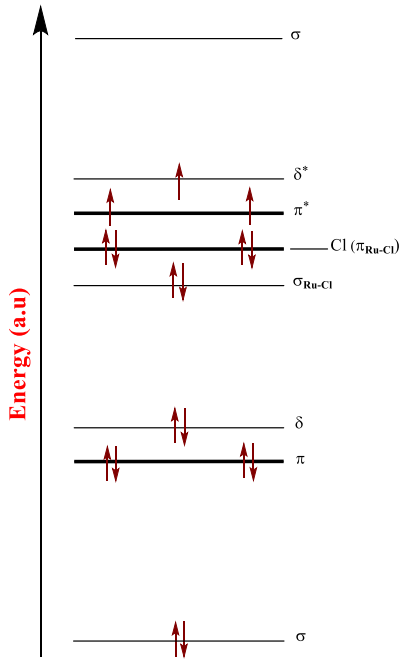

Figure 3.15 Molecular orbital diagram for mixed valent $[Ru_2(O_2CCH_3)_4Cl]$ and for the paramagnetic $[Ru_2(O_2CCH_3)_3(R\text{-}ap)Cl]$ complexes as reproduced from M.A.S Aquino et.al[3] and Guillermina Estiu et al.[6]

The paramagnetic properties of the paddlewheel complexes **C1**, **C3, C7** and **C8** are here in discussed. In the ^{1}H NMR spectrum of **C1** (Figure 3.12), an acetone solvent signal is observed at a chemical shift of 2.05 ppm. In addition, a broad major signal confirming the presence of a paramagnetic sample was observed further downfield at 2.10 ppm. Similarly, magnetic

susceptibility experiments were performed for complexes **C3** (Figure 3.13) and **C8** (Figure 3.14). In the ^{1}H NMR spectrum of **C3**, a D_2O solvent signal is observed at 4.682 ppm while a broad signal characteristic of the diruthenium(II, III) paramagnetic species in solution (D_2O: H_2O v/v) is observed at 4.699 ppm. For **C8**, a slight up-field shift of an acetone solvent [$(CD_3)_2CO$)] signal is observed at 1.959 ppm while a broad sharp signal is observed at 2.103 ppm, characteristic of the presence of the paramagnetic species dissolved in $(CD_3)_2CO$ NMR solvent. Similarly, for **C7** (Figure 6.63), the acetone solvent signal and the signal resulting from the Ru_2^{5+} paramagnetic species are observed in the same region as those signals observed for **C8**. The use of equations (1) - (3) led to the determination of the magnetic susceptibility of complexes **C1**, **C3** - **C8** being 5.2 x 10^{-3} cm^3 mol^{-1}, 5.7 x 10^{-3} cm^3 mol^{-1}, 7.2 x 10^{-3} cm^3 mol^{-1}, respectively. Their magnetic moments were in the order of magnitude 3.50 μ_B, 3.64 μ_B, and 4.11μ_B at 293K, as shown in Table 3.6. Indeed, these values correspond with the reported [39,40,9] paramagnetic moments reported for diruthenium(II, III) complexes with 3 unpaired electrons present in the near degenerate π^* and δ^* antibonding molecular orbitals (Figure 3.15).

Table 3.6 The raw data used to obtain the number of unpaired electrons for **C1**, **C3** - **C8**.

	C1 dissolved in $[(CD_3)_2CO]$	**C3** dissolved in $[D_2O]$	**C4** dissolved in $[(CD_3)_2CO]$	**C5** dissolved in $[(CD_3)_2CO]$	**C6** dissolved in $[(CD_3)_2CO]$	**C7** dissolved in $[(CD_3)_2CO]$	**C8** dissolved in $[(CD_3)_2CO]$
Mass (g)	0.0010	0.0010	0.0012	0.0020	0.0015	0.0022	0.0020
molar mass (g/mol)	583.9800	597.9800	598.0070	598.0070	612.0340	601.9300	601.9300
No. of moles (µmol)	1.7124	1.6723	2.0067	3.3444	2.4508	3.6549	3.3226
Solvent volume (mL)	0.7500	2.0000	0.8000	0.8000	0.8000	0.7500	0.7000
Concentration, C (µmol/mL)	2.2832	8.3615	2.5083	4.1806	3.0636	4.8732	4.7466
Signal 1 (ppm x Hz)	630.6000	1410.6000	630.0000	640.8000	633.6000	630.9000	630.9000
Signal 2 (ppm x Hz)	615.6000	1404.6000	615.0000	615.0000	615.0000	591.9000	588.0000
Change in peaks (Δf)	15.0000	6.0000	15.0000	25.8000	18.6000	39.0000	42.9000
Magnetic susceptibility (XM)	0.0052	0.0057	0.0048	0.0049	0.0048	0.0064	0.0072
Magnetic moment (µB)	3.5007	3.6585	3.3682	3.4217	3.3938	3.8571	4.1059
No. of unpaired e-	2.6407	2.7927	2.5135	2.5648	2.5381	2.9846	3.2259

*3.2.5.5 Mass spectrometry of [$Ru_2(O_2CCH_3)_3$(R-ap)Cl] (**C1 - C8**).*

High-resolution (ESI) mass spectroscopy for all [$Ru_2(O_2CCH_3)_3$(R-ap)Cl] (**C1 - C8**) were recorded in the positive mode. The ESI spectra of **C1**, **C3** and **C8** are presented in Figures 3.16 - 3.18, while those of the complexes **C2**, **C4 - C7** are shown in Figures 6.69 - 6.73 (Chapter 6). All spectroscopic molecular base peaks and assignments are represented in Table 3.7.

Table 3.7 High resolution (ESI) mass spectroscopic assignments of [$Ru_2(O_2CCH_3)_3$(R-ap)Cl] (**C1** - **C8**) complexes.

Complexes	ESI mass spectroscopic data assignments		
	Calculated (m/z)	Found (m/z)	Assignment
C1	583.9302	583.8955	$[M + H]^+$
		548.9274	$[M - Cl]^+$
		626.9416	$[M + MeCN + 2H]^+$
C2	597.957	563.9435	$[M - Cl + H]^+$
C3	597.957	562.9424	$[M - Cl]^+$
C4	611.9831	577.8895	$[M - Cl + H]^+$
C5	611.9831	577.8892	$[M - Cl + H]^+$
C6	626.0092	626.9418	$[M + H]^+$
		591.9733	$[M - Cl + H]^+$
		688.9884	-
C7	601.9203	567.9189	$[M - Cl + H]^+$
		679.0449	-
C8	601.9203	567.9159	$[M - Cl + H]^+$
		607.9426	-

For **C1** (Figure 3.16), there are three isotopic envelopes in the mass spectral data, which is in correlation with the isotopic distribution of the ruthenium metal centres. The parent base molecular ion peak centred at 583.8955 m/z corresponds to the $[M + H]^+$. The second and third isotopic envelopes have parent molecular ion peaks centred at 548.9274 m/z and 626.9416 m/z, assigned to the $[M - Cl]^+$ and $[M + MeCN + 2H]^+$ fragments, respectively. The molecular ion peaks matched with the predicted molecular ion fragments for **C1**.

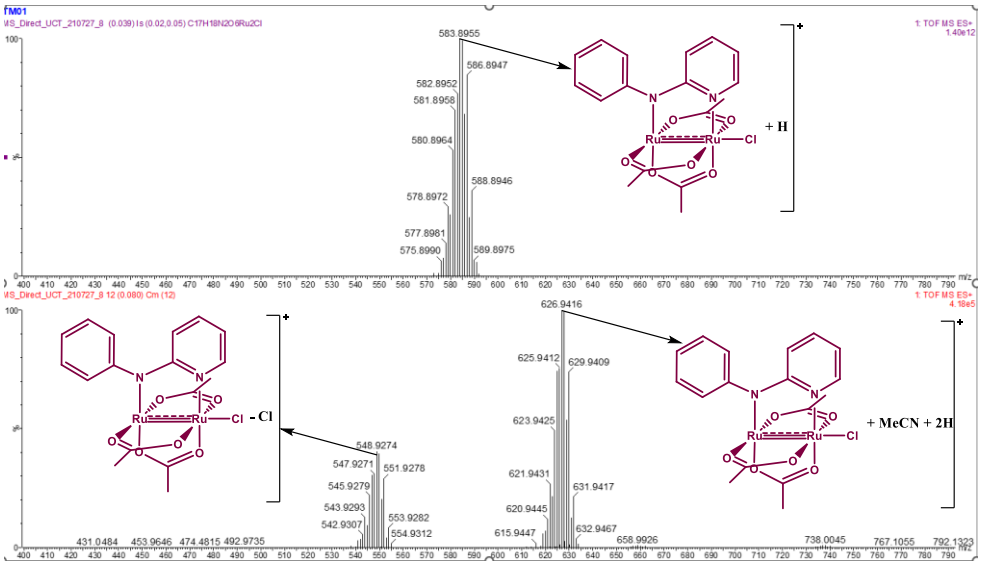

Figure 3.16 High resolution (ESI) mass spectrum of the assigned molecular fragments characteristic of **C1**, recorded in the positive-ion mode (+ve). The molecular base peak fragments were confirmed using the Molecular Weight Calculator Excel spreadsheet provided by Fiehn Lab, UC Davis Genome Centre - Metabolomics.[41]

For **C3** (Figure 3.17), the parent molecular ion peak observed at 563.9405 m/z corresponds to the $[M - Cl]^+$ fragment in the spectrum and agrees with the predicted molecular fragments expected for **C3**. Thus, confirming the successful synthesis of the desired **C3** complex.

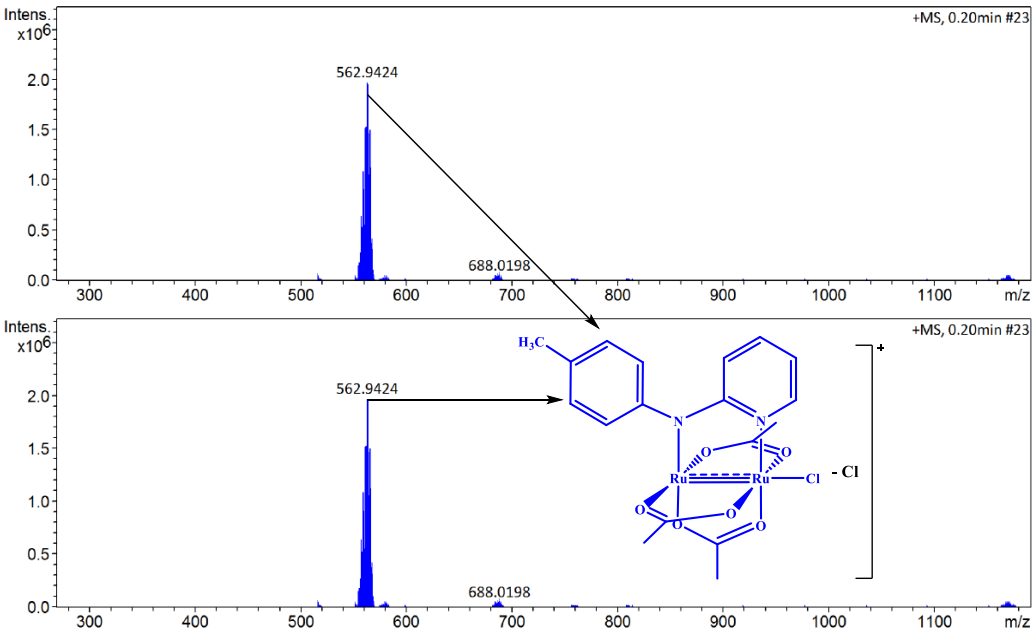

Figure 3.17 High resolution (ESI) mass spectrum of the assigned molecular fragments characteristic of **C3**, recorded in the positive-ion (+ve) mode. The molecular base peak fragments were confirmed using the Molecular Weight Calculator Excel spreadsheet provided by Fiehn Lab, UC Davis Genome Centre - Metabolomics.[41]

For **C8** (Figure 3.18), the parent base molecular ion peak observed at 583.8955 m/z corresponds to the $[M - Cl]^+$ ion peak. This molecular fragment matched the predicted molecular fragments for **C8**.

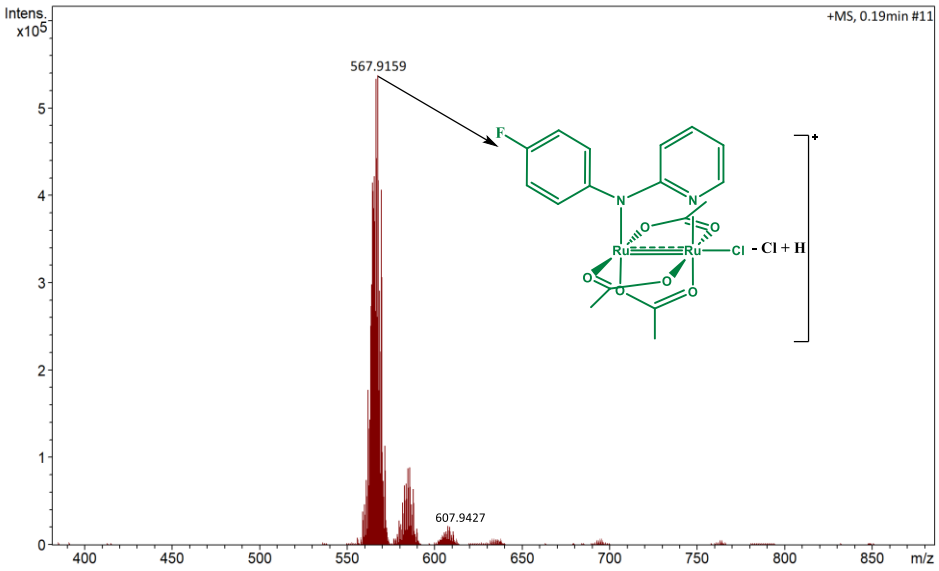

Figure 3.18 High resolution (ESI) mass spectrum of the assigned molecular fragments characteristic of **C8**, recorded in the positive-ion (+ve) mode. The molecular base peak fragments were confirmed using the Molecular Weight Calculator Excel spreadsheet provided by Fiehn Lab, UC Davis Genome Centre - Metabolomics.[41]

As indicated in Table 3.7, all high-resolution (ESI) mass spectroscopic data obtained agrees with the predicted m/z molecular fragment values of the proposed structures, with the data analysis of all complexes confirming the successful synthesis of the proposed complexes along with the collected spectroscopic and analytical data.

3.2.5.6 Electrochemical measurements (Cyclic Voltammetry) of [$Ru_2(O_2CCH_3)_3$(R-ap)Cl].

To elucidate the electrochemical redox chemical properties of [$Ru_2(O_2CCH_3)_3$(R-ap)Cl] complexes, cyclic voltammetry techniques were performed in 0.10 mM $TBAClO_4$ and TBACl as supporting electrolytes. The analytes were dissolved in CH_2Cl_2 (5.00 mM) solution, and measurements were recorded at room temperature. A three-electrode system consisting of a platinum wire electrode used as a counter electrode (CE), a glassy carbon electrode used as the working electrode (WE) and an electrode containing Ag/Ag^+ (0.10 mM) solution used as the reference electrode (RE). The electrochemical measurements were recorded at 0.10 V/s scan rate. The cyclic voltammograms of **C1**, **C3** and **C8** were recorded in 0.10 mM $TBAClO_4$ and are shown in Figures 3.19 - 3.21 while those of **C4** (Figure 6.82), **C5** (Figure 6.83), and **C7** (Figure 6.84) are shown in Chapter 6. Anilinopyridinate diruthenium(II, III) complexes are amongst the most studied and electrochemically characterized Ru_2^{5+} compounds with *N,N′*-

equatorially bridging ligands, closely followed by the diphenylformamidinate (dphf) ligands.[40] Diruthenium(II, III) complexes with ap bridging ligands undergo two $Ru_2^{5+/4+}$ reduction couples and a single $Ru_2^{5+/6+}$ oxidation reactions (Scheme 3.9). Furthermore, there are additional redox processes reported to occur due to the redox active bridging ligands.

$$Ru_2^{5+} \rightleftharpoons Ru_2^{6+} + e^- \qquad \text{Oxidation 1/2 reaction}$$

$$Ru_2^{5+} + e^- \rightleftharpoons Ru_2^{4+} \qquad \text{Reduction 1/2 reaction}$$

Scheme 3.9 Electrochemical redox processes of Ru_2^{5+} with anillinopyridinate (ap) equatorially bridging ligands.

For **C1** (Figure 3.19), when sweeping negatively, there is a two-step metal-centred reductive process observed at cathodic peak potentials (E_{pc}) of -0.55 V and -0.69V vs saturated calomel electrode (SCE). These electrochemical processes are assigned to the $Ru_2^{5+/4+}$ reductive couple of the neutral and cationic forms of **C1** in dichloromethane (in 0.10 M $TBAClO_4^-$ as supporting electrolyte). Additionally, upon reverse and sweeping positively, the anodic peak potentials (E_{pa}) for the $Ru_2^{5+/6+}$ oxidative couples were characterized and observed at 0.94 V - 1.08 V. Figure 3.19 consists of isolated well-defined reductive $Ru_2^{5+/4+}$ couples with $E_{1/2}$ potentials = 0.48V and -0.60 V, confirming the existence of the established chemical equilibrium between the neutral and cationic species of $[Ru_2(O_2CCH_3)_3(ap)Cl]$ complex in solution. The presence of two electron reductive processes is further explained by the ECE mechanism, as shown in Scheme 3.10.[42]

The first reductive couple ($E_{1/2}$ = -0.48 V) is assigned to the cationic $[Ru_2(O_2CCH_3)_3(ap)]^+$ species while the second reductive couple ($E_{1/2}$ = -0.69 V) is assigned to the neutral $[Ru_2(O_2CCH_3)_3(ap)Cl]$ species. The cationic species has a strong affinity for electrons and in this case, the negatively charged Cl^- ion.

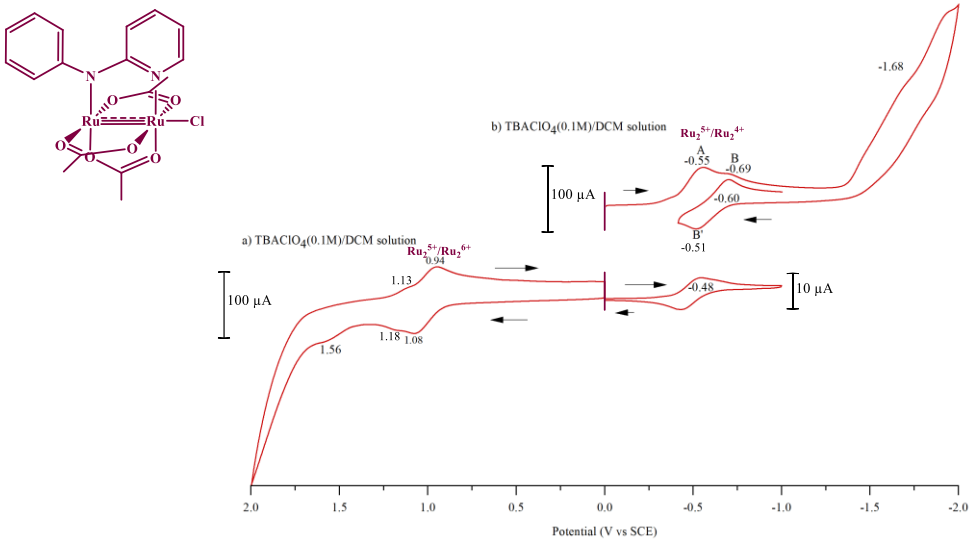

Figure 3.19 Cyclic voltammogram of **C1** (5.00×10^{-3} M) in CH_2Cl_2 recorded at room temperature. 0.1M $TBAClO_4^-$ was used as the supporting electrolyte. The CV shows two reductive one-electron $Ru_2^{5+/}Ru_2^{4+}$ couple and one oxidative Ru_2^{5+}/Ru_2^{6+} chemical process. Scan rate = 0.100 mV/s.

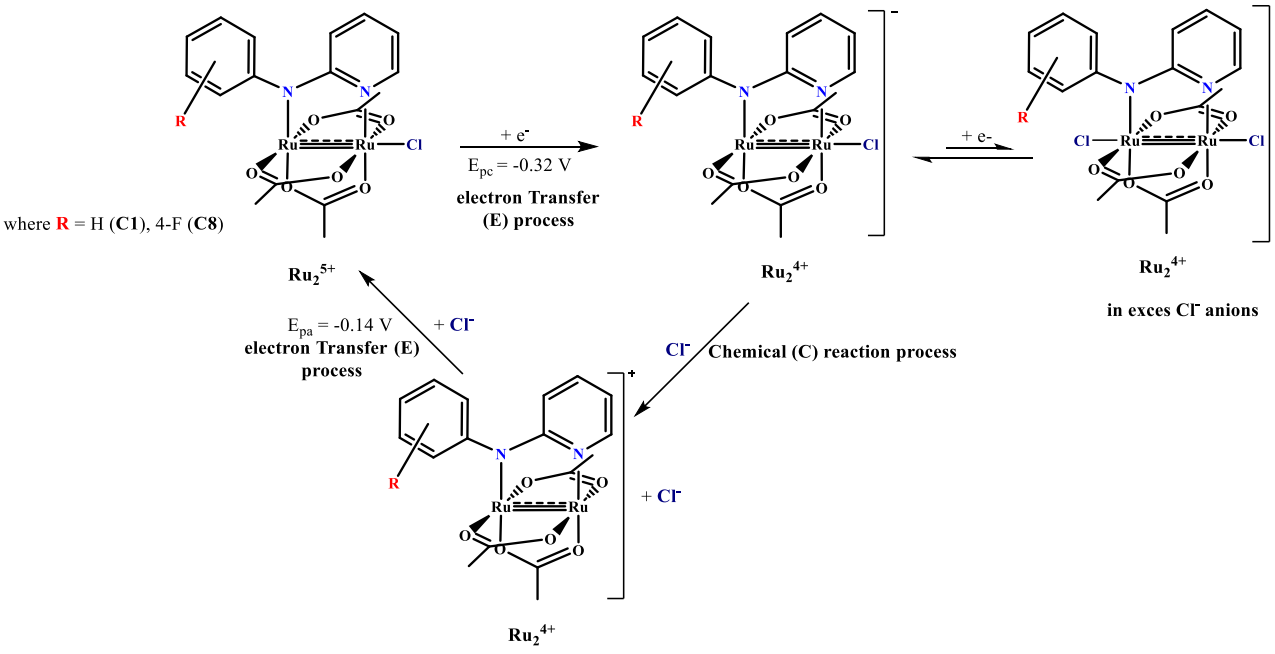

Scheme 3.10 Proposed electron transfer chemical reaction mechanism[42] for $[Ru_2(O_2CCH_3)_3(R\text{-ap})Cl]$ in non-coordinating dichloromethane solvent constituting excess 0.10 M TBACl. The mechanism is attributed to the existence of chemical equilibria which involves the association and dissociation of the anionic Cl^- axially coordinated ligand on the neutral, reduced and/or oxidized species of $[Ru_2(O_2CCH_3)_3(R\text{-ap})Cl]$ complexes, as discussed in the literature.[12]

Thus, the binding of the chloride ion occurs with ease to the positively charged cationic species, decreasing the oxidation state of the Ru_2 cores from 5+ to 4+. Upon sweeping positively (oxidation chemical processes), the anodic peak potential (E_{pa}) of 1.08 V is assigned to the neutral species, $[Ru_2(O_2CCH_3)_3(ap)Cl]$ while the second oxidation is further observed at E_{pa} = 1.18 V and assigned to the $[Ru_2(O_2CCH_3)_3(ap)]^+$ species which is slightly harder to oxidize.

The replacement with a methyl-substituted ligand (**C3**, Figure 3.20) results in two well-defined anodic peak potentials (E_{pa}) of 1.10 V (slightly shifted by 80 mV) and 0.87 V (shifted by 210 mV), respectively. The peaks shifted towards lower potentials due to the electron-donating methyl group which increases the electron density around the diruthenium(II, III) cores, thus making it easier to oxidize or for electron abstraction. Furthermore, when sweeping negatively (reduction process), the two cathodic peak potentials were observed at -0.55 V and -0.71 V (shifted by 20 mV), respectively. The cathodic peak potentials for the two reductive potentials did not shift significantly regardless of the increase in electron density around the metal centers, induced by the methyl substituent. The reductive $Ru_2^{5+/4+}$ couple with the cathodic peak potential (E_{pc}) = -0.71 V is irreversible and thus suggesting the formation of a newly formed species now present in solution upon the reverse of the reductive couple.

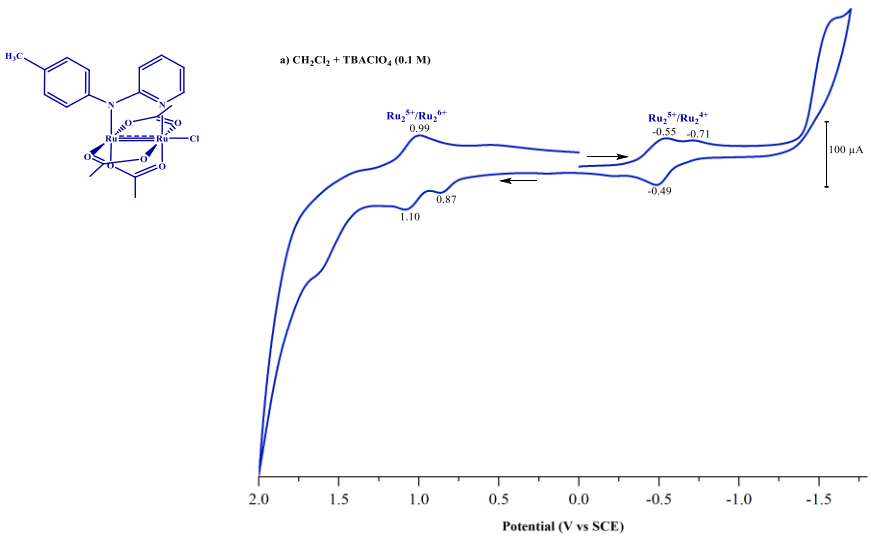

Figure 3.20 Cyclic voltammogram of **C3** (5.00 x 10^{-3} M) in CH_2Cl_2 recorded at room temperature. 0.1M $TBAClO_4$ was used as the supporting electrolyte. The CV shows two reductive one-electron $Ru_2^{5+/}Ru_2^{4+}$ couple and one oxidative Ru_2^{5+}/Ru_2^{6+} chemical process. Scan rate = 0.10 mV/s.

For **C8** (Figure 3.21), upon substitution with a fluorine electron-withdrawing ligand, the second reductive $Ru_2^{5+/4+}$ cathodic peak potential occurs at -0.72 V and is slightly shifted to greater potentials by 30 mV. This suggests that the fluorine substituent withdraws electrons away from the Ru_2 metal centres and thus, making the neutral $[Ru_2(O_2CCH_3)_3(4\text{-Fap})Cl]$ species harder to reduce to Ru_2^{4+}.

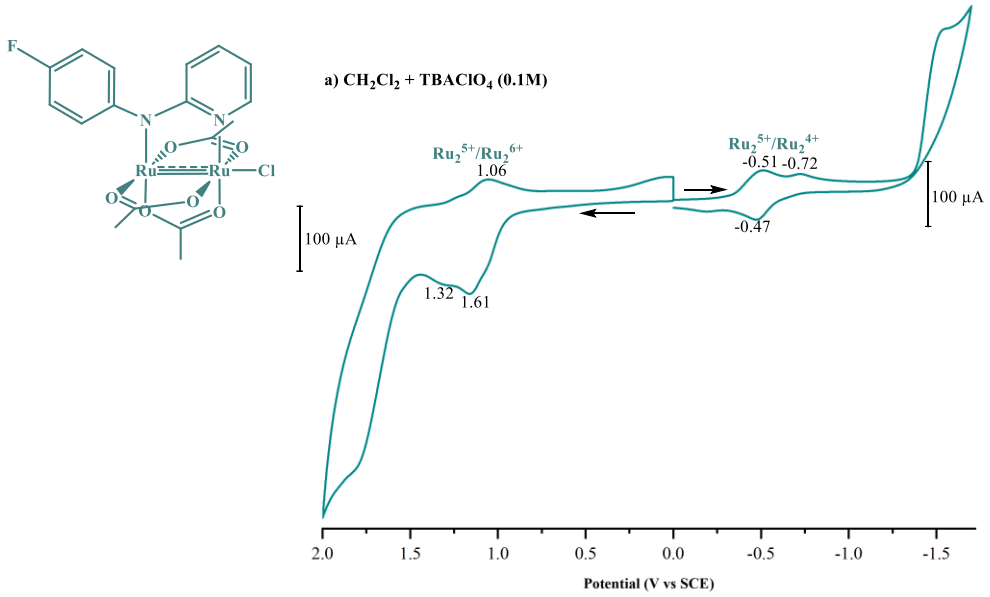

Figure 3.21 Cyclic voltammogram of **C8** (5.00 x 10^{-3} M) in CH_2Cl_2 recorded at room temperature. 0.1M $TBAClO_4^-$ was used as the supporting electrolyte. The CV shows two reductive one-electron $Ru_2^{5+/}Ru_2^{4+}$ couple and one oxidative Ru_2^{5+}/Ru_2^{6+} chemical process. Scan rate = 0.100 mV/s.

Similar to the cyclic voltammogram of **C3**, this reductive $Ru_2^{5+/4+}$ couple is irreversible and thus suggests the formation of a newly formed species now present in solution upon the reverse of the reductive couple. Upon sweeping in the positive direction, two oxidative couples with anodic peak potentials (E_{pa}) were observed at 1.61 V (due to the cationic species) and 1.32 V (due to the anionic species) for the $Ru_2^{5+/6+}$. These anodic peak potentials shift significantly to greater potentials by 430 mV and 240 mV, respectively. Thus, indicating the difficulty of oxidizing both species from Ru_2^{5+} to Ru_2^{6+}.

The cyclic voltammograms of **C1**, **C3** and **C8** in dichloromethane containing 0.1 M $TBAClO_4$ suggest that varying the substituents of the R-ap ligands influences the half-wave potential ($E_{1/2}$) of the redox chemical processes. In addition, the greater the electron-withdrawing nature

of the substituents, the greater the difficulty to oxidize and the easier the irreversible reduction reaction processes.

To characterize the electrochemical behaviour of the neutral $[Ru_2(O_2CCH_3)_3(R\text{-}ap)Cl]$ and cationic $[Ru_2(O_2CCH_3)_3(R\text{-}ap)]^+$ species existing in chemical equilibrium in non-coordinating dichloromethane solvent, the cyclic voltammograms were recorded at room temperature. Furthermore, their voltammograms were recorded *in excess* TBACl (0.100 M) to shift the equilibrium towards the electrogenerated $[Ru_2(O_2CCH_3)_3(R\text{-}ap)Cl]$ derivatives. The voltammograms of **C1**, **C3**, and **C8** complexes are shown in Figures 3.22 - 3.24, while those of **C4** and **C7** are shown in Figures 6.85 - 6.82 (Chapter 6).

All cyclic voltammograms performed in TBACl quaternary salt display Ru_2^{5+} based irreversible one electron reductive couple, $Ru_2^{5+/4+}$, while the oxidative $Ru_2^{5+/}Ru_2^{6+}$ processes were not visibly clear in CH_2Cl_2 solution containing excess 0.10 M TBACl conditions. This is in response to the presence of the excess Cl^- ions in solution which favours the axial coordination of the Cl^- anion in solution and thus the electro-generation of the neutral $[Ru_2(O_2CCH_3)_3(R\text{-}ap)Cl]$ species which can be explained by the ECE mechanism (Scheme 3.10).

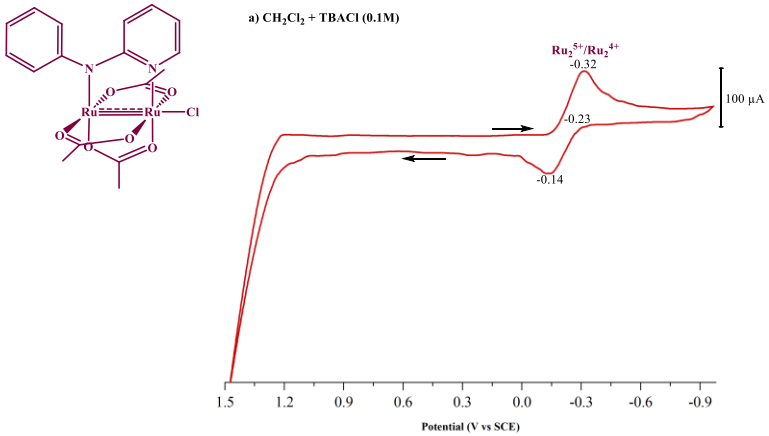

Figure 3.22 Cyclic voltammogram of **C1** (5.00×10^{-3} M) in CH_2Cl_2 recorded at room temperature. 0.1M TBACl was used as the supporting electrolyte. The CV shows a single one-electron $Ru_2^{5+/}Ru_2^{4+}$ reduction redox couple process. Scan rate = 0.100 mV/s.

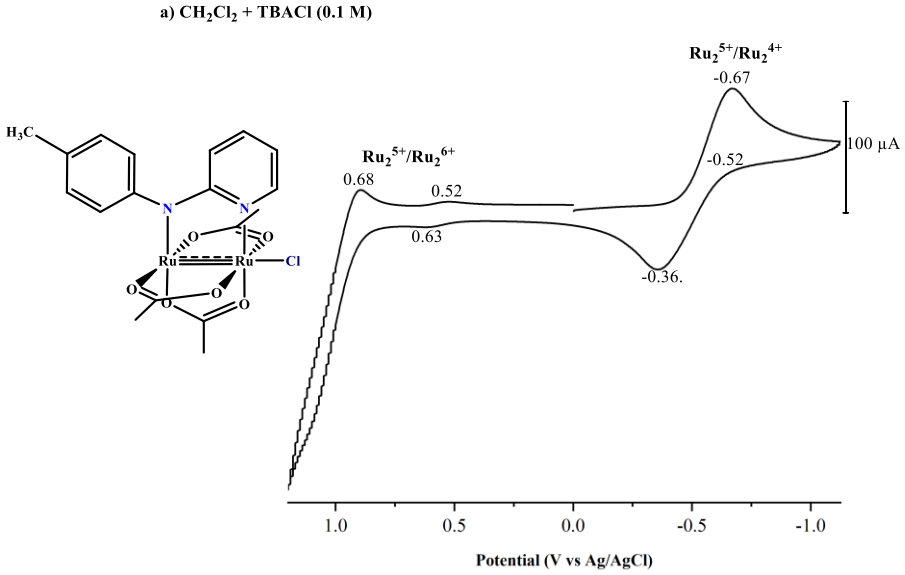

Figure 3.23 Cyclic voltammogram of **C3** (5.00 x 10^{-3} M) in CH_2Cl_2 recorded at room temperature. 0.1M TBACl was used as the supporting electrolyte. The CV shows a single one-electron $Ru_2^{5+/}Ru_2^{4+}$ reduction redox couple process. Scan rate = 0.100 mV/s.

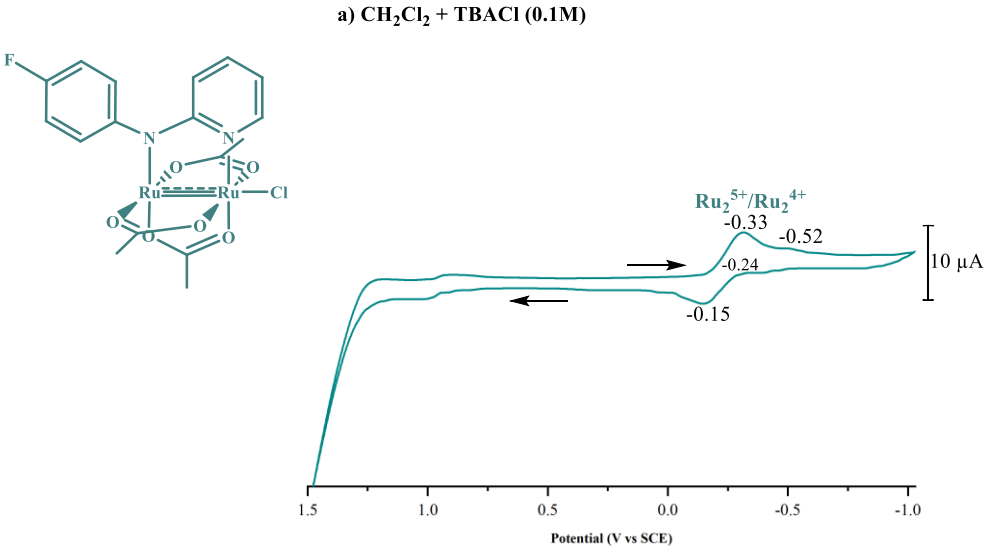

Figure 3.24 Cyclic voltammogram (CV) of **C8** (5.00 x 10^{-3} M) in CH_2Cl_2 recorded at room temperature containing 0.10 M of TBACl used as the supporting electrolyte. The CV shows a one-electron $Ru_2^{5+/}Ru_2^{4+}$ reduction redox couple process. Scan rate = 0.100 mV/s. The electrolytic system consisted of the glassy carbon as the WE (working electrode), platinum wire as the RE (reference electrode), and the Ag/AgCl solution electrode as the CE (counter electrode).

Successive axial coordination and substitutions of H_2O molecules with the Cl^- anion leads to a greater difficulty and higher reduction of halfwave potentials (vs SCE), as evidenced by the electrochemical reactions of $[Ru_2(\mu\text{-}O_2CCH_3)_4(H_2O)_2]^+$ with excess Cl^- anion (Scheme 3.11).[4,43,44]

$$[Ru_2(\mu\text{-}O_2CCH_3)_4(H_2O)_2]^+ + e^- \underset{}{\overset{E_{1/2} = 0.007\ V}{\rightleftharpoons}} [Ru_2(\mu\text{-}O_2CCH_3)_4(H_2O)_2]$$

$$[Ru_2(\mu\text{-}O_2CCH_3)_4(H_2O)(Cl)]^+ + e^- \underset{}{\overset{E_{1/2} = -0.015\ V}{\rightleftharpoons}} [Ru_2(\mu\text{-}O_2CCH_3)_4(H_2O)(Cl)]^-$$

$$[Ru_2(\mu\text{-}O_2CCH_3)_4(Cl)_2]^- + e^- \underset{}{\overset{E_{1/2} = -0.055\ V}{\rightleftharpoons}} [Ru_2(\mu\text{-}O_2CCH_3)_4(Cl)_2]^{2-}$$

Scheme 3.11 Electrochemical reduction reactions of successfully chlorinated species.[4,43,44]

Upon sweeping negatively, the cyclic voltammograms of **C1** (Figure 3.22) show the presence of well-defined single metal-centred Ru_2^{5+}/Ru_2^{4+} reductive chemical processes. The cathodic peak potential (E_{pc}) observed at - 0.32 V suggests that the $[Ru_2(O_2CCH_3)_3(ap)]^+$ species is the major product that is chemically favoured in solution to form $[Ru_2(O_2CCH_3)_3(ap)Cl]$. This cathodic peak potential does not correlate with the anodic peak potential (E_{pa}) observed at - 0.14 V upon reverse sweeping, possibly due to the two-electron processes that occur and are explained by the ECE mechanism (Scheme 3.10). The Ru_2^{5+} analogue is chemically favoured in solution due to the excess TBACl (0.10M) anions and is easier to reduce to Ru_2^{4+} by association with the Cl^- anion through axial coordination.

Similarly, for **C3**, the cyclic voltammograms (Figure 3.23) show the presence of a well-defined single quasi-reversible metal-centred Ru_2^{5+}/Ru_2^{4+} reductive chemical process. The Ru_2^{5+}/Ru_2^{4+} reductive couple occurs at $E_{1/2}$ = -0.52 V, with a cathodic shift of 35 mV upon substitution with a methyl group on the para position of the R-ap ligand. The methyl substituent increases the electron density around the Ru_2^{5+} metal cores, owing to its electron-donating properties. This brings about the great difficulty in reducing the metal-centred reductive process from Ru_2^{5+} to Ru_2^{4+} of the neural $[Ru_2(O_2CCH_3)_3(R\text{-}ap)Cl]$ species. Thus, the higher reductive couple chemical process occurs at higher potentials relative to **C1**.

The cyclic voltammogram of **C8** (Figure 3.24) shows the presence of a well-defined single reversible metal-centred Ru_2^{5+}/Ru_2^{4+} reductive chemical processes while the oxidation $Ru_2^{5+/}Ru_2^{6+}$ processes were not visibly clear in excess TBACl (0.100M) conditions. The half-wave potential of the Ru_2^{5+}/Ru_2^{4+} reductive couple occurs at -0.24 V. The shift in half-wave potential by 10 mV relative to **C1**, suggests that **C8** is harder to reduce due to the presence of the equatorially coordinated fluorine electron-withdrawing R-ap ligand, which draws electrons furthest from the Ru_2 metal centres. However, relative to **C3**, **C8** brings about an easier irreversible reduction. This, in turn, requires greater energy to reduce the charge of the oxidation state to 4+. Additionally, the neutral $[Ru_2(O_2CCH_3)_3(4\text{-Fap})Cl]$ species in solution is evidenced by a cathodic peak potential at -0.52 V belonging to the Ru_2^{5+}/Ru_2^{4+} reductive couple. Similarly, the reductive Ru_2^{5+}/Ru_2^{4+} couple of **C8** in TBACl (0.100M) is irreversible. Thus, suggesting the presence of a newly formed species in solution upon the reverse of the reductive couple.

The half-wave potentials of **C1**, **C3**, and **C8** for the irreversible reductive chemical process of Ru_2^{5+}/Ru_2^{4+}. The presented redox chemistry allows for an establishment of a Hammett[40,45] linear free relationship between the measured reduction half-wave potentials (determined using equation 4) and $\sum\sigma$ through a modified Hammett equation (equation 5):

Half wave potential ($E_{1/2}$) = $\frac{Epc+Epa}{2}$ …….. (4)

where E_{pc} = the cathode peak potential,

E_{pa} = the anodic peak potential,

and

$\Delta E_{1/2} = E_{1/2}(X) - E_{1/2}(H) = \sum(\sigma)\rho$……... (5)

where, $E_{1/2}$ (X) = the potential for each substituted bridging ligand derivative,

$E_{1/2}$ (H) = the potential for the non-substituted bridging ligand,

σ = the Hammett substituent constants for electron-donating or electron-withdrawing groups on the bridging ligand, and

ρ = reaction constant measuring the degree of interaction between the substituent and the site of electron transfer.

The are several factors that influence the experimentally determined value of ρ in Eq. (5). These include the site of electron transfer, the solvent used to record the electrochemical measurements, the supporting electrolyte, and the temperature.[40] The respective Hammett's constant values based on the para unsubstituted and substituted fluorine and methyl substituents are documented in Table 3.8, while the Hammett constant plot is shown in Figure 3.25.

Table 3.8 Cathodic peak potentials (E_{pc}, V vs Ag/AgCl) of **C1**, **C3**, and **C8** complexes in CH_2Cl_2 (0.50 mM) containing TBACl (0.1 M), recorded at room temperature. Scan rate = 0.1 V/s.

Complex	Substituent on the R-ap ligand	Half-wave potential (V vs Ag/AgCl)	σ
C1	*p*-H	-0.23	0.00
C3	*p*-CH_3	-0.52	-0.17
C8	*p*-F	-0.24	0.06

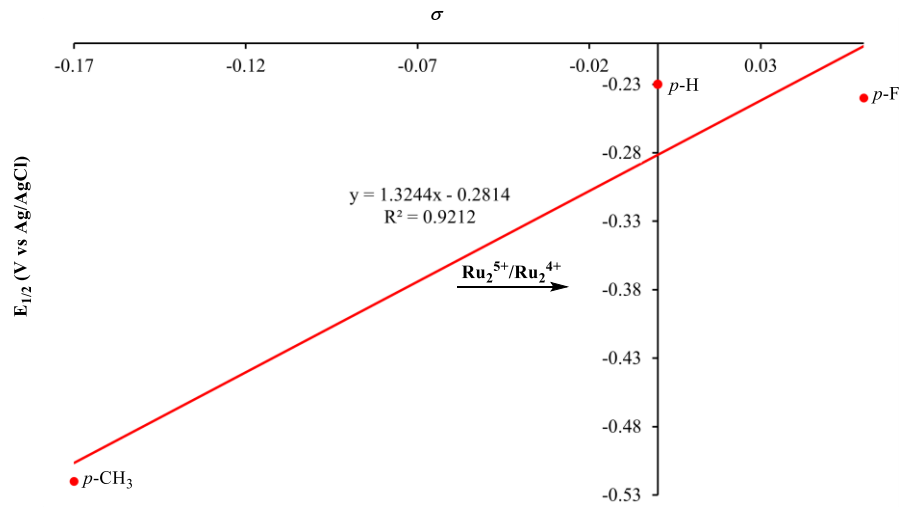

Figure 3.25 Hammett plot of sigma (σ) vs the half-wave potential ($E_{1/2}$, V vs Ag/AgCl) for $Ru_2^{5+/}Ru_2^{4+}$ reduction couple.

Figure 3.25 shows a linear free energy relationship between the nature of the substituent on the *para*-position of the coordinated R-ap ligand and the potential energy required for the charge of the Ru_2 metal cores to be reduced from Ru_2^{5+} to Ru_2^{4+}. The linear fit shows a good to an excellent correlation between the half-wave potentials of the reductive Ru_2^{5+}/Ru_2^{4+} couple and the Hammett constants of the individual substituents of the paddlewheel complexes. Furthermore, the reactivity constant (ρ) derived from the linear least-square fitting of $E_{1/2}$ is

1.32 V. Thus, suggesting that the electron-withdrawing and donating nature of the substituents facilitate the reduction processes occurring at the diruthenium metal cores.

3.3 SUMMARY

A library of anilinopyridinate (R-ap) ligands (**L1** – **L8**) was successfully prepared and fully characterized using spectroscopic and analytical techniques. The crude products purified *via* recrystallized technique from hot hexanes ligands were purified *via* recrystallization from hot hexanes obtained in moderate yields (29% – 62%). All ligands were fully characterized using an array of spectroscopic and analytical techniques including NMR (^{1}H, ^{13}C{H}, HSQC and COSY) spectroscopy, infrared spectroscopy, mass spectrometry, thus confirming the identity of the prepared ligands. All spectroscopic and analytical data collected correlate well with the proposed synthesized structures and agree with the published material.

The stoichiometric reaction of the prepared R-ap ligands (**L1** – **L8**) with the paddlewheel precursor $[Ru_2(O_2CCH_3)_3(R\text{-ap})Cl]$ complex led to the successful synthesis of the desired air-stable and water-soluble monosubstituted paddlewheel triacetatechlorodiruthenium(II, III) complexes, $[Ru_2(O_2CCH_3)_3(R\text{-ap})Cl]$ (**C1** – **C8**) complexes. This chapter seeks to explore and report on two different synthetic procedures, with the latter procedure modified by deprotonation of the substituted R-ap ligands and the addition of the LiCl to the reaction mixture to ensure axial coordination of the chloride axial ligand. Both methods involve a metathesis displacement of a single moiety of an acetate group followed by the replacement with an equivalence of the nitrogen-nitrogen R-ap bridging ligand. This procedure was used to prepare all desired mono-substituted $[Ru_2(O_2CCH_3)_3(R\text{-ap})Cl]$ (**C1** - **C8**) complexes, obtained in moderate to good yields (44% - 83%) which improved significantly compared to when the former synthetic procedure was employed to synthesize the desired complexes. Furthermore, the chapter seeks to contribute towards the development of a high-yield synthetic procedure to prepare an array of paddlewheel diruthenium tetraacetate structures and enhance the water-soluble properties and stability of the $[Ru_2(O_2CCH_3)_4Cl]$ metal-centred cores in aqueous solutions for easy evaluation *in vitro* biological assays used to screen for their potential anticancer properties. The incorporation of two ruthenium metal centres may be efficacious compared to the discussed mono-ruthenium complexes by enhancing the cytotoxic properties of the complexes and thus, their potential anticancer effects. All paddlewheel $[Ru_2(O_2CCH_3)_3(R\text{-ap})Cl]$ (**C1** - **C8**) complexes were fully characterized using an array of spectroscopic and analytical techniques including infrared and ultraviolet-visible spectroscopy, high-resolution mass spectrometry (HRMS), cyclic voltammetry, magnetic susceptibility, and single crystal XRD analysis to confirm their purity and structural identity. All spectroscopic

and analytical data collected and discussed correlate well with the proposed synthesized $[Ru_2(O_2CCH_3)_3(R\text{-}ap)Cl]$ complexes and agree with the published material.

The ultraviolet-visible spectra of the investigated $[Ru_2(O_2CCH_3)_3(R\text{-}ap)Cl]$ (**C1 - C8**) complexes revealed characteristic spectral features of diruthenium(II, III) complexes. The spectra of all complexes show the presence of two Ru_2^{5+} species existing in chemical equilibrium in coordinating (CH_2Cl_2) and non-coordinating (MeOH, MeCN, and DMSO) solvents (observed by the presence of the broad absorption bands in the visible region). In coordinating solvents, the axially vacant site is susceptible to solvent coordination, binding weakly to the axial site trans to the Cl^- anion with the possibility of forming Ru_2^{5+}analogues of the form $[Ru_2(O_2CCH_3)_3(R\text{-}ap)Cl]$, $[Ru_2(O_2CCH_3)_3(R\text{-}ap)(Cl)(S)]$, $[Ru_2(O_2CCH_3)_3(R\text{-}ap)]^+$, and $[Ru_2(O_2CCH_3)_3(R\text{-}ap)(S_2)]^+$ depending on the donor strength of the coordinating solvents. To further provide evidence for the existence of two $[Ru_2(O_2CCH_3)_3(R\text{-}ap)Cl]$ species in solution, ultraviolet-visible and cyclic voltammetry measurements were recorded in non-coordinating CH_2Cl_2 solutions containing quaternary salts such as $TBAClO_4$ and TBACl (0.100M). The spectral changes recorded suggest that the chemical equilibrium is shifted towards the formation of the neutral $[Ru_2(O_2CCH_3)_3(R\text{-}ap)Cl]$ species, according to Le Chatelier's principles.[32] This was further evidenced by the presence of one reductive Ru_2^{5+}/Ru_2^{4+} couple in the cyclic voltammograms of the $[Ru_2(O_2CCH_3)_3(R\text{-}ap)Cl]$ (**C1**, **C3,** and **C8**). The linear-free energy relationship graph shows a good to an excellent correlation between the half-wave potentials of the reductive Ru_2^{5+}/Ru_2^{4+} couple and the Hammett constants of the individual substituents of the paddlewheel complexes. Furthermore, the derived from the linear least-square fitting of $E_{1/2}$ is 1.32 V. Thus, suggesting that the electron-withdrawing and donating nature of the substituents facilitate the reduction processes occurring at the diruthenium metal cores, as evidenced by the reactivity constant (ρ) of $E_{1/2}$ = 1.32 V.

3.4 EXPERIMENTAL

3.4.1 Chemicals and Reagents.

Schlenk line techniques were employed to synthesize all complexes reported in this chapter. High-purity graded nitrogen (N_2) and argon (Ar) were purchased from Air Liquide, South Africa (Pty) Ltd. All solvents (AR graded) used for synthetic purposes and to work-up reactions were purchased from commercial sources (KIMIX chemicals, Lab Supplies CC and Science World). Solvents were purified further *via* distillation and kept under inert atmospheric conditions over activated molecular sieves. All solvents used for spectroscopic techniques were purchased from Sigma-Aldrich/Merck Co. and were unless stated otherwise, used as received for electrochemical measurements. Silica gel (70 - 230 Mesh, 63- 200 µM, 60 Å) used for column chromatography was purchased from Sigma-Aldrich/Merck Co. Tetrabutylammonium perchlorate (TBAP) and tetrabutylammonium chloride (TBACl) were purchased from Sigma-Aldrich. 2-Bromopyridine (C_5H_4NBr), 2-aniline (C_6H_7N), 2-methylaniline (C_7H_9N), 2-fluoroaniline (C_6H_6NF) were purchased from Sigma-Aldrich/Merck Co.

3.4.2 General Methods and Physical Instrumentation

Nuclear Magnetic Resonance (NMR) spectroscopic data were recorded on a Varian Mercury XR400 (^{1}H: 399.95 MHz, $^{13}C\{^1H\}$: 100.65 MHz) or Varian Mercury XR300 (^{1}H: 300.08 MHz, $^{13}C\{^1H\}$: 75.500 MHz) spectrometers, using a Bruker Bio-spin GmbH casing and sample injector. Chemical shifts are reported δ (ppm) relative to the internal standard tetramethylsilane (TMS, δ 0.00). The residual solvent peak (δ 7.26 for $CDCl_3$) was used as an internal reference. Coupling constants were recorded in Hz. Magnetic susceptibility measurements were recorded on a Varian Mercury XR300 (^{1}H: 300.08 MHz) spectrometer using NMR coaxial insert sample tubes, with the paramagnetic (**C1 - C3**, **C8**) sample material prepared in acetone or D_2O. The magnetic moments were calculated using the D.F Evans[35] method from the NMR spectra obtained. Attenuated total reflectance (ATR) infrared spectra of ligands and complexes were acquired in the solid state and recorded on a Perkin-Elmer Spectrum One FT-IR spectrophotometer and measurements made recorded between 4000 - 500 cm^{-1}. Melting points of anilinopyridinate (R-ap) ligands were determined using a Büchi B-540 melting point apparatus and were uncorrected. Electrospray ionization (ESI) mass spectra were recorded and obtained on a Bruker Compact Ultimate 3000 UHPLC-QTOF-High Resolution Mass Spectrometer (University of Witwatersrand, Johannesburg, South Africa), or waters Synapt G2 quadrupole time-of-flight mass spectrometer, ESI probe (+ve mode), CV 15 V instrument (MS Unit, JC Smuts building, Private Bag X1, Matieland, 7602, Stellenbosch University, South

Africa). An Agilent LC-MS instrument comprising of an Agilent 1260 Infinity Binary Pump, Agilent 1260 Infinity Diode Array Detector, Agilent 1290 Infinity Column Compartment, Agilent 1260 Infinity Autosampler, Agilent 6120 Quadrupole MS, and Peak Scientific Genius 1050 Nitrogen Generator and fitted with an X-bridge (C18, 2.5 μm, 3.0 mm (ID) × 50 mm length) column maintained at either 35 or 40 °C was used to monitor the progress of reactions including percentage purity determinations (University of Cape Town, Cape Town, South Africa). Ligands **L1 - L8** are confirmed to be >95% pure. Elemental analysis data of the precursor complex, $[Ru_2(O_2CCH_3)_4Cl]$ was obtained at ICP-MS Laboratory, Central Analytical Facilities (CAF), Stellenbosch University on an Agilent 7900 ICP-MS or Agilent 8800 QQQ ICP-MS instrument. Electronic absorption spectra were recorded on an Agilent Cary 5454 UV-Visible and a Shimadzu 1800 UV-Vis series scanning spectrophotometers, over 1200 - 200 nm and 800 - 200nm wavelengths. The UV spectra were recorded using a 1 cm path-length quartz cell. Electrochemical measurements were obtained by cyclic voltammetry with measurements carried out using Basi Epsilon Eclipse Electrochemical Analyzer Potentiostat/Galvanostat. A three (3) electrode system consisting of a glassy carbon disk as the working electrode, platinum (Pt) wire as the counter/auxiliary electrode and Ag/Ag^+ as the reference electrode. The electrodes were mounted in a single-compartment cell configuration. Cyclic voltammograms were obtained from a 1.0 x 10^{-3} M stock solution of analyte (**C1**, **C3** and **C8**) in a solvent containing 0.10 M of the supporting electrolyte ($TBAClO_4$ and TBACl).

3.4.3 General synthetic procedure and characterization of R-ap (**L1 - L8**).

All R-substituted *N*,*N*-type R-ap bridging ligands (**L1 - L8**) were synthesized following literature procedures[16,15,17] with a few modifications. A mixture of 2-bromopyridine (1 equiv.) and 2 - aniline (2 equiv.) were added to a 2-neck round bottom flask and heated in a solventless reaction at 100°C overnight under consistent magnetic stirring. During this time, the solution changed colour from light to dark brown. The solution was cooled to room temperature. After cooling, the reaction mixture was treated with 10% NaOH (100 mL) aqueous solution (w/v). The unreacted materials were steam-distilled using water as an internal steam source to get rid of the excess aniline. The compound was extracted with CH_2Cl_2 (50 mL) and transferred into a separating funnel. The resulting organic layer was collected, dried over magnesium sulphate ($MgSO_4$), and filtered *via* suction followed by solvent removal *in vacuo*. The residue was recrystallized numerous times in hot hexane to give a cream to pure white crystalline material. To achieve greater purity, ligands were sublimed at 100°C to give pure white crystalline material.

Anilinopyridinate [H(ap)] (**L1**)

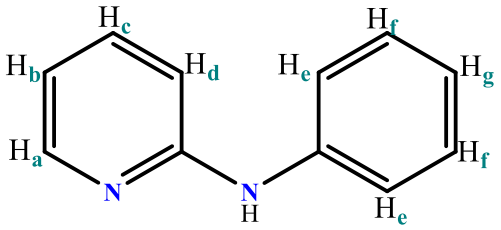

L1. 2-Bromopyridine (948 mg, 0.572 mL, 5.88 mmol) and 2-aniline (1.10 g, 1.08 mL, 11.8 mmol). **Yield**: 618 mg (62%). **Melting point**: 109 - 111°C (decomposition). **FT-IR (ATR)** (ν_{max}.cm^{-1}): 3096 ($\nu_{asym,}$ N – H), 3058 (ν_{sym}, N – H), 2953 (ν_s, C – H), 1657 (ν_s, C = N), 1588 (ν_s, C = C), 1444 (ν_s, C – C). **MS (LC, *m/z*)** = Calculated: 170.0844, Found: 171.01 [M + H]$^+$. **Purity (LC)**: 100% (t_R = 0.211 min.). **^{1}H NMR (399.95 MHz, CDCl$_3$, ppm)**: δ 8.23 (ddd, $^3J_{HH}$ = 5.0 Hz, $^4J_{HH}$ = 1.9 Hz, $^4J_{HH}$ = 0.9 Hz, 1H, H$_a$), 7.49 (ddd, $^3J_{HH}$ = 8.4 Hz, $^3J_{HH}$ = 7.2, $^4J_{HH}$ = 1.9, 1H, H$_c$), 7.34 (s, 2H, H$_e$), 7.33 (s, 2H, H$_f$), 7.09 - 7.01 (m, 1H, H$_g$), 6.88 (dt, $^3J_{HH}$ = 8.4 Hz, $^4J_{HH}$ = 0.9 Hz, 1H, H$_d$), 6.75 (broad s, 1H, H$_{N-H}$), 6.73 (ddd, $^3J_{HH}$ = 7.2 Hz, $^3J_{HH}$ = 5.0 Hz, $^4J_{HH}$ = 0.9 Hz, 1H, H$_b$). **^{13}C{^{1}H} NMR (100.65 MHz, CDCl$_3$, ppm)**: δ 156.11, 148.41 (C$_a$), 140.56, 137.64 (C$_C$), 129.28 (2C, C$_e$), 122.84 (C$_g$) 120.41 (2C, C$_f$), 115.02 (C$_b$), 108.07 (C$_d$).

2-methyl-anilinopyridinate [H(2-CH$_3$)ap] (**L2**)

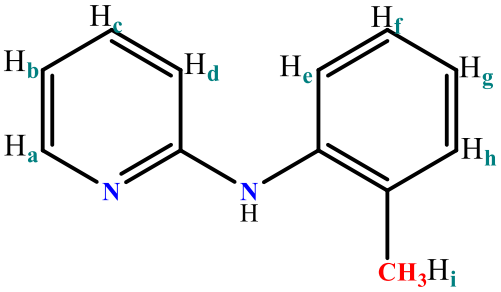

L2. 2-Bromopyridine (10.0 g, 6.04 mL, 54.3 mmol) and 2-methylaniline (11.6 g, 9.82 mL, 109 mmol. **Yield**: 5.71 g (57%). **Melting point**: 87 - 88°C (decomposition). **FT-IR (ATR)** (ν_{max}.cm^{-1}): 3091 (ν_{asym}, N – H), 3064 (ν_{sym}, N – H), 2924 (ν_s, C – H), 1592 (ν_s, C = N), 1580 (ν_s, C = C), 1438 (ν_s, C – H). **MS (LC, *m/z*)** = Calculated: 184.1000, Found: 185.20 [M + H]$^+$. **Purity (LC)**: 100% (t_R = 0.266 min.). **^{1}H NMR (399.95 MHz, CDCl$_3$, ppm)**: 8.18 (ddd, $^3J_{HH}$ = 5.0 Hz, $^4J_{HH}$ = 2.0 Hz, $^4J_{HH}$ = 0.9 Hz, 1H, H$_a$), 7.48 - 7.41 (m, 2H, H$_{c,d}$), 7.24 - 7.18 (m, 2H, H$_e$,H$_g$), 7.20 (td, $^3J_{HH}$ = 7.4 Hz, $^4J_{HH}$ = 1.4 Hz, 1H, H$_f$), 6.70 (ddd, $^3J_{HH}$ = 7.2 Hz, $^3J_{HH}$ = 5.0 Hz, $^4J_{HH}$ = 0.9 Hz 1H, H$_b$), 6.65 (dt, $^3J_{HH}$ = 8.4 Hz, $^4J_{HH}$ = 0.9 Hz, 1H, H$_h$), 6.29 (broad s, 1H, H$_{N-}$

$_H$), 2.28 (s, 3H, H_i). **$^{13}C\{^1H\}$ NMR (100.65 MHz, $CDCl_3$, ppm)**: δ 156.87, 148.53 (C_a), 138.50, 137.65 (C_d), 131.39, 131.04 (C_e), 126.78 (C_g), 124.40 (C_f), 122.94 (C_d), 114.64 (C_b), 107.51 (C_h), 30.87 (C_i).

4-methyl-anilinopyridinate [H(4-CH_3)ap] (**L3**)

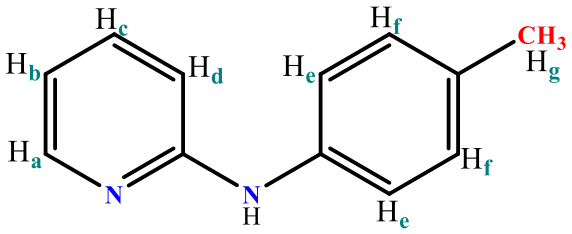

L3. 2-Bromopyridine (8.58 g, 5.18 mL, 54.3 mmol) and 4-methylaniline (11.6 g, 12.0 mL, 109 mmol). **Yield**: 4.89 g (49%). **Melting point**: 108 - 109°C (decomposition). **FT-IR (ATR)** (ν_{max}.cm^{-1}): 3090 (ν_{asym}, N – H), 3063 (ν_{sym}, N – H), 2854 (ν_s, C – H), 1594 (ν_s, C = N), 1510 (ν_s, C = C), 1438 (ν_s, C – C). **MS (LC, *m/z*)** = Calculated: 184.1000, Found: 185.10 $[M + H]^+$. **Purity (LC)**: 100% (t_R = 0.986 min.). **^1H NMR (399.95 MHz, $CDCl_3$, ppm)**: δ 8.18 (ddd, $^3J_{HH}$ = 5.0 Hz, $^4J_{HH}$ = 1.9 Hz, $^4J_{HH}$ = 0.9 Hz, 1H, H_a), 7.45 (ddd, $^3J_{HH}$ = 8.4 Hz, $^3J_{HH}$ = 7.1 Hz, $^4J_{HH}$ = 1.9 Hz, 1H, H_c), 7.23 - 7.19 (m, 2H, H_e), 7.16 - 7.12 (m, 2H, H_f), 6.81 (dt, $^3J_{HH}$ = 8.4 Hz, $^4J_{HH}$ = 1.0 Hz, 1H, H_d), 6.69 (ddd, $^3J_{HH}$ = 7.2 Hz, $^3J_{HH}$ = 5.0 Hz, $^4J_{HH}$ = 0.9 Hz, 1H, H_b), 6.61 (broad s, 1H, H_{N-H}), 2.33 (s, 3H, H_g). **$^{13}C\{^1H\}$ NMR (100.65 MHz, $CDCl_3$, ppm)**: δ 156.64, 148.40 (C_a), 137.84, 137.57 (C_c), 132.79, 129.83 (2C, C_e), 121.27 (2C, C_f), 114.61 (C_b), 107.73 (C_d), 20.76 (C_g).

2,4-dimethyl-anilinopyridinate [H(2,4-$(CH_3)_2$ap] (**L4**)

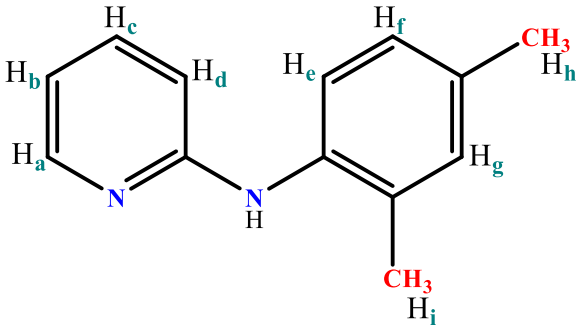

L4. 2-Bromopyridine (8.06 g, 4.86 mL, 51.0 mmol) and 2,4-dimethylaniline (12.4 g, 12.6 mL, 102 mmol). **Yield**: 2.92g (29%). **Melting point**: 79 °C (decomposition). **FT-IR (ATR)**

(ν_{max}.cm^{-1}): 3089 (ν_{asym}, N-H), 2950 (ν_{asym}, C-H), 2918 (ν_{sym}, C-H), 1593 (ν_{s}, C=N), 1519, 1501 ($\nu_{s,}$ C=C), 1436 (ν_{s}, C-H). **MS (LC, *m/z*)** = Calculated: 198.1157, Found: 199.20 [M + H]$^{+}$. **Purity (LC)**: 100% (t_R = 0.489 min.). **^{1}H NMR (399.95 MHz, CDCl$_3$, ppm)**: δ 8.07 (ddd, $^{3}J_{HH}$ = 5.0 Hz, $^{4}J_{HH}$ = 2.0 Hz, $^{4}J_{HH}$ = 0.9 Hz, 1H, H$_a$), 7.33 (ddd, $^{3}J_{HH}$ = 8.7 Hz, $^{3}J_{HH}$ = 7.1 Hz, $^{4}J_{HH}$ = 1.9 Hz, 1H, H$_c$), 7.19 - 7.15 (m, 1H, H$_f$), 7.00 - 6.91 (overlapping m, 2H, H$_{h/e}$), 6.58 (ddd, $^{3}J_{HH}$ = 7.2 Hz, $^{3}J_{HH}$ = 5.0 Hz, $^{4}J_{HH}$ = 1.0 Hz, 1H, H$_b$), 6.45 (dt, $^{3}J_{HH}$ = 8.4 Hz, $^{4}J_{HH}$ = 1.0 Hz, 1H, H$_d$), 6.20 (broad s, 1H, H$_{N-H}$), 2.24 (s, 3H, H$_g$), 2.15 (s, 3H, H$_i$). **^{13}C{^{1}H} NMR (100.65 MHz, CDCl$_3$, ppm)**: *δ* 157.45, 148.45 (C$_a$), 137.61 (C$_c$), 135.74, 134.55, 132.36, 131.73 (C$_h$), 127.39 (C$_e$), 124.19 (C$_f$), 114.18 (C$_b$), 107.04 (C$_d$), 20.84 (C$_g$), 17.88 (C$_i$).

2,6-dimethyl-anilinopyridinate [H(2,6-(CH$_3$)$_2$ap] (**L5**)

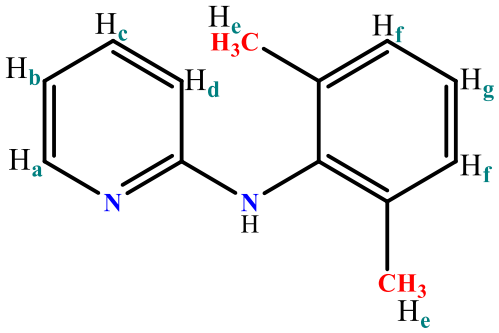

L5. 2-Bromopyridine (3.984 g, 2.40 mL, 25.2 mmol) and 2,6-dimethylaniline (6.11 g, 6.21 mL, 50.4 mmol). **Yield**: 1.84 g (37%). **Melting point**: 122 °C (decomposition). **FT-IR (ATR)** (ν_{max}.cm^{-1}): 3088 (ν_{asym}, N-H), 3064 (ν_{sym}, N-H), 2958 (ν_{asym}, C-H), 2924 (ν_{sym}, C-H), 1589 (ν_{s}, C=N), 1450 (ν_{s}, C=C), 1436 (ν_{s}, C-C), 1322 (ν_{s}, C-H). **MS (LC, *m/z*)** = Calculated: 198.1157, Found: 199.20 [M +H]$^{+}$. **Purity (LC)**: 100% (t_R = 0.353 min.). **^{1}H NMR (399.95 MHz, CDCl$_3$, ppm)**: *δ* 8.17 (ddd, $^{3}J_{HH}$ = 5.0 Hz, $^{4}J_{HH}$ =1.9 Hz, $^{4}J_{HH}$ = 0.9 Hz, 1H, H$_a$), 7.36 (ddd, $^{3}J_{HH}$ = 8.4 Hz, $^{4}J_{HH}$ = 7.2 Hz, $^{4}J_{HH}$ = 1.9 Hz, 1H, H$_c$), 7.14 - 7.12 (d, ^{4}J = 0.8 Hz, 3H, H$_{f/g}$), 6.63 (ddd, $^{3}J_{HH}$ = 7.2 Hz, $^{4}J_{HH}$ = 5.0 Hz, $^{4}J_{HH}$ = 1.0 Hz, 1H, H$_d$), 6.17 (broad s, 1H, H$_{N-H}$), 6.03 (dt, $^{3}J_{HH}$ = 8.4 Hz, $^{4}J_{HH}$ = 1.0 Hz, 1H, H$_b$), 2.26 (s, 6H, H$_e$). **^{13}C{^{1}H} NMR (100.65 MHz, CDCl$_3$, ppm)**: *δ* 157.81, 148.47 (C$_a$), 137.79 (C$_c$), 136.77, 136.47, 128.56 (3C, 2C$_f$ and C$_g$), 126.77, 113.66 (C$_d$), 113.46 (C$_d$), 105.70 (C$_b$), 18.33 (C$_e$).

2,4,6-trimethyl-anilinopyridinate [H(2,4,6-$(CH_3)_3$ap] (**L6**)

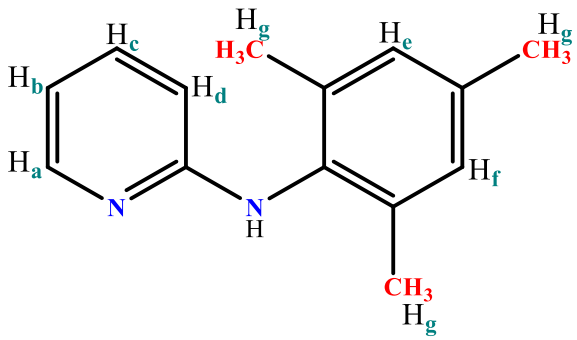

L6. 2-Bromopyridine (790 mg, 0.82 mL, 10.0 mmol) and 2,4,6-trimethylaniline (2.70 g, 2.80 mL, 20.0 mmol). **Yield**: 1.50g (71%). **Melting point**: 127 - 128 °C (decomposition). **FT-IR (ATR)** (ν_{max}.cm^{-1}): 3090 (ν_{asym}, N-H), 3070 (ν_{sym}, N-H), 2956 (ν_{asym}, C-H), 2918 (ν_{sym}, C-H), 1593 (ν_s, C=N), 1453 (ν_s, C=C), 1437 (ν_s, C=C), 1325 (ν_s, C-H). **MS (LC, *m/z*)** = Calculated: 212.1313, Found: 212.30 $[M + H]^+$. **Purity (LC)**: 100% (t_R = 0.610 min.). **^{1}H NMR (399.95 MHz, $CDCl_3$, ppm)**: δ 8.13 (ddd, $^3J_{HH}$ = 5.0 Hz, $^4J_{HH}$ = 1.9 Hz, $^4J_{HH}$ = 0.9 Hz, 1H, H_a), 7.35 (ddd, $^4J_{HH}$ = 8.5, $^3J_{HH}$ = 7.1 Hz, $^3J_{HH}$ = 1.9 Hz, 1H, H_c), 6.95 (h, $^4J_{HH}$ = 0.7 Hz, 2H, H_f), 6.61 (ddd, $^3J_{HH}$ = 7.2 Hz, $^4J_{HH}$ = 5.0 Hz, $^4J_{HH}$ = 1.0 Hz, 1H, H_c), 6.09 (broad s, 1H, H_{N-H}), 6.00 (dt, $^3J_{HH}$ = 8.4 Hz, $^4J_{HH}$ = 0.9 Hz, 1H, H_d), 2.31 (s, 3H, H_g), 2.21 (s, 6H, H_e). **^{13}C{^{1}H} NMR (100.65 MHz, $CDCl_3$, ppm)**: δ 158.08, 148.45 (C_a), 137.74 (C_c), 136.59, 136.41, 133.81, 129.24 (2C_f), 113.46 (C_b), 105.62 (C_d), 20.91 (3C, C_g), 18.22 (6C, C_e).

2-fluoro-anilinopyridinate [H(2-F)ap] (**L7**)

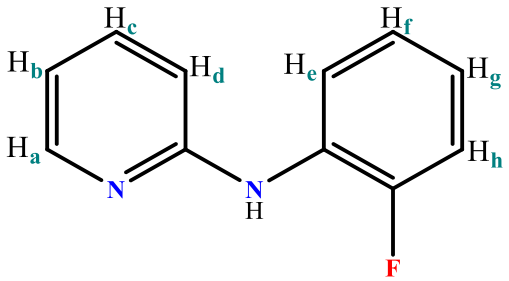

L7. 2-Bromopyridine (4.36 g, 2.63 mL, 27.6 mmol) and 2-fluoroaniline (6.13 g, 5.33 mL, 55.2 mmol). **Yield**: 2.90 g (58%). **Melting point**: 85 - 87°C (decomposition). **FT-IR (ATR)** (ν_{max}.cm^{-1}): 3091 (ν_{sym}, N – H), 2977 (ν_{asym}, C – H), 2935 (ν_{sym}, C – H), 1660 (ν_s, C = N), 1533 (ν_s, C = C), 1438 (ν_s, C – C). **MS (LC, *m/z*)** = Calculated: 188.0750, Found: 189.20 $[M + H]^+$. **Purity (LC)**: 100% (t_R = 0.270 min.). **^{1}H NMR (399.95 MHz, $CDCl_3$, ppm)**: δ 8.23 (ddd, $^3J_{HH}$

= 5.0 Hz, $^4J_{HH}$ = 2.0 Hz, $^4J_{HH}$ = 0.9 Hz, 1H, H_a), 8.00 (td, $^3J_{HH}$ = 8.2 Hz, $^4J_{HH}$ = 1.5 Hz, 1H, Hc), 7.54 - 7.50 (m, 1H, H_b), 7.14 - 7.07 (m, 2H, $H_{h,e}$), 6.99 - 6.93 (m, 1H, H_f), 6.81 - 6.76 (m, 2H, $H_{d,g}$), 6.64 (broad s, 1H, H_{N-H}). **$^{13}C\{^1H\}$ NMR (100.65 MHz, $CDCl_3$, ppm)**: δ 155.28, 154.68, 152.27, 148.15 (C_a), 134.65 (C_b), 124.36 (C_h), 122.32 (C_f), 120.83 (C_c), 115. 5737 (C_g), 115.35 (C_e), 109.43 (C_d).

4-fluoro-anilinopyridinate [H(4-F)ap] (**L8**)

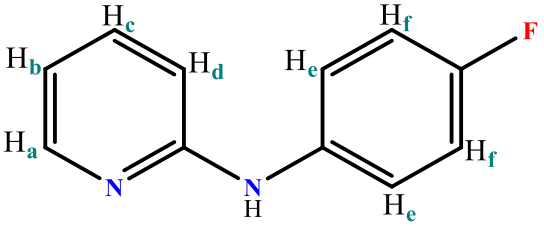

L8. 2-Bromopyridine (4.18 g, 2.53 mL, 26.6 mmol) and 4-fluoroaniline (5.90 g, 5.03 mL, 53.2 mmol). **Yield**: 2.95 g (59%). **Melting point**: 121.8 - 123.4°C (decomposition). **FT-IR (ATR)** (ν_{max}.cm^{-1}): 3097 (ν_{asym}, N – H), 3078 (ν_{sym}, N – H), 3024 (ν_s, C – H), 2978 (ν_s, C – H), 1587 (ν_s, C = N), 1580 (ν_s, C = C), 1439 (ν_s, C – C). **MS (LC, *m/z*)** = Calculated: 188.0750, Found 189.20 $[M + H]^+$. **Purity (LC)**: 100% (t_R = 0.244 min.). **^1H NMR (399.95 MHz, $CDCl_3$, ppm)**: δ 8.16 - 8.14 (m, 1H, H_a), 7.49 (ddd, $^3J_{HH}$ = 8.5 Hz, J_{HH} = ^{3}7.4 Hz, J_{HH} = ^{4}1.9 Hz, 1H, H_c), 7.32 - 7.28 (m, 2H, H_f), 7.05 - 7.01 (m, 2H, H_e), 6.81 (broad s, 1H, H_{N-H}), 6.74 - 6.71 (m, 2H, H_d, H_b). **$^{13}C\{^1H\}$ NMR (100.65 MHz, $CDCl_3$, ppm)**: δ 160.35, 157.94, 156.22, 147.58 (C_a), 138.15 (C_c), 123.18-123.10 (2C_f), 116.09-115.70 (2C_e), 114.81 (C_d), 108.15 (C_b).

3.4.4 General synthetic procedure of the precursor, $[Ru_2(O_2CCH_3)_4Cl]$

The precursor complex $[Ru_2(O_2CCH_3)_4Cl]$ was synthesized according to a modified literature procedure.[1,46] Briefly, $RuCl_3 \cdot 3H_2O$ (1.00 g, 7.69 mmol) was added to a mixture of acetic anhydride (13.0 g, 0.13 mol, 12.0 mL) and glacial acetic acid (46.2 g, 0.77 mol, 44.0 mL) to which anhydrous LiCl (0.20 g, 4.70 mmol) was added. The solution was refluxed overnight. The product was filtered *via* suction, washed with minimal amounts of diethyl ether, dried *in vacuo* and isolated as a brown powder.

[$Ru_2(O_2CCH_3)_4Cl$]

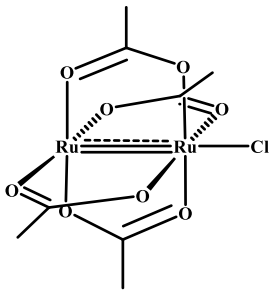

[$Ru_2(O_2CCH_3)_4Cl$]. **Yield**: 63.0 mg (63%). **FT-IR (ATR)** (ν_{max}.cm^{-1}): 1476 (ν_{asym}, COO), 1394 (ν_{sym}, COO), 1342 (ν_{sym}, COO), 685 (δ, COO). **UV-vis** spectrum in CH_3OH [λ_{max}, nm (ε x 10^{-4}, $Lmol^{-1}cm^{-1}$)]: 232 (0.17), 334 (0.14), 424 (0.003). **MS (HR-ESI, *m/z*)**: Calculated: 473.7678 $[C_8H_{12}O_8Ru_2Cl]^+$ $([M+H])^+$, 438.3148 $[C_8H_{12}O_8Ru_2]^+$ $([M-Cl])^+$; Found: 438.8630 $[C_8H_{12}O_8Ru_2]^+$ $([M-Cl])^+$. **Elemental Analysis** for $[C_8H_{12}O_8Ru_2Cl]$ (473.7678 g/mol): Calculated (%): C, 20.28; H, 2.55. Found (%): C, 20.99; H, 2.44.

3.4.5 General synthetic procedure of mixed ligand mono-substituted anilinopyridinatotriacetatochlorodiruthenium(II, III) complexes, $[Ru_2(O_2CCH_3)_3$(R-ap)Cl] (**C1** - **C8**).

$[Ru_2(O_2CCH_3)_4Cl]$ (1 equiv.) was placed in a round bottom flask (250 mL) equipped with a magnetic stirrer bar, followed by the addition of methanol (40 mL) and stirred. The reaction mixture was refluxed to dissolve the precursor $[Ru_2(O_2CCH_3)_4Cl]$. The R-ap ligand (1 equiv.) was dissolved in methanol (10 mL) in a separate round bottom flask and added dropwise to the reaction mixture. The mixture slowly changed colour from light brown to an emerald-green solution, and then eventually to a dark blue colour. Triethylamine (6 equiv.) was added dropwise to the refluxing reaction mixture to deprotonate the respective R-ap ligand. LiCl (6 equiv.) was added in excess to the refluxing reaction mixture to favour and ensure the axial ligation of the chloride. The progress of the reaction was monitored on TLC silica. After 4 hours the reaction was cooled to room temperature and the solvent was removed on a rotary evaporator. The residual compound was dissolved in dichloromethane (3 x 5 mL) and filtered off *via* suction to remove the unreacted precursor $[Ru_2(O_2CCH_3)_4Cl]$. The filtrate compound was subjected to column chromatography with hexane/ethyl acetate (3:7) as the eluent. The blue major product band observed on the column was isolated and the solvent was removed *in vacuo*. The desired products were concentrated with dichloromethane and layered with pentane to give dark blue microcrystals.

[$Ru_2(O_2CCH_3)_3$(ap)Cl] ***(C1)***

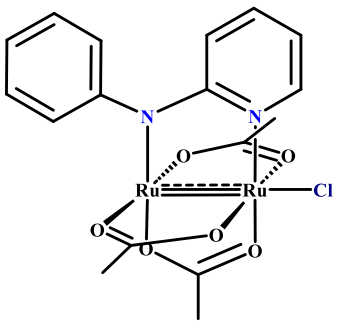

C1. **Yield**: 66.0 mg (66%). **R_f value (3:7 hexane: EtOAc)**: 0.25. **FT-IR (ATR)** (ν_{max}.cm^{-1}): 2921 (ν_{asym}, C – H), 2852 (ν_{sym}, C – H), 1603 (ν_s, C = N), 1504 (ν_{asym}, COO), 1484 (ν_{sym}, COO), 1422 (ν_s, C=O), 1347 (ν_s, C=C), 687.66 (δ_s, OCO), 655.94 (δ_s, OCO). **MS (HR-ESI, *m/z*)**: Calculated: 583.9302 $[C_{17}H_{18}N_2O_6Ru_2Cl]^+$ ($[M+H]^+$), 548.4772 $[C_{17}H_{18}N_2O_6Ru_2]^+$ ($[M-Cl]^+$); Found: 583.8955 $[C_{17}H_{18}N_2O_6Ru_2Cl]^+$ ($[M+H]^+$), 548.9274 $[C_{17}H_{18}N_2O_6Ru_2]^+$ ($[M-Cl]^+$). **UV-Vis** spectrum in CH_2Cl_2 [λ_{max}, nm (ε x 10^{-4}, $Lmol^{-1}cm^{-1}$)]: 306 (0.02), 412 (0.003), 582 (0.01), 654 (0.01). **Magnetic moment**: 3.50 μ_B at 293 K.

*[$Ru_2(O_2CCH_3)_3$(2-CH_3ap)Cl]****(C2)***

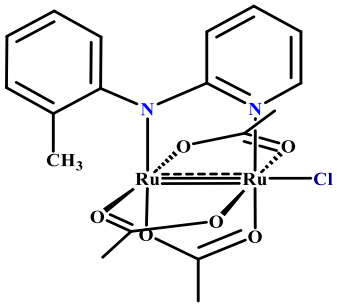

C2. **Yield**: 207 mg (83%). **R_f value (3:7 hexane: EtOAc)**: 0.21. **FT-IR (ATR)** (ν_{max}.cm^{-1}): 2962 (ν_{asym}, C – H), 2924 (ν_{sym}, C – H), 1603 (ν_s, C = N), 1506 (ν_{asym}, COO) 1486 (ν_{sym}, COO), 1421 (ν_s, C=O), 1346 (ν_s, C=C), 688 (δ_s, OCO). **MS (HR-ESI, *m/z*)**: Calculated: 597.9570 $[C_{18}H_{20}N_2O_6Ru_2Cl]^+$ ($[M+H]^+$), 562.5040 $[C_{18}H_{20}N_2O_6Ru_2]^+$ ($[M-Cl]^+$); Found: 563.9435 $[C_{18}H_{20}N_2O_6Ru_2]$ $([M-Cl])^+$. **UV-Vis** spectrum in CH_2Cl_2 [λ_{max}, nm (ε x 10^{-4}, $Lmol^{-1}cm^{-1}$)]: 307 (0.37), 422 (0.66), 602 (0.13), 653 (0.11).

*$[Ru_2(O_2CCH_3)_3(4\text{-}CH_3ap)Cl]$ (**C3**)*

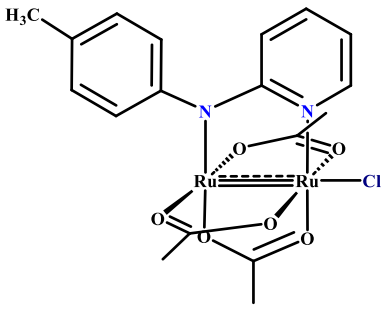

C3. **Yield**: 43.5 mg (54%). **R_f value (3:7 hexane: EtOAc)**: 0.21. **FT-IR (ATR)** (ν_{max}.cm^{-1}): 2931 (ν_{asym}, C – H), 2870 (ν_{sym}, C – H), 1602 (ν_s, C = N), 1517 ($\nu_{asym\ sh}$, COO), 1505 (ν_{sym}, COO), 1424 (ν_s, C=O), 1349 (ν_s, C=C), 688 (δ_s, OCO). **MS (HR-ESI, *m/z*)**: Calculated: 597.9570 $[C_{18}H_{20}N_2O_6Ru_2Cl]^+$ ($[M+H]^+$), 562.5040 $[C_{18}H_{20}N_2O_6Ru_2]^+$ ($[M\text{-}Cl]^+$). Found: 562.9424 $[C_{18}H_{20}N_2O_6Ru_2]^+$ $([M\text{-}Cl])^+$. **UV-Vis** spectrum in CH_2Cl_2 [λ_{max}, nm (ε x 10^{-4}, Lmol^{-1}cm^{-1})]: 304 (0.10), 418 (0.02), 578 (0.03), 660 (0.03). **Magnetic moment**: 3.66 μ_B at 293 K.

*$[Ru_2(O_2CCH_3)_3(2,4\text{-}CH_3ap)_2Cl]$ (**C4**)*

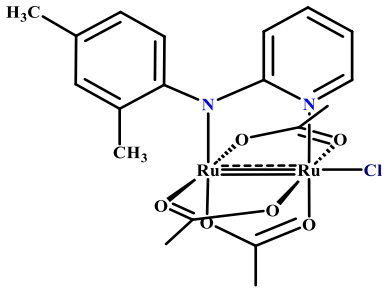

C4. **Yield**: 36.7 mg (45%). **R_f value (3:7 hexane: EtOAc)**: 0.26. **FT-IR (ATR)** (ν_{max}.cm^{-1}): 2922 (ν_{sym}, C – H), 2852 (ν_{sym}, C -H), 1603 (ν_s, C=N), 1493 (ν_{sym}, COO), 1424 (ν_s, C=O), 1349 (ν_s, C=C), 763 (δ_s, OCO), 688 (δ_s, OCO). **MS (HR-ESI, *m/z*)**: Calculated: 611.9838 $[C_{19}H_{22}N_2O_6Ru_2Cl]^+$ ($[M+H]^+$), 576.5308 $[C_{19}H_{22}N_2O_6Ru_2]^+$ ($[M\text{-}Cl]^+$); Found 577.8895 $[C_{19}H_{22}N_2O_6Ru_2]^+$ ($[M\text{-}Cl]^+$). **UV-Vis** spectrum in CH_2Cl_2 [λ_{max}, nm (ε x 10^{-4}, Lmol^{-1}cm^{-1})]: 424 (0.10), 590 (0.09), 668 (0.07), 962 (0.03). **Magnetic moment**: 3.37 μ_B at 293 K.

*$[Ru_2(O_2CCH_3)_3(2,6\text{-}CH_3ap)_2Cl]$ (**C5**)*

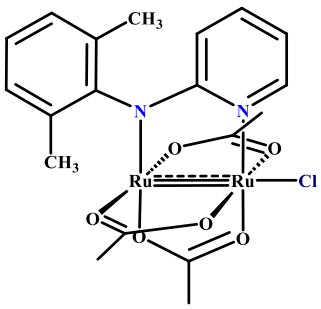

C5. **Yield**: 42.0 mg, (68%). **R_f value (3:7 hexane: EtOAc)**: 0.20. **FT-IR (ATR)** (ν_{max}.cm^{-1}): 2921 (ν_{asym}, C – H), 2852 (ν_{sym}, C – H), 1603 (ν_s, C=N), 1493 (ν_{sym}, COO), 1424 (ν_s, C=O), 1349 (ν_m, C=C), 762 (δ_s, OCO), 687 (δ_s, OCO). **MS (HR-ESI, *m/z*)**: Calculated: 611.9838 $[C_{19}H_{22}N_2O_6Ru_2Cl]^+$ ($[M+H]^+$), 576.5308 $[C_{19}H_{22}N_2O_6Ru_2]^+$ ($[M\text{-}Cl]^+$); Found: 577.8892 $[C_{19}H_{22}N_2O_6Ru_2]^+$ ($[M\text{-}Cl]^+$). **UV-Vis** spectrum in CH_2Cl_2 [λ_{max}, nm (ε x 10^{-4}, Lmol^{-1}cm^{-1})]: 423 (0.04), 597 (0.06), 647 (0.06), 946 (0.01). **Magnetic moment**: 3.42 μ_B at 293 K.

*$[Ru_2(O_2CCH_3)_3(2,4,6\text{-}CH_3ap)_3Cl]$ (**C6**)*

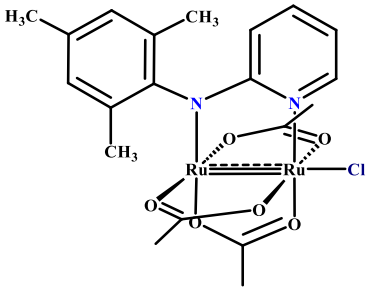

C6. **Yield**: 44.0 mg, (44%). **R_f value (3:7 hexane: EtOAc)**: 0.14. **FT-IR (ATR)** (ν_{max}.cm^{-1}): 2921 (ν_{asym}, C – H), 2856 (ν_{sym}, C – H), 1603 (ν_s, C=N), 1508 (ν_{sym}, COO), 1424 (ν_s, C=O), 1346 (ν_m, C=C), 794 (δ_s, OCO), 689 (δ_s, OCO). **MS (HR-ESI, *m/z*)**: Calculated: 626.0.106 $[C_{20}H_{24}N_2O_6Ru_2Cl]^+$ ($[M+H])^+$, 590.5576 $[C_{20}H_{24}N_2O_6Ru_2]^+$ ($[M\text{-}Cl])^+$; Found: 626.9418 $[C_{20}H_{24}N_2O_6Ru_2Cl]^+$ ($[M+H])^+$, 591.9733 $[C_{20}H_{24}N_2O_6Ru_2]^+$ ($[M\text{-}Cl])^+$. **UV-Vis** spectrum in CH_2Cl_2 [λ_{max}, nm (ε x 10^{-4}, Lmol^{-1}cm^{-1})]: 423 (0.07), 591 (0.07), 668 (0.06), 956 (0.02). **Magnetic moment**: 3.39 μ_B at 293 K.

*$[Ru_2(O_2CCH_3)_3(2\text{-}Fap)Cl]$ (**C7**)*

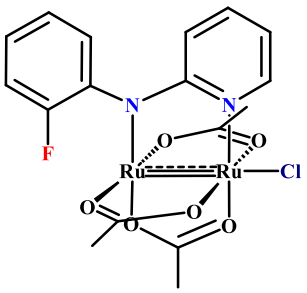

C7. **Yield**: 56.0 mg (70%). **R_f value (3:7 hexane: EtOAc)**: 0.24. **FT-IR (ATR)** (ν_{max}.cm^{-1}): 2958 (ν_{asym}, C – H), 2928 (ν_{sym}, C – H), 1603 (ν_s, C = N), 1490 (ν_{sym}, COO), 1426 (ν_s, C=O), 1350 (ν_m, C=C) 688 (δs, OCO). **ESI-MS** (m/z, fragment): Calculated: 602.9282 $[C_{17}H_{17}N_2O_6Ru_2ClF]^+$ $([M\text{-}Cl])^+$, 567.4752 $[C_{17}H_{17}N_2O_6Ru_2F]^+$ $([M+H])^+$; Found: 567.9189 $[C_{17}H_{17}N_2O_6Ru_2F]^+$ $[(M\text{-}Cl)]^+$. **UV-Vis** spectrum in CH_2Cl_2 [λ_{max}, nm (ε x 10^{-4}, Lmol^{-1}cm^{-1})]: 302 (0.13), 416 (0.02), 576 (0.04), 656 (0.04). **Magnetic moment**: 3.86 μ_B at 293 K.

*$[Ru_2(O_2CCH_3)_3(4\text{-}Fap)Cl]$ (**C8**)*

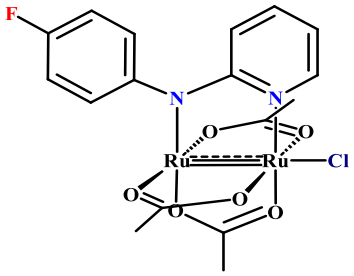

C8. **Yield**: 132 mg (66%). **R_f value (3:7 hexane: EtOAc)**: 0.23. **FT-IR (ATR)** (ν_{max}.cm^{-1}): 2923 (ν_{asym}, C – H), 2852 (ν_{sym}, C – H), 1603 (ν_s, C = N), 1490 (ν_{sym}, COO), 1425 (ν_s, C=O), 1348 (ν_s, C=C) 688 (δ_s, OCO). **ESI-MS** (m/z, fragment): Calculated: 602.9282 $[C_{17}H_{17}N_2O_6Ru_2ClF]^+$ $([M+H])^+$, 567.4752 $[C_{17}H_{17}N_2O_6Ru_2F]^+$ $([M\text{-}Cl])^+$. Found: 567.9159 $[C_{17}H_{17}N_2O_6Ru_2F]^+$ $([M\text{-}Cl])^+$. **UV-Vis** spectrum in CH_2Cl_2 [λ_{max}, nm (ε x 10^{-4}, Lmol^{-1}cm^{-1})]: 304 (0.30), 420 (0.04), 587 (0.08), 653 (0.07). **Magnetic moment**: 4.10 μ_B at 293 K.

3.4.6 X-Ray Crystallography of [(**C1**·OH)·OH_2], [(**C3**·OH_2)]·OH_2·$(CHCl_3)_3$ and [(**C8**·OH_2)]·OH_2·$(CHCl_3)_3$.

Crystals suitable for single-crystal X-ray structural analysis were grown and obtained by the slow evaporation method of a concentrated solvent mixture of **C1** and by a slow diffusion method for complexes **C3** and **C5**, respectively. **C1** was concentrated with dichloromethane and layered with pentane (1:3 ratio, v:v). **C3** and **C5** were grown from a concentrated solution of chloroform and pentane solvent diffusing into the concentrated complex/chloroform mixture (1:3 ratio, v:v). The complex/solvent mixtures could evaporate at room temperature with no exposure to light rays and be left undisturbed to induce single-crystal formation. The structure refinement and crystallographic data are represented in Table 1. Single-crystal X-ray diffraction data were collected on a Bruker KAPPA APEX II DUO diffractometer using graphite-monochromated Mo-Kα radiation (α = 0.71073 Å). Data collection was carried out at 173 (2) K. Temperature was controlled by an Oxford Cryostream cooling system (Oxford Cryostat). Cell refinement and data reduction were performed using the program SAINT.[47] The data were scaled and absorption correction was performed using SADABS. The structures were solved by direct methods using SHELXS-97[48] and refined by full-matrix least-squares methods based on F using SHELXL-2014 and using the graphical interface program X-Seed.[49,50,51] The programs X-Seed[49] and POV-Ray[52] were used to prepare molecular graphic images.

Table 3.9 Crystallographic data and structure refinement parameters for [**C1**·H_2O]·H_2O, [**C3**·H_2O]·H_2O·$(CHCl_3)_3$ and [**C8**·H_2O]·H_2O·$(CHCl_3)_3$.

Empirical formula	$C_{17}H_{22}N_2O_8ClRu_2$	$C_{21}H_{27}N_2O_8Cl_{10}Ru_2$	$C_{20}H_{24}N_2O_8Cl_{20}FRu_2$
F_w(g. mol^{-1})	619.96	992.12	1350.61
Crystal system	triclinic	triclinic	Triclinic
Space group	P-1	P-1	P-1
a/Å	8.5360(6)	10.5933(13)	10.4643(6)
b/Å	10.6627(7)	12.0749(16)	12.6964(8)
c/Å	12.6098(9)	14.8024(19)	14.7321(9)
α/°	97.495(1)	92.817(3)	78.130(2)
β/°	91.922(1)	106.502(2)	73.415(2)
γ/°	108.613(1)	98.592(3)	71.978(2)
Volume/$Å^3$	1074.92(13)	1786.7(4)	1768.97(19)
Z	2	2	2
ρ_{calc}g/cm^3	1.9153	1.8403	1.870
μ/mm^{-1}	1.575	1.636	1.657
Crystal size/mm^3	0.3 × 0.18 × 0.13	0.15 × 0.12 × 0.1	0.130 × 0.100 × 0.080
Crystal colour and shape	Dark blue	Dark blue	Dark blue-purple
Radiation Mo Kα (λ)	0.71073	0.71073	0.71073
2Θ Range/°	3.26 to 56.72	2.88 to 56.66	4.214 to 56.692
Reflections collected	35035	44478	78806
Independent reflections	5363 [R_{int} = 0.0375, R_{sigma} = 0.0247]	8851 [R_{int} = 0.0750, R_{sigma} = 0.0608]	8793 [R_{int} = 0.0652, R_{sigma} = 0.0418]
Goodness-of-fit on F^2	1.040	1.002	1.021
Final R indexes [I>=2σ (I)]	R_1 = 0.0229, wR_2 = 0.0518	R_1 = 0.0429, wR_2 = 0.0918	R_1 = 0.0413, wR_2 = 0.0773
Final R indexes (all data)	R_1 = 0.0283, wR_2 = 0.0545	R_1 = 0.0660, wR_2 = 0.1026	R_1 = 0.0725, wR_2 = 0.0920

3.5 REFERENCES

1 T. A. Stephenson and G. Wilkinson, *J. Inorg. Nucl. Chem.*, 1966, **28**, 2285–2291.

2 M. J. Bennett, K. G. Caulton and F. A. Cotton, *Inorg. Chem.*, 1969, **8**, 1–6.

3 M. A. S. Aquino, *Coord. Chem. Rev.*, 2004, **248**, 1025–1045.

4 M. A. S. Aquino, *Coord. Chem. Rev.*, 1998, **170**, 141–202.

5 A. C. Murillo, F. A. Cotton and A. R. Walton, *Multiple Bonds Between Metal Atoms*, Springer Science and Business media, New York, Boston, Dordrecht, London, Moscow, 3rd edn., 2005.

6 G. Estiú, F. D. Cukiernik, P. Maldivi and O. Poizat, *Inorg. Chem.*, 1999, **38**, 3030–3039.

7 T. Ren, V. DeSilva, G. Zou, C. Lin, L. M. Daniels, C. F. Campana and J. C. Alvarez, *Inorg. Chem. Commun.*, 1999, **2**, 301–304.

8 M. C. Barral, S. Herrero, R. Jiménez-Aparicio, M. R. Torres and F. A. Urbanos, *Inorg. Chem. Commun.*, 2004, **7**, 42–46.

9 W. R. Osterloh, G. Galindo, M. J. Yates, E. Van Caemelbecke and K. M. Kadish, *Inorg. Chem.*, 2020, **59**, 584–594.

10 P. Angaridis, F. A. Cotton, C. A. Murillo, D. Villagrán and X. Wang, *Inorg. Chem.*, 2004, **43**, 8290–8300.

11 F. A. Cotton and A. Yokochi, *Inorg. Chem.*, 1998, **37**, 2723–2728.

12 K. M. Kadish, R. Garcia, T. Phan, J. Wellhoff, E. Van Caemelbecke and J. L. Bear, *Inorg. Chem.*, 2008, **47**, 11423–11428.

13 D. de Oliveira Silva, *Anticancer. Agents Med. Chem.*, 2010, **10**, 312–323.

14 U. Jungwirth, C. R. Kowol, B. K. Keppler, C. G. Hartinger, W. Berger and P. Heffeter, *Antioxid. Redox Signal.*, 2011, **15**, 1085–1127.

15 S. Ngubane, K. M. Kadish, J. L. Bear, E. Van Caemelbecke, A. Thuriere and K. P. Ramirez, *Dalt. Trans.*, 2013, **42**, 3571–3580.

16 T. Hisano, T. Matsuoka, K. Tsutsumi, K. Muraoka and M. Ichikawa, *Chem. Pharm. Bull.*, 1981, **29**, 3706–3712.

17 J. L. Bear, J. Wellhoff, G. Royal, E. Van Caemelbecke, S. Eapen and K. M. Kadish, *Inorg. Chem.*, 2001, **40**, 2282–2286.

18 K. Mashiloane, J. Van Wyk and S. Ngubane, University of the Witwatersrand, Johannesburg, 2018.

19 R. W. Mitchell, A. Spencer and G. Wilkinson, *J. Chem. Soc. Dalt. Trans.*, 1973, 846–854.

20 M. Mukaida, T. Nomura and T. Ishimori, *Bull. Chem. Soc. Jpn.*, 1972, **45**, 2143–2147.

21 K. M. Kadish, M. Nguyen, E. Van Caemelbecke and J. L. Bear, *Inorg. Chem.*, 2006, **45**, 5996–6003.

22 A. R. Chakravarty, F. A. Cotton and D. A. Tocher, *Inorg. Chem.*, 1985, **24**, 172–177.

23 A. R. Corcos, M. D. Roy, M. M. Killian, S. Dillon, T. C. Brunold and J. F. Berry, *Inorg. Chem.*, 2017, **56**, 14662–14670.

24 A. R. Corcos and J. F. Berry, *Dalt. Trans.*, 2017, **46**, 5532–5539.

25 K. M. Kadish, L.-L. Wang, A. Thuriere, E. Van Caemelbecke and J. L. Bear, *Inorg. Chem.*, 2003, **42**, 834–843.

26 K. M. Kadish, L.-L. Wang, A. Thuriere, L. Giribabu, R. Garcia, E. Van Caemelbecke and J. L. Bear, *Inorg. Chem.*, 2003, **42**, 8309–8319.

27 K. M. Kadish, M. Nguyen, E. Van Caemelbecke and J. L. Bear, *Inorg. Chem.*, 2006, **45**, 5996–6003.

28 A. R. Chakravarty and F. A. Cotton, *Inorganica Chim. Acta*, 1986, **113**, 19–26.

29 V. M. Miskowski and H. B. Gray, *Inorg. Chem.*, 1988, **27**, 2501–2506.

30 G. Ribeiro, M. Benadiba, A. Colquhoun and D. de Oliveira Silva, *Polyhedron*, 2008, **27**, 1131–1137.

31 M. Manowong, B. Han, T. R. McAloon, J. Shao, I. A. Guzei, S. Ngubane, E. Van Caemelbecke, J. L. Bear and K. M. Kadish, *Inorg. Chem.*, 2014, **53**, 7416–7428.

32 R. S. Treptow, *J. Chem. Educ.*, 1980, **57**, 417–420.

33 M. Manowong, B. Han, T. R. McAloon, J. Shao, I. A. Guzei, S. Ngubane, E. Van

Caemelbecke, J. L. Bear and K. M. Kadish, *Inorg. Chem.*, 2014, **53**, 7416–7428.

34 M. Nguyen, T. Phan, E. Van Caemelbecke, W. Kajonkijya, J. L. Bear and K. M. Kadish, *Inorg. Chem.*, 2008, **47**, 7775–7783.

35 D. F. Evans, *J. Chem. Soc.*, 1959, 2003–2005.

36 E. M. Schubert, *J. Chem. Educ.*, 2009, **69**, 62.

37 J. G. Norman, G. E. Renzoni and D. A. Case, *J. Am. Chem. Soc.*, 1979, **101**, 5256–5267.

38 F. A. Cotton, V. M. Miskowski and B. Zhong, *J. Am. Chem. Soc.*, 1989, **111**, 6177–6182.

39 J. L. Bear, B. Han, Z. Wu, E. Van Caemelbecke and K. M. Kadish, *Inorg. Chem.*, 2001, **40**, 2275–2281.

40 E. Van Caemelbecke, T. Phan, W. R. Osterloh and K. M. Kadish, *Coord. Chem. Rev.*, 2021, **434**, 1–35.

41 N. Huang, M. M. Siegel, G. H. Kruppa and F. H. Laukien, *J. Am. Soc. Mass Spectrom.*, 1999, **10**, 1166–1173.

42 Á. Molina, E. Laborda, J. M. Gómez-Gil, F. Martínez-Ortiz and R. G. Compton, *Electrochim. Acta*, 2016, **195**, 230–245.

43 A. C. Dema and R. N. Bose, *Inorg. Chem.*, 1989, **28**, 2711–2713.

44 M. Everhart and J. E. Earley, *Polyhedron*, 1988, **7**, 1393–1396.

45 C. Hansch, A. Leo and R. W. Taft, *Chem. Rev.*, 1991, **91**, 165–195.

46 R. L. S. R. Santos, R. van Eldik and D. de Oliveira Silva, *Inorg. Chem.*, 2012, **51**, 6615–6625.

47 G. M. Sheldrick, *Acta Crystallogr. Sect. A Found. Crystallogr.*, 2008, **64**, 112–122.

48 G. M. Sheldrick, *Acta Crystallogr. Sect. C Struct. Chem.*, 2015, **71**, 3–8.

49 L. J. Barbour, *J. Supramol. Chem.*, 2001, **1**, 189–191.

50 J. L. Atwood and L. J. Barbour, *Cryst. Growth Des.*, 2003, **3**, 3–8.

51 L. J. Barbour, *J. Appl. Crystallogr.*, 2020, **53**, 1141–1146.

52 L. W. Finger, M. Kroeker and B. H. Toby, *J. Appl. Crystallogr.*, 2007, **40**, 188–192.

CHAPTER 4

In vitro cytotoxic activity of the lantern type mono-substituted anilinopyridinato triacetatochlorodiruthenium(II, III) complexes against oestrogen receptor-positive MCF-7, triple negative MDA-MB-231 adenocarcinoma and mammary non-malignant epithelial MCF-12A human breast cell lines with preliminary mechanistic studies.

4.1 INTRODUCTION

The lantern-type diruthenium(II, III) complexes of the formula $[Ru_2(O_2CR)_4Cl]$ (where R = CH_3 or CH_2CH_3) have been evaluated for their potential anticancer properties against various tumour cells.[1] These Ru_2^{5+} complexes were among the first to be evaluated for their cytotoxic properties against the P388 leukaemia cells. However, they were poor to moderately soluble in aqueous solutions and therefore further research efforts entailed enhancing the solubility properties through structural modifications. This resulted in the first series of compounds with the chemical formula $[Ru_2(O_2CR)_4L_2]PF_6$, where R is CH_3, and L can be imidazole or 1-methylimidazole or H_2O (represented in Figure 4.1, Series 1). Subsequently, a 2nd series of compounds were synthesized where R is Fc (ferrocenyl) or Fc–CH=CH–CH_3, and L is ethanol (Figure 4.1, Series 2). The modifications in the series 1 and 2 compounds did indeed enhance the solubility properties of the lantern-type diruthenium(II, III) complexes. These compounds were therefore assessed for their cytotoxicity against Hela breast cancer and the multidrug-resistant CoLo 320DM colon cancer cells.[2]

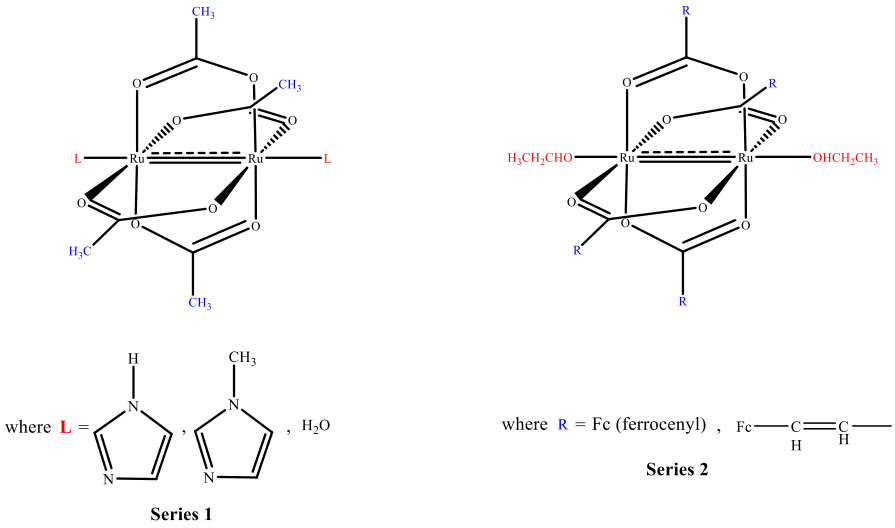

Figure 4.1 Lantern-type diruthenium(II, III) complexes tested for their cytotoxic properties against Hela and the multidrug-resistant CoLo 320DM human cancer cells.[2]

Further investigations focused on the potential anticancer properties of lantern-type Ru_2^{5+} complexes where the Ru_2^{5+} structure was modified through axial ligation or by substitution of the equatorial bridging ligands. The latter included Non-Steroidal Anti-Inflammatory Drugs (NSAID) which were equatorially coordinated to the Ru_2^{5+} cores to form complexes of the

formula $[Ru_2(NSAID)_4Cl]$ (Figure 4.2).[3,4,5] These complexes were evaluated for their antiproliferative against malignant U87MG and A1725 and human glioma cell lines.

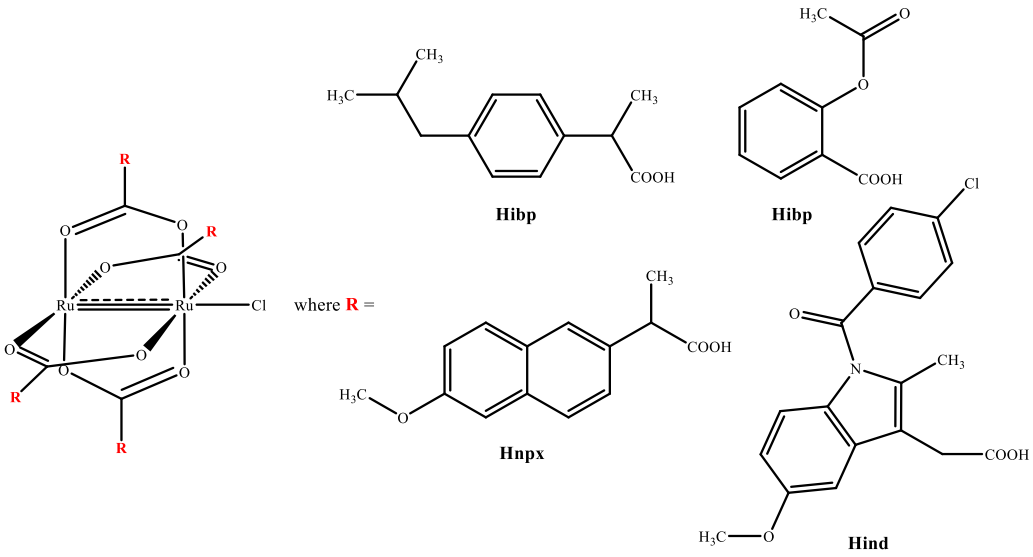

Figure 4.2 Diruthenium(II, III) cores equatorially bridged by non-steroidal anti-inflammatory drugs.[3,4,5]

$[Ru_2(Ibp)_4Cl]$, the lead compound of the class of Ru_2-NSAIDs, showed a dose- and time-dependent decrease in the number of viable p53 wild-type (U87MG and A1725) and mutant (U138MG and U251MG) cells. The p53 wild-type cells were however more sensitive and underwent apoptosis after 72-hour treatment with $[Ru_2(Ibp)_4Cl]$.[4] This metallodrug also exhibited promising antiproliferative properties against the C6 rat glioma cell line and induced the expression levels of the cell cycle regulators p21, p27, p53, BAX and cyclooxygenase 1 (COX1)[6]. Importantly, the same study showed that intraperitoneal (*ip*) injections or chronic Alzet osmotic pump infusion of $[Ru_2(Ibp)_4Cl]$, led to a decrease in tumour size in the C6 rat orthotopic glioma model. In addition, acute and chronic toxicology experimental data suggest that the $[Ru_2(Ibp)_4Cl]$ metallodrug exhibited poor to moderate toxicity effects in normal Wistar rats.[4]

When the Ru_2^{5+} structure of the $[Ru_2(Ibp)_4Cl]$ was modified through axial ligation with a triflate ($CF_3SO_3^-$) which occupies one axial site it resulted in a metallodrug with the chemical formula $[Ru_2(Ibp)_4(CF_3SO_3)]$. Axial ligation with a hexafluorophosphate (PF_6^-) ion, however, resulted in the PF_6^- ion existing as a counterion that balances the overall charge of the complex. This

led to the formation of the complexes $[Ru_2(Ibp)_4(CF_3SO_3)]$ and $[Ru_2(Ibp)_4(CH_3CH_2OH)_2]PF_6$, as represented in Figure 4.3.

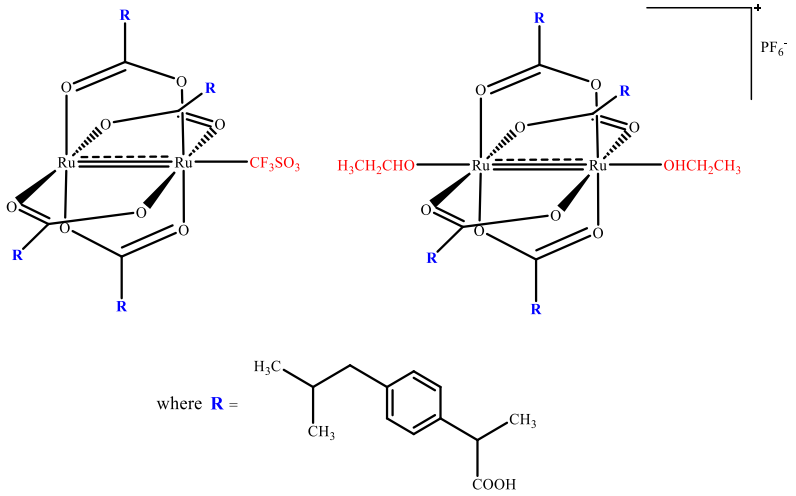

Figure 4.3 Lantern type $[Ru_2(Ibp_4)]^+$ structure with the triflate ($CF_3SO_3^-$) coordinated axially (inner sphere coordination) and hexafluorophosphate (PF_6^-) as a counterion balancing the charge of the $[Ru_2(Ibp_4)]^+$ complex.

The synthesized $[Ru_2(Ibp_4)]^+$ complexes were capable of inhibiting the migration of human glioma U87MG and A172 cell lines. Furthermore, complexes induced apoptosis and significantly decreased the number of mitotic A172 cells. It is for this reason that $[Ru_2(Ibp_4)]^+$ complexes have the potential as future anticancer agents targeting human glioma cells[3]. Indeed, further research efforts were directed at improving the drug delivery system for these compounds.[7]

With much research performed on paddlewheel diruthenium(II, III) complexes and ongoing investigations of their potential anticancer properties, this chapter addresses and evaluates the cytotoxic properties of the synthesized ligands **L1** - **L8** and complexes **C1** - **C8**, reported in the previous chapter. Their short- and long-term cytotoxic properties were assessed by performing cell viability and colony formation assays against human breast MCF-7 and MDA-MB-231 cancer, and the non-malignant mammary MCF-12A epithelial cell lines. **C3** selectively inhibited the cell viability of MCF-7 cells significantly over the MCF-12A cell line. **C3** was further evaluated for its interactions with biological molecules to investigate the mode of action responsible for its cytotoxic properties. This was achieved *via* spectroscopic and analytical techniques.

4.2 RESULTS AND DISCUSSION

4.2.1 In vitro cytotoxic activity: Cell viability assay of ligands **L1** - **L8** and complexes **C1** - **C8** against human breast MCF-7 and MDA-MB-231 cancer, and non-malignant mammary MCF-12A epithelial cell lines.

*4.2.1.1 In vitro cytotoxicity of R-ap ligands, **L1** - **L8***

The preliminary screening for *in vitro* cytotoxicity of R-ap ligands **L1** - **L8** was performed in the human breast MCF-7 and MDA-MB-231, and against the non-malignant mammary MCF-12A epithelial cells. Briefly, all three cell lines were treated at a single dose (100 µM) of each compound or vehicle (DMSO) for 72 hours. Cell viability assays were performed using the MTT colourimetric assay.[8] The percentage of cell viability of human breast cell lines after 72 hours of ligand exposure is herein represented in Figure 4.4.

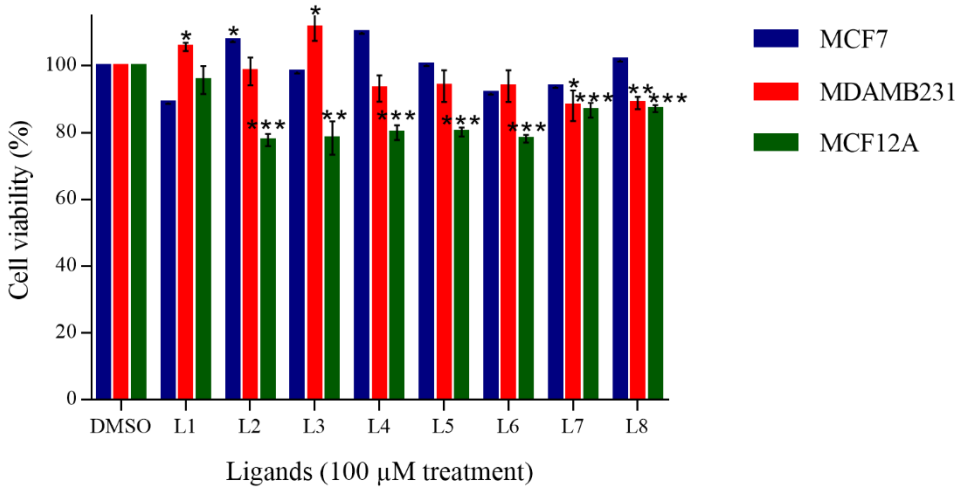

Figure 4.4 *In vitro* cell viability assays: single dose-response treatment (100 µM) after 72-hour exposure with ligands L1 - L8 against human breast MCF-7, MDA-MB-231 and MCF-12A cell lines. GraphPad Prism 7.0 was used for analysis of the data and a parametric unpaired t-test was performed to calculate statistical significance, where *p < 0.05, **p < 0.01, ***p < 0.001.

Table 4.1 represents the percentage cell viability (survival rate) ± SEM after 72 - hours, with experiments conducted in triplicates and each ligand tested in quadruplicate.

Table 4.1 Percentage cell viability (µM ± SEM) screen test for R-ap ligands (**L1 - L8**) against the human breast MCF-7, MDA-MB-231 adenocarcinoma and the non-malignant MCF-12A cell lines.

		100 µM treatment (µM ± SEM)		
anilinopyridiante (ap) ligand (L)	R-substituent	MCF-7	MDA-MB-231	MCF-12A
L1	H	89.09 ± 0.50	105.66 ± 1.23	95.74 ± 4.20
L2	2 – CH_3	107.70 ± 0.58	98.35 ± 4.17	77.75 ± 1.83
L3	4 – CH3	98.29 ± 0.58	111.47 ± 4.04	78.35 ± 5.00
L4	2,4 – $(CH_3)_2$	110.16 ± 1.79	93.20 ± 3.89	79.94 ± 2.20
L5	2,6 – $(CH_3)_2$	100.37 ± 4.34	93.94 ± 4.72	80.14 ± 1.36
L6	2,4,6 – $(CH_3)_3$	91.92 ± 3.60	93.88 ± 4.73	78.15 ± 1.18
L7	2 – F	93.84 ± 3.43	88.01 ± 4.62	86.70 ± 2.22
L8	4 – F	101.87 ± 1.93	88.81 ± 1.85	87.16 ± 1.09

None of the tested ligands caused a significant inhibition of cell viability against the human breast MCF-7 and MDA-MB-231 cells. However, ligands **L2 - L8** significantly inhibited the cell viability of the MCF-12A cells, at 100 µM. **L2**, which has a methyl donating group located on the *ortho*-position of the aniline phenyl ring, inhibited 22.25% of viable MCF-12A cells but did not cause significant inhibition of both breast cancer cell lines. Similarly, the same trend is observed for **L3 - L8** ligands and thus suggesting that the ligands are slightly toxic to the non-malignant MCF-12A cell line. The nature and localization of the substituents (either on the *ortho*- or *para*- positions) on the aniline phenyl ring appears to have a significant impact on the MDA-MB-231 cell viability. Particularly, ligands **L7** and **L8**, possess increased short-term cytotoxic properties against MDA-MB-231 cells compared to ligands with methyl-donating substituents localised either on the *ortho*- or *para*-positions of the aniline ring. To conclude, although the MCF-12A cell line was slightly more sensitive to treatment with **L2 - L8**, the breast cancer cell lines are largely resistant to the ligand treatments.

*4.2.1.2 In vitro cytotoxicity of mono-substituted [$Ru_2(O_2CCH_3)_3$(R-ap)Cl], **C1** - **C8**.*

To evaluate the short-term cytotoxicity of the corresponding complexes **C1** - **C8** *in vitro*, breast cancer cells were treated with a range of concentrations (20 - 100 µM) of complexes and MTT assay experiments were performed. To evaluate their selectivity for breast cancer cells, non-malignant mammary MCF-12A breast epithelial cells were included in these experiments. Figures 4.5 - 4.7 represent the cell viability of MCF-7, MDA-MB-231, and MCF-12A cell lines, respectively.

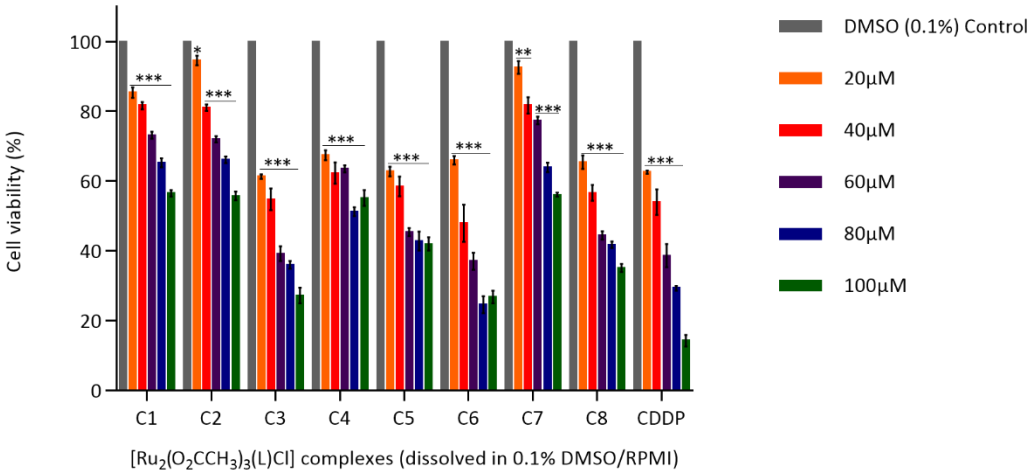

Figure 4.5 Cell survival rate response of oestrogen receptor-positive human breast MCF-7 cell line after 72 - hours of drug exposure with complexes (**C1** - **C8**). GraphPad Prism 7.0 was used to analyse the data and a parametric unpaired t-test was performed, where *p<0.05, **P<0.01 and ***p<0.001 were accepted and considered to be significant. DMSO was used as vehicle control. Cisplatin (CDDP) was used as the positive control compound in assays.

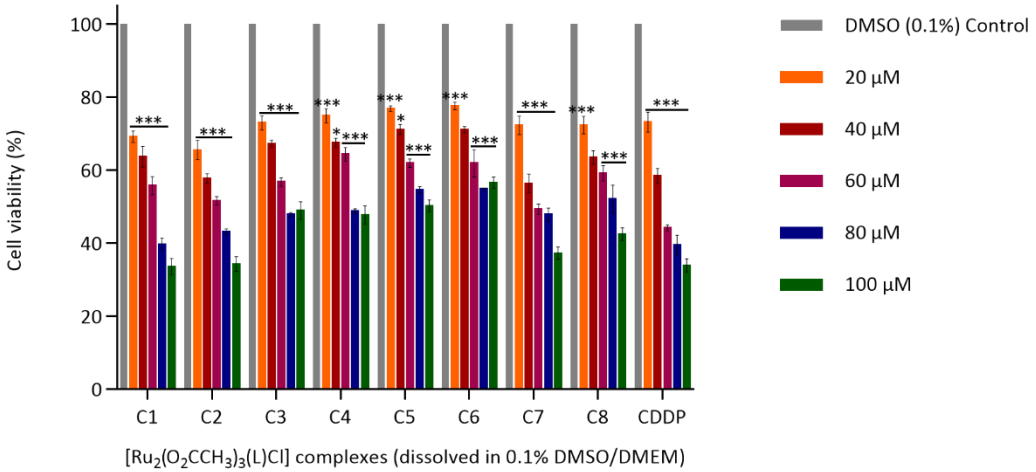

Figure 4.6 Cell survival rate response of triple-negative human breast MDA-MB-231 cell line after 72 - hours of drug exposure with complexes (**C1 - C8**). GraphPad Prism 7.0 was used to analyse the data and a parametric unpaired t-test was performed, where *p<0.05, **P<0.01 and ***p<0.001 were accepted and considered to be significant. DMSO was used as vehicle control. Cisplatin (CDDP) was used as the positive control compound in assays.

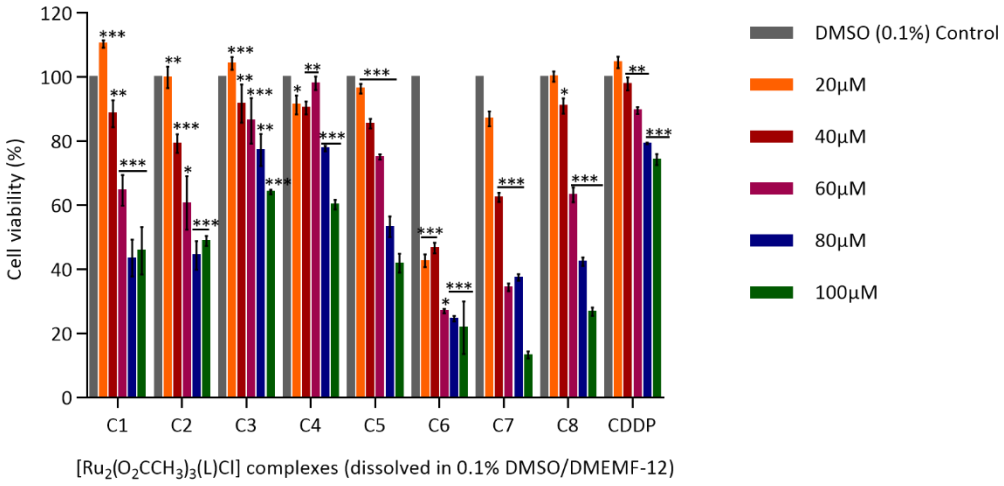

Figure 4.7 Cell survival rate response of epithelial human breast MCF-12A cell line after 72 - hours of drug exposure with complexes (**C1 - C8**). GraphPad Prism 7.0 was used to analyse the data and a parametric unpaired t-test was performed, where *p<0.05, **P<0.01 and ***p<0.001 were accepted and considered to be significant. DMSO was used as vehicle control. Cisplatin (CDDP) was used as the positive control compound in assays.

Dose-response curves (Figure 6.87-Figure 6.89) were obtained from a non-linear regression analysis, with sigmoidal curves fitted using GraphPad Prism version 7.0 software.

As presented from the multidose-response treatments (Figures 4.5 - 4.7), all complexes possess cytotoxic properties and cause a significant dose-dependent inhibition in cell viability of MCF-7, MD-AMB231, and MCF-12A cells after 72-hour treatment. Complexes **C3** and **C8** were the most potent among all complexes and led to a decrease in the survival rate of MCF-7 cells (Figure 4.5) to less than 50% at higher dosages (80 - 100 µM). Additionally, all complexes were able to inhibit MDA-MB-231 viable cells (Figure 4.6), with cells being more sensitive to treatment with complexes **C1**, **C2,** and **C7**. Taken together, these results demonstrate that all complexes under investigation do have potent cytotoxic effects against the breast cancer cell lines. However, when cell viability assays were performed against the non-malignant MCF-12A cell line (Figure 4.7), cells were more sensitive to **C1**, **C2**, **C6** - **C8**. The accumulated results suggest that coordinating the free R-ap ligands to the Ru_2(II, III) metal cores led to enhanced cytotoxic properties of the paddlewheel Ru_2^{5+} complexes of this nature. Additionally, by varying the nature of substituents and ultimately tuning the electronic properties of the investigated complexes, the anticancer properties can be enhanced to achieve the desired therapeutic benefit.

To quantify the short-term cytotoxicity of complexes **C1** - **C8**, half maximal inhibitory concentrations (IC_{50}) values were determined. From these values, the selectivity indices of the complexes were calculated for each breast cancer cell line. In chemotherapy, anticancer agents should be selective towards cancer cells with desirable selectivity indices above 2.0.[9] Compounds are considered selective towards cancer cells when the compound exhibits high cytotoxicity and causes less harm to normal cells.[10,11] In this work, selectivity indices (SI) ≥ 2 were considered acceptable and selective for human breast cancer cells over the MCF-12A cells. Table 4.2 below represents the IC_{50} (µM) ± SEM as calculated and determined from GraphPad Prism v7.0 software and selectivity indices (SI).

Table 4.2 IC_{50} (µM) ± SEM of human breast MCF-7 and MDA-MB-231 cancer and non-malignant mammary MCF-12A epithelial cell lines of $[Ru_2(O_2CCH_3)_3(R\text{-ap})Cl]$ complexes after 72-hour treatment.

Complex	R-substituent attached to the ligand	IC_{50} (µM) ± SEM			$SI^{c/a}$	$SI^{c/b}$
		MCF-7[a]	MDA-MB231[b]	MCF-12A[c]		
C1	H	165 ± 0.14	59.7 ± 0.161	80.1 ± 0.75	0.49	1.34
C2	2 – CH_3	136 ± 0.16	55.5 ± 0.087	81.3 ± 0.48	0.60	1.47
C3	4 – CH_3	39.7 ± 0.13	85.0 ± 0.10	138 ± 1.02	3.47	1.62
C4	2,4 – $(CH_3)_2$	110 ± 0.12	90.9 ± 0.124	110 ±1.23	0.99	1.21
C5	2,6 - $(CH_3)_2$	53.9 ± 0.11	103 ± 0.095	89.5 ± 0.23	1.66	0.87
C6	2,4,6 – (CH3)3	37.0 ± 0.17	119 ± 0.138	21.8 ± 0.16	0.58	0.18
C7	2 – F	152 ± 0.30	60.3 ± 0.11	49.6 ± 0.25	0.33	0.82
C8	4 – F	49.1 ± 0.09	79.3 ± 0.15	72.8 ± 0.26	1.48	0.92
CDDP[a]	-	39.0 ± 0.02	52.2 ± 0.12	151 ± 0.59	3.86	2.89

[a]CDDP = Clinically prepared cisplatin drug, a chemotherapeutic drug used in the treatment of various cancerous cells and used as a positive control in cell viability assays.

IC_{50} = half minimal inhibitory concentration required to inhibit the growth of viable cells by 50%.

[c/a]SI = selectivity index value, calculated as IC_{50} (µM) value of MCF-12A normal cell line divided by the IC_{50} (µM) value of human breast adenocarcinoma MCF-7 (ER +ve) cell line.

[b/a]SI = selectivity index value, calculates as IC_{50} (µM) value of MCF-12A normal cell line divided by the IC_{50} (µM) value of human.

Complexes with SI values ≥ 2 were rendered to be highly selective for cancerous cell lines, while those with SI values 1.5 ≥ SI ≤ 2 were rendered to possess moderate to good selectivity for carcinoma cell lines.

C3, consisting of an IC_{50} value of 39.7µM, is the most potent against the MCF-7 cancer cell line among all the investigated complexes. The complex possesses cytotoxic properties comparable to cisplatin (IC_{50} value of 39.0 µM obtained for MCF-7 cell line). Additionally, **C3** is selective for both cancer cells with favourable selectivity for MCF-7 cells (SI value being 3.47) and moderate selectivity for MDA-MB-231 cells (SI value of 1.62), respectively.

This phenomenon serves as evidence and suggests that **C3** may be associated with minimal or reduced side effects. Most complexes (namely, **C1**, **C2**, **C4**, **C6** and **C7**) were poorly selective for human breast MCF-7 cancer cells, with selectivity indices ranging between 0.33 to 0.60 (Table 2). **C8** shows moderate but promising anticancer properties with IC_{50} values of 49.1 and 72.3 µM obtained when treated against the MCF-7 and MDA-MB-231 cancer cells, respectively. Furthermore, most complexes (**C1**, **C2**, **C4**, and **C7**) were moderately selective for the MDA-MB-231 cancer cell line, with selectivity indices ranging between 0.82 to 1.47. Overall, these results indicate that most complexes show poor to moderate selectivity for both human breast cancer cells and are more cytotoxic to MCF-12A cells. Given that the complexes **C3** and **C8** possessed promising potential anticancer effects and were selective for breast cancer cells, these complexes were further evaluated downstream in the other biological assays.

4.2.2 Colony formation assay experiments.

Many breast cancer cells exhibit intrinsic or acquired resistance to commonly used conventional chemotherapeutic agents and radiation, which often results in their regeneration through proliferation.[12] Thus, the need to formulate effective drugs to inhibit and prevent the recurrence of breast cancers while being selective for tumours over normal cells. Therefore, any prodrug/drug candidate needs to inhibit cellular growth and proliferation of cancer cells long-term.[13] To assess the ability of **C3** and **C8** to inhibit the survival and proliferation of MCF-7 cells and MCF-12A cells, colony formation experiments were performed.[14] The concentration of both complexes was varied at IC_{50} value concentrations namely, ¼ x IC_{50}, IC_{50} and 2 x IC_{50}, where the IC_{50} values were experimentally determined from *in vitro* short-term cell viability assays. Figures 4.8 and 4.9 represent the photographed images of MCF-7 and MCF-12A cell colonies after the removal of **C3** and **C8** drug treatments.

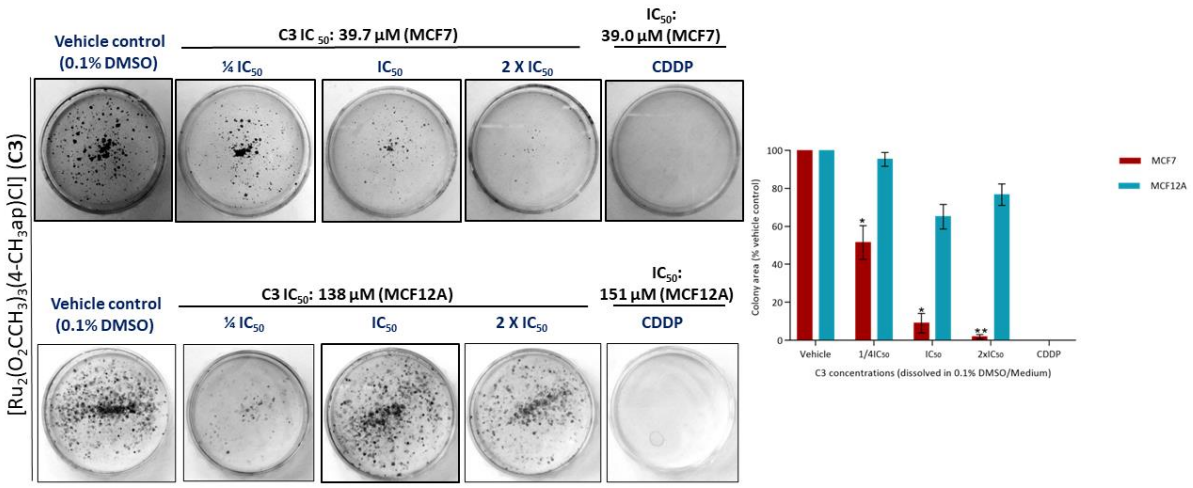

Figure 4.8 Representative images and quantification of MCF-7 and MCF-12A cells treated with vehicle (0.1% DMSO), ¼ IC_{50}, IC_{50} or 2 X IC_{50} concentrations of **C3** for 48 hours. Cells were plated at low densities in a drug-free medium and monitored for 7 days to allow colonies to form. Colonies were stained with crystal violet and images from two independent repeats were quantified using the ImageJ plugin colony area. The graph plotted represents the mean colony area ± SEM of each treatment as a percentage of the vehicle control. GraphPad Prism 7.0 was used to analyse the data and a parametric unpaired t-test was performed, where *p<0.05, **P<0.01 and ***p<0.001 were accepted and considered to be significant.

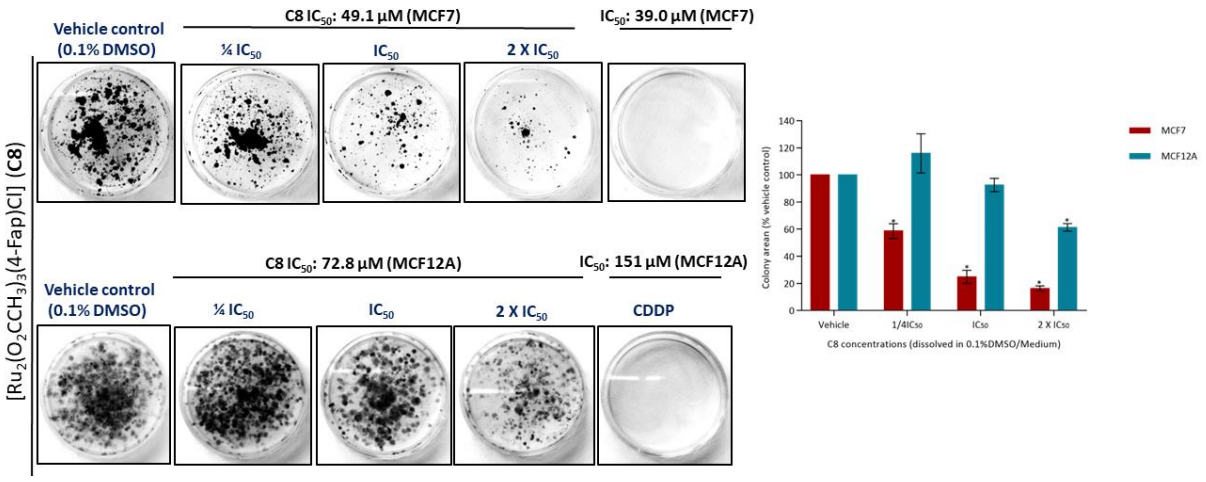

Figure 4.9 Representative images and quantification of MCF-7 and MCF-12A cells treated with vehicle (0.1% DMSO), ¼ IC_{50}, IC_{50} or 2 X IC_{50} concentrations of **C8** for 48 hours. Cells were plated at low densities in a drug-free medium and monitored for 7 days to allow colonies to form. Colonies were stained with crystal violet and images from two independent repeats were quantified using the ImageJ plugin colony area. The graph plotted represents the mean colony area ± SEM of each treatment as a percentage of the vehicle control. GraphPad Prism 7.0 was used to analyse the data and a parametric unpaired t-test was performed, where *p<0.05, **P<0.01 and ***p<0.001 were accepted and considered to be significant.

DMSO was used as the vehicle control and the clinically prepared cisplatin drug (CDDP) was included as positive control. Both complexes caused a dose-dependent inhibition of the long-term survival and proliferation of MCF-7 cancer cells. From Figure 4.8, **C3** treatment against MCF-7 cells resulted in few to no colonies and significantly inhibited long-term survival in a dose-dependent manner at all concentrations tested. Similarly, **C8** significantly hinders the formation of MCF-7 colonies with minimal regeneration and proliferation of MCF-7 cells upon increasing the IC_{50} dosage, as represented in Figure 4.9. Importantly, **C3** and **C8** did not inhibit colony formation in the non-malignant MCF-12A cells. In all trials performed, CDDP inhibited the growth and survival of both MCF-7 cancer and non-malignant MCF-12A cells, thus not showing good selectivity for MCF-7 cancer cells at the tested IC_{50} concentration. Cisplatin and its derivatives such as oxaliplatin and carboplatin are the most widely used anti-tumor agents in the treatment of cancers. However, this line of chemotherapeutic treatment is well known for its horrendous adverse side-effects, severe toxicity and tumour drug resistanceand thus there is a need to develop more efficacious antitumour therapeutic drugs.[15] In these experiments, both **C3** and **C8** treatments were more selective to MCF-7 cancer cells than cisplatin and thus their potential to have minimal toxicity and adverse side effects.

4.2.3 Western blot analyses

To determine whether **C3** induces double-stranded DNA breaks or damage, human breast MCF-7 cancer cells were subjected to 48 and 72 hours of **C3** treatment and protein samples extracted from the above-mentioned cancer cell line were subjected to western blotting with antibodies to ɣ-H2AX (Figure 4.10A and B). The induction of double-stranded DNA breaks can be measured and confirmed by the presence of ɣ-H2AX, a robust marker and variant form of histone directly phosphorylated at Ser139 in response to double-stranded DNA breaks.[16,17]

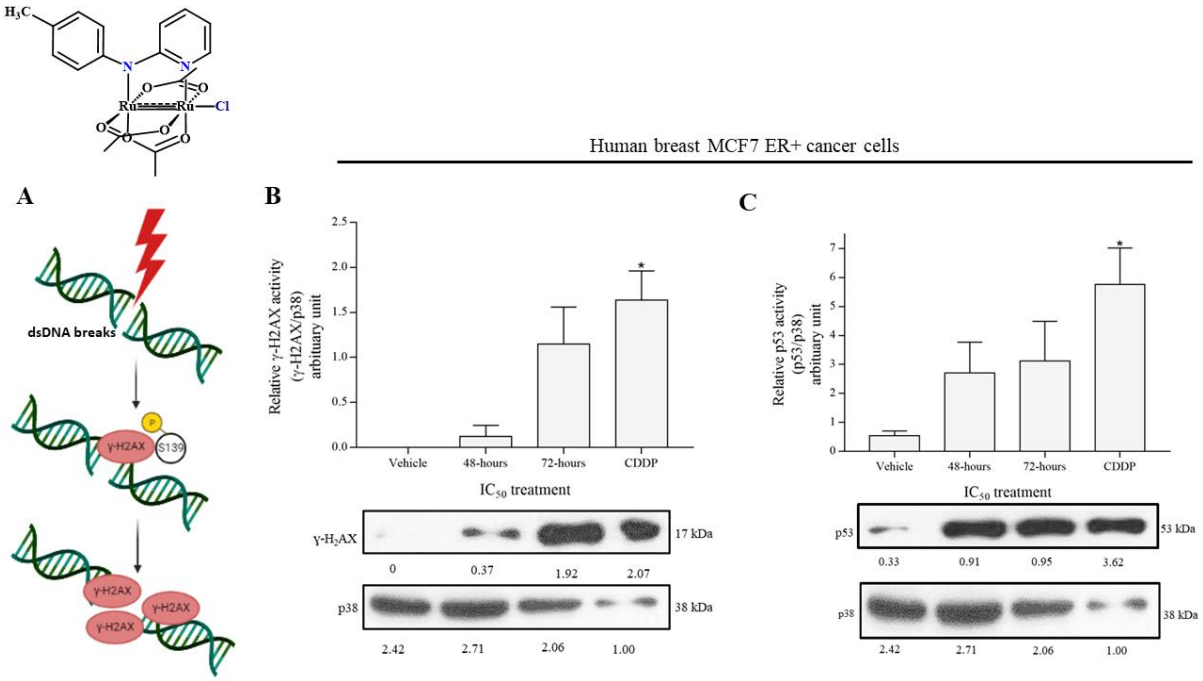

Figure 4.10 **C3** induces double-stranded DNA breaks when MCF-7 cells were subjected to 48 and 72-hour treatment. In all experiments, cisplatin (CDDP) was used as a positive control and cells were subjected to 72-hour treatment. Western blotting analysis with antibodies to ɣ-H2AX (B) and p53 (C) show that **C3** treatment against MCF-7 cells induces a double-stranded DNA damage response. Total p38 was used as a loading control. The expression of each protein was quantified as the densitometry value analysed by ImageJ software and is normalised to p38 levels. The data represent the mean of two independent biological repeats ± SEM. Figure A was redrawn and created using BioRender.com online software.

From the results obtained, MCF-7 cells treated with **C3** display a time-dependent increase in the expression levels of ɣ-H2AX. Thus, this suggests that **C3** activates the canonical double-stranded DNA breaks. To determine whether p53 activation is associated with the mechanism of action of cytotoxicity induced by **C3** treatment, western blotting experiments were

performed (Figure 4.10B). P53 is a tumour suppressor protein and a common transcriptional activator that plays a significant role in mediating cellular response to DNA damage and other cell stress conditions, thus inducing cell cycle arrest and ultimately apoptosis.[18] **C3** treated MCF-7 cells displayed a time-independent increase in expression levels of p53 particularly pronounced after 72-hour of **C3** treatment. This was expected as MCF-7 cells are known to contain to express the wild-type p53. On the other hand, cisplatin (CDDP) positive control induced p53 cell stress greatly compared to the **C3** and vehicle (DMSO) treated cells after 72 hours. Taken together, these results show that **C3** induced double-stranded DNA breaks and induced p53 activation, likely as part of a DNA damage stress signalling pathway in ER+ MCF-7 breast cancer cells. The DNA damage was possibly induced *via* ROS induction. Many Ru(II) metal and organometallic arene complexes are reported to induce ROS in a variety of cancers as a mechanism of action and as a signalling pathway responsible for cancer cell death. For example, cyclometalated Ru(II) β-carboline complexes induce cellular apoptosis in Hela cells by causing mitochondrial dysfunction, the accumulation of intracellular ROS and ROS-DNA damage. The induction of double-stranded DNA breaks was evidenced by the protein expression levels of the phosphorylated ɣ-H2A.X, ATR, and ATM which further phosphorylates the downstream effectors ChK1/2. Complexes further promoted intrinsic apoptosis by inducing the activation of caspase-3/8/9, the effectors of intrinsic apoptotic pathway.[19] Furthermore, ruthenium(II)-amino acid complexes target triple-negative human breast MDA-MB-231 cancer cells and induced cellular apoptosis by causing double-stranded DNA breaks and interfering with the mitochondria.[20] These Ru(II)-amino acid complexes induced intrinsic apoptosis which was evidenced by the relation of DNA damage due to ROS production, p53 activation indicating cell stress, and the cleavage of parp. From the western blotting experiments accumulated, it is evidenced that **C3** causes cell stress (as shown by the activation of p53 protein levels) by inducing double-stranded DNA breaks.

There are two main apoptotic pathways responsible for inducing apoptotic cell death. This includes intrinsic and extrinsic pathways (represented in Scheme 4.1).[21]

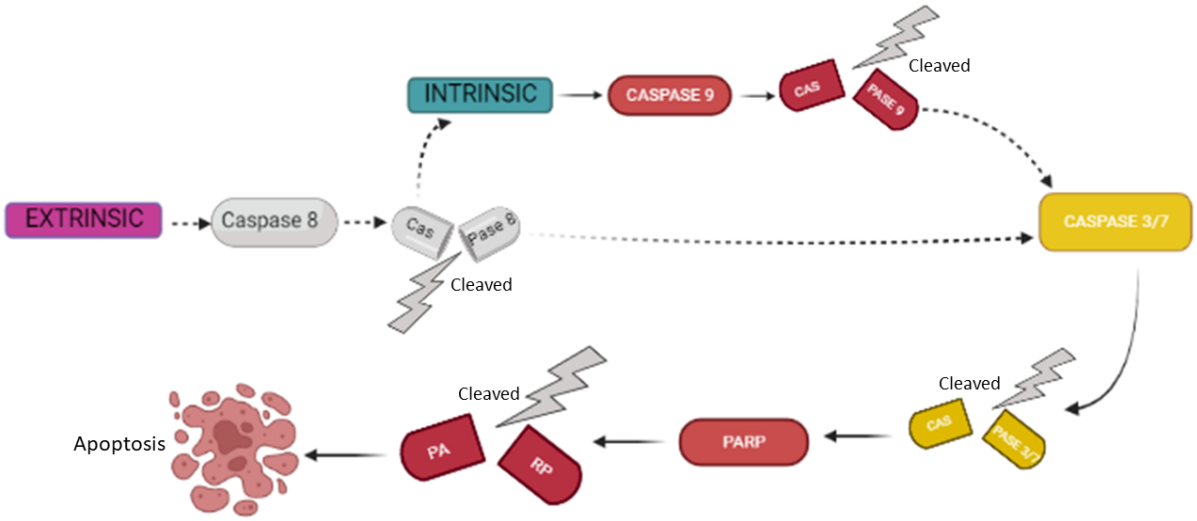

Scheme 4.1 Intrinsic and extrinsic apoptotic pathways responsible for inducing apoptotic cell death. The diagram was redrawn and created using BioRender.com online software.

Extrinsic apoptotic pathway is characterized by caspase 8 activation and is mediated by death receptors[22], whereas intrinsic apoptosis is often triggered by intracellular signals such as DNA damage and hypoxia and is mediated by the mitochondria.[23] To confirm whether the cytotoxicity of **C3** involves the induction of intrinsic apoptosis, the levels of intrinsic apoptotic molecular markers namely, caspase 9 and PARP were investigated by western blotting technique. The downstream markers following DNA damage were investigated (Figure 4.11A - C) and the harvested protein samples were subjected to gel electrophoresis.

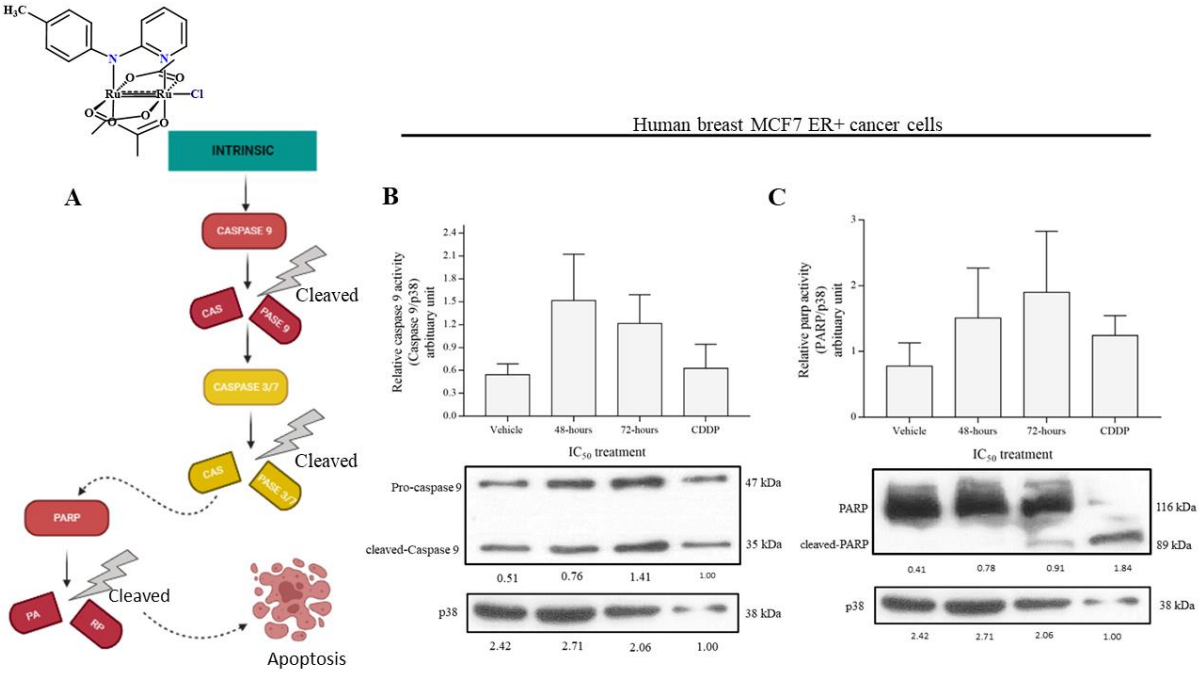

Figure 4.11 **C3** induces intrinsic cellular apoptosis when MCF-7 cells were subjected to 48 and 72-hour treatment. In all experiments, cisplatin (CDDP) was used as a positive control and cells were subjected to 72-hour treatment. Western blotting analysis with antibodies to caspase 9 (C) and parp (D) shows that C3 treatment against MCF-7 cells induces a double-stranded DNA damage response. Total p38 was used as a loading control. The expression of each protein was quantified as the densitometry value analysed by ImageJ software and is normalised to p38 levels. The data represent the mean of two independent biological repeats ± SEM. The diagram was redrawn and created using BioRender.com online software.

From Figure 4.11B, the results indicate that **C3** induced an increase in expression protein levels of one of the effectors of the intrinsic pathway, caspase 9, with increasing **C3** treatment exposure against MCF-7 cells. The expression protein levels of full-length caspase 9 (47 kDa) and its cleaved version (35 kDa) were identified, thus serving as evidence that the intrinsic apoptotic signalling pathway is activated. The treatment of **C3** against MCF-7 cells induced caspase 9 cleavage after 72 hours significantly, compared to the protein levels of caspase 9 cleavage when MCF-7 cells were treated with cisplatin (CDDP).

Similarly, it is possible to identify full-length parp (117 kDa) and the cleaved product of parp (89 kDa), a poly (ADP-ribose) polymerase protein which is found further downstream the cleavage of caspase3/7 (Figure 4.11C). The expression levels of cleaved parp showed increasing parp cleavage with increasing **C3** treatment exposure from 48- to 72 hours and thus

implying that MCF-7 cells have undergone cell death by apoptosis. The cleavage of parp is likely to result in the inactivation of the enzyme by terminating its ability to respond to double-stranded DNA breaks during drug-induced apoptosis in breast cancer cells.[24] Most probably, in response to DNA damage in MCF-7 cells induced by **C3** treatment, the p53 cell stress molecular marker is activated. This is likely to lead to cell cycle arrest, inhibition of parp and caspase activation, thus resulting in cell death.

4.2.4 DNA binding studies: Interaction of **C3** with DNA.

Many metal-based complexes are known to interact and bind with inter- and intracellular biological molecules such as molecular proteins and DNA. From the lantern type metal-metal bonded complexes, dirhodium tetracarboxylate complexes ($Rh_2(\mu\text{-}O_2CR)_4$, where R = methyl, ethyl, propyl, butyl) possessing significant anticancer effects against L1210[25] tumour, sarcoma 180 and P388 tumour cell lines, were reported to bind to double-stranded DNA[26] by forming intra-strand cross-links and inhibiting DNA replication[27,28] and protein synthesis.[29] In fact, dirhodium tetracarboxylate complexes are notorious for inhibiting transcription *in vitro*. Furthermore, varying the nature and the type of substituents on the equatorial and axial positions of the bimetallic cores indicated that it is possible to induce the compound's inhibitory effects and toxicity along with the compound's potential to covalently bind or intercalate with DNA base pairs.[28] Complexes constituting strong electron-withdrawing substituents particularly the $[Rh_2(\mu\text{-}O_2CCF_3)_4]$, $[Rh_2(\mu\text{-}HNCOCCF_3)_4]$ and $[Rh_2(\mu\text{-}O_2CCH_3)_2(CH_3CN)_6]^{2+}$ bind strongly to the bacteriophage T7-RNAP (T7-ribonucleic acid) enzyme, an enzyme involved *in vitro* mRNA synthesis, by possibly involving partial displacement of the equatorial groups by Lewis basic sites of the enzyme.[29] Concerning diruthenium paddlewheel compounds, the thermodynamic and kinetic properties of the interactions of non-steroidal anti-inflammatory drugs coordinated to the paddle wheel Ru_2-core moiety ([Ru_2-NSAID]) with amino acids were reported in the literature.[30] These studies revealed that the axial coordination of amino acids such as cysteine, tryptophan and glycine to the paddle diruthenium(II, III) cores through their thiol and imidazole groups occurs follows a ligand substitution reaction where chloride ligand is displaced and replaced with one moiety of the amino acid. Due to such extensive research studies conducted on bimetallic compounds and their interactions with biological cellular molecules, preliminary experimental studies aimed at identifying pharmacological targets of the synthesized $[Ru_2(O_2CCH_3)_3(4\text{-}CH_3ap)Cl]$ (**C3**) were performed. Such experiments include investigating the interactions of *salmon sperm*-DNA and *pBluescript* DNA plasmid with **C1**, **C3**, and **C8**. Interactions of the complexes with salmon sperm DNA

were probed by performing titrations of **C3** (at a fixed concentration) with salmon-sperm DNA at room temperature and followed using ultraviolet-visible spectroscopy. Furthermore, modifications in the electrophoretic mobility of the various forms of *pBluescript* plasmid DNA were probed using agarose gel electrophoresis experiments.

*4.2.4.1 DNA binding study using UV-visible spectroscopy: Interaction of **C3** (dissolved in 0.1% DMSO: PBS mixture) with salmon sperm-DNA.*

The interaction of DNA with metal complexes can be investigated by monitoring modifications in the absorbance spectrum of either the DNA or the metal complex *via* the ultraviolet-visible spectroscopic technique. Metal complexes interact with DNA either *via* covalent or non-covalent bonding and are known to bind to DNA *via* intercalation or groove binding mode, often constituting an interaction of an aromatic heterocyclic moiety that disrupts the hydrogen bonds between the nitrogen base pairs thus leading to the disorientation of the DNA helical structure. To probe the DNA binding ability of $[Ru_2(O_2CCH_3)_3(4\text{-}CH_3ap)Cl]$ (**C3**) with salmon sperm DNA, titration experiments were performed with C3 kept at a fixed concentration (5 x 10^{-4} $mol.dm^{-3}$) dissolved in DMSO (0.1% in PBS Buffer). Salmon sperm (sp) DNA was used as a titrate and concentrations varied from 0.53 to 12.2 µl. All spectra were recorded at room temperature, with the absorbance values fitted and plotted using OriginLab software (represented in Figure 4.12).

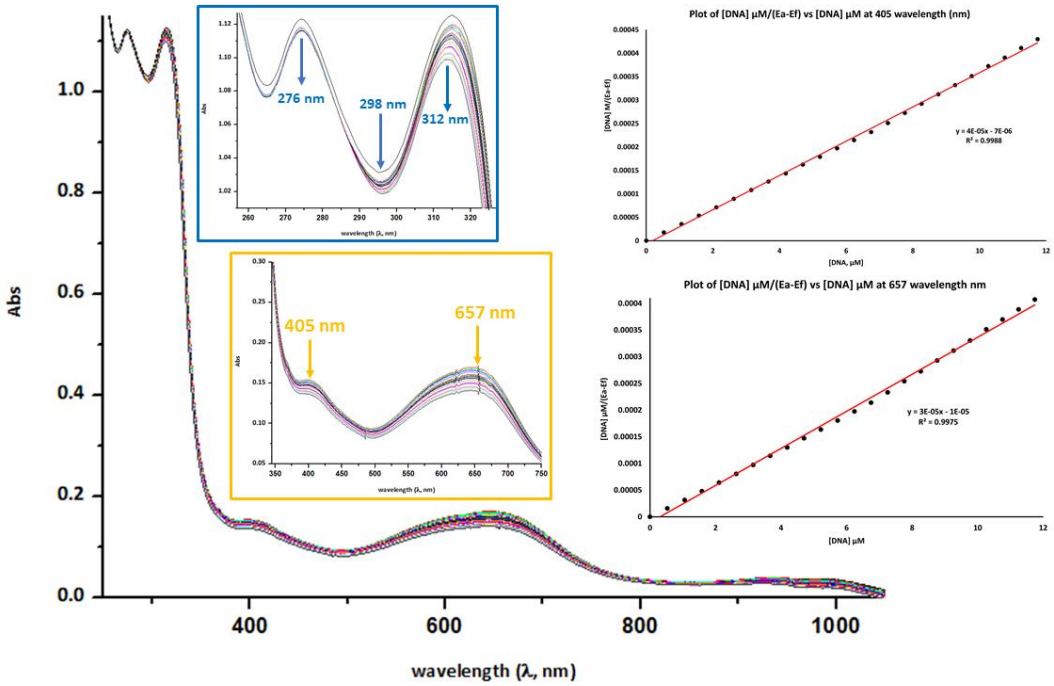

Figure 4.12 Ultraviolet-visible spectra of **C3** (5 x 10^{-4} M, dissolved in DMSO (0.1%)/PBS solution): titration with salmon sperm (sp) DNA (concentration ranging from 0.53 to 12.2 µl). Salmon sperm DNA was added in increments of 5 microlitres (µl). Each spectrum was recorded at room temperature after 5 mins of incubation period.

Spectral changes were significant upon increasing the concentration of the salmon sperm-DNA. Absorption intensities of the spectral bands were followed at wavelengths 405 and 675 nm to determine the intrinsic binding constant of DNA to **C3**. Upon minute increments of the salmon sperm DNA, a distinct hypochromic effect (a decrease in the molar absorption coefficient) along with a slight bathochromic shift for the above-mentioned absorption maximum bands were observed. This is indicative of the intercalation mode of binding between the drug compound and DNA base pairs. Often intercalation binding mode involves a π-π stacking interaction of an aromatic chromophore and a DNA base pair, with the degree of the hypochromic shift being related to the strength of this stacking interaction.[31,32] This stacking interaction of the π-π electrons of the DNA base pair and the drug's aromatic chromophore results in a decrease in the energy gap of the π - π^* electronic transition, thus causing a bathochromic shift of the absorption spectrum and contributes to the hypochromic effect.[32]

The absorption spectrum of the complex acquired before titrating with salmon-sperm DNA resembles that of $[Ru_2(O_2CCH_3)_3(L)Cl]$ complexes, where L is the *N*,*N*- type R-ap bridging complexes in solution (DMSO (0.1%)/PBS). The ultraviolet absorption shoulder band

(observed at $\lambda_{nm} \approx 368$), initially assigned to the ligand to metal charge transfer π (Cl) $\rightarrow \pi^*$ (Ru_2) and σ (Cl) $\rightarrow \pi^*$ (Ru_2) electronic transitions, disappears upon titrating **C3** with salmon sperm DNA. In addition, the absorption maxima of the band observed at $\lambda_{nm} = 405$, assigned to the π (Ru – O) $\rightarrow \pi^*$ (Ru_2) electronic transition and the band observed in the ultraviolet-visible region ($\lambda_{nm} = 657$), decreases upon additions of the salmon-sperm DNA. A distinct hypochromic effect is significant for both the ultraviolet-visible $\pi - \pi^*$ metal to ligand charge transfer electronic transitions upon increasing the concentration of the DNA. This phenomenon was clear evidence that the complex may bind to DNA *via* partial intercalation or electrostatic interaction with the phosphate backbone of the DNA base pair, as confirmed by the hypochromic shift of the metal-to-ligand charge transfer transitions. The extent of the hyperchromic effect in absorbance of the spectrum was observed at $\lambda = 405$ nm (H = 10.22%) and 657 nm (H = 4.52%) nm and measured using the following equation:

$$H(\%) = \frac{A_{free\ complex} - A_{bound\ to\ DNA}}{A_{free\ complex}} \text{ x } 100, \text{ where:}$$

H (%) = the extent of the hyperchromic effect,

$A_{free\ complex}$ = absorbance of the free complex,

$A_{bound\ to\ DNA}$ = absorbance of the complex bound to DNA.

The hypochromic effect values obtained suggest that the binding interaction of **C3** to salmon sperm DNA is weaker. Thus, **C3** binds to the DNA partially *via* intercalation binding mode. The intrinsic binding constant (K_b) of **C3**-*salmon sperm* DNA interaction at wavelengths 405 and 657 nm and, the results obtained were fitted to the Benesi – Hilderbrand equation[33] below:

$$\frac{[DNA]}{(\varepsilon_a - \varepsilon_f)} = \frac{[DNA]}{(\varepsilon_b - \varepsilon_f)} + \frac{1}{K_b(\varepsilon_b - \varepsilon_f)}, \text{ where:}$$

[DNA] = Molar concentration of salmon sperm DNA in base pairs,

K_b = the intrinsic equilibrium binding constant,

ε_a = apparent extinction coefficient of the complex bound to DNA; corresponds to $\frac{A}{[\boldsymbol{C3}]}$,

ε_b = extinction coefficient of the complex fully bound to DNA,

ε_f = extinction coefficient of the complex free in solution.

A plot of $\frac{[DNA]}{(\varepsilon_a - \varepsilon_f)}$ versus [DNA] gives a linear graph and the binding constant, K_b was calculated as the $\frac{slope}{intercept}$ ratio.

The binding constants, K_b for **C3** were determined at various wavelengths and were found to be 4 x 10^{-5} M^{-1}(at wavelength 405 nm) and 3 x 10^{-5} M^{-1} (at wavelength 657 nm). The obtained binding constants suggest that the interaction of complex **C3** with salmon sperm DNA is weak. The binding constants correlate with the hypochromic effect values obtained, which also suggests weaker binding modes between **C3** and salmon sperm DNA at concentrations (500 μM) 10-fold greater than the half-maximal inhibitory concentrations determined in cytotoxicity studies.

*4.2.4.2 DNA migration study using gel electrophoresis; Interaction of **C1**, **C3** and **C8** with pBluescript plasmid DNA.*

The interaction of three paddlewheel diruthenium(II, III) complexes, **C1**, **C3** and **C8**, with promising cytotoxic properties against human breast adenocarcinoma cell lines, were investigated for their abilities to bind to p*Bluescript* plasmid DNA using agarose gel electrophoresis technique. Plasmids are of paramount importance in these experiments since they are primarily found in three distinguishable forms, often migrating at different rates on agarose gels. In order of fastest to slowest in the migration rate, the various forms of plasmid DNA are as follows: i) supercoiled or helical (ccc) DNA plasmid, ii) linear plasmid DNA (*l*), both resulting in the cleavage of double-stranded DNA and iii) open circular (*oc*) plasmid DNA, observed because of single-strand cleavage of the DNA.[34,35] Any modifications in the electrophoretic mobility of various forms of this plasmid DNA are considered to confirm the interaction of compounds with plasmid DNA. Agarose gels were stained with ethidium bromide after electrophoresis to prevent competitive binding and to make it easy to visualize the travelled bands. Figure 4.13 is a photographed image of the agarose gel electrophoresis of plasmid DNA incubated with complexes **C1**, **C3** and **C8**. An untreated λ DNA marker was used as a positive control marker for any presence of linear DNA.

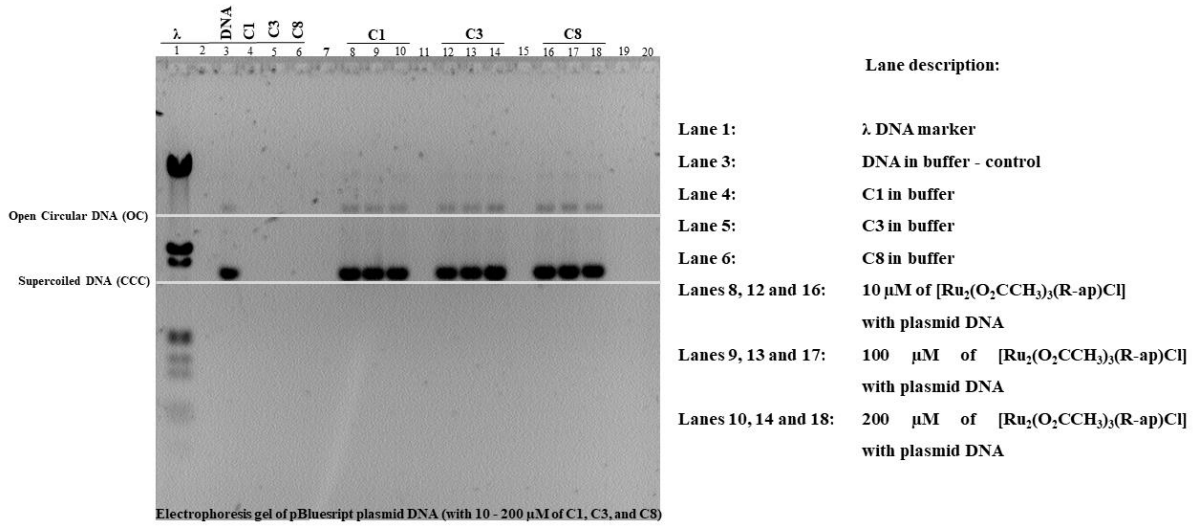

Figure 4.13 Photographed images obtained of the horizontal gel electrophoresis patterns for the cleavage of pBluescript plasmid DNA (40 µM). Compounds **C1**, **C3** and **C8** were investigated with various increasing concentrations of 10, 100 and 200 µM as shown. Both images of the gels are a replica of one another for better visualization and representation.

From the agarose gel presented in Figure 4.13, the supercoiled DNA (ccc) is the prominent band of the plasmid DNA. This demonstrates that the incubation of complexes **C1**, **C3** and **C8** with *pBluescript* plasmid DNA did not cause significant modifications in the plasmid DNA. nor did the complexes induce changes in the rate of migration of various forms of the plasmid DNA at the tested concentrations (10, 100 and 200 µL). Thus, no interactions of complexes (particularly for **C1** and **C3**) with the plasmid DNA were confirmed. However, **C8** caused a slight retardation in the supercoiled DNA band at the highest tested concentration (200 µM), a concentration that is 2-fold greater than the IC_{50} value concentration of **C8**. Based on these *plasmid* DNA binding experiments, complexes do not cause a significant change in the plasmid DNA or induce any slight changes in the electrophoretic mobility of the different forms of DNA and therefore, DNA binding may probably not be the preferred mode of action of these types of complexes. To conclude the binding modes of **C3** with salmon sperm DNA and agarose gel electrophoresis experiments (**C1**, **C3**, and **C8**), the ultraviolet-visible titration results obtained agree with the agarose gel electrophoresis experiments, where **C3** showed weaker interactions with pBluescript plasmid and salmon sperm DNA even at concentrations greater than the experimentally obtained *in vitro* cytotoxic IC_{50} value. These results further highlight that the mode of action of the investigated paddlewheel compounds does not involve binding to DNA, as a chemotherapeutic target.

For complexes to be investigated for their *in vitro* and *in vivo* biological applications, the stability of compounds in aqueous and biological media is of great paramount for cellular uptake and accumulation. Metal complexes are notorious for their interactions with biomolecules to form prodrugs *via* cellular processes such as coordinating their metal-ions to cellular ligands, before reaching intracellular targets. Such processes may involve ligand substitution, aquation and redox reactions in the blood stream or the cancerous cells, which is of great significance to elucidate their chemical and biological behaviour to aid in understanding their mode that could ultimately be the main cause for their anticancer properties. Ruthenium(III) complexes in clinical trials namely NAMI-A, KP1019 and its analogue NKP1339 are postulated to exert their anticancer effects from undergoing chloride-water exchange (aquation/hydrolysis) reaction, interactions with the serum proteins and DNA. Thus, to investigate the stability of the complexes synthesized in solution, preliminary time-dependent solution studies were conducted in pure solvent (100% DMSO) and foetal bovine serum (FBS) and penicillin/strep (P/S) supplemented RPMI cell culture media.

4.2.5 Stability study of **C3** in a coordinating solvent, DMSO

Many metallodrugs screened for their cytotoxic properties *in vitro* biological assays are often dissolved in the organic solvent, dimethyl sulfoxide (DMSO). The determination of their stability in solution, in aqueous media and in blood plasma, is of key importance in understanding their integrity and reactivity with biomolecules, discovering their mode of action concerning their cytotoxic effects and ultimately, their identification as potential anticancer drug-lead candidates. Diruthenium(II, III) paddlewheel complexes are notorious for being susceptible to axial exchange ligation or coordination with organic solvent molecules, as previously discussed in published material[36] and this work. With this knowledge in mind, it is for this reason that the stability of **C3** was investigated in the presence of a coordinating solvent (DMSO) probed using the ultraviolet-visible spectroscopic technique. The complex was dissolved and prepared in anhydrous DMSO (5×10^{-4} M) and incubated for 7 days, with the complex solution kept in the dark. Each spectrum was recorded at room temperature after a 24-hour time interval. The recorded spectra were collected and plotted using Origin v8.0 software, with the spectra represented in Figure 4.14.

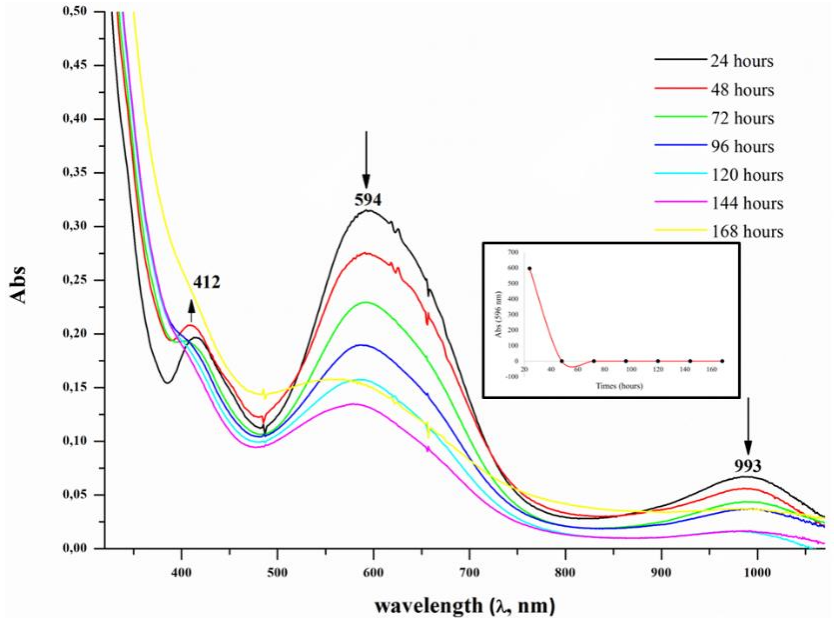

Figure 4.14 Solvent stability study: ultraviolet-visible spectra of **C3** (5.0 x 10^{-4} M) in DMSO (100%) recorded at room temperature.

The electronic absorption spectra recorded showed characteristic absorption band features of the nature of the diruthenium ($[Ru_2(L)_4Cl]$) complexes in solution as reported in literature[37] and discussed in Chapter 3. Complexes showed good stability in DMSO for 144 hours, with a hyperchromic effect being observed at the absorption band observed at ≈ 412 nm, assigned to the σ (Cl) → $\pi^*(Ru_2)$ electronic transition. This is indicative of the coordination of the solvent molecule on the vacant axial site, followed by the replacement of the axially coordinated chloride ligand with the same solvent molecule with time (> 168 hours). A proposed schematic diagram depicting the chloride exchange reaction of the complex with the DMSO molecules is represented in Scheme 4.2, occurring over a period of 7 days. Furthermore, a pronounced hypochromic shift was observed for absorption bands observed in the visible and the near nuclear-infrared region (≈ 594 nm and ≈ 993 nm) which decreased in intensity over a period of 7 days.

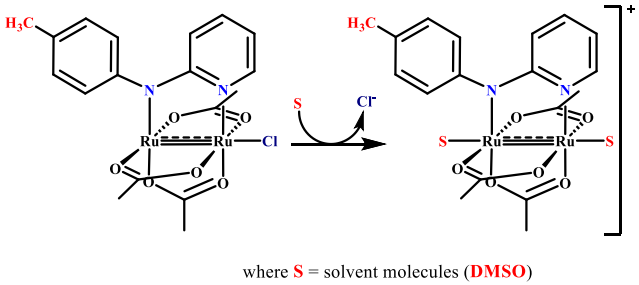

Scheme 4.2 Schematic diagram of the chloride displacement reaction monitored over 7 days, with DMSO molecules occupying the vacant axial sites. The proposed scheme was obtained from $[Ru_2(L)_4Cl]$ analogues examples depicted in literature.[37]

From the ultraviolet-visible spectra collected, **C3** showed great stability at room temperature conditions, with minimal significant changes in the absorption spectra observed for 72 hours at 100% DMSO concentrations. This confirms that the integrity of the complex is kept intact, with no cleavage or disintegration of the diruthenium core to yield adducts or byproducts, apart from the possible coordination of the solvent. To maintain and mimic physiological conditions within cellular entities, stability study experiments are often conducted in saline-buffered solutions (pH = 7.4) at NaCl concentrations of (100 mM) and intracellular concentrations (4 mM). To further gauge the stability of complexes in solution, stability study experiments were conducted in fully supplemented cell culture RPMI media, supplemented with foetal bovine serum (FBS) and penstrip (P/S) supplements.

4.2.6 Interaction of **C3** with supplemented biological media (Rosewell Park Memorial Institute-1640)

The reaction of $[Ru_2(O_2CCH_3)_3(4\text{-}CH_3ap)Cl]$ (**C3)** in supplemented *Rosewell Park Memorial Institute-1640* (RPMI-1640) culture media was investigated *via* ultraviolet-visible spectroscopic technique at room temperature. All spectra were recorded after every 5 minutes of the incubation period for 520 mins and represented in Figure 4.15.

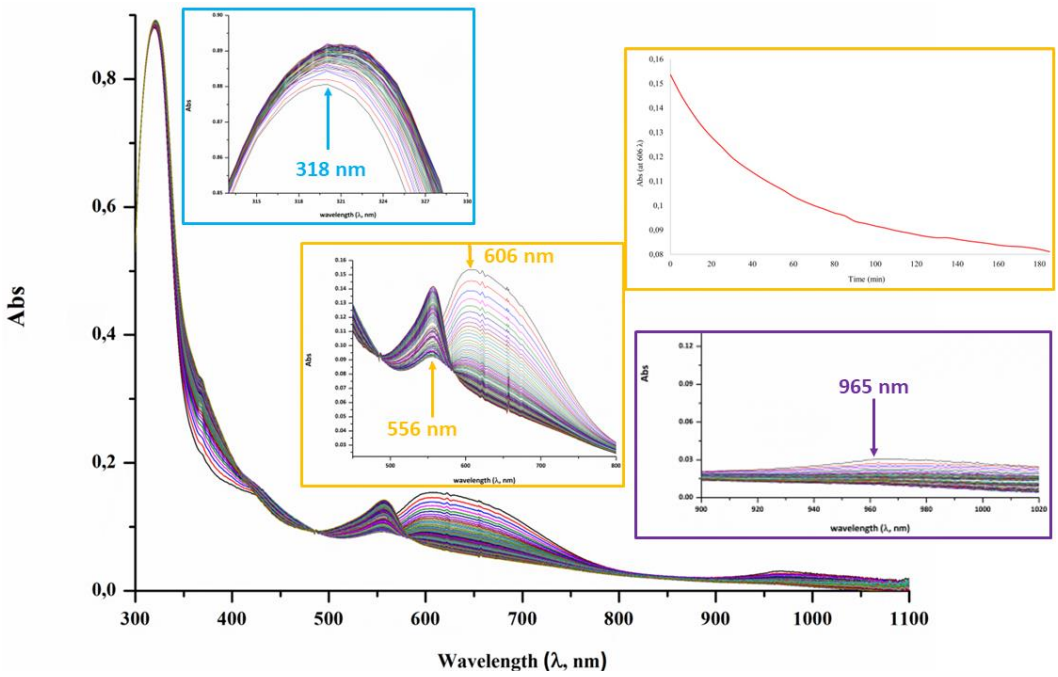

Figure 4.15 Ultraviolet-visible spectra of **C3** (5.0 x 10^{-4}M, dissolved in DMSO (0.1%)/RPMI medium) recorded at room temperature. Each spectrum was recorded every 5 mins for approximately 8 hours (520 mins).

As observed from the spectra of **C3** dissolved in DMSO (0.1%)/RPMI culture media, the ligand to metal charge transfer (LMCT) σ(Cl) → σ* (Ru_2) electronic transition bands appear in their respective region, at ≈ 318 nm accompanied by a shoulder band at 370 nm. The band at ≈ 318 nm experiences a hyperchromic shift with a prolonged incubation period. Absorption bands observed in the ultraviolet-visible (606 λ, nm) and near-infrared (965 λ, nm) regions assigned to the π (Ru–O) → π* (Ru_2), π (Ru–N) → π* (Ru_2) with the possible influence of σ → σ* and the δ(Ru_2) → δ*(Ru_2) electronic transitions, decreases in intensity and experiences a hypochromic shift. Upon such shift, a new band observed in the visible region at 556 nm is formed. The presence of an isosbestic point is observed at 485 nm wavelength, conforming the formation of a new species in solution.

4.2.7 Interaction of the reduced L-glutathione (GSH) and oxidized L-glutathione/methionine form (GSSG) and with **C3**.

Organometallic ruthenium(III) and ruthenium(II) metal complexes are known to target redox cellular homeostasis indirectly by serving as catalysts for the oxidation of glutathione (GSH) to glutathione disulphide (GSSH/GSSG).[38,39] This, in turn, may be responsible for their anticancer properties. A class of organometallic ruthenium arene complexes were reported to

be highly cytotoxic against A2780 human ovarian and A549 lung cancer cell lines regardless of their inertness towards hydrolysis reaction.[38] Their cytotoxic properties were attributed to their ability to catalyse GSH to GSSG, by following a proposed catalytic cycle involving the reduction of the azo group to hydrazine which is initiated by the nucleophilic addition of the GSH to the azo group. This is followed by the oxidative regeneration of the azo group with the molecular oxygen.[38,40]

Glutathione is a major reductant tripeptide molecule produced by cancer cells in large quantities and plays a significant role in initiating drug and xenobiotics detoxification, with the aid of glutathione-s-transferases.[41] The tripeptide molecule is produced by all organs, more so in the liver, and is found intracellularly in concentrations ranging from 0.5 to 10 mM.[42] Generally, high levels of GSH peptide molecules in cancer cells serve as a protective intracellular response mechanism against irradiation, and oxidative stress by reducing levels of reactive oxygen species and stabilising the redox imbalance within the cellular environment as well as against chemotherapeutic antitumour agents.[40,43] The eradication of glutathione intracellularly could affect the cell's capability to cope with the redox imbalance of the reactive oxygen species (ROS) and the resulting oxidative damage. The high elevated levels of GSH within the cell have been reported to be concerning drug resistance. The strong and irreversible binding of intracellular thiolate ligands to the cisplatin chemotherapeutic drug, used in the treatment of solid tumours, resulted in the detoxification of the drug (drug inactivation), forming GSH-adducts and thus reducing its therapeutic efficacy and excretion from the cell.[44,45] Therefore, low affinities of metal complexes to glutathione may be a favourable potential therapeutic strategy in the treatment of cancers.[39]

On such basis, this experimental design focuses on following the reaction of these class of diruthenium(II, III) paddlewheel complexes with GSH and thus investigating the abilities of **C3** to catalyse the GSH as a biological target, probed by performing a preliminary titration experimental. Both biological reducing agents, the reduced L-glutathione (GSH, 0.1 mM with spectra represented in Figure 4.16) and oxidized L-glutathione/methionine (GSSG, 0.1 mM with spectra represented in Figure 4.17) form were treated as titrants and complex **C3** kept as the titrate. Titrations were performed at room temperature and the pH of the phosphate buffer solution was kept constant at 7.4. Each ultraviolet-visible spectrum was recorded after successive increments (2.5 μL) of both the reduced and oxidized forms of glutathione.

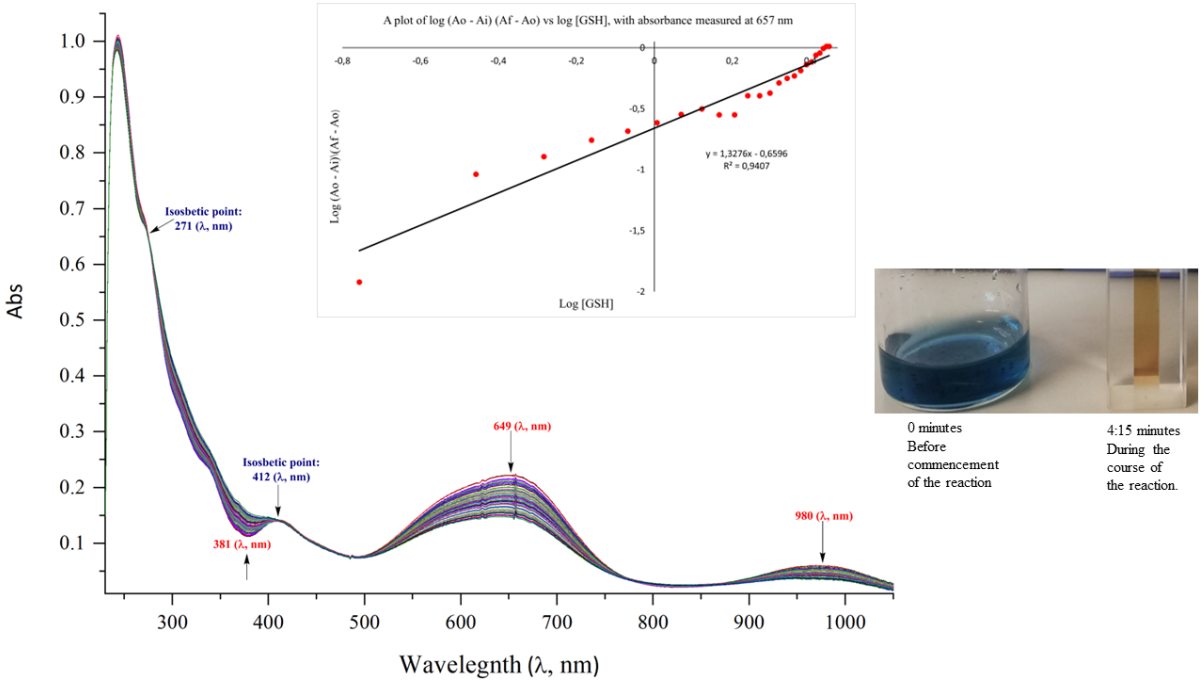

Figure 4.16 Ultraviolet-visible spectrum of **C3** (5.0 x 10^{-4} M) titrated with GSH (L-ɣ-glutamyl-L-cysteinnylglycine, 0.1 mM) in aqueous phosphate buffer solution (pH = 7.4) at room temperature.

As observed in Figure 16, a significant hypochromic shift was observed in the visible (649 λ, nm) and near-infrared (980 λ, nm) regions accompanied by a hyperchromic shift observed in the ultraviolet-visible region (381 λ, nm). In addition, two isosbestic points were observed in the ultraviolet-visible region at 217 nm and 412 nm wavelength. All these changes in the spectrum suggest a strong and significant interaction and possible coordination of the GSH molecule in the axial site of the diruthenium(II, III) core metal centres. The presence of the isosbestic point (observed at 271 λ, nm) at higher energy (lower wavelength) could suggest the displacement of the axially ligated chloride ion followed by the replacement of the chloride molecule with the coordination of equivalence of the GSH molecule. The latter isosbestic point observed at the beginning of the visible region (412 λ, nm) may suggest the possible coordination bond between the ruthenium metal centre and another equivalence of the GSH molecule. The binding constant (K_b) of the glutathione to the paddlewheel **C3** complex was determined and is of magnitude 2.19 x 10^{-7} M^{-1}. This is attributed to the interaction of the glutathione molecules possibly binding axially to the diruthenium(II, III) cores subsequently (represented in the proposed Scheme 4.3), and that the binding of glutathione molecule is weakly coordinated to the diruthenium(II, III) metal centres possibly due to the low

concentration of glutathione (0.1 mM) prepared to perform the titration experiment at room temperature.

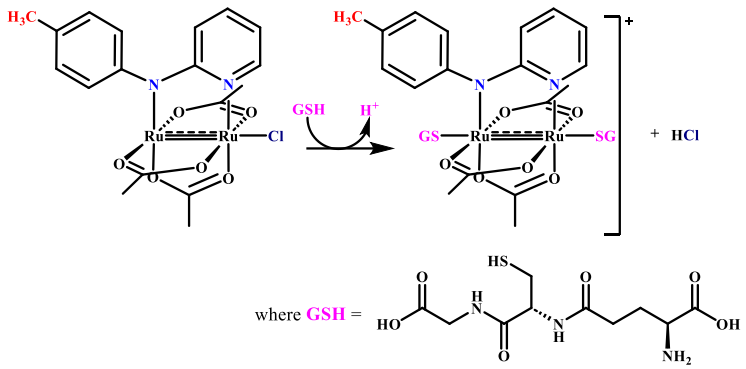

Scheme 4.3 Proposed sequential binding of glutathione (GSH) molecules to diruthenium(II, III) cores of **C3** complex. The proposed scheme was obtained from $[Ru_2(L)_4Cl]$ analogues examples depicted in literature.[37]

Similarly, a titration experiment was performed with the oxidized L-glutathione/methionine (GSSG, 0.1 mM and spectrum represented in Figure 4.17). The reaction was monitored for 02H:66 minutes, with each spectrum recorded after successive increments (2.5 µL), and incubation (5 minutes) with the GSSG (0.1 mM) titrant.

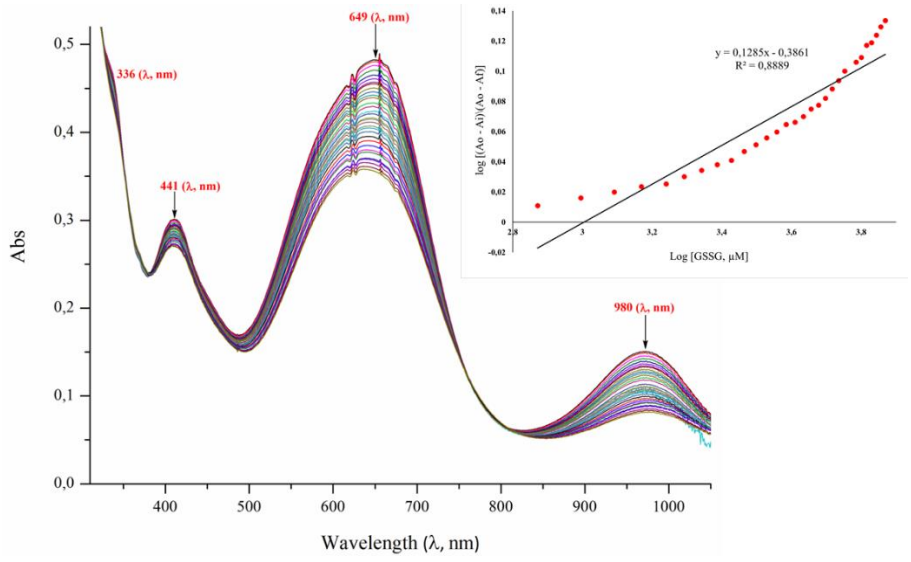

Figure 4.17 Ultraviolet-visible spectrum of **C3** (5.0×10^{-4} M) titrated with GSSG (L-glutathione/methionine, 0.1 mM) in aqueous phosphate buffer solution (pH = 7.4) at room temperature.

From the spectrum, significant hyperchromic shifts were observed in the ultraviolet-visible (441 and 649 λ, nm) and near-infrared (980 λ, nm) regions with no noticeable isosbestic points observed. The binding constant (K_b) of the oxidized form of GSH, L-glutathione/methionine to the paddlewheel **C3** complex was determined and is of magnitude 4.11×10^{-7}. The absence of isosbestic points and the magnitude of the binding constant (Kb) suggests that **C3** does not coordinate or bind to the oxidized form of glutathione, L-glutathione/methionine.

4.3 SUMMARY

In summary, the synthesized R-ap ligands (**L1 - L8**) were evaluated for their cytotoxic properties by initially performing preliminary screen tests against the human breast cancer cells (MCF-7 and MDA-MB-231) of different hormone receptor status at 100 µM. the MTT assay test kit to determine the % viable cells after 72-hour treatment with the respective ligands. These pre-screen tests show that the ap ligands did not inhibit the survival growth of both cell lines significantly, with the percentage cell viability of MCF-7 and MDA-MB-231 cells being ≥ 88.0 after treatment. All ligands were further tested for their toxicity properties against the mammary non-malignant human breast MCF-12A cell line. Compared to their activity against the cancer cells, several ligands were slightly toxic and inhibited cell viability of MCF-12A cells significantly, decreasing the % cell viability to 77.0 after 72-hour treatment. The respective corresponding complexes ($[Ru_2(O_2CCH_3)_3(R\text{-}ap)Cl]$, **C1 - C8**) were evaluated for their potential anticancer properties and MTT assays were performed on the above-mentioned cell lines. The half maximal inhibitory concentration (IC_{50}) values were determined, with $[Ru_2(O_2CCH_3)_3(4\text{-}CH_3ap)Cl]$ (**C3)** and $[Ru_2(O_2CCH_3)_3(4\text{-}Fap)Cl]$ (**C8**) showing promising potential anticancer properties against oestrogen receptor-positive (ER +ve) MCF-7 cells, having an IC_{50} value of 39.0 µM and 49.1 µM, respectively. However, a similar trend was not observed when similar complexes were subjected to *in vitro* MTT cell viability assays. Complexes showed moderate capabilities of reducing MDA-MB-231 cell viability and less favourable significant inhibitory effects when tested against the triple-negative and invasive MDA-MB-231 cell line. The selected complexes had low cytotoxic properties towards the mammary non-malignant MCF-12A epithelial cell line and showed favourable selectivity towards the human breast MCF-7 cells, with selectivity indices (SI) ≥ 1.5. Clonogenic assay experiments showed that **C3** inhibited the ability of MCF-7 cells to survive significantly after monitoring 35 mm dishes for the formation of cell colonies for 7 days. Western blotting revealed that **C3** induces double-stranded DNA breaks, observed by the increase in protein expression levels of key DNA damage response (ɣ-H2AX). Furthermore, **C3** activates the intrinsic apoptotic signalling marker cleaved caspase-9 and cleaved parp, a poly (ADP-ribose) polymerase protein which is found further downstream the cleavage of caspase3/7 as observed by the time-dependent increase in protein expression levels of both protein expression levels.

Solvent stability experiments of the selected **C3** complex were performed using ultraviolet-visible spectroscopy and show that paddle complexes of this type were stable in DMSO, with the ligand-metal and metal-metal charge transfer ultraviolet-visible transition bands prominent

and observed for 7 days in solution at room temperature. Furthermore, the stability of **C3** was investigated in DMSO (0.1%)/RPMI media solution. The acquired spectra suggest that **C3** is only stable in the above-mentioned aqueous solution for the first 3-hours and undergoes ligand exchange reactions, forming a new species in the solution.

Preliminary mechanistic studies investigating the biological molecular targets of **C3** were performed by studying the interactions of **C3** with salmon-sperm DNA, the bluescript plasmid DNA and glutathione (GSH) and probed using ultraviolet-visible spectroscopic and agarose gel electrophoretic techniques. The salmon sperm DNA binding studies suggest that the complex **C3** does not bind or interact with the DNA nucleotide basis. Similarly with the agarose gel electrophoresis experiments, complexes **C1**, **C2** and **C7** did not cause any modifications in the bands of the DNA plasmids or cause any slight retardations or changes in the electrophoretic mobility of the DNA plasmid bands when complexes were prepared at 200 μM, the concentration beyond the IC_{50} values determined *in vitro* MTT biological assays. Lastly, glutathione binding assays were performed at stoichiometric ratios with **C3** and suggest that complexes of this type react rapidly (binding constant ≈ 2.19 x 10^{-7} M^{-1}) with glutathione at room temperature, as indicated by the presence of two isosbestic bands observed in the ultraviolet (271 λ, nm) and visible region (412 λ, nm). The first isosbestic band suggests that the chloride ion was displaced followed by the coordination of glutathione whereas the second band suggests the displacement of the weakly bound solvent (H_2O) molecule which was replaced with another GSH molecule. This titration study suggests that the Ru_2^{5+} oxidation state is reduced to Ru_2^{4+}, and further reduced to Ru_2^{3+}.

4.4 EXPERIMENTAL

4.4.1 Cell culture

Human breast MCF-7, MDA-MB-231 cancer and the mammary non-malignant breast epithelial MCF-12A cell lines were grown and maintained in Roswell Park Memorial Institute Medium-1640 (RPMI-1640, Sigma Aldrich), Dulbecco's Modified Eagle's Medium (DMEM, Sigma Aldrich) and Dulbecco's Modified Eagle's Medium/Nutrient mixture F/12 (DMEM/F-12), respectively. RPMI-1640 and DMEM culture media were supplemented with Foetal Bovine Serum (FBS, 10%) and penicillin (100 U/mL) and streptomycin (100 µg/mL). DMEM/F-12 medium was supplemented with FBS (5%), penicillin/streptomycin (1%), epidermal growth factor (EGF, 10 µl), hydrocortisone (16.6µl), choleratoxin (8.3 µl) and insulin (125 µl). Cells were adherent in monolayers, grown and maintained in 10 cm petri dishes and T75 cm flasks Dishes were handled under sterile conditions to prevent any bacterial contamination or infections and maintained in a 95% air-humidified incubator at 37°C and 5% CO_2. When confluent, cell adhesion was weakened with trypsin-EDTA (Gibco) and the resultant cells in suspension were split and replated as required. Media was replaced every 2 - 3 days and cells were passaged as needed. The clinically prepared cisplatin drug solution was purchased and obtained from the University of Cape Town's Private hospital (Groote Schuur Hospital).

4.4.2 Mycoplasma Infection

Cells were seeded on sterilized coverslips in culture plates (35 mm) and incubated overnight in an antibiotic-free medium. After an incubation period, cells were fixed with a fixative solution (1 mL) in a 1:3 glacial acetic acid: methanol mixture for 10 seconds. After 10 seconds, cells were rinsed with distilled water 3 times and the coverslips were air-dried at room temperature for a few minutes. Once dried, DNA was stained with Hoechst (1 mL, 0.5 µg/mL, Sigma St Louis, MO, USA) for 30 seconds. The excess stain was washed off with distilled water and the coverslips were mounted on a slide with mounting fluid (Chapter 6). Cells were viewed under fluorescence microscopy (EVOS^{TM} M5000, ThermoFisher Scientific, Massachusetts, USA) using the DAPI filter and viewed at 40x magnification. Mycoplasma-free cells stained positive with Hoechst only in the nucleus, while cells infected with mycoplasma showed staining in both the nucleus and the cytoplasm.

4.4.3 Preparation of drug treatments

*4.4.3.1 Anilinopyridinate (R-ap) ligands (**L1 - L8**) drug preparation for screen tests.*

A single dose (100 µM) screen test was performed to evaluate the anticancer effects of ligands against human breast MCF-7, MDA-MB-231 cancer and mammary epithelial MCF-12A normal cell lines. All ligands were dissolved in DMSO (Sigma Aldrich, Missouri, USA) to give a drug stock solution (10 mM). The mixtures were further diluted in a cell culture medium to achieve the desired final concentration (100 µM).

*4.4.3.2 $[Ru_2(O_2CCH_3)_3(R\text{-}ap)Cl]$ (**C1 - C8**) drug preparation for cell culture treatment.*

$[Ru_2(O_2CCH_3)_3(R\text{-}ap)Cl]$ complexes were prepared in DMSO to give a drug stock solution (10 mM). The mixtures were diluted down with the working cell culture medium to give a stock concentration of 1000 µM and further diluted to the final desired concentrations (20, 40, 60, 80 and 100 µM) as working drugs for treatment in the respective medium. The vehicle DMSO control concentration was prepared at 100 µM and CDDP positive control was prepared simultaneously at the same concentrations of the $[Ru_2(O_2CCH_3)_3(L)Cl]$ drugs. Complexes were prepared on the same day of treatment to avoid possible coordination of biological molecules or DMSO on vacant axial sites/positions of the Ru_2 metal cores.

4.4.4 *In vitro* cytotoxicity: cell viability MTT assays

Cell viability assay experiments were performed on MCF-7 cells using the 3-(4,5-dimethylthiazol-2-yl)-2,5-diphenyl tetrazolium (MTT) cell proliferation kit[8]. The assay kit was utilized according to the manufacturer's instructions or MTT (M218, Sigma Aldrich, Missouri, USA) and solubilizing reagents prepare according to protocols provided by the Sharon Prince Lab (Chapter 6). The principle of the assay is based on the ability of viable cells to metabolize the yellow tetrazolium salt (MTT) to purple formazan crystals by the mitochondrial succinate dehydrogenase.[8] Cells were seeded at a density of 4500, 2800 and 5500 for MCF-7, MDA-MB-231, and MCF-12A cells per well to obtain confluency between 60 - 70% on the day of treatment in 96 well plates. For MCF-12A cells, cells were seeded and starved of nutrients (supplements) for 48 - hours before treatment with compounds. Cell lines were subjected to a single-dose treatment with ligands (**L1** - **L8**, screen tests) and multidose treatments with paddlewheel diruthenium complexes (**C1** - **C8**) for 72 - hours. Cell viability was measured using the 3-(4,5-dimethylthiazol-2-yl)-2,5-diphenyl-trazolium bromide (MTT) test (Sigma Aldrich) according to the manufacturer's instructions[46] and solubilizing reagents prepared according to lab protocols provided. After 72-hour treatment with compounds, 10µL of MTT

(5mg/mL) solution was added and cells were re-incubated for 4 hours, followed by the addition of the solubilizing reagent. 96 well cell dishes were re-incubator for 24 hours. The results were recorded using a microplate reader (Promega Glomax Explorer Multimode Microplate Reader) at an absorbance reading of 600 nm. Each treatment was performed in quadruplicate, and three independent experiments were performed for all three cell lines. The wells of the 96 well plate consisting of the biological culture medium and drug only (no cells) were utilized as blanks. Mean cell viability was calculated as a percentage of the mean vehicle control ± standard error of the means. Percentage cell viability was calculated as follows:[8]

$$\% \text{ Cell viability} = \left(\frac{\text{absorbance value of the tested sample utilised in treatment}}{\text{absorbance value of the uncontrol treated cell}} \right) \times 100$$

4.4.5 *Determination of half maximal inhibitory concentrations (IC_{50}) and selectivity indices (SI)*

IC_{50} values were determined from the multidose-response 72-hour cell viability assays and the data accumulated was fitted to draw dose-response curves using GraphPad Prism version 7.0 software (GraphPad Software, California, USA). The software was used to calculate these values from the fitted dose-response curves and were obtained in the µM range. IC_{50} values obtained for **C3** and **C8** were utilized for *in vitro* cellular colony formation assay experiments. To determine the complex's capabilities to select human breast cancers over epithelial normal cell lines, selectivity indices were determined.[47] This was achieved by the equation given below:

$$\text{SI} = \frac{IC_{50} \text{ value of the non-malignant human breast MC12A cell line}}{IC_{50} \text{ value of the human breast adenocarcinoma cell line}}$$

Good selectivity and sensitivity for human breast cancer cells were considered to have an $SI \geq 2$, a moderate selectivity as $1.5 \leq SI \leq 2$, and an $SI \leq 1.5$ as not selective to cancerous cells. An anticancer drug candidate should consist of a selectivity value higher than 2 as this indicates the therapeutic potential of the drug candidate to be selective towards cancer cells.

4.4.6 Colony formation assay experiments.

Experiments were conducted to determine the long-term survival and proliferation of breast cancer (MCF-7) and epithelial normal (MCF-12A) cell colonies formed after 72 hours of drug treatment (**C3** and **C8**). Briefly, cells were seeded in 6-well plates at density 4.5 x 10^5 (MCF-7) and 5.5 x 10^5 (MCF-12A) cells/dish. MCF-12A cells were seeded in an unsupplemented medium. After 48 - hours of incubation and reaching 50% confluency, cells were treated with vehicle control (DMSO), concentrations ¼ IC_{50}, IC_{50} and 2 x IC_{50} with **C3** and **C8** working drugs, and positive vehicle control (CDDP), for 48 hours. For MCF-12A cells, complexes were prepared in a supplemented medium. After drug treatment, cells were trypsinized, resuspended in fresh media, seeded in 35 mm dishes at a lower cell density of 1 000 (MCF-7) and 500 (MCF-12A) cells/dish in drug-free media and incubated at 37°C. Cells were monitored for any colonies formed and media was replaced every 2 to 3 days. Cells were immediately fixed, after control dishes showed around 50% colony growth, with 3:1 methanol: acetic acid and stained with crystal violet stain (Sigma Aldrich, 0.5%) in methanol (100%). Dishes were photographed and percentage colonies were counted and determined using ImageJ v1.50i.[48] and the plugin ColonyArea.[49] The number of cells counted using the ImageJ v1.50i. The software was determined for each concentration of the working drug and expressed as a percentage of cell survival rate against % of vehicle-treated control.

4.4.7 Western Blot assays analysis

Western blotting analysis was performed to detect any modifications in protein expression levels of proteins of interest in response to 48- and 72-hours of treatment with **C3** and **CDDP**, prepared at their IC_{50} concentrations. Proteins were harvested from human breast MCF-7 cells using the RIPA buffer method as described.

4.4.7.1 Protein Harvest

Human breast MCF-7 cells were seeded in 6 cm dishes (25 x 10^4 cells/mL). Cells were treated at 60 - 70% confluence with either negative vehicle (DMSO), positive control (CDDP) or **C3** at their IC_{50} concentration for 48- and 72 hours. After 48 and 72 hours of drug treatment, RPMI-1640 cell culture medium was collected in a falcon tube (15 mL), and culture dish washed with 1x PBS solution (1 mL). Cells were lifted with Trypsin/EDTA solution (1 mL) and collected with the RPMI-1640 culture medium (2 mL). Cell suspensions were centrifuged at 2 500 rpm for 2 minutes. The supernatants were discarded by aspiration, and cell pellets were resuspended in 1x PBS (1 mL) to remove the excess or residual cell culture media. The 1x PBS cell

suspensions were centrifuged at 2 500 rpm for 2 minutes and the 1x PBS supernatants were discarded. Complete RIPA buffer solution (Chapter 6) was prepared in an Eppendorf tube (1 mL) and added to the cell pellets, depending on the pellet size (70 - 100 µL). Cell extracts were rolled at 4°C for a minimum of 30 minutes, centrifuged at 12 000 rpm for 20 min at 4°C and the supernatants recovered. The concentrations of proteins were determined using the bicinchoninic acid (BCA) assay (Pierce, Rockford, Illinois, USA), according to the manufacturer's instructions with RIPA buffer used as a standard. Equal amounts of proteins were loaded and PageRuler™ Prestained Protein Ladder, 10 to 180 kDa (Thermo Fisher Scientific, Massachusetts, USA) used for protein sizing. Proteins were separated on 8 - 12% sodium dodecyl sulphate-polyacrylamide gels (SDS-PAGE, Chapter 6) and transferred onto Hybond ECL nitrocellulose membranes (Amersham, BioSciences, United Kingdom). Membranes were stained with Ponceau S stain (Sigma-Aldrich, Missouri, USA) to ensure successful loading and transfer of protein bands. Membranes with water to remove the excess stain. Membranes were blocked for an hour at room temperature with 1x Tris-buffered saline consisting of 0.1% Tween® 20 (TBS/T) in 5% fat-free milk with shaking. After blocking period, membranes were probed with the appropriate primary antibodies (1:1 000 v/v) from cell signalling technology (Massachusetts, USA) rabbit monoclonal antibodies specific to Phospho-Histone H2A.X (Ser139) (#9718), total p53 (Sc-126, mouse monoclonal), caspase 9 (#9502), poly[ADP-ribose] polymerase (Parp, #9542) and p38 (M0800, #9212). The membranes were incubated at 4°C with shaking overnight. Total p38 was used as the loading control. After primary antibody incubation, membranes were washed with 1x TBS/T solution (3 mL) and incubated with horseradish peroxidase (HRP)-conjugated anti-mouse or anti-rabbit secondary antibodies (1:5 000 v/v, BioRad Laboratories, Hercules, California, USA) for an hour at room temperature. Membranes were washed with 1x TBS/T solution (3 mL) and reactive proteins were visualized by enhanced chemiluminescence using SuperSignal West Pico Chemiluminescent Substrate Kit (Thermo Fisher Scientific, Massachusetts, USA). X-ray film was used to capture the protein signal. Densitometry readings were obtained using ImageJ v1.50i[48] and protein expression levels were represented as a ratio of protein of interest/p38 loading control normalised to the vehicle-treated control sample. All western blots are representative of at least three independent biological repeats.

4.4.8 Statistical Analysis

Statistical analysis was conducted with the acquisition of the data represented as mean values and the calculated standard error of the means (SEM) of the three independent experiments. Data were analyzed using GraphPad Prism version 7.0 (GraphPad Software). A parametric unpaired t-test (a student's statistical hypothesis test) was performed, where *p<0.05, **P<0.01 and ***p<0.001 were accepted and considered to be significant.

4.4.9 DNA Binding studies using **C3**

*4.4.9.1 Titration of **C3** with salmon sperm DNA: Interaction of **C3** (dissolved in 0.1% DMSO: PBS mixture) with salmon sperm DNA probed using the ultraviolet-visible spectroscopic technique*

Complex-DNA interaction experiments were performed in PBS buffer solution (pH = 7.4). A stock solution of **C3** (5 mM) was prepared in DMSO (100%) and further diluted with PBS buffer to yield a final solution of 5 x 10^{-4} mol.dm^{-3} of the complex (0.1% DMSO/PBS solution). A reference sample (0.1% DMSO/PBS) was prepared, and the ultraviolet-visible spectrum was recorded on a single beam ultraviolet-visible Agilent instrument from 300 to 1100 nm (λ) range. Before the commencement of the experiments, the spectrum of the *sp*-DNA was recorded to ensure that the DNA was indeed healthy and had not denatured, with an absorption band observed at 250 nm wavelength. Denatured *sp*-DNA often has an absorption band that is visible at wavelengths between 290 - 312 nm. The concentration of *sp*-DNA per nucleotide was determined by ultraviolet-visible absorption measurements following Beer-Lambert's law using molar absorption coefficient ε_{250} = 1 193 M^{-1} cm^{-1}. During the experiments, the concentration of **C3** was kept constant and a solution of *salmon sperm* DNA (120 µL) was added to the 1cm quartz cuvette in increments of 5 µl to the test solution. After each addition of the salmon sperm DNA, the complex-DNA solution was stirred manually and incubated for 5 minutes of equilibration time under physiological conditions at room temperature before the absorbance spectrum was recorded. This process was repeated until the difference in the extinction coefficients of spectra obtained after three consecutive additions of *salmon sperm*-DNA solution were insignificant, indicative of saturation is achieved. This method has an inherent dilution factor occurring with each DNA stock solution being added to the sample cell. To minimize the dilution, a DNA stock solution of a higher concentration was utilized, and the data obtained was adjusted accordingly. Spectra were collected from 250 to 1100 nm after successive additions of salmon sperm DNA into a 2.0 mL of a complex solution. To determine the binding constant (K_b) of **C3**-*salmon sperm* DNA interaction at wavelengths 405

and 657 nm, the results obtained were fitted to the Benesi - Hilderbrand equation,[33] as represented in the results and discussion of the salmon sperm DNA binding titration experiment.

4.4.9.2 pBluescript plasmid DNA agarose gel electrophoresis

pBluescript plasmid DNA was isolated using a Zyppy plasmid isolation kit by following the product protocol. The concentration of DNA was determined and adjusted to 32 µg/mL with 1xTBE buffer. Stock solutions of $[Ru_2(O_2CCH_3)_3(ap)Cl]$ (**C1**), $[Ru_2(O_2CCH_3)_3(4\text{-}CH_3ap)Cl]$ (**C3**), and $[Ru_2(O_2CCH_3)_3(4\text{-}Fap)Cl]$ (**C8**) complexes were prepared in DMSO (34, 340 and 680 µM, 5 µL) and added to pBluescript DNA (40 µg/mL, 10 µL) solution to obtain samples with final concentrations of 10, 100 and 200 µM (total volume 15 µL). Samples were incubated for 24 hours at room temperature. Agarose gel (0.800 g/100 mL) was prepared in 1 x TBE (Tris/borate/EDTA, 100 mL) buffer, followed by 30 seconds intervals of microwave radiation at 300 W to dissolve agarose. The agarose solution was transferred onto the gel mould and allowed to settle at room temperature for 1 hour. After 24 hours of incubation, samples were centrifuged at 6 000 rpm for 1 minute to ensure any condensation droplets that may have formed settled at the bottom of the microtubes. Loading dye (2 µL) was added to each sample before being loaded onto a prepared agarose gel. Samples were loaded in 15 µL quantities onto the gel along with a λ marker. All samples were subjected to electrophoresis for 3 hours at 80 V in 1x TBE buffer. Three hours later, the gel was stained with ethidium bromide (10 mg/mL, 30 µL) in 1x TBE buffer (100 mL). The gel was stained for 15 minutes with constant linear agitation, followed by washings with distilled water (100 mL) for 5 minutes to remove excess stain. The gel was viewed under a UV (254 nm) lamp and photographed.

4.4.10 Preliminary mechanistic solution experimental studies probed using the ultraviolet-visible spectroscopic technique.

*4.4.10.1 Stability study of **C3** in coordinating solvent (DMSO)*

A solution of the complex **C3** (5×10^{-4} mol.dm^{-3}) dissolved in anhydrous DMSO (100%) was prepared followed by a sonication to dissolve all the complex particles. Solutions were further diluted to give a final concentration of 100 µM in DMSO (100%). UV-visible spectra were recorded at various time intervals (after 24 hours) at room temperature. The spectra were recorded on an Agilent Cary 5454 UV-visible spectrophotometer over 800 - 200 nm. The spectral data was plotted, and the binding constants were determined using OriginLab Pro v8.5

software. The complex solution was stored in a vial pill no. 8, 15 x 49 mm, 8.0 mL and kept in a dark cupboard with no exposure to light at room temperature.

*4.4.10.2 Interaction of **C3** with biological media: stability study of **C3** in DMSO/RPMI-1640 medium solution.*

A solution of **C3** was prepared in pure DMSO (5 mM, 100%) and was further diluted in Rosewell Park Memorial Institute medium to give a **C3** concentration of 5 x 10^{-4} M (0.1% DMSO). A reference sample of DMSO (0.1%)/RPMI medium was prepared and the ultraviolet-visible spectrum was recorded on a single beam uv-visible machine from 1100 to 300 nm (λ) range. The solution was decanted and replaced with the sample solution, with spectra recorded after 5 minutes intervals for 520 minutes at room temperature. This process was repeated until the difference in the extinction coefficients of the spectra obtained was insignificant.

*4.4.11 Interaction of the reduced L-glutathione (GSH) and oxidized L-glutathione/methionine form (GSSG) and with **C3**.*

To evaluate the interaction of complex **C3** with glutathione reduced and its disulphide tripeptide molecule GSSG the oxidized form, ultraviolet-visible absorption titration experiments were performed following literature procedures applied for the determination of ruthenium complex-GSH interactions.[50,51]

A phosphate PBS tablet was dissolved in distilled water in a 250 mL volumetric flask (pH = 7.4). **C3** (2.98 mg, 0.005 mmol) was dissolved in DMSO (0.1%)/PBS buffer solution (5 x 10^{-6} mol.dm^{-3}, 10.0 mL). The spectrum of the **C3** solution was recorded on a single beam ultraviolet-visible Agilent instrument from 200 to 1100 nm range and obtained as the sample solution, while the DMSO (0.1%)/PBS buffer solution was used as a reference sample. A stock solution of 0.1 mM of glutathione (1.54 mg, 0.005 mmol) was prepared in phosphate buffer solution (50 mL) and the spectrum of the glutathione solution was recorded, with absorption band peak observed in the ultraviolet region (204 λ, nm). Upon commencement of the titration experiment, the concentration of **C3** was kept constant while the solution of GSH (50 mL) was added to the 1cm quartz cuvette in increments of 2.5 µl to the test (**C3**) solution. After each addition of GSH, the **C3** - GSH solution was stirred manually and incubated for 5 seconds of equilibration time under physiological conditions at room temperature before another absorbance spectrum was recorded. This process was repeated until a significant number of

spectra were collected with clear observable isosbestic points, indicative of the possible dissociation of the axial chloride ligand followed by the coordination of GSH on both vacant axial sites of the Ru_2(II, III) cores. This method has an inherent dilution factor occurring with each increment (2.5 µL) of GSH stock solution to the sample 1 cm quartz cuvette. To minimize the dilution, a GSH stock solution of a higher concentration was utilized, and the data obtained was adjusted accordingly. Spectra were collected from 250 to 1100 nm after successive additions of GSH into a 1.3 mL of **C3** solution. To determine the binding constant (K_b) of **C3** - GSH interaction at wavelength 657 nm, the results obtained were fitted using the equation outlined below from published methods.[51,50] A similar titration experiment was repeated with 0.1 mM of GSSG (3.04 mg, 0.005 mol), an oxidized derivative of glutathione, to investigate the binding strength of **C3** with the produced GSSG intracellularly. The binding constant was calculated from the ultraviolet-visible titration spectra, and using the following the concepts described below:

For chemical reactions where a ligand binds to a metal centre, M, as represented in equation (1), the relationship between the concentration of the species in solution and the equilibrium constant is given by equation (2) as follows:

$$M + nL \rightleftharpoons ML_n \qquad (1)$$

$$\log\left(\frac{[MLn]}{[M]}\right) = \log(K) + n\log(L) \qquad (2)$$

If the ligand and metal complex species both have peculiar ultraviolet-visible absorption profiles, the initial (A_i) and final (A_f) absorbances at a specific wavelength are described by equations (3), (4) and (5) given below:

$$A_i = \varepsilon_M\, b\, C_M \qquad (3)$$

$$A_f = \varepsilon_{MLn}\, b\, C_{MLn} \qquad (4)$$

$$A_o = A_i + A_f$$

$$\therefore A_o = \varepsilon_M\, b\, C_M + \varepsilon_{MLn}\, b\, C_{MLn} \qquad (5)$$

where, A_o = the absorbance at a given point during the titration. According to the mass balance equation,

$$C_M = C_{MLn}$$

$$\therefore C_M = [M] + [ML_n], \text{ in solution}$$

Equation (3) can be expressed in absorbance terms from the equations above (3, 4 and 5). This will solve for equation (6) below, where the [M] and [MLn] terms are substituted for by the absorbance terms:

$$\log [(A_o - A_i) / (A_f - A_o)] = \log (K) + n \log [L] \qquad (6)$$

A plot of log $[(A_o - A_i)/(A_f - A_o)]$ versus log [L], should yield a linear straight graph with the slope corresponding to the number of bound ligands, *n*. The y-intercept determined from the linear plot can be equated to the y-intercept in equation 7 to determine the binding constant.

4.5 REFERENCES

1 B. K. Keppler, M. Henn, U. M. Juhl, M. R. Berger, R. Niebl and F. E. Wagner, 1989, vol. 10, pp. 41–69.

2 C. E. J. Van Rensburg, E. Kreft, J. C. Swarts, S. R. Dalrymple, D. M. MacDonald, M. W. Cooke and M. A. S. Aquino, *Anticancer Res.*, **22**, 889–92.

3 Hanif-Ur-Rehman, T. E. Freitas, R. N. Gomes, A. Colquhoun and D. de Oliveira Silva, *J. Inorg. Biochem.*, 2016, **165**, 181–191.

4 G. Ribeiro, M. Benadiba, A. Colquhoun and D. de Oliveira Silva, *Polyhedron*, 2008, **27**, 1131–1137.

5 A. Andrade, S. . Namora, R. . Woisky, G. Wiezel, R. Najjar, J. A. . Sertié and D. de Oliveira Silva, *J. Inorg. Biochem.*, 2000, **81**, 23–27.

6 M. Benadiba, R. R. P. dos Santos, D. de O. Silva and A. Colquhoun, *J. Inorg. Biochem.*, 2010, **104**, 928–935.

7 S. R. Alves, A. Colquhoun, X. Y. Wu and D. de Oliveira Silva, *J. Inorg. Biochem.*, 2020, **205**, 1–9.

8 T. L. Riss, R. A. Moravec, A. L. Niles, S. Duellman, H. A. Benink, T. J. Worzella and L. Minor, *Cell Viability Assays*, 2004.

9 A. Koch, P. Tamez, J. Pezzuto and D. Soejarto, *J. Ethnopharmacol.*, 2005, **101**, 95–99.

10 M.-N. T. Nguyen and T.-D. Ho-Huynh, *BMC Complement. Altern. Med.*, 2016, **16**, 1–10.

11 R. B. Badisa, S. F. Darling-Reed, P. Joseph, J. S. Cooperwood, L. M. Latinwo and C. B. Goodman, *Anticancer Res.*, 2009, **29**, 2993–6.

12 M. Al-Hajj, M. S. Wicha, A. Benito-Hernandez, S. J. Morrison and M. F. Clarke, *Proc. Natl. Acad. Sci.*, 2003, **100**, 3983–3988.

13 N. A. P. Franken, H. M. Rodermond, J. Stap, J. Haveman and C. van Bree, *Nat. Protoc.*, 2006, **1**, 2315–2319.

14 L. Galluzzi, S. A. Aaronson, J. Abrams, E. S. Alnemri, D. W. Andrews, E. H. Baehrecke, N. G. Bazan, M. V. Blagosklonny, K. Blomgren, C. Borner, D. E. Bredesen, C. Brenner, M. Castedo, J. A. Cidlowski, A. Ciechanover, G. M. Cohen, V. De Laurenzi, R. De Maria, M. Deshmukh, B. D. Dynlacht, W. S. El-Deiry, R. A. Flavell, S. Fulda, C. Garrido, P. Golstein, M.-L. Gougeon, D. R. Green, H. Gronemeyer, G. Hajnóczky, J. M. Hardwick, M. O. Hengartner, H. Ichijo, M. Jäättelä, O. Kepp, A. Kimchi, D. J. Klionsky, R. A. Knight, S. Kornbluth, S. Kumar, B. Levine, S. A. Lipton, E. Lugli, F. Madeo, W. Malorni, J.-C. Marine, S. J. Martin, J. P. Medema, P. Mehlen, G. Melino, U.

M. Moll, E. Morselli, S. Nagata, D. W. Nicholson, P. Nicotera, G. Nuñez, M. Oren, J. Penninger, S. Pervaiz, M. E. Peter, M. Piacentini, J. H. M. Prehn, H. Puthalakath, G. A. Rabinovich, R. Rizzuto, C. M. P. Rodrigues, D. C. Rubinsztein, T. Rudel, L. Scorrano, H.-U. Simon, H. Steller, J. Tschopp, Y. Tsujimoto, P. Vandenabeele, I. Vitale, K. H. Vousden, R. J. Youle, J. Yuan, B. Zhivotovsky and G. Kroemer, *Cell Death Differ.*, 2009, **16**, 1093–1107.

15 A.-M. Florea and D. Büsselberg, *Cancers (Basel).*, 2011, **3**, 1351–1371.

16 V. Valdiglesias, S. Giunta, M. Fenech, M. Neri and S. Bonassi, *Mutat. Res. Mutat. Res.*, 2013, **753**, 24–40.

17 A. Kinner, W. Wu, C. Staudt and G. Iliakis, *Nucleic Acids Res.*, 2008, **36**, 5678–5694.

18 R. V. Sionov and Y. Haupt, *Oncogene*, 1999, **18**, 6145–6157.

19 J. Chen, F. Peng, Y. Zhang, B. Li, J. She, X. Jie, Z. Zou, M. Chen and L. Chen, *Eur. J. Med. Chem.*, 2017, **140**, 104–117.

20 F. Mello-Andrade, A. P. M. Guedes, W. C. Pires, V. S. Velozo-Sá, K. A. Delmond, D. Mendes, M. S. Molina, L. Matuda, M. A. M. de Sousa, P. Melo-Reis, C. C. Gomes, C. H. Castro, M. A. P. Almeida, C. F. M. Menck, A. A. Batista, R. Burikhanov, V. M. Rangnekar and E. Silveira-Lacerda, *J. Inorg. Biochem.*, 2022, **226**, 1–12.

21 S. Fulda and K.-M. Debatin, *Oncogene*, 2006, **25**, 4798–4811.

22 D. Ghatage, S. Gosavi, S. Ganvir and V. Hazarey, *J. Orofac. Sci.*, 2012, **4**, 103–107.

23 O. Surova and B. Zhivotovsky, *Oncogene*, 2013, **32**, 3789–3797.

24 A. H. Boulares, A. G. Yakovlev, V. Ivanova, B. A. Stoica, G. Wang, S. Iyer and M. Smulson, *J. Biol. Chem.*, 1999, **274**, 22932–22940.

25 R. A. Howard, A. P. Kimball and J. L. Bear, *Cancer Res.*, 1979, **39**, 2568–2573.

26 H. T. Chifotides, J. M. Koomen, M. Kang, S. E. Tichy, K. R. Dunbar and D. H. Russell, *Inorg. Chem.*, 2004, **43**, 6177–6187.

27 K. Sorasaenee, P. K. L. Fu, A. M. Angeles-Boza, K. R. Dunbar and C. Turro, *Inorg. Chem.*, 2003, **42**, 1267–1271.

28 H. T. Chifotides and K. R. Dunbar, *Acc. Chem. Res.*, 2005, **38**, 146–156.

29 H. T. Chifotides, P. K. L. Fu, K. R. Dunbar and C. Turro, *Inorg. Chem.*, 2004, **43**, 1175–1183.

30 R. L. S. R. Santos, R. van Eldik and D. de Oliveira Silva, *Inorg. Chem.*, 2012, **51**, 6615–6625.

31 J. Liu, T. Zhang, T. Lu, L. Qu, H. Zhou, Q. Zhang and L. Ji, *J. Inorg. Biochem.*, 2002, **91**, 269–276.

32 M. Sirajuddin, S. Ali and A. Badshah, *J. Photochem. Photobiol. B Biol.*, 2013, **124**, 1–19.

33 A. Wolfe, G. H. Shimer and T. Meehan, *Biochemistry*, 1987, **26**, 6392–6396.

34 P. H. Johnson and L. I. Grossman, *Biochemistry*, 1977, **16**, 4217–4225.

35 K. E. Prosser, S. W. Chang, F. Saraci, P. H. Le and C. J. Walsby, *J. Inorg. Biochem.*, 2017, **167**, 89–99.

36 K. Dunlop, R. Wang, T. Stanley Cameron and M. A. S. Aquino, *J. Mol. Struct.*, 2014, **1058**, 122–129.

37 K. M. Kadish, L.-L. Wang, A. Thuriere, L. Giribabu, R. Garcia, E. Van Caemelbecke and J. L. Bear, *Inorg. Chem.*, 2003, **42**, 8309–8319.

38 S. J. Dougan, A. Habtemariam, S. E. McHale, S. Parsons and P. J. Sadler, *Proc. Natl. Acad. Sci.*, 2008, **105**, 11628–11633.

39 M. Nešić, I. Popović, A. Leskovac and M. Petković, *BioMetals*, 2016, **29**, 921–933.

40 P. K. Sasmal, C. N. Streu and E. Meggers, *Chem. Commun.*, 2013, **49**, 1581–1587.

41 A. Pompella, A. Visvikis, A. Paolicchi, V. De Tata and A. F. Casini, *Biochem. Pharmacol.*, 2003, **66**, 1499–1503.

42 P. Schluga, C. G. Hartinger, A. Egger, E. Reisner, M. S. Galanski, M. A. Jakupec and B. K. Keppler, *Dalt. Trans.*, 2006, **6**, 1796–1802.

43 N. Traverso, R. Ricciarelli, M. Nitti, B. Marengo, A. L. Furfaro, M. A. Pronzato, U. M. Marinari and C. Domenicotti, *Oxid. Med. Cell. Longev.*, 2013, **2013**, 1–10.

44 A. K. Godwin, A. Meister, P. J. O'Dwyer, C. S. Huang, T. C. Hamilton and M. E. Anderson, *Proc. Natl. Acad. Sci.*, 1992, **89**, 3070–3074.

45 S. Daubeuf, P. Leroy, A. Paolicchi, A. Pompella, M. Wellman, M. M. Galteau and A. Visvikis, *Biochem. Pharmacol.*, 2002, **64**, 207–216.

46 Roche Diagnostics GmbH, *Protocol*, 2016, 6–9.

47 G. Indrayanto, G. S. Putra and F. Suhud, in *Profiles of Drug Substances, Excipients and Related Methodology*, Elsevier Inc., 1st edn., 2021, vol. 46, pp. 273–307.

48 C. A. Schneider, W. S. Rasband and K. W. Eliceiri, *Nat. Methods*, 2012, **9**, 671–675.

49 C. Guzmán, M. Bagga, A. Kaur, J. Westermarck and D. Abankwa, *PLoS One*, 2014, **9**, 1–9.

50 T. J. Egan, W. W. Mavuso, D. C. Ross and H. M. Marques, *J. Inorg. Biochem.*, 1997, **68**, 137–145.

51 C. C. Sousa, G. A. Dziwornu, H. C. Quadros, J. H. Araujo-Neto, K. Chibale and D. R. M. Moreira, *ACS Infect. Dis.*, 2022, **8**, 1700–1710

CHAPTER 5

Conclusions and future work

5.1 CONCLUSIONS

The overall aim of this project was to synthesize mono-substituted anilinopyridinate triacetatechlorodiruthenium(II, III) complexes as promising anticancer agents against oestrogen receptor-positive (ER +ve) MCF-7 and triple-negative aggressive and invasive MDA-MB-231 human breast cancer cells. This study further seeks to contribute novel findings and shed light on the mode of action of these paddlewheel Ru_2^{5+} compounds. Complexes are moderately cytotoxic against human breast MCF-7 and MDA-MB-231 cancer cells. Initially, eight (8) *N,N′*-anilinopyridinate ligands (R-ap) were synthesized by following published literature procedures from commercially available reagents. The synthesis was successfully achieved by following an addition elimination reaction of 2-bromobenzene with a respective R-aniline to yield the desired ligands with electron-donating (CH_3) and withdrawing (F) substituent localized within the *ortho*- and *para*-positions of the aniline phenyl ring. All ligands (**L1** - **L8**) were successfully isolated in favourable moderate to good yields and purified *via* recrystallization with hot hexanes to give pure and cream-white crystalline materials. To confirm and ascertain their structures, the synthesized ligands were fully characterized using 1-D and 2-D NMR, infrared spectroscopy, and mass spectrometry. The obtained spectroscopic data agrees with the published methods and correlates well with the proposed structural features of the compounds.

Ligands (**L1** - **L8**) were evaluated for their *in vitro* cytotoxic properties by performing preliminary screen MTT cell viability assay tests against oestrogen receptor-positive MCF-7 and triple-negative and invasive MDA-MB-231 human breast cancer subtypes. Their toxicity properties were evaluated against the mammary non-malignant MCF-12A epithelial cell line. All ligands did not cause significant inhibition of viable MCF-7 and MDA-MB-231 cancer cells. However, the human breast MCF-12A epithelial cells were the most sensitive to treatment with all the synthesized ligands.

All synthesized ligands were complexed by following a metathesis displacement of a single acetate bridging ligand, followed by the equatorial coordination of one equivalence of the nitrogen-nitrogen anilinopyridnate equatorial bridging ligand to yield the desired mono-substituted anilinopyridinate triacetatechlorodiruthenium(II, III) complexes (**C1** - **C8**). The synthetic procedure yielded complexes of the general chemical formula $[Ru_2(O_2CCH_3)_3(R\text{-}ap)Cl]$, where R is the substituted methyl or fluorine group localized on the *ortho*- or *para*-positions of the aniline phenyl ring of the ligand. To ascertain the structural identity, the

synthesized complexes were characterized fully using spectroscopic and analytical techniques namely, ultraviolet-visible, and infrared spectroscopy, x-ray single crystallography and high-resolution mass spectrometric techniques. The obtained characterization data was in full agreement with the published reports and correlated to the proposed paddlewheel diruthenium(II, III) complexes.

All synthesized complexes (**C1 - C8)** were tested for their cytotoxic properties against the above-mentioned human breast cancer cells and subjected to a multidose 72-hour treatment. $[Ru_2(O_2CCH_3)_3(4\text{-}CH_3ap)Cl]$ (**C3**) and $[Ru_2(O_2CCH_3)_3(4\text{-}Fap)Cl]$ (**C8**) complexes showed promising anticancer properties and were selective for MCF-7 cells, with favourable IC_{50} values of 39.0 µM (**C3**) and 47.0 µM (**C8**) and selectivity indices ≥ 1.50. **C3** showed comparable cytotoxic properties to cisplatin (IC_{50} = 37.0 µM) when subjected to similar concentrations and treatment conditions. Overall, these compounds showed favourable toxicity profiles tested on human breast MCF-12A cells, which further suggests that compounds may be associated with minimal side effects. Both compounds inhibited the long-term survival and regeneration of MCF-7 cell colonies when monitored over a period of seven days. **C3** was shown to mediate its anticancer activity in MCF-7 cells through double-stranded DNA breaks and induced apoptosis markers.

The stability of the paddlewheel Ru_2^{5+} complex, **C3** (selected as a prototype) was studied in DMSO (solvent used in *in vitro* biological assays) and in DMSO (0.1%)/RPMI media solution. Experiments were performed by incubation of the compound dissolved in an aqueous solution and monitored over an extended period. Experiments were probed using the ultraviolet-visible technique and spectra were collected over time. Ultraviolet-visible spectra collected **C3** show good stability when dissolved in the organic solvent, DMSO with the ligand-metal and metal-metal charge transfer transition bands being prominent and observed for 7 days in solution at room temperature. Furthermore, the stability of **C3** was followed in DMSO (0.1%)/RPMI media solution. The acquired spectra suggest that **C3** is only stable in DMSO (0.1%)/RPMI media for a few hours (≈ 3 - hours) and further undergoes ligand exchange reactions, forming a new species in solution.

C1, **C2** and **C7** were investigated for their interactions with plasmid DNA *via* agarose gel electrophoresis at various concentrations. Compounds did not cause any electrophoretic modifications of the plasmid DNA bands nor did they induce retardations of the bands. This

suggests that compounds do not interact with plasmid double-stranded DNA. Furthermore, salmon-sperm DNA titrations were performed and probed using an ultraviolet-visible spectroscopic technique to investigate whether **C3** binds to salmon sperm DNA and thus targets DNA as a mechanism of action responsible for the compound's cytotoxic properties. The spectra and the binding constants obtained from the linear plots of $\frac{[DNA,\mu M]}{(Ea-Ef)}$ versus [DNA, µM] suggest that compounds do not interact with salmon sperm (*sp*) DNA as the binding constants obtained were insignificant. Lastly, interactions with glutathione binding probed *via* titration experiments using ultraviolet-visible spectroscopic technique suggest that **C3** reacts rapidly with glutathione at room temperature. The first isosbestic band suggests that the chloride ion is displaced, followed by the coordination of a single moiety of a glutathione molecule while the presence of the second band suggests the displacement of the weakly bound solvent water molecule being replaced with another GSH molecule.

Overall, it is worth noting and can be concluded that in this study, the incorporation of a single moiety of the nitrogen-based anilinopyridinate ligands into the paddlewheel acetate diruthenium(II, III) coordination increased the hydrophilicity of complexes and thus offers the possibility of performing biological assays and investigating their anticancer properties.

5.2 FUTURE WORK

5.2.1 Structural modifications to enhance the efficacy of the studied paddlewheel complexes.

The synthesized paddlewheel mono-substituted R-ap triacetatechlorodiruthenium(II, III) complexes studied herein display promising cytotoxic properties against human breast cancer cells. These results raise a few new ideas to further enhance their cytotoxic properties through axial and equatorial modifications as shown in Figure 5.1. In addition, further biological experiments to gain more insights into their mechanism of action owing to their anticancer activity and profiles can be performed.

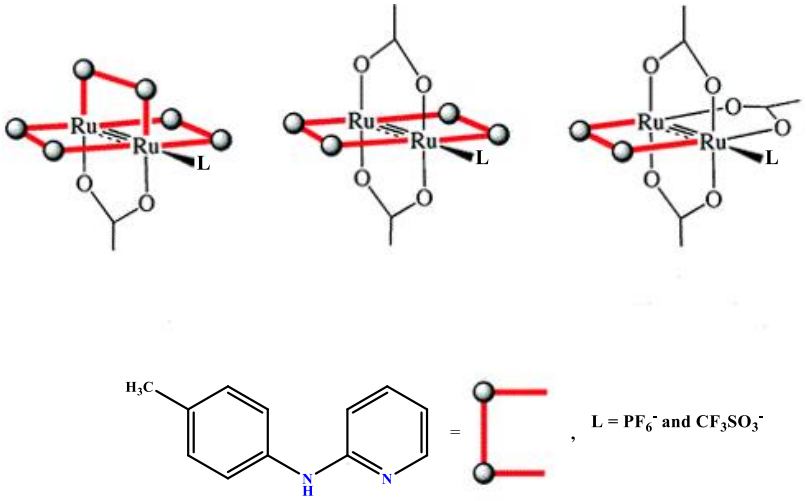

Figure 5.1 The equatorial and axial substitution on the Ru_2^{5+} core.

Based on obtained *in vitro* biological data of **C3** against MCF-7 human breast cancer cells, structural modifications can include the substitution of the axially coordinate chloride ligand with a more electron-withdrawing substituent such as a hexafluorophosphate (Pf_6^-) or a triflate anion ($CF_3SO_3^-$) on the axial sites of the diruthenium(II, III) cores and further substitution of the equatorial bridging ligands with the 4-methyl anilinopyridinate ligand (*n* = 2 or 3, where n = the number of 4-CH_3ap ligands to be substituted on the equatorial positions). The cytotoxic properties and activity of **C3** may be the result of the increased water-soluble properties and redox accessibility relative to the $[Ru_2(O_2CCH_3)_4Cl]$ precursor complex reported to be insoluble in aqueous solvents.

5.2.2 Further screening of complexes: Biological assays to be conducted.

While the library of ruthenium coordination compounds has been extensively reported to possess favourable cytotoxic effects against a wide variety of cancers and with less or minimal side effects compared to the platinum-based chemotherapeutic drugs such as cisplatin, the mechanism of action of the compounds is yet to be fully elucidated and well understood. Future work entails further characterization of molecular apoptotic protein markers to ascertain that indeed **C3** induces apoptosis as a mechanism of cell death in human breast MCF-7 cancer cells. In-depth characterization of the anticancer mechanisms of **C3** and **C8** and investigations involving other potential mechanisms of cell death are yet to be performed. These ideas may contribute novel findings towards the anticancer mechanistic properties of paddlewheel Ru_2^{5+} compounds.

CHAPTER 6

APPENDICES

Nuclear Magnetic Resonance (NMR) spectroscopy of arene mono-ruthenium(II) complexes

*^{1}H NMR spectrum of [RuCl$_2$(η^6-C$_6$H$_5$OCH$_2$CH$_2$OH)(P{Ph}$_3$)] (**C10**).*

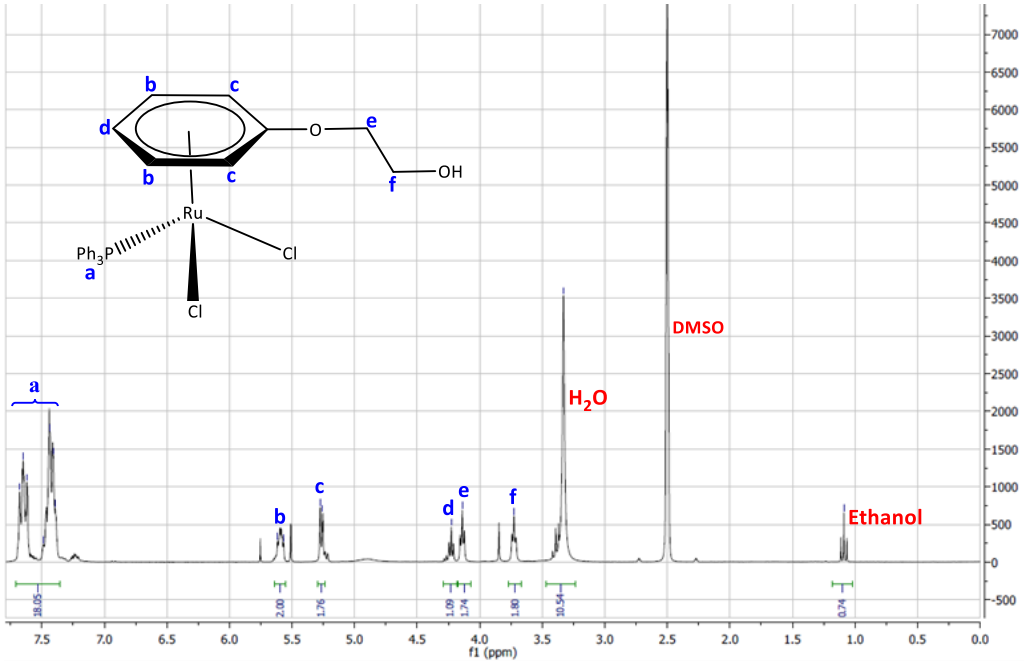

Figure 6.1 ^{1}H NMR spectrum of **C10** recorded in DMSO-d$_6$.

*^{1}H NMR spectrum of [RuCl$_2$(η^6-C$_6$H$_5$OCH$_2$CH$_2$OH)(P{OPh}$_3$)] (**C11**).*

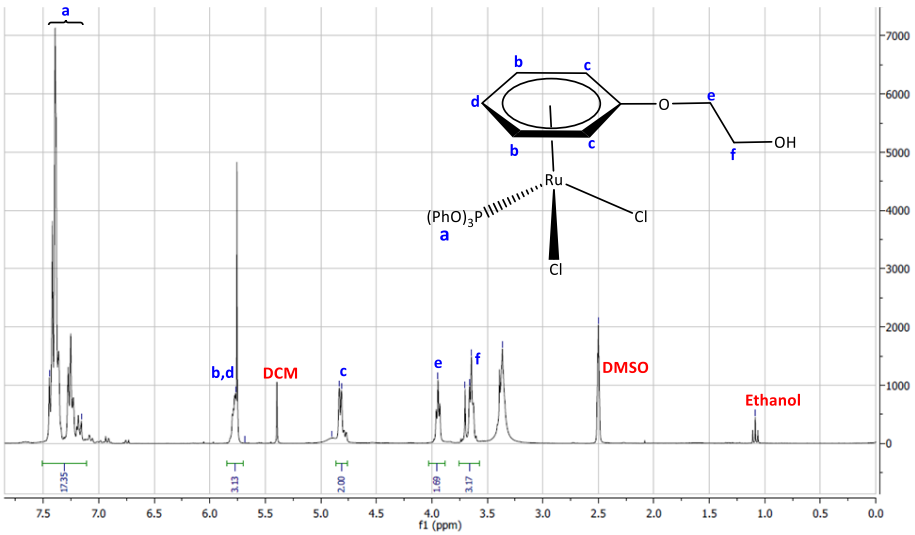

Figure 6.2 ^{1}H NMR spectrum of complex **C11** recorded in DMSO-d$_6$.

*^{1}H NMR spectrum of [RuCl$_2$(η^6-C$_6$H$_5$OCH$_2$CH$_2$OH){O(CH$_3$)$_3$}] (**C12**).*

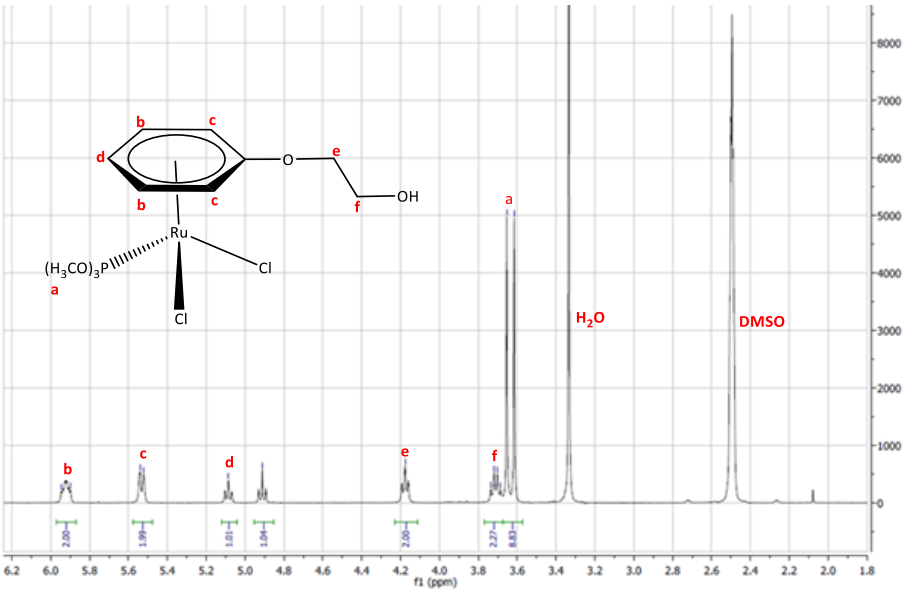

Figure 6.3 ^{1}H NMR spectrum of complex **C12** recorded in DMSO-d$_6$.

^{1}H NMR spectrum of [RuCl$_2$(η^6-C$_6$H$_5$OCH$_2$CH$_2$OH){O(CH$_3$)$_3$}] (**C13**).

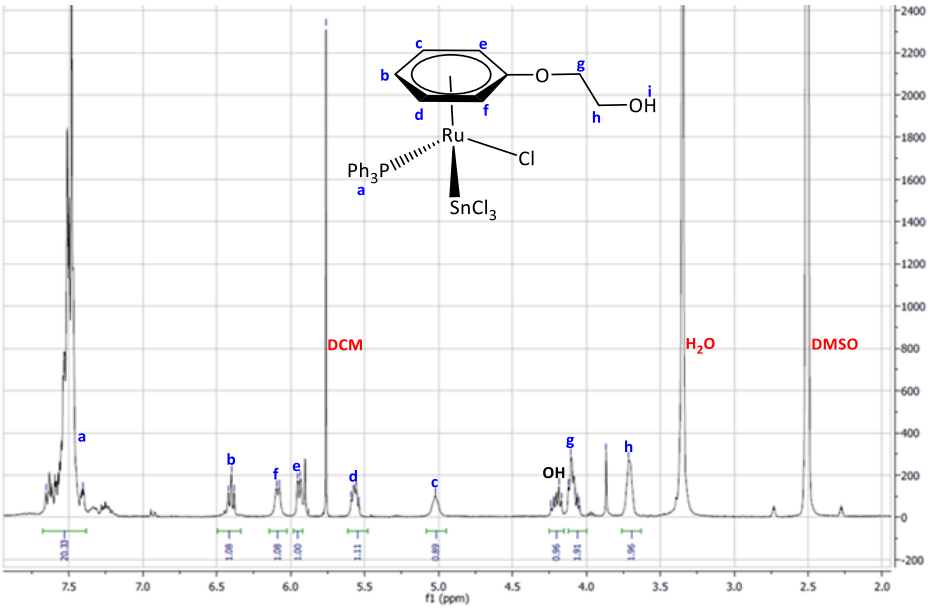

Figure 6.4 ^{1}H NMR spectrum of complex **C13** recorded in DMSO-d$_6$.

$^{31}P\{1H\}$ *spectrum of* $[RuCl(\eta^6\text{-}C_6H_5OCH_2CH_2OH)(PPh_3)(SnCl_3)]$ (**C13**).

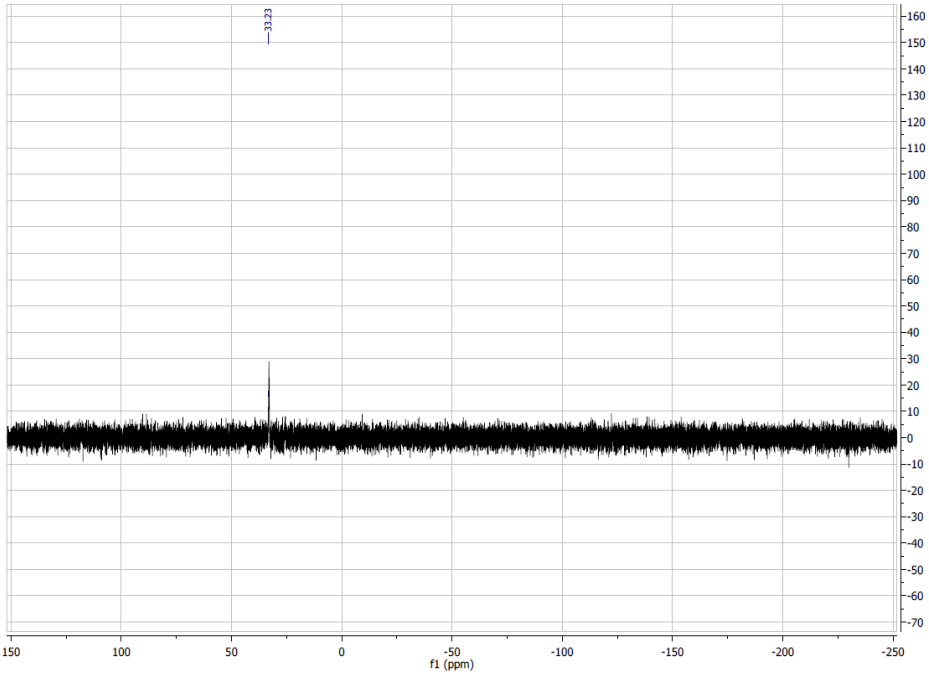

Figure 6.5 $^{31}P\{1H\}$ NMR spectrum of **C13** recorded in H_3PO_3.

^{1}H-*NMR* spectrum of complex $[RuCl(\eta^6\text{-}C_6H_5OCH_2CH_2OH)(P\{OPh\}_3)(SnCl_3)]$ **C14.**

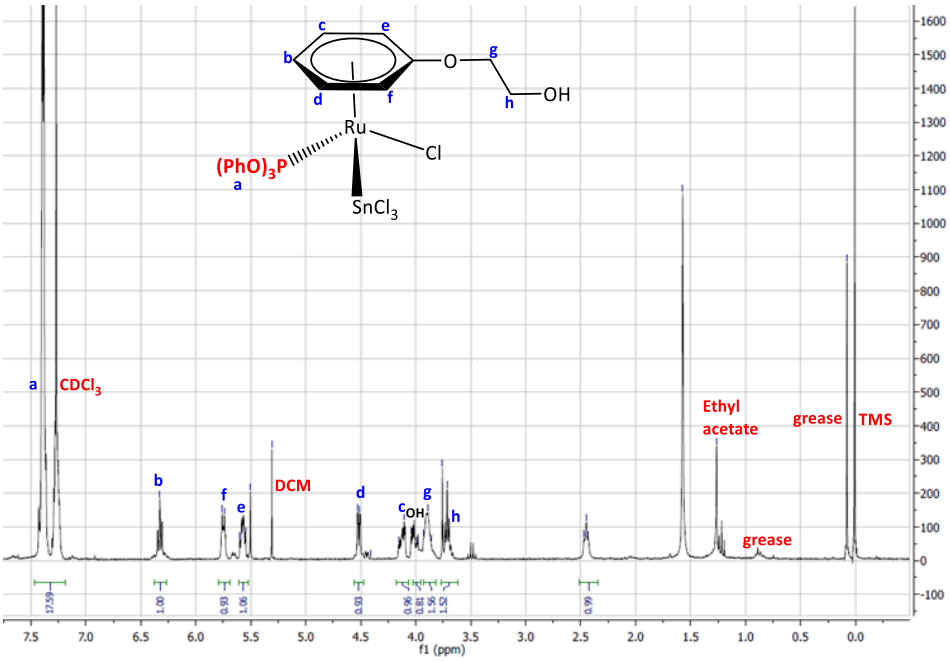

Figure 6.6 ^{1}H NMR spectrum of complex **C14** recorded in $CDCl_3$.

$^{31}P\{1H\}$ spectrum of $[RuCl(\eta^6\text{-}C_6H_5OCH_2CH_2OH)(P\{OPh\}_3)(SnCl_3)]$ (**C14**).

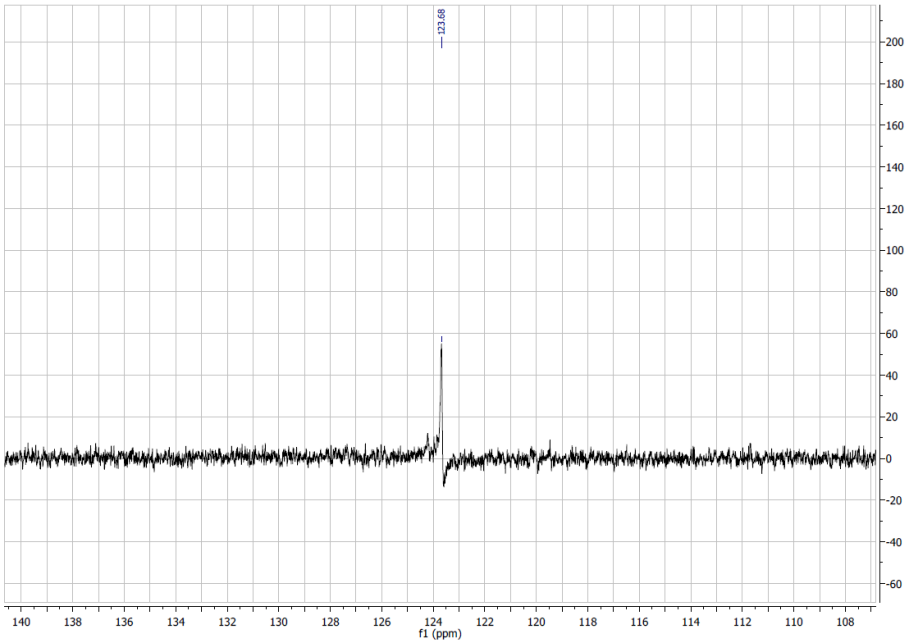

Figure 6.7 $^{31}P\ \{^1H\}$ NMR spectrum of **C14**.

*Single X-ray crystallographic CheckCIF Report of **C14***

18/12/2023, 20:24 checkCIF/PLATON report

No syntax errors found. CIF dictionary
Please wait while processing .... Interpreting this report

Datablock: 1258j

Bond precision: C-C = 0.0280 A Wavelength=0.71073
Cell: a=14.599(3) b=10.723(2) c=18.291(4)
alpha=90 beta=90 gamma=90
Temperature: 100 K

	Calculated	Reported
Volume	2863.4(10)	2863.5(10)
Space group	P c a 21	Pca2(1)
Hall group	P 2c -2ac	?
Moiety formula	C26 H25 Cl4 O5 P Ru Sn	?
Sum formula	C26 H25 Cl4 O5 P Ru Sn	C26 H25 Cl4 O5 P Ru Sn
Mr	810.01	809.99
Dx,g cm-3	1.879	1.879
Z	4	4
Mu (mm-1)	1.865	1.865
F000	1592.0	1592.0
F000'	1587.61	
h,k,lmax	17,12,21	17,12,21
Nref	5842[2610]	5842
Tmin,Tmax	0.799,0.861	0.755,0.865
Tmin'	0.742	

Correction method= # Reported T Limits: Tmin=0.755 Tmax=0.865
AbsCorr = MULTI-SCAN
Data completeness= 1.93/1.00 Theta(max)= 25.000
R(reflections)= 0.0988(4685) wR2(reflections)= 0.1928(5842)
S = 1.273 Npar= 355

The following ALERTS were generated. Each ALERT has the format
test-name_ALERT_alert-type_alert-level.
Click on the hyperlinks for more details of the test.

Alert level A

PLAT213_ALERT_2_A Atom C22 has ADP max/min Ratio ..... 5.1 prolat
PLAT375_ALERT_2_A Strange C-O-H Geometry (C-O > 1.45 Ang) ..... O5 Check

Alert level B

PLAT213_ALERT_2_B Atom C3 has ADP max/min Ratio ..... 4.7 oblate
PLAT213_ALERT_2_B Atom C18 has ADP max/min Ratio ..... 4.1 oblate
PLAT220_ALERT_2_B Non-Solvent Resd 1 C Ueq(max)/Ueq(min) Range 7.8 Ratio
PLAT241_ALERT_2_B High 'MainMol' Ueq as Compared to Neighbors of C26 Check
PLAT242_ALERT_2_B Low 'MainMol' Ueq as Compared to Neighbors of C18 Check
PLAT342_ALERT_3_B Low Bond Precision on C-C Bonds ..... 0.028 Ang.
PLAT415_ALERT_2_B Short Inter D-H..H-X H17 ..H55 . 1.91 Ang.
1/2+x,-y,z = 3_555 Check
PLAT420_ALERT_2_B D-H Without Acceptor O5 --H55 . Please Check

Alert level C

STRVA01_ALERT_4_C Flack test results are ambiguous.
From the CIF: _refine_ls_abs_structure_Flack 0.450
From the CIF: _refine_ls_abs_structure_Flack_su 0.080
PLAT090_ALERT_3_C Poor Data / Parameter Ratio (Zmax > 18) ..... 7.35 Note
PLAT213_ALERT_2_C Atom Cl3 has ADP max/min Ratio ..... 3.1 prolat
And 5 other PLAT213 Alerts
More ...
PLAT220_ALERT_2_C Non-Solvent Resd 1 O Ueq(max)/Ueq(min) Range 3.5 Ratio
PLAT222_ALERT_3_C Non-Solv. Resd 1 H Uiso(max)/Uiso(min) Range 7.9 Ratio
PLAT230_ALERT_2_C Hirshfeld Test Diff for C18 --C26 . 5.5 s.u.
PLAT232_ALERT_2_C Hirshfeld Test Diff (M-X) Ru1 --C14 . 5.7 s.u.
PLAT232_ALERT_2_C Hirshfeld Test Diff (M-X) Ru1 --C17 . 5.5 s.u.
PLAT234_ALERT_4_C Large Hirshfeld Difference C1 --C5 . 0.22 Ang.
And 4 other PLAT234 Alerts
More ...
PLAT241_ALERT_2_C High 'MainMol' Ueq as Compared to Neighbors of O3 Check
And 3 other PLAT241 Alerts
More ...
PLAT360_ALERT_2_C Short C(sp3)-C(sp3) Bond C18 - C26 . 1.37 Ang.

18/12/2023, 20:24 checkCIF/PLATON report

Alert level G

PLAT003_ALERT_2_G	Number of Uiso or Uij Restrained non-H Atoms ...	8 Report
PLAT005_ALERT_5_G	No Embedded Refinement Details Found in the CIF	Please Do !
PLAT007_ALERT_5_G	Number of Unrefined Donor-H Atoms	1 Report
PLAT083_ALERT_2_G	SHELXL Second Parameter in WGHT Unusually Large	53.69 Why ?
PLAT301_ALERT_3_G	Main Residue Disorder .....(Resd 1)	3% Note
PLAT432_ALERT_2_G	Short Inter X...Y Contact Cl33 ..C26 x,1+y,z =	3.19 Ang. 1_565 Check
PLAT860_ALERT_3_G	Number of Least-Squares Restraints	49 Note
PLAT899_ALERT_4_G	SHELXL97 is Deprecated and Succeeded by SHELXL	2018 Note

2 ALERT level A = Most likely a serious problem - resolve or explain
8 ALERT level B = A potentially serious problem, consider carefully
23 ALERT level C = Check. Ensure it is not caused by an omission or oversight
8 ALERT level G = General information/check it is not something unexpected

0 ALERT type 1 CIF construction/syntax error, inconsistent or missing data
27 ALERT type 2 Indicator that the structure model may be wrong or deficient
5 ALERT type 3 Indicator that the structure quality may be low
7 ALERT type 4 Improvement, methodology, query or suggestion
2 ALERT type 5 Informative message, check

It is advisable to attempt to resolve as many as possible of the alerts in all categories. Often the minor alerts point to easily fixed oversights, errors and omissions in your CIF or refinement strategy, so attention to these fine details can be worthwhile. In order to resolve some of the more serious problems it may be necessary to carry out additional measurements or structure refinements. However, the purpose of your study may justify the reported deviations and the more serious of these should normally be commented upon in the discussion or experimental section of a paper or in the "special_details" fields of the CIF. checkCIF was carefully designed to identify outliers and unusual parameters, but every test has its limitations and alerts that are not important in a particular case may appear. Conversely, the absence of alerts does not guarantee there are no aspects of the results needing attention. It is up to the individual to critically assess their own results and, if necessary, seek expert advice.

Publication of your CIF in IUCr journals

A basic structural check has been run on your CIF. These basic checks will be run on all CIFs submitted for publication in IUCr journals (*Acta Crystallographica*, *Journal of Applied Crystallography*, *Journal of Synchrotron Radiation*); however, if you intend to submit to *Acta Crystallographica Section C* or *E* or *IUCrData*, you should make sure that full publication checks are run on the final version of your CIF prior to submission.

Publication of your CIF in other journals

Please refer to the *Notes for Authors* of the relevant journal for any special instructions relating to CIF submission.

PLATON version of 07/08/2019; check.def file version of 30/07/2019

Datablock 1258j - ellipsoid plot

18/12/2023, 20:24 checkCIF/PLATON report

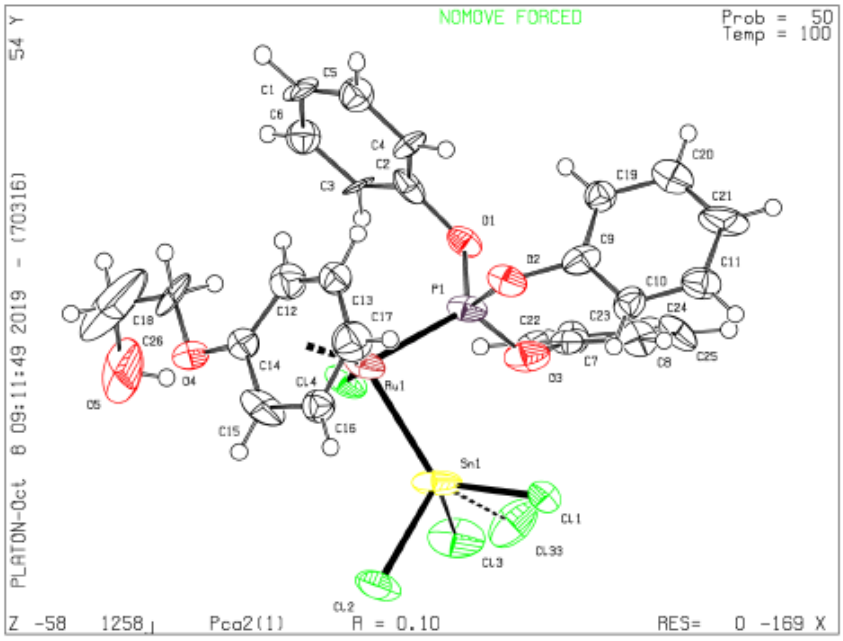

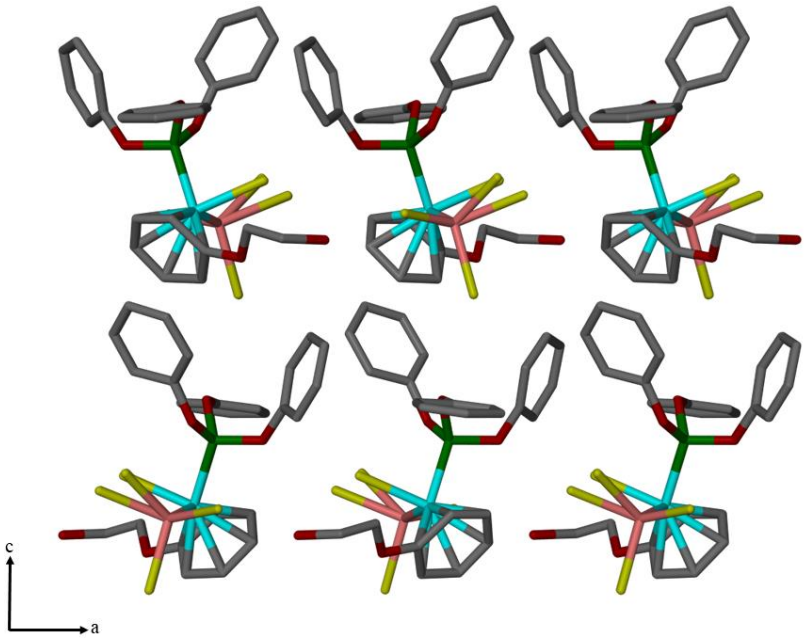

Figure 6.8 Single X-ray crystallographic packing diagram of **C14** around the b-axis.

Thermogravimetric analysis curves of **C13** and **C14**.

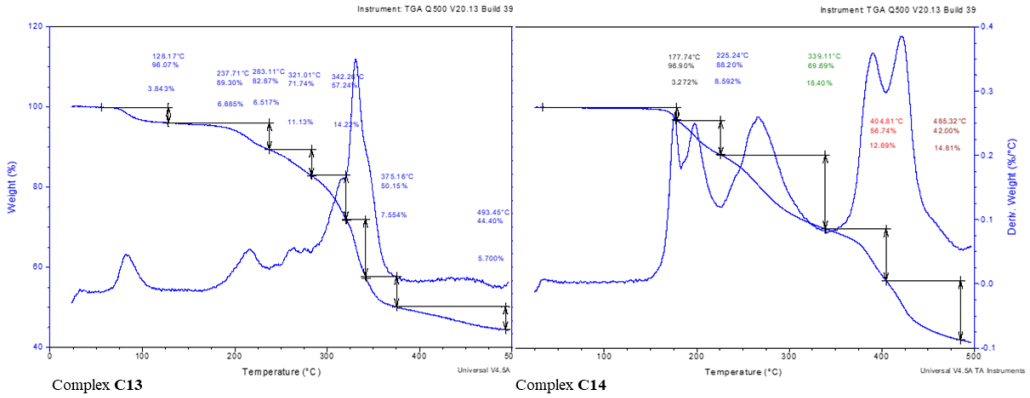

Figure 6.9 Thermogravimetric analysis curves of complexes **C13** and **C14**, respectively.

Dose-response curves of **C13** and **C14**.

*Dose-response curves for complex **C13***

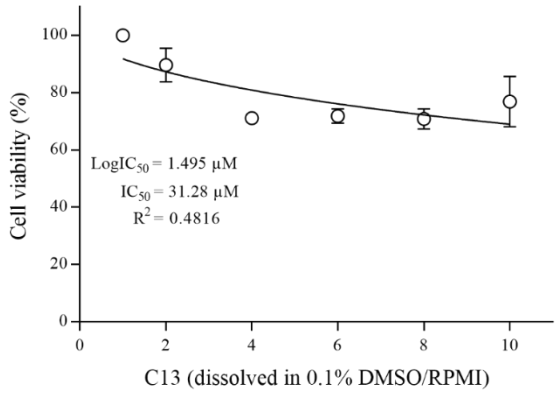

Figure 6.10 Dose-response curve for complex **C13** (dissolved in 0.1% DMSO) after 24-hour multidose (2 - 10 µM) treatment.

*Dose-response curves for **C14***

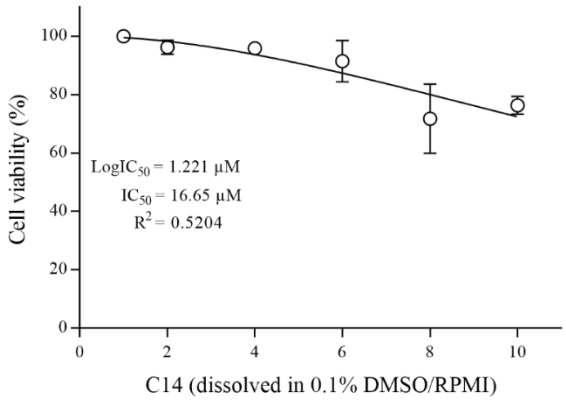

Figure 6.11 Dose-response curve for complex **C14** (dissolved in 0.1%DMSO) after 24-hour multidose (2 - 10 µM) treatment.

*Dose-response curves for **CDDP***

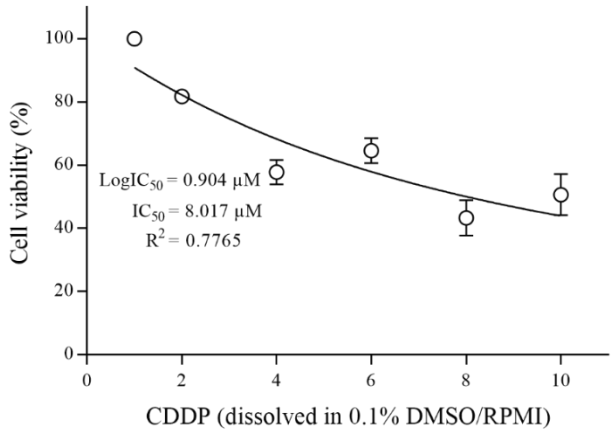

Figure 6.12 Dose-response curve for the clinically prepared cisplatin drug (CDDP, diluted in RPMI) after 24-hour multidose (2 - 10 µM) treatment.

*Synthesis of the precursor ruthenium(II) dimer, [$RuCl_2(\eta^6$-$C_6H_6OCH_2CH_2OH)$] (**C9**)*

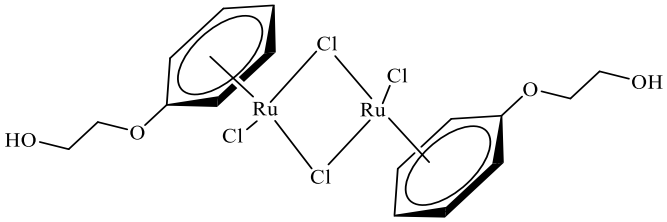

The synthesis of the precursor complex was achieved by following literature methods[1]. A mixture of ruthenium trichloride trihydrate and 1-methoxy-1,4-cyclohexadiene was dissolved in 1,2-ethanediol and heated to 80 ℃ for 3 hours. On standing overnight at room temperature, a red-orange precipitate separated. This was filtered off, washed with methanol, and dried in vacuo. Additional product was obtained by evaporating under reduced pressure the original filtrate to approximately a third of the volume.

*Synthesis of [$RuCl_2(\eta^6$-$C_6H_5OCH_2CH_2OH)(PPh_3)$] (**C10**)*

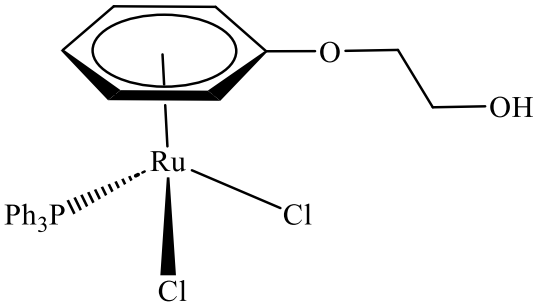

A mixture of [{Ru(μ-Cl)Cl(η^6-$C_6H_5OCH_2CH_2OH$)}$_2$] (0.300g, 0.484 mmol) and (PPh_3)$_3$ (1.161 mmol, 304 µL) dissolved in dichloromethane (150 mL) was stirred for 9 hours at room temperature. The resulting solution was filtered through Kieselguhr and evaporated to dryness. The crude product was purified *via* column chromatography over silica gel, using a mixture of dichloromethane/acetone (2:1) mixture over silica gel, affording the desired compound **C11** as an orange solid. **^{1}H NMR (300.1 MHz, DMSO-*d*$_6$)**: (δ, ppm) 7.68 – 7.62 (15H, t, P(Ph_3)), 5.62 – 5.57 (2H, m, C_6H_5), 5.27 – 2.26 (2H, d, C_6H_5), 4.23 (1H, t, C_6H_5), 4.14 (2H, t, OCH_2), 3.73 (2H, t, CH_2OH).

*Synthesis of [$RuCl_2(\eta^6$-$C_6H_5OCH_2CH_2OH)\{P(OPh_3)\}$] (**C11**)*

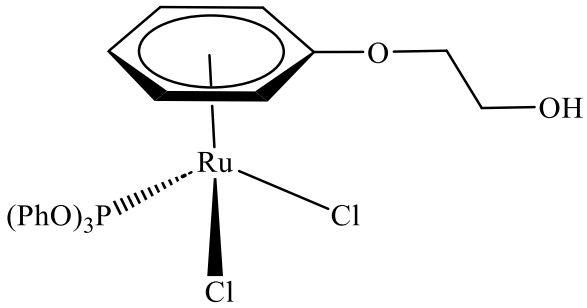

A mixture of [{Ru(μ-Cl)Cl(η^6-$C_6H_5OCH_2CH_2OH$)}$_2$] (0.300g, 0.484 mmol) and P(OPh_3)$_3$ (1.161 mmol, 304 µL) dissolved in dichloromethane (150 mL) was stirred for 9 hours at room temperature. The resulting solution was filtered through Kieselguhr and evaporated to dryness. The crude product was purified *via* column chromatography over silica gel, using a mixture of dichloromethane/acetone (1:1) mixture over silica gel, affording the desired compound **C11** as a red solid. **^{1}H NMR (300.1 MHz, DMSO-*d*$_6$)**: (δ, ppm) 7.45 (15H, m, P(OPh_3)), 5.77 – 5.68 (3H, broad m, C_6H_5), 4.90 – 4.82 (2H, d, C_6H_5), 3.94 (2H, t, OCH_2), 3.66 – 3.64 (2H, t, CH_2OH).

*Synthesis of [$RuCl_2(\eta^6$-$C_6H_5OCH_2CH_2OH)(P(OCH_3)_3)$] (**C12**)*

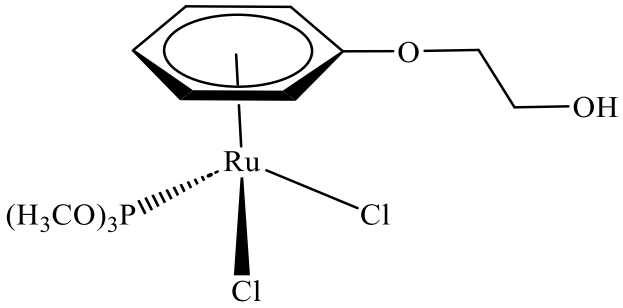

A mixture of [{Ru(μ-Cl)Cl(η^6-$C_6H_5OCH_2CH_2OH$)}$_2$] (0.300g, 0.484 mmol) and $P(OCH_3)_3$ (1.161 mmol, 137 µL) dissolved in dichloromethane (150 mL) was stirred for 9 hours at room temperature. The resulting solution was filtered through Kieselguhr and evaporated to dryness. The crude product was purified *via* column chromatography over silica gel, using a mixture of dichloromethane/acetone (1:2) mixture over silica gel, affording the desired compound **C12** as a red solid. **^{1}H NMR (300.1 MHz, DMSO-d_6)**: (δ, ppm) 5.95 – 5.90 (2H, m, C_6H_5), 5.54 – 5.52 (2H, d, C_6H_5), 5.09 (1H, t, C_6H_5), 4.18 (2H, t, OCH_2), 3.74 – 3.68 (2H, m, OCH_2), 3.65 – 3.62 (9H, d, $P(OCH_3)$).

Cell culture: Preparation of reagents and protocols

Preparation of MTT reagent

MTT (5 mg/mL) was prepared in a sterile filtered 1x PBS solution as described by the manufacturer. Briefly, MTT (100 mg) was dissolved in 1x PBS (20 mL). The solution was incubated at 37°C for 15 minutes and filtered through a 0.2 µM filter. The solution was wrapped in foil and was refrigerated at 4°C.

Preparation of the solubilization buffer reagent

To prepare non-sterilized 10 % SDS (0.01M) in deionized water, SDS (25 g) was dissolved in deionized water (dH_2O, 250 mL). Concentrated hydrochloric acid (32.1%, 76.6 µl) was added to the solution.

Preparation of the mycoplasma staining reagent (mounting fluid)

To prepare mounting fluid, citric acid (20 mM) was added to a beaker containing $Na_2HPO_4 \cdot 2H_2O$ (55 mM). The pH of the acidic solution was adjusted to 5.5 pH reading with glycerol (50%). The solution was stored at 4°C before usage.

Preparation of 10x and 1x phosphate-buffered saline (PBS) solution

To prepare phosphate buffer saline solution (10x, 2 L), NaCl (160 g) and KCl (4 g) were placed in a beaker. Distilled water (2 L) was added to the beaker and stirred. Na2HPO4 (28.8 g) and KH2PO4 (4 g) were added to the solution and the pH of the solution was adjusted to 7.4. The solution was further transferred and diluted down to 1x concentration into a glass bottle (100 mL of 10x PBS + 900 mL distilled water).

The SN_{Ar} reaction occurs via a two-step reaction mechanism (Scheme 3.3). The first step involves the addition of a nucleophile which displaces the leaving group (in this case, a bromide halogen) on an aromatic ring. This is followed by the formation of an intermediate stabilized by the electron-withdrawing bromide ion. The reaction proceeds forward to form the final product, which is formed by the subsequent elimination of the halogen from the pyridine aromatic ring and successive proton transfer from the primary amine to the desired product.

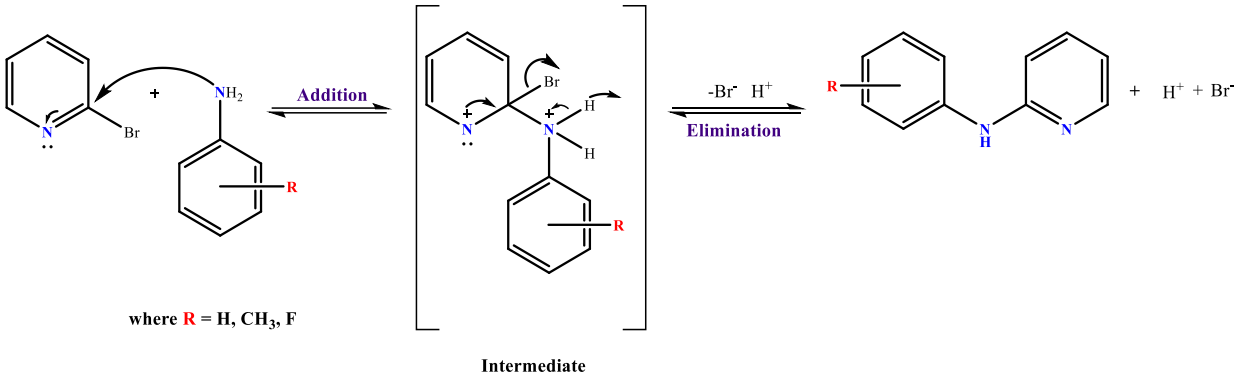

Scheme 6.1 Proposed SN_{Ar} reaction mechanism of R-ap ligands.

H^1 NMR spectra of R-ap (**L1** - **L8**) ligands

*^{1}H-NMR (400 Hz, $CDCl_3$) spectrum of **L1**.*

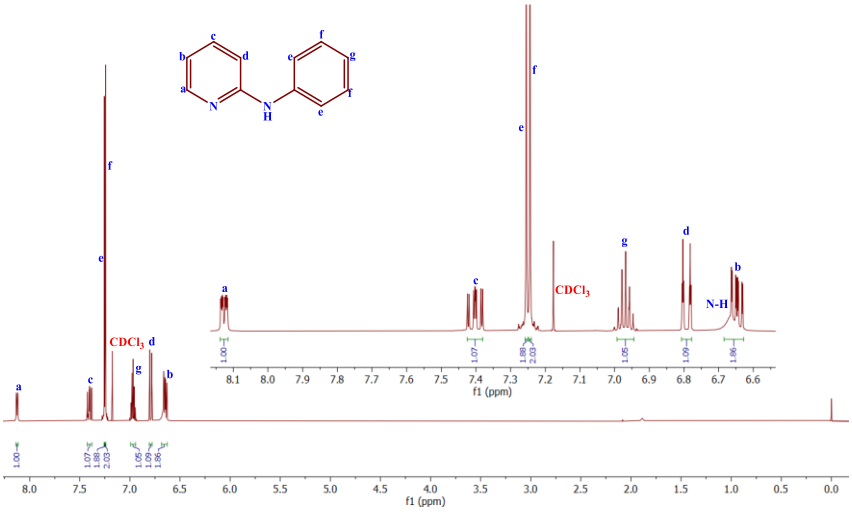

Figure 6.13 ^{1}H-NMR (400 Hz, $CDCl_3$) spectrum of **L1**. Assignments have been made based on the molecular structures and with the assistance of 2D NMR (HSQC).

*^{1}H-NMR (400 Hz, $CDCl_3$) spectrum of **L2**.*

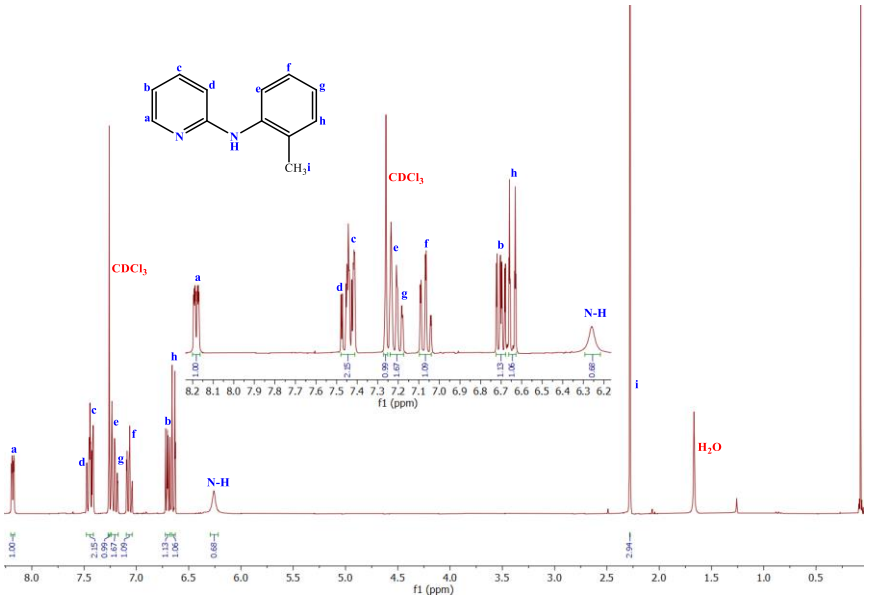

Figure 6.14 ^{1}H-NMR (400 Hz, $CDCl_3$) spectrum of **L2**. Assignments have been made based on the molecular structures and with the assistance of 2D NMR (HSQC).

*^{1}H-NMR (400 Hz, $CDCl_3$) spectrum of **L3**.*

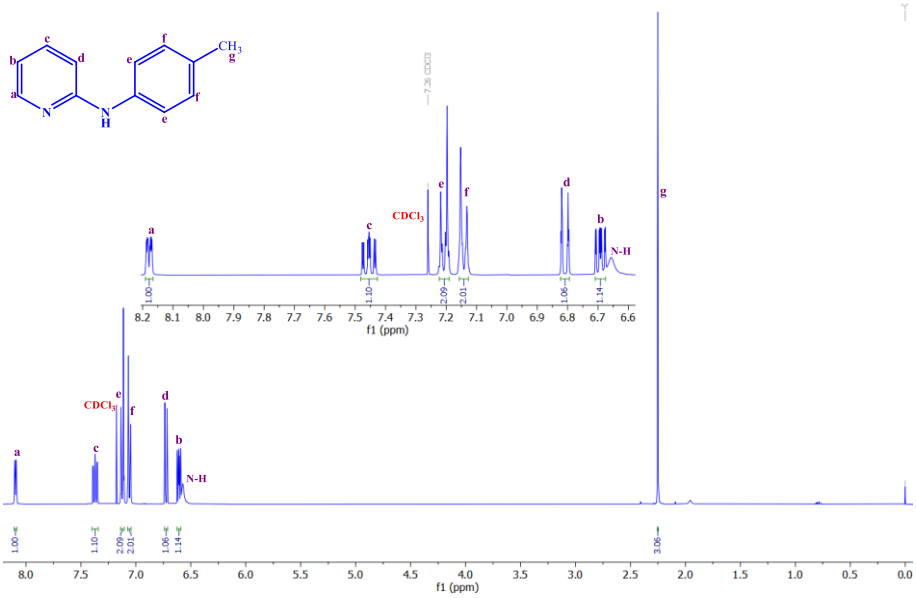

Figure 6.15 ^{1}H-NMR (400 Hz, $CDCl_3$) spectrum of **L3**. Assignments have been made based on the molecular structures and with the assistance of 2D NMR (HSQC).

*^{1}H-NMR (400 Hz, $CDCl_3$) spectrum of **L4**.*

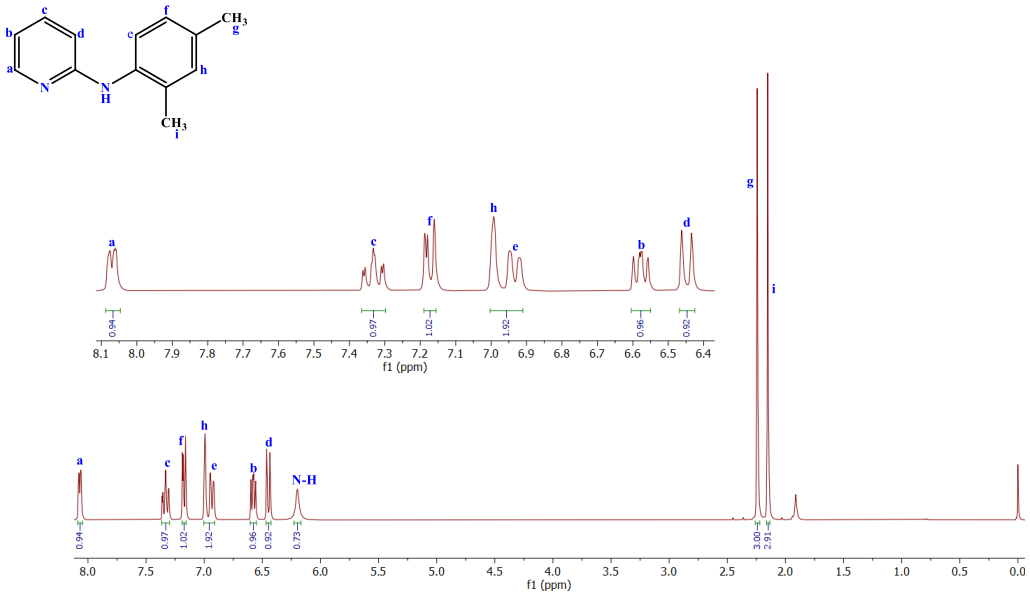

Figure 6.16 ^{1}H-NMR (400 Hz, $CDCl_3$) spectrum of **L4**. Assignments have been made based on molecular structures and with the assistance of 2D NMR (HSQC).

*^{1}H-NMR (400 Hz, $CDCl_3$) spectrum of **L5**.*

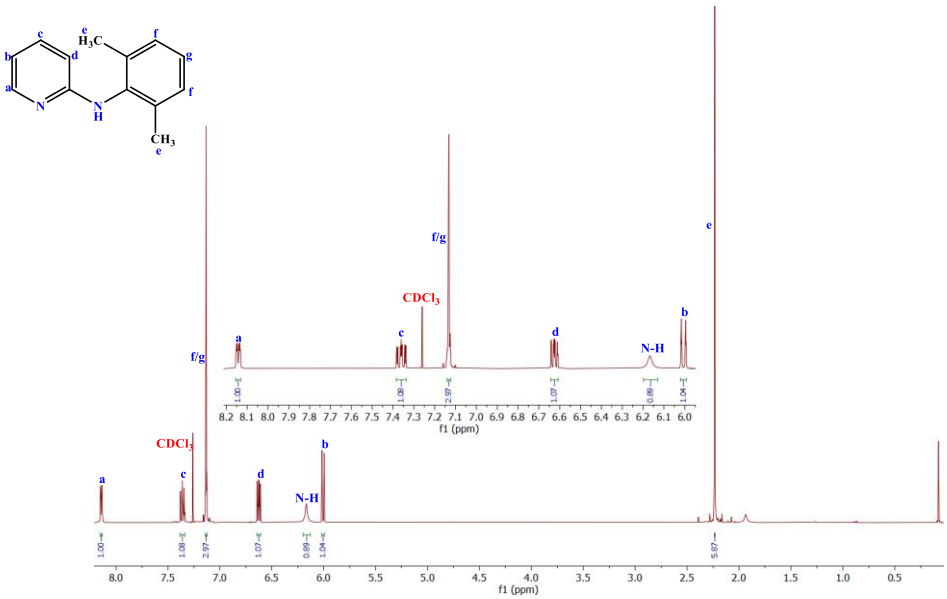

Figure 6.17 ^{1}H-NMR (400 Hz, $CDCl_3$) spectrum of **L5**. Assignments have been made based on molecular structures and with the assistance of 2D NMR (HSQC).

*^{1}H-NMR (400 Hz, $CDCl_3$) spectrum of **L6**.*

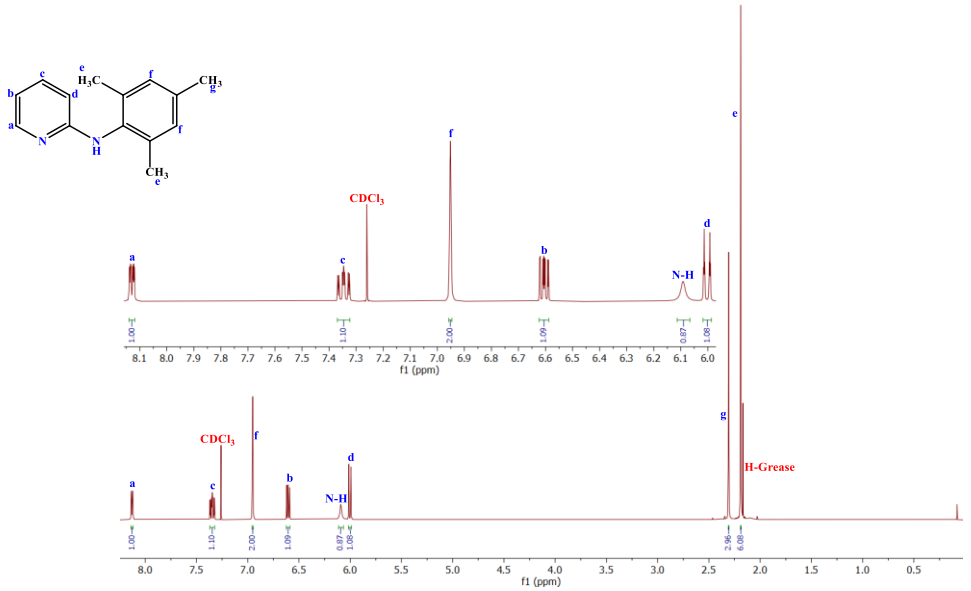

Figure 6.18 ^{1}H-NMR (400 Hz, $CDCl_3$) spectrum of **L6**. Assignments have been made based on molecular structures and with the assistance of 2D NMR (HSQC).

*^{1}H-NMR (400 Hz, $CDCl_3$) spectrum of **L7**.*

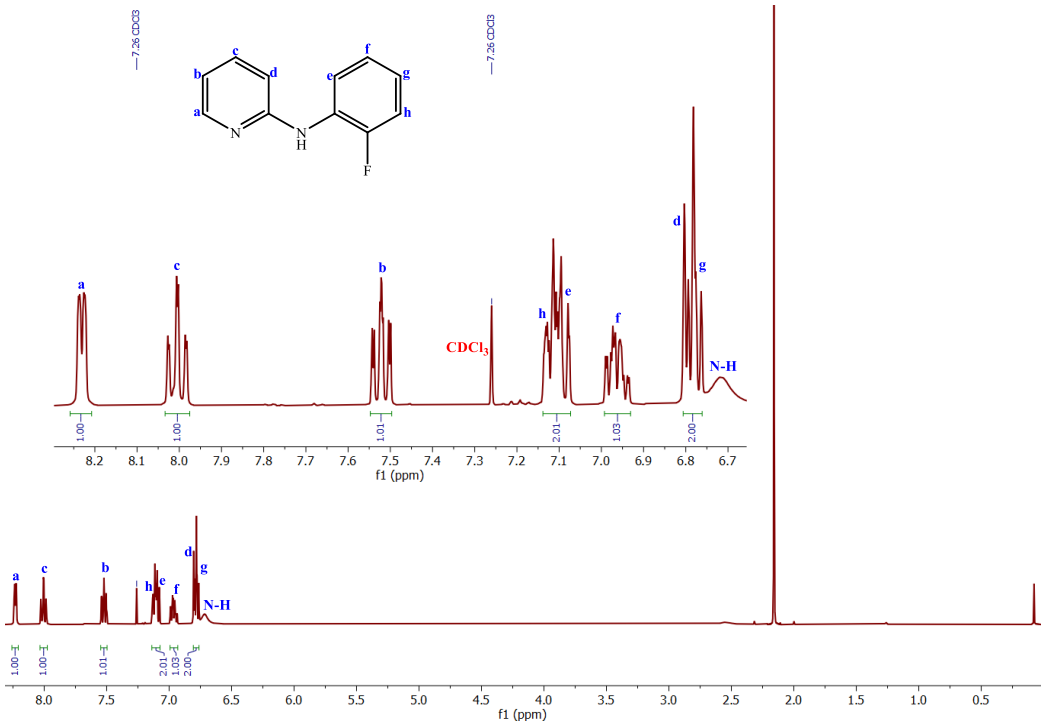

Figure 6.19 ^{1}H-NMR (400 Hz, $CDCl_3$) spectrum of **L7**. Assignments have been made based on molecular structures and with the assistance of 2D NMR (HSQC).

*^{1}H-NMR (400 Hz, $CDCl_3$) spectrum of **L8**.*

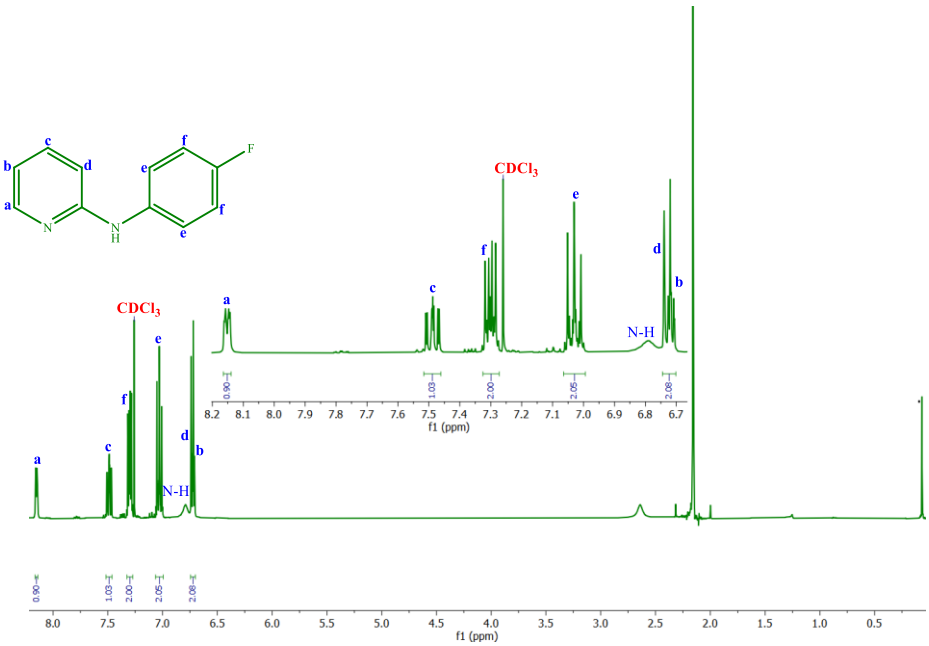

Figure 6.20 ^{1}H-NMR (400 Hz, $CDCl_3$) spectrum of **L8**. Assignments have been made based on the molecular structures and with the assistance of 2D NMR (HSQC).

^{13}C NMR spectra of R-ap ligands (**L1 - L8**).

*^{13}C NMR (400 Hz, $CDCl_3$) spectrum of **L1.***

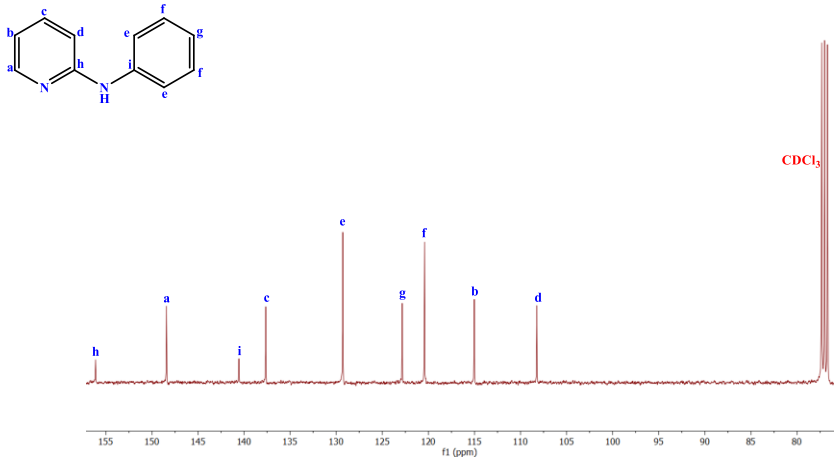

Figure 6.21 ^{13}C NMR (400 Hz, $CDCl_3$) spectrum of **L1**. Assignments have been made based on the molecular structures and with the assistance of 2D NMR (HSQC).

*^{13}C NMR (400 Hz, $CDCl_3$) spectrum of **L2.***

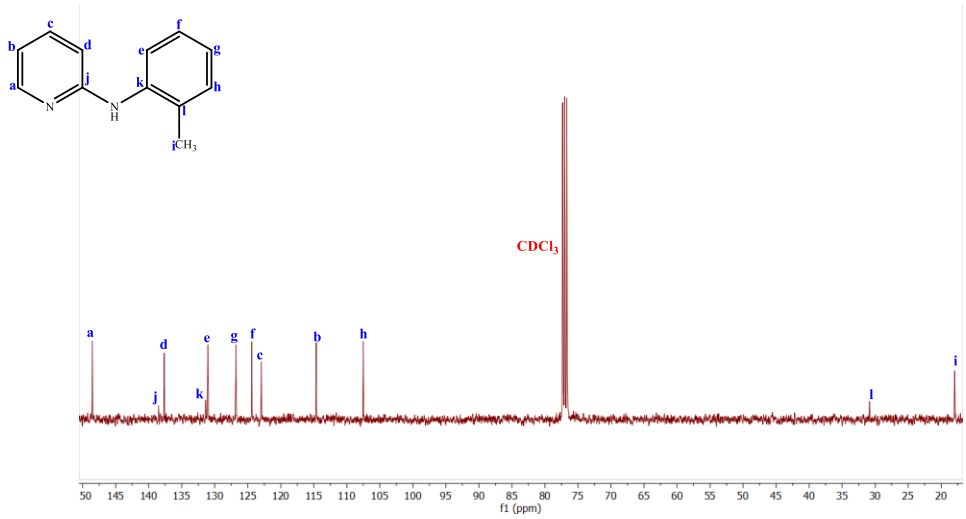

Figure 6.22 ^{13}C NMR (400 Hz, $CDCl_3$) spectra of **L2**. Assignments have been made based on the molecular structures and with the assistance of 2D NMR (HSQC).

*^{13}C NMR (400 Hz, $CDCl_3$) spectrum of **L3.***

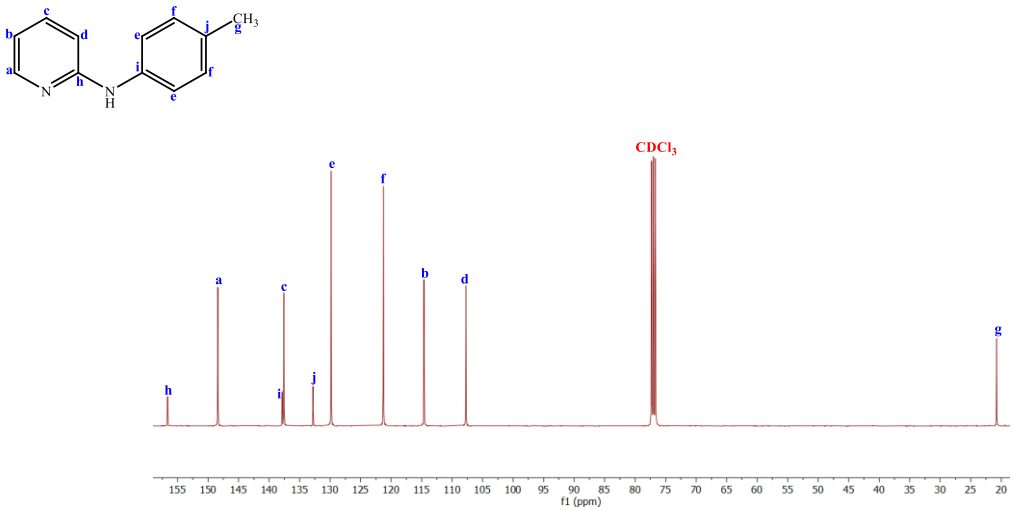

Figure 6.23 ^{13}C NMR (400 Hz, $CDCl_3$) spectrum of **L3**. Assignments have been made based on the molecular structures and with the assistance of 2D NMR (HSQC).

*^{13}C NMR (400 Hz, $CDCl_3$) spectrum of **L4.***

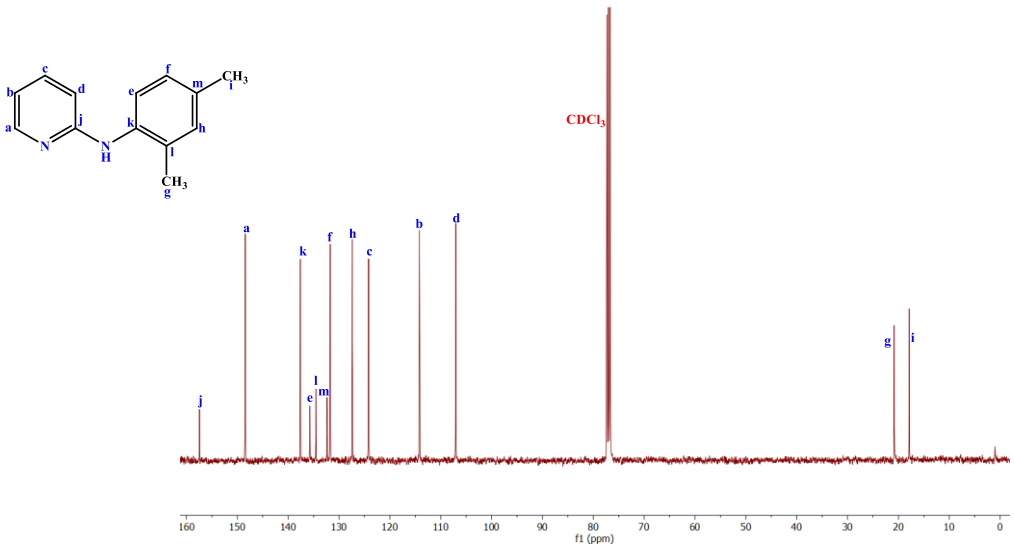

Figure 6.24 ^{13}C NMR (400 Hz, $CDCl_3$) spectrum of **L4**. Assignments have been made based on the molecular structures and with the assistance of 2D NMR (HSQC).

*^{13}C NMR (400 Hz, $CDCl_3$) spectrum of **L5.***

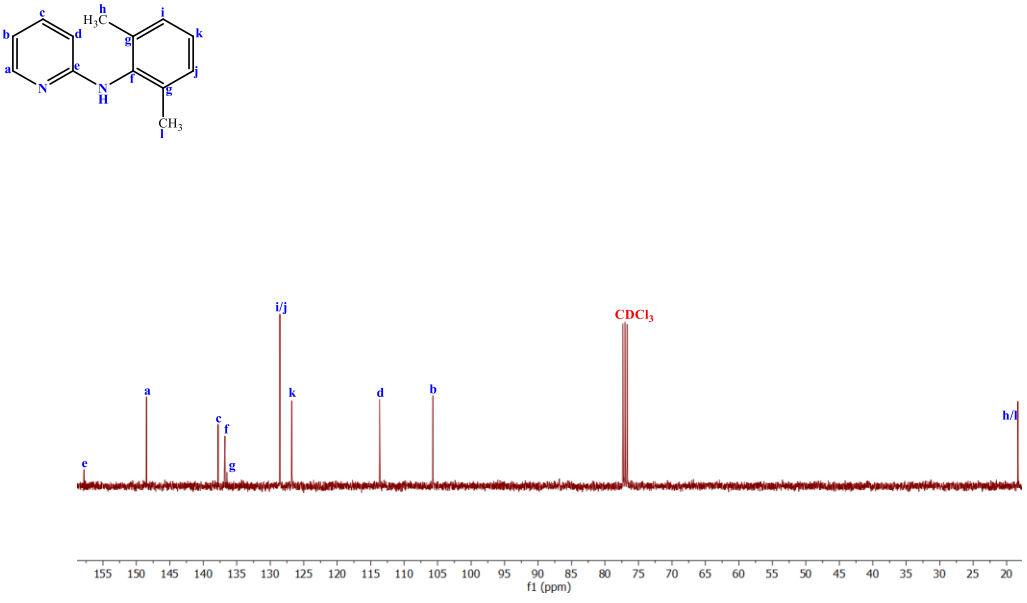

Figure 6.25 ^{13}C NMR (400 Hz, $CDCl_3$) spectrum of **L5**. Assignments have been made based on the molecular structures and with the assistance of 2D NMR (HSQC).

*^{13}C NMR (400 Hz, $CDCl_3$) spectrum of **L6.***

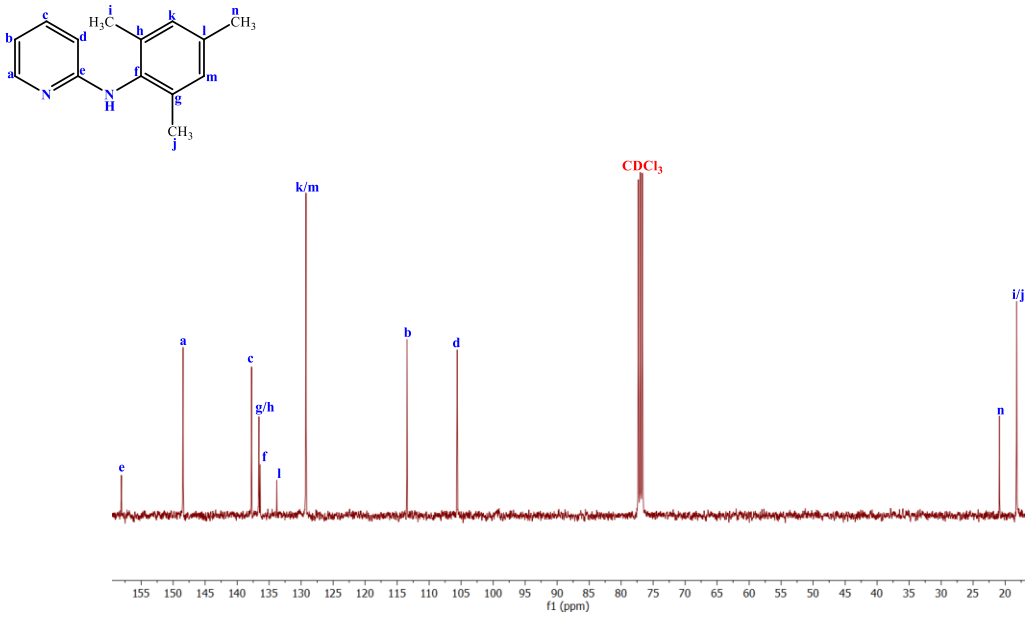

Figure 6.26 ^{13}C NMR (400 Hz, $CDCl_3$) spectrum of **L6**. Assignments have been made based on the molecular structures and with the assistance of 2D NMR (HSQC).

*^{13}C NMR (400 Hz, $CDCl_3$) spectrum of **L7**.*

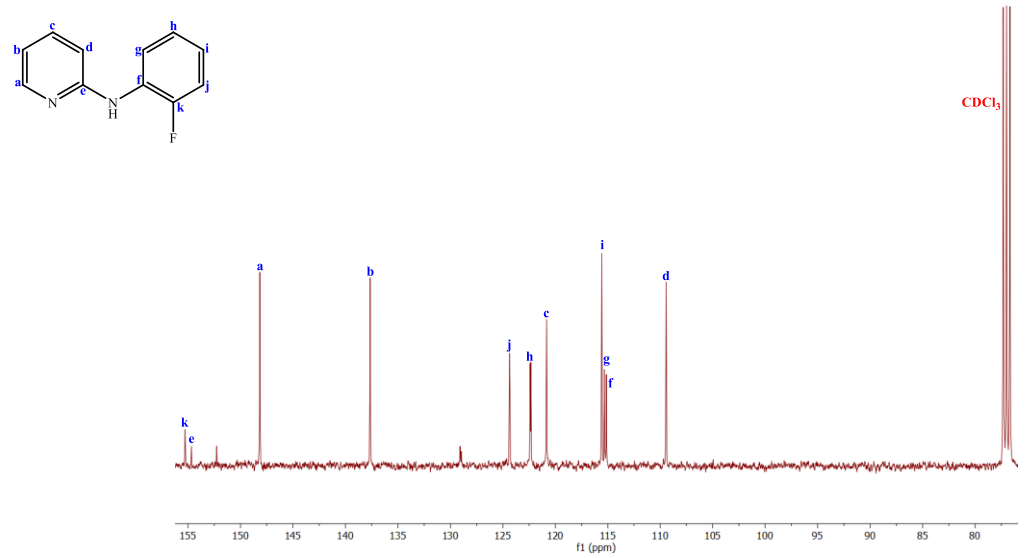

Figure 6.27 ^{13}C NMR (400 Hz, $CDCl_3$) spectrum of **L7**. Assignments have been made based on the molecular structures and with the assistance of 2D NMR (HSQC).

*^{13}C NMR (400 Hz, $CDCl_3$) spectrum of **L8**.*

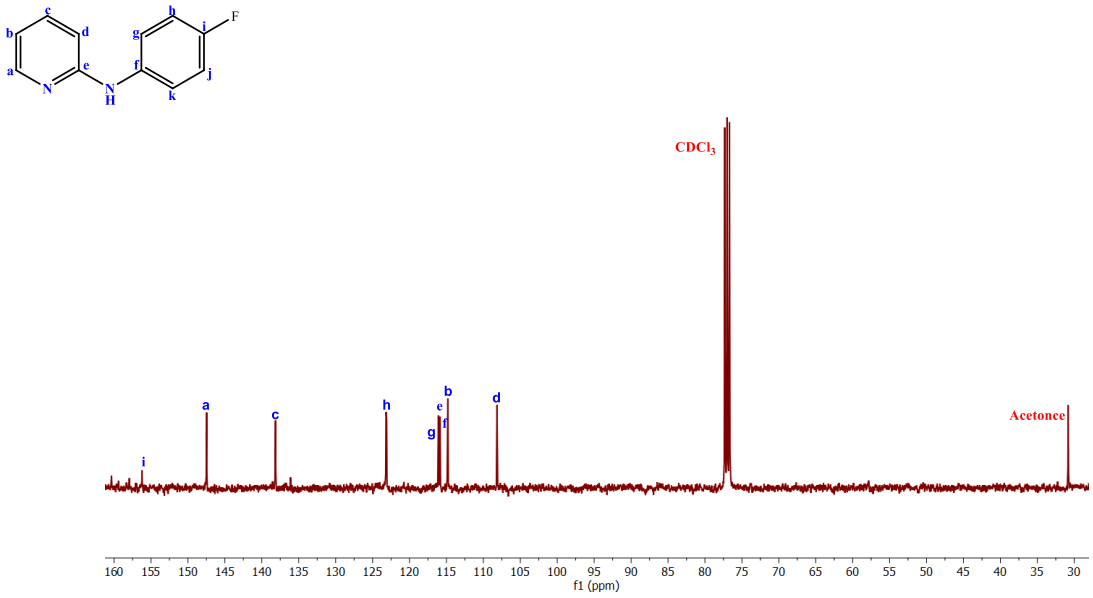

Figure 6.28 ^{13}C NMR (400 Hz, $CDCl_3$) spectrum of **L8**. Assignments have been made based on the molecular structures and with the assistance of 2D NMR (HSQC).

HSQC spectra of R-ap ligands (**L1** - **L8**).

*HSQC-NMR (400 Hz, $CDCl_3$) spectrum of **L1**.*

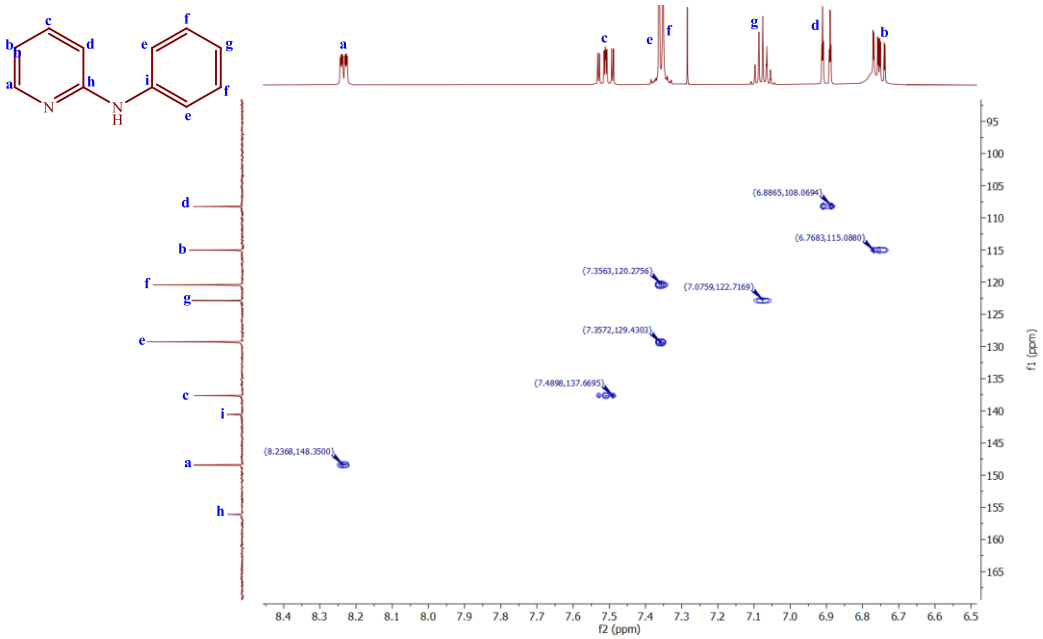

Figure 6.29 HSQC-NMR (400 Hz, $CDCl_3$) spectrum of **L1**.

*HSQC-NMR (400 Hz, $CDCl_3$) spectrum of **L2**.*

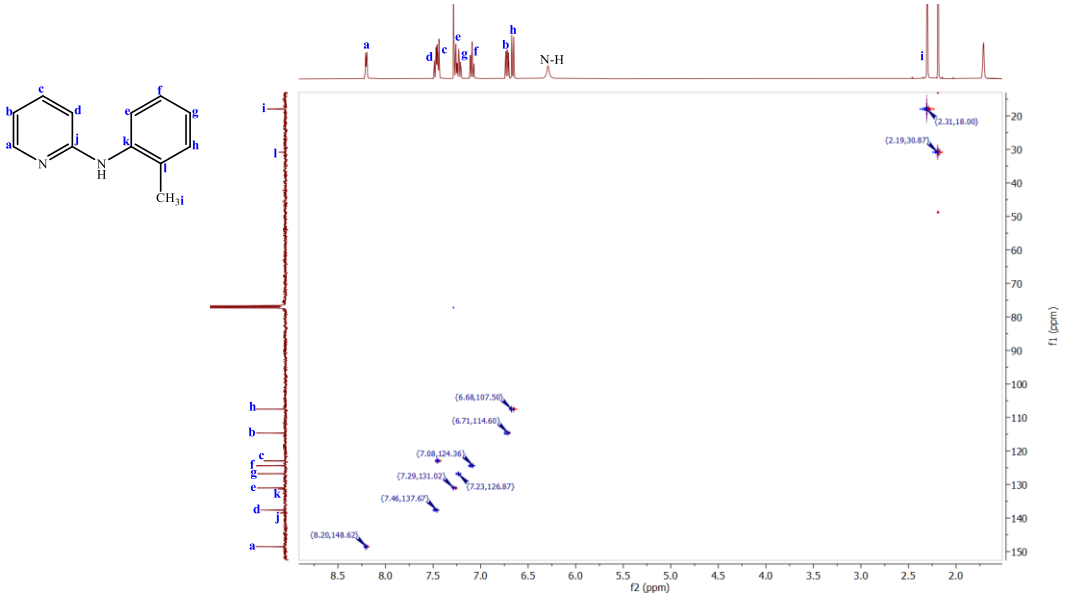

Figure 6.30 HSQC-NMR (400 Hz, $CDCl_3$) spectrum of **L2**.

*HSQC-NMR (400 Hz, $CDCl_3$) spectrum of **L3**.*

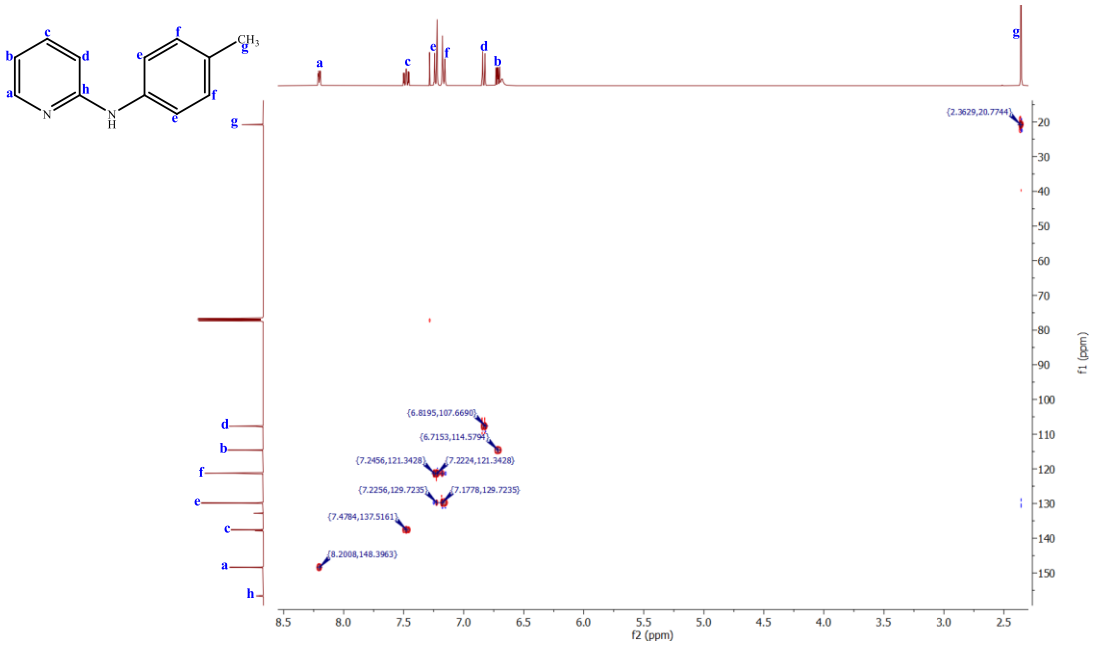

Figure 6.31 HSQC-NMR (400 Hz, $CDCl_3$) spectrum of **L3**.

*HSQC-NMR (400 Hz, $CDCl_3$) spectrum of **L4**.*

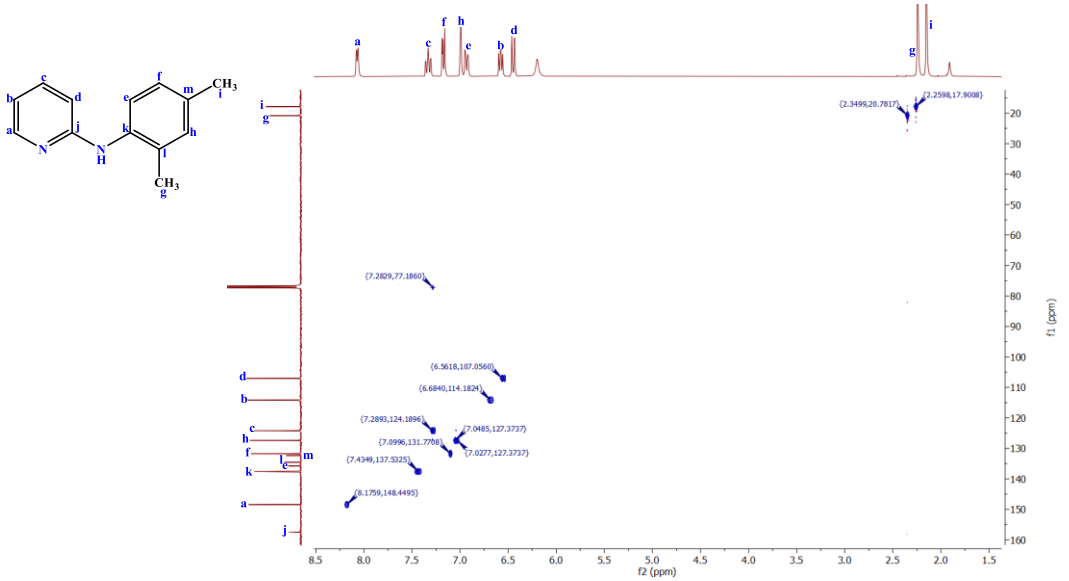

Figure 6.32 HSQC-NMR (400 Hz, $CDCl_3$) spectrum of **L4**.

*HSQC-NMR (400 Hz, $CDCl_3$) spectrum of **L5**.*

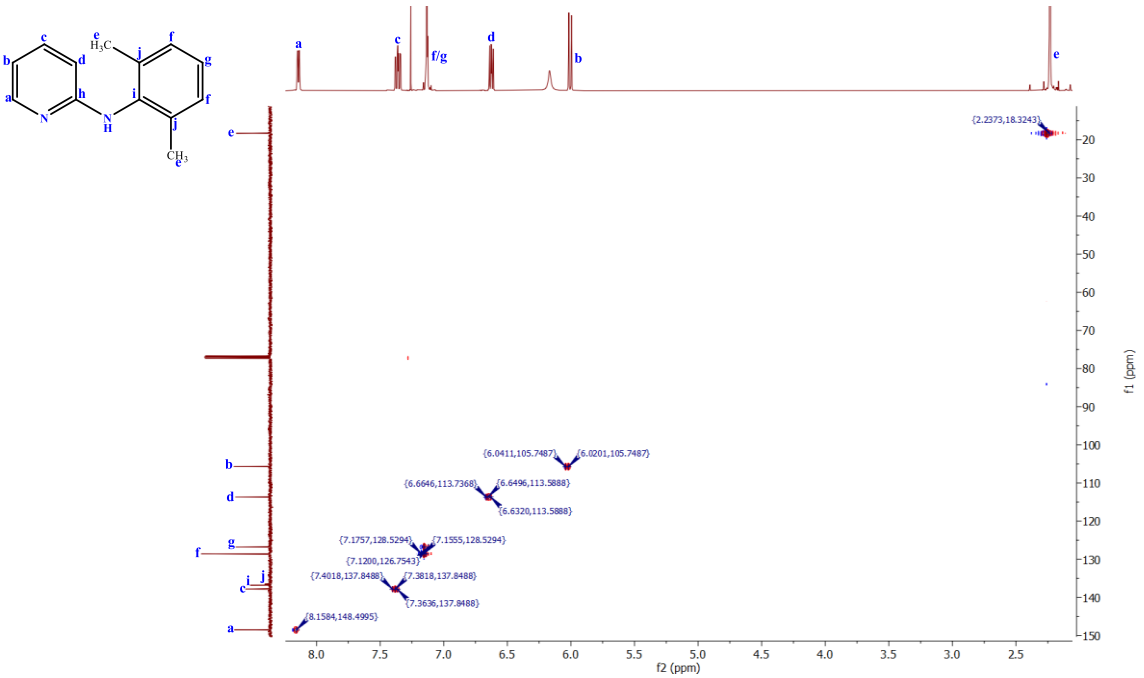

Figure 6.33 HSQC-NMR (400 Hz, $CDCl_3$) spectrum of **L5**.

*HSQC-NMR (400 Hz, $CDCl_3$) spectrum of **L6**.*

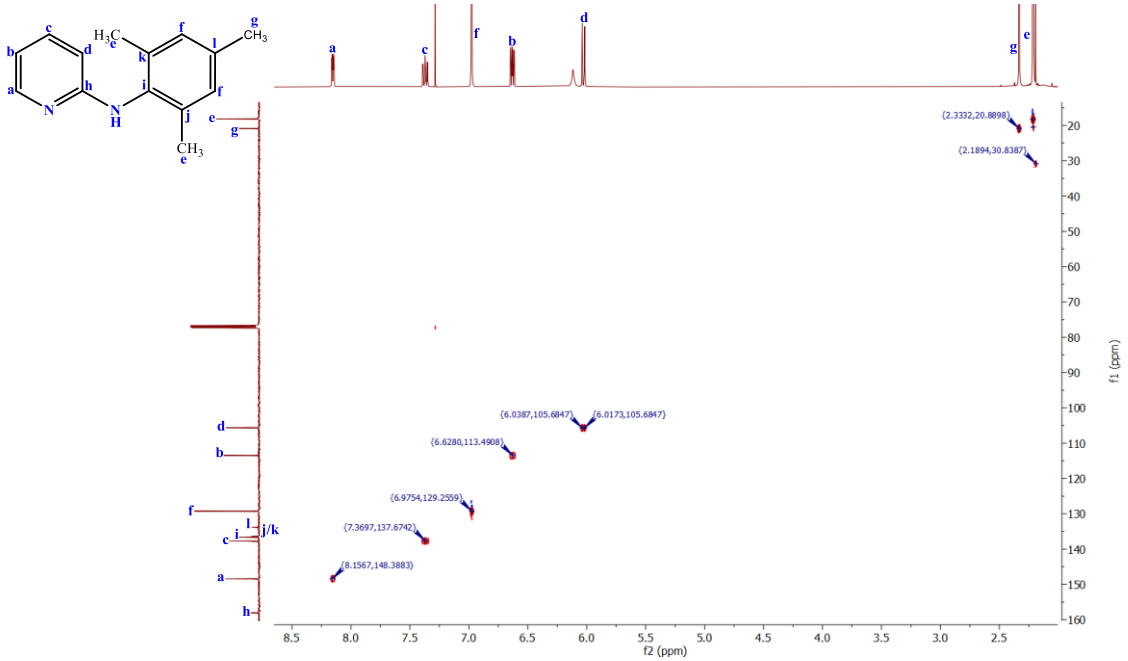

Figure 6.34 HSQC-NMR (400 Hz, $CDCl_3$) spectrum of **L6**.

*HSQC-NMR (400 Hz, $CDCl_3$) spectrum of **L7**.*

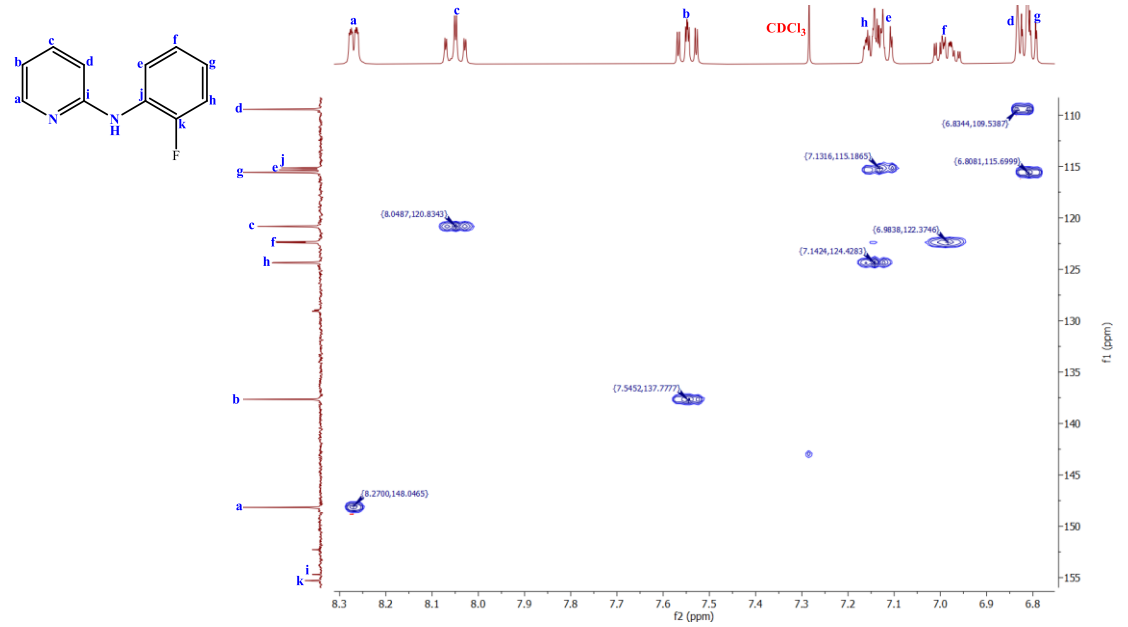

Figure 6.35 HSQC-NMR (400 Hz, $CDCl_3$) spectrum of **L7**.

*HSQC-NMR (400 Hz, $CDCl_3$) spectrum of **L8**.*

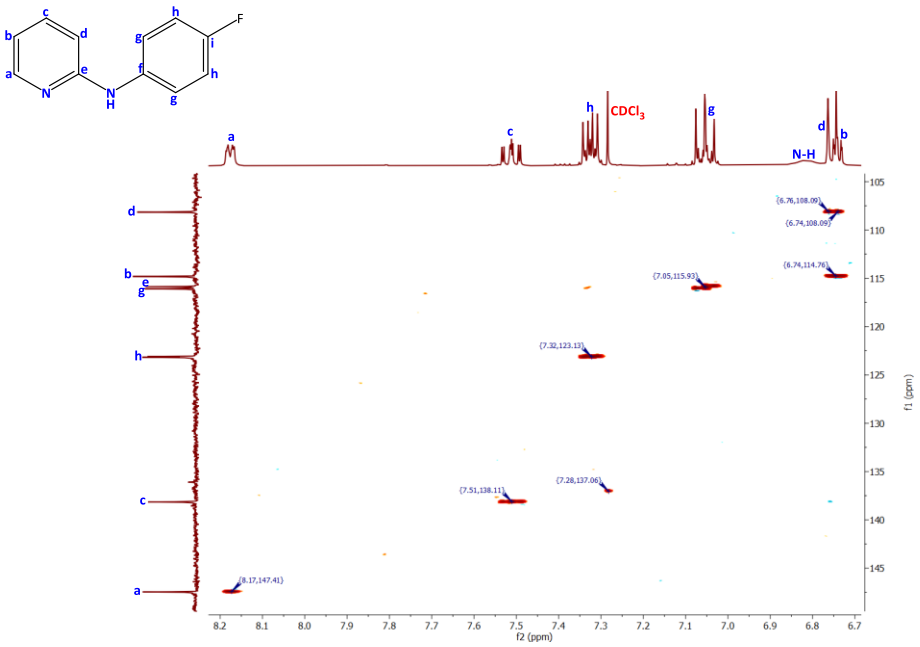

Figure 6.36 HSQC-NMR (400 Hz, $CDCl_3$) spectrum of **L8**.

Infrared spectra of R-ap ligands (**L1 - L8**).

*Infrared (IR-ATR) spectrum of **L1.***

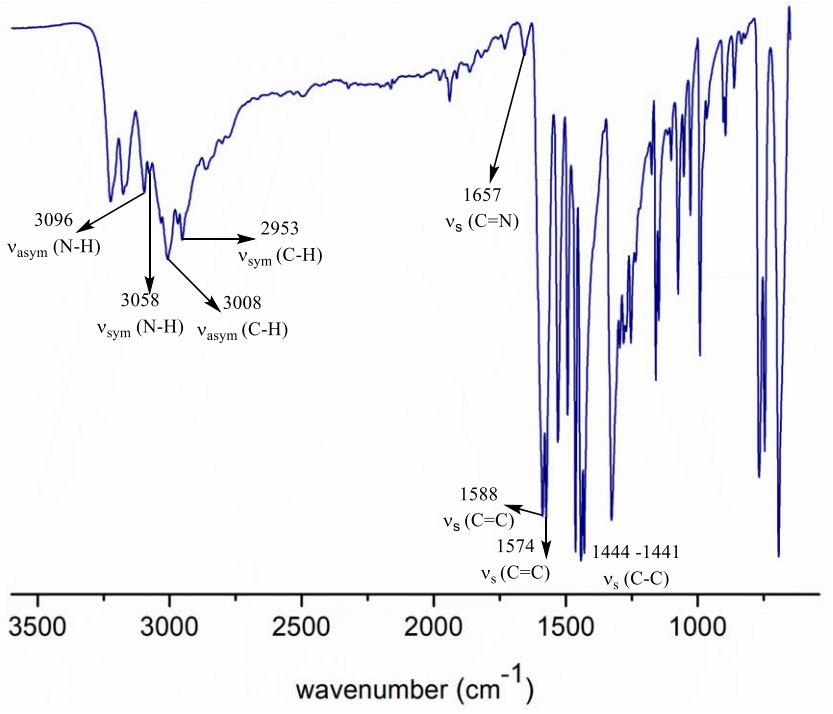

Figure 6.37 Infrared (IR-ATR) spectrum of **L1**.

*Infrared (IR-ATR) spectrum of **L2.***

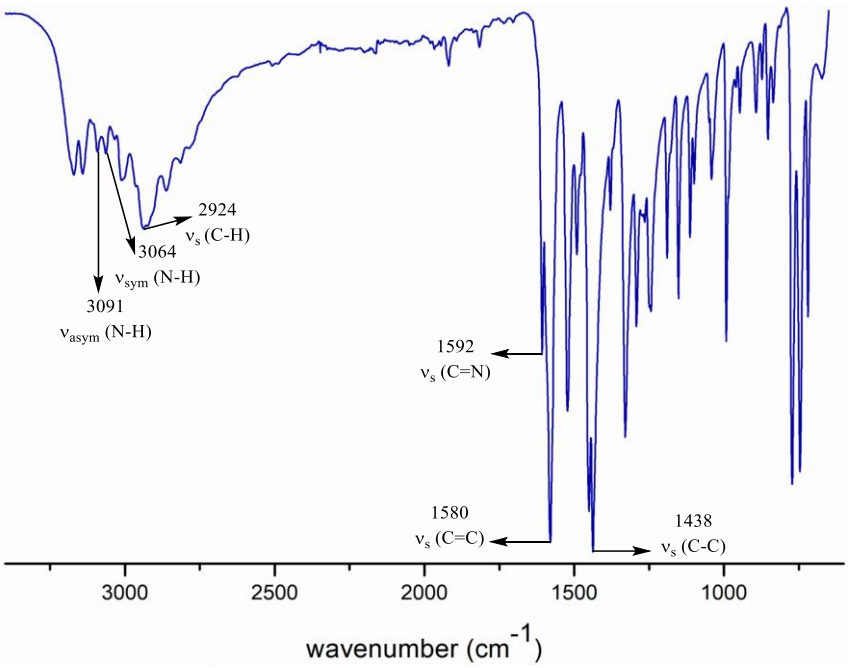

Figure 6.38 Infrared (IR-ATR) spectrum of **L2**.

*Infrared (IR-ATR) spectrum of **L3**.*

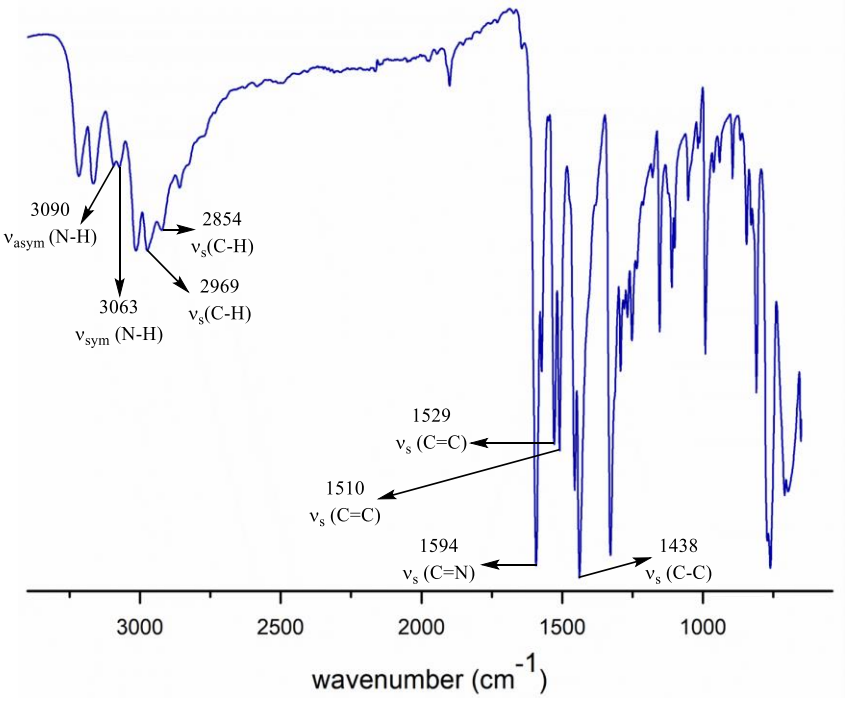

Figure 6.39 Infrared (IR-ATR) spectrum of **L3**.

*Infrared (IR-ATR) spectrum of **L4**.*

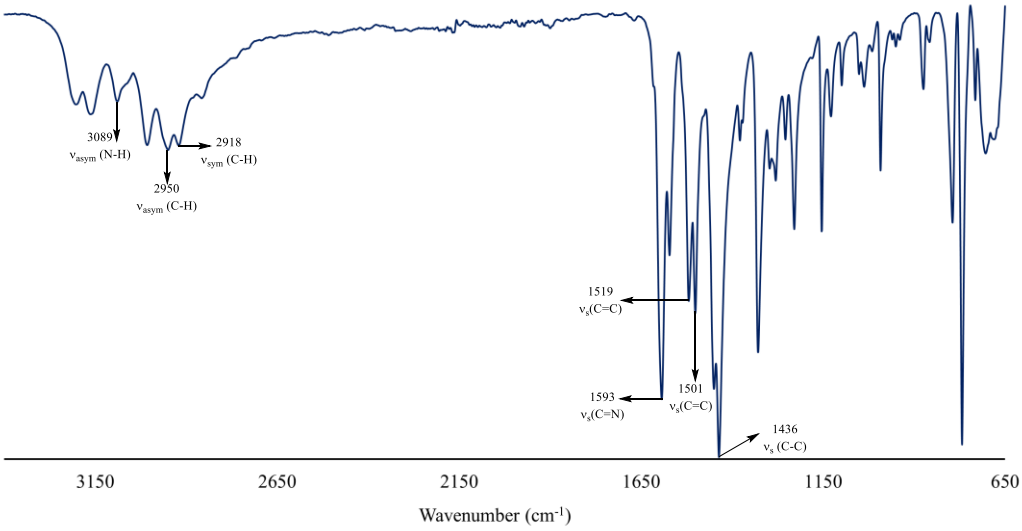

Figure 6.40 Infrared (IR-ATR) spectrum of **L4**.

*Infrared (IR-ATR) spectrum of **L5**.*

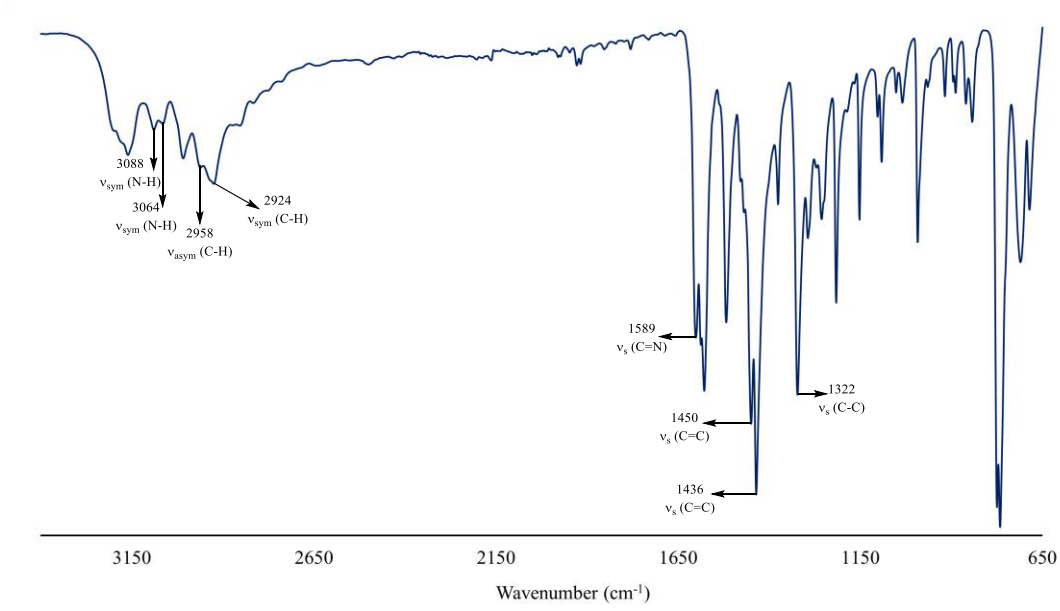

Figure 6.41 Infrared (IR-ATR) spectrum of **L5**.

*Infrared (IR-ATR) spectrum of **L6**.*

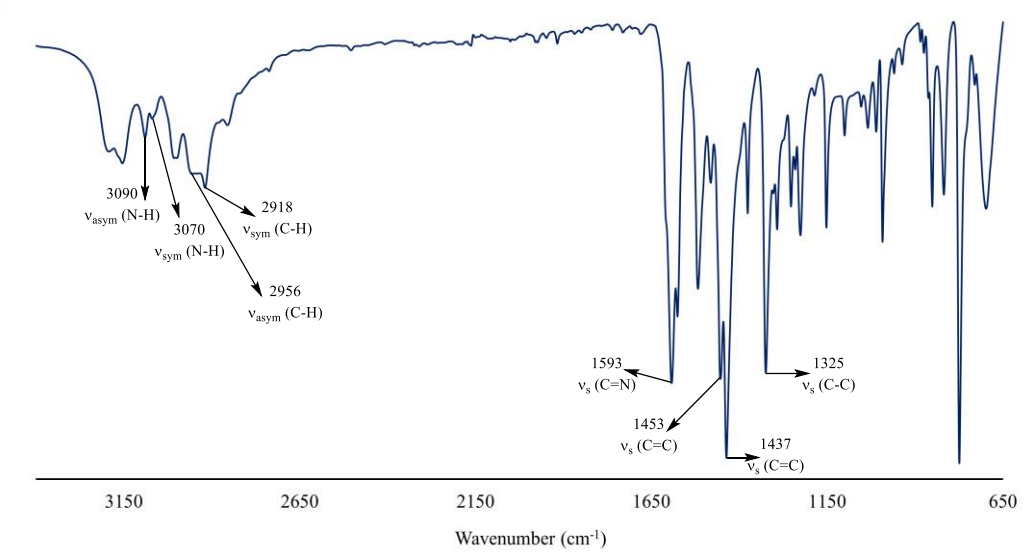

Figure 6.42 Infrared (IR-ATR) spectrum of **L6**.

*Infrared (IR-ATR) spectrum of **L7**.*

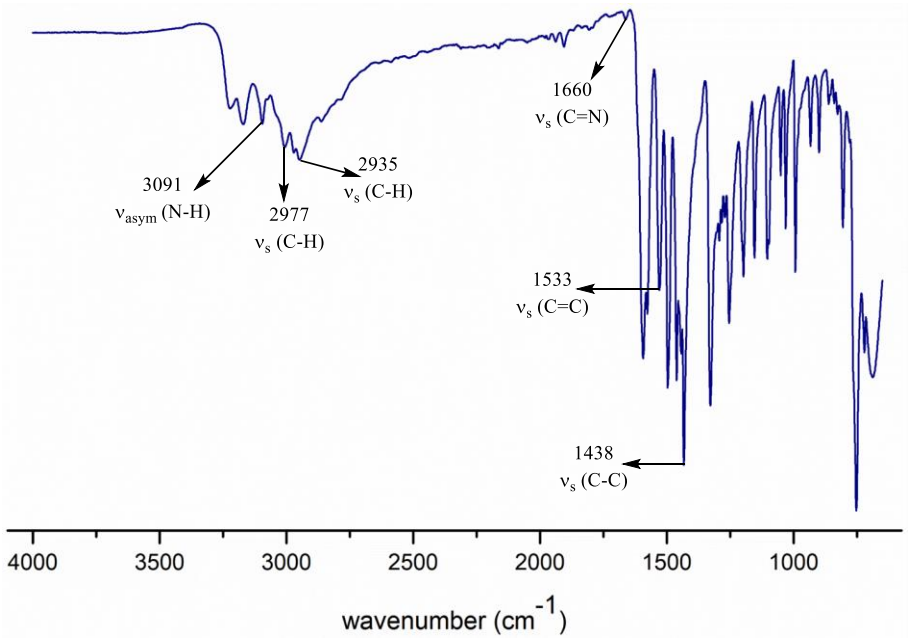

Figure 6.43 Infrared spectrum of **L7**.

*Infrared (IR-ATR) spectrum of **L8**.*

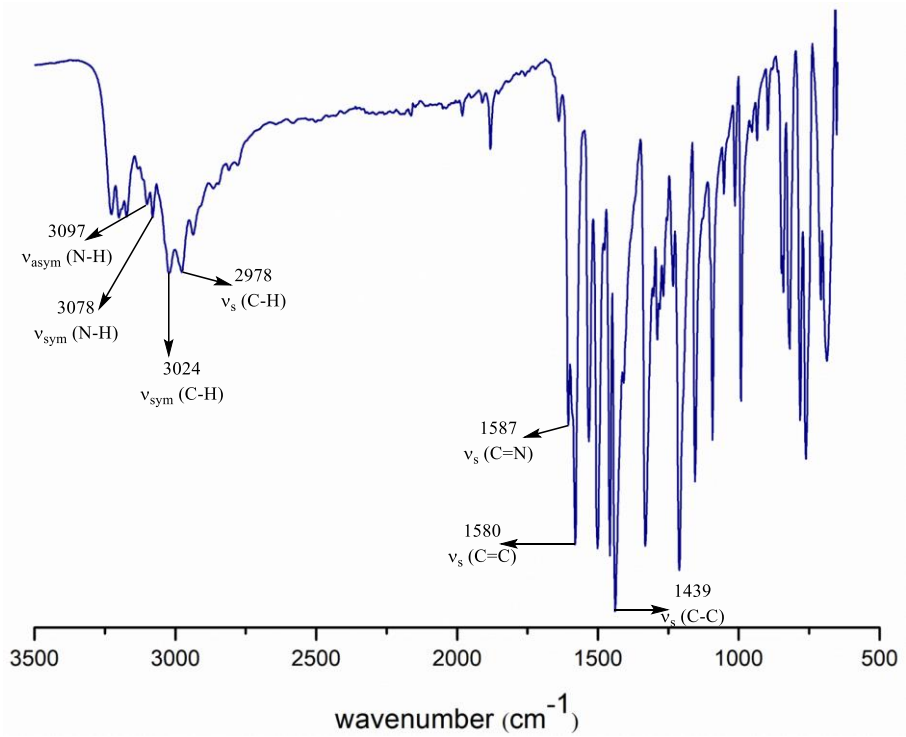

Figure 6.44 Infrared (IR-ATR) spectrum of **L8**.

Liquid chromatography-mass spectrometry [ESI (LC)-MS] data of R-ap ligands (**L1** - **L8**).

*ESI (LC)-MS spectrum of **L1**.*

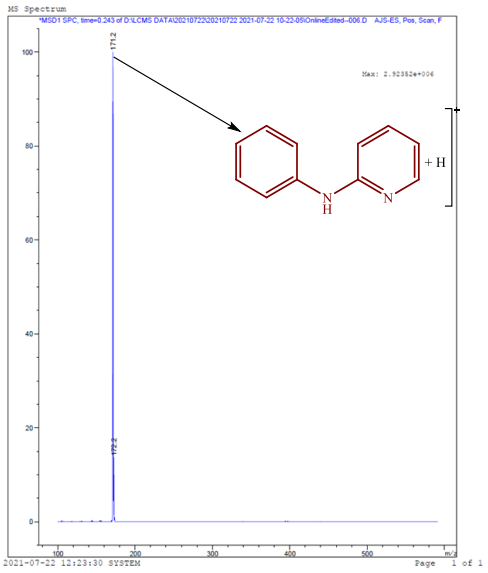

Figure 6.45 ESI (LC) - MS of the **L1**. The molecular ion base peak fragment was confirmed using the Molecular Weight Calculator Excel spreadsheet provided by Fiehn Lab, UC Davis Genome Centre - Metabolomics.[2]

*ESI (LC)-MS spectrum of **L2**.*

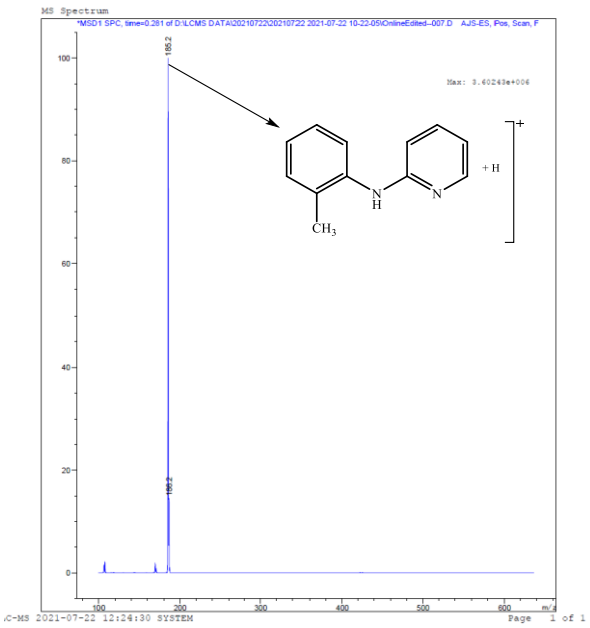

Figure 6.46 ESI (LC) - MS of the **L2**. The molecular ion base peak fragment was confirmed using the Molecular Weight Calculator Excel spreadsheet provided by Fiehn Lab, UC Davis Genome Centre - Metabolomics.[2]

*ESI (LC)-MS spectrum of **L3**.*

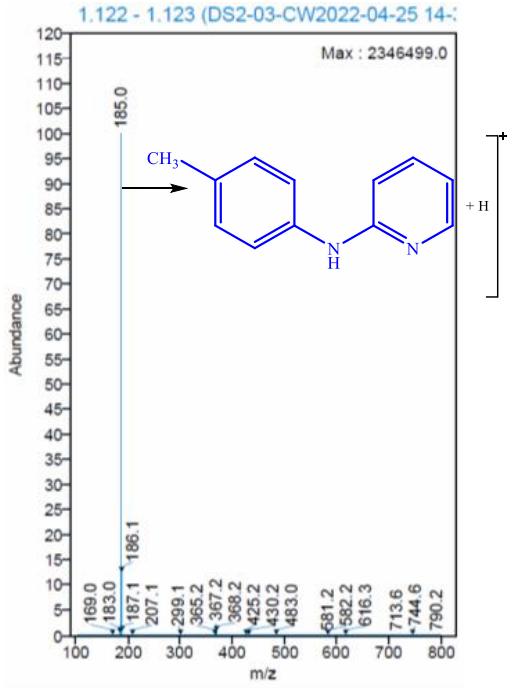

Figure 6.47 ESI (LC) - MS of the **L3**. The molecular ion base peak fragment was confirmed using the Molecular Weight Calculator Excel spreadsheet provided by Fiehn Lab, UC Davis Genome Centre - Metabolomics.[2]

*ESI (LC)-MS spectrum of **L4**.*

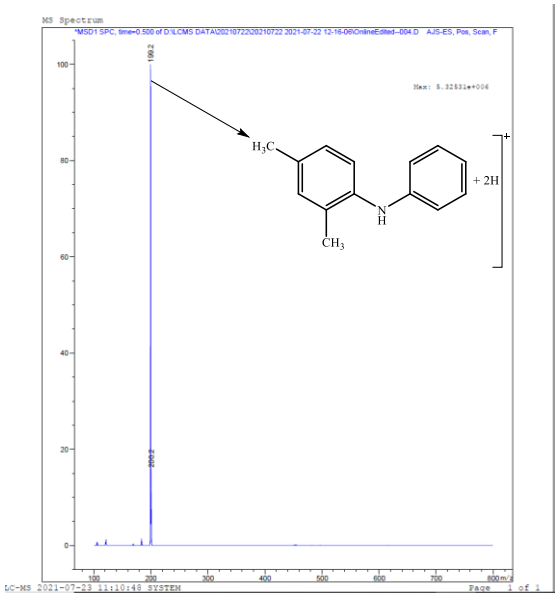

Figure 6.48 ESI (LC) - MS of the **L4**. The molecular ion base peak fragment was confirmed using the Molecular Weight Calculator Excel spreadsheet provided by Fiehn Lab, UC Davis Genome Centre - Metabolomics.[2]

*ESI (LC)-MS spectrum of **L5**.*

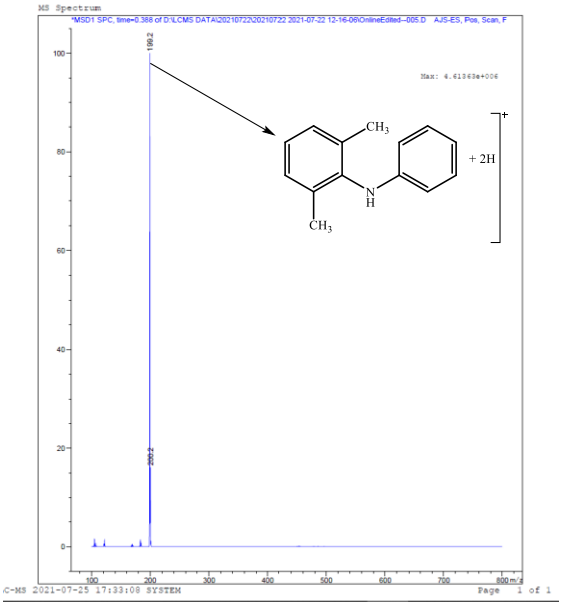

Figure 6.49 ESI (LC) - MS of the **L5**. The molecular ion base peak fragment was confirmed using the Molecular Weight Calculator Excel spreadsheet provided by Fiehn Lab, UC Davis Genome Centre - Metabolomics.[2]

*ESI (LC)-MS spectrum of **L6**.*

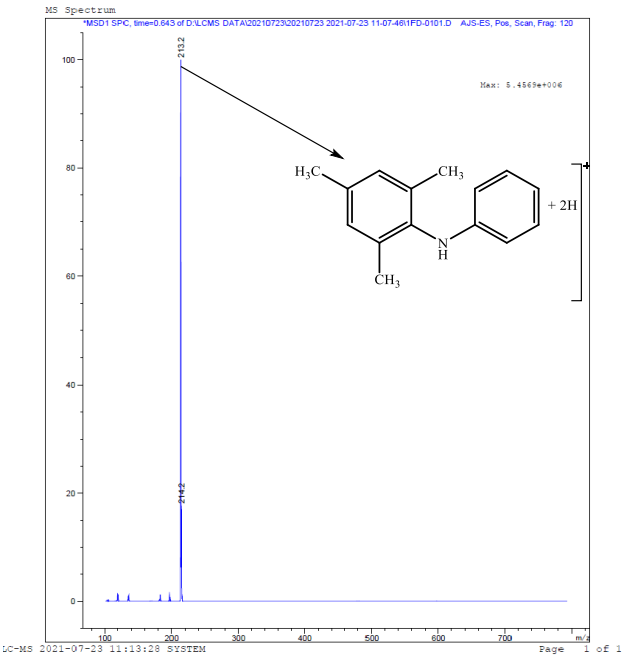

Figure 6.50 ESI (LC) - MS of the **L6**. The molecular ion base peak fragment was confirmed using the Molecular Weight Calculator Excel spreadsheet provided by Fiehn Lab, UC Davis Genome Centre - Metabolomics.[2]

*ESI (LC)-MS spectrum of **L7**.*

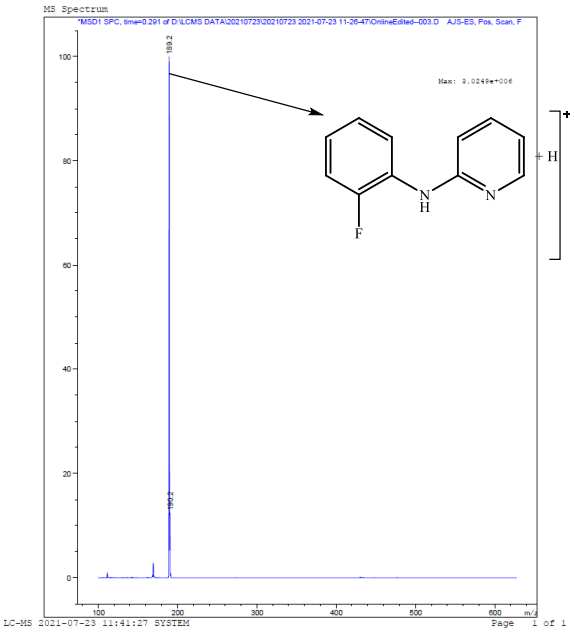

Figure 6.51 ESI (LC) - MS of the **L7**. The molecular ion base peak fragment was confirmed using the Molecular Weight Calculator Excel spreadsheet provided by Fiehn Lab, UC Davis Genome Centre - Metabolomics.[2]

*ESI (LC)-MS spectrum of **L8**.*

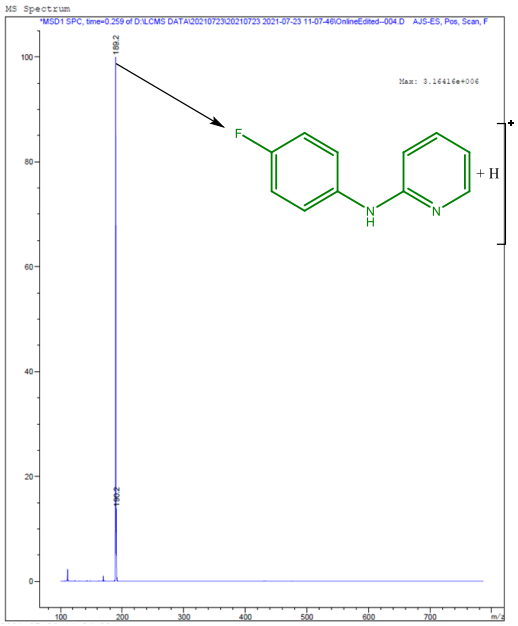

Figure 6.52 ESI (LC) - MS of the **L8**. The molecular ion base peak fragment was confirmed using the Molecular Weight Calculator Excel spreadsheet provided by Fiehn Lab, UC Davis Genome Centre - Metabolomics.[2]

Characterization of $[Ru_2(O_2CCH_3)_4Cl]$ precursor complex

Infrared spectroscopy

The infrared spectrum of $[Ru_2(O_2CCH_3)_4Cl]$ precursor complex was recorded at room temperature and represented in Figure 6.51. The spectrum shows peaks characteristic of similar tetraacetatechlorodiruthenium(II, III) complexes reported in the literature.[3,4,5,6]

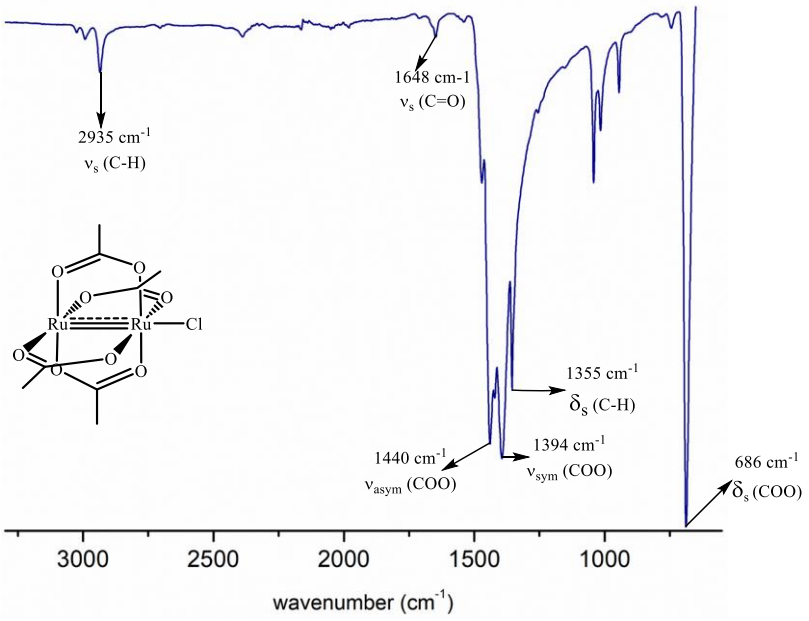

Figure 6.53 Infrared spectrum of the precursor complex, $[Ru_2(O_2CCH_3)_4Cl]$.

The most diagnostic infrared vibrational peaks are the symmetrical and unsymmetrical peaks of the equatorial bridging acetate stretching modes. The broad shallow peak observed at 1648 cm^{-1} corresponds to the carboxylate (COO) vibrational stretching frequency of the equatorially coordinated acetate groups. The two acetate vibrational stretching modes (ν_{asym} and ν_{sym} (COO)) are observed at 1440 cm^{-1} and 1394 cm^{-1}, respectively. The separation between the two absorption bands (Δ = 46 cm^{-1}) may indicate the symmetrical coordination of the carboxylate ligands.[3,5] Additionally, the sharp peak observed at 686 cm^{-1} is assigned to the deformation mode (δ_s (COO)) of the coordinated acetate groups. The $-CH_3$ deformation vibrational stretching frequencies are observed at 1355 cm^{-1} while the vibrational stretching modes of the terminal methyl ($-CH_3$) group of the acetates are observed at a higher wavenumber (2935 cm^{-1}). These infrared peaks serve as confirmation of the successful coordination of the acetate molecules to the diruthenium metal cores and all agree with the published reported infrared spectra assignments.[5]

UV-visible spectroscopy

The UV-visible spectrum of a methanol solution of $[Ru_2(O_2CCH_3)_4Cl]$ complex (Figure 6.52) was recorded using a Shimadzu 1800 UV-Vis series scanning spectrophotometer over an 800 - 200 nm range at a medium scanning rate. The spectrum was recorded at a constant temperature (25.0 ± 0.2°C) maintained using a water bath and a 0.5 mL quartz cuvette with a 1 cm path length used to store the solution.

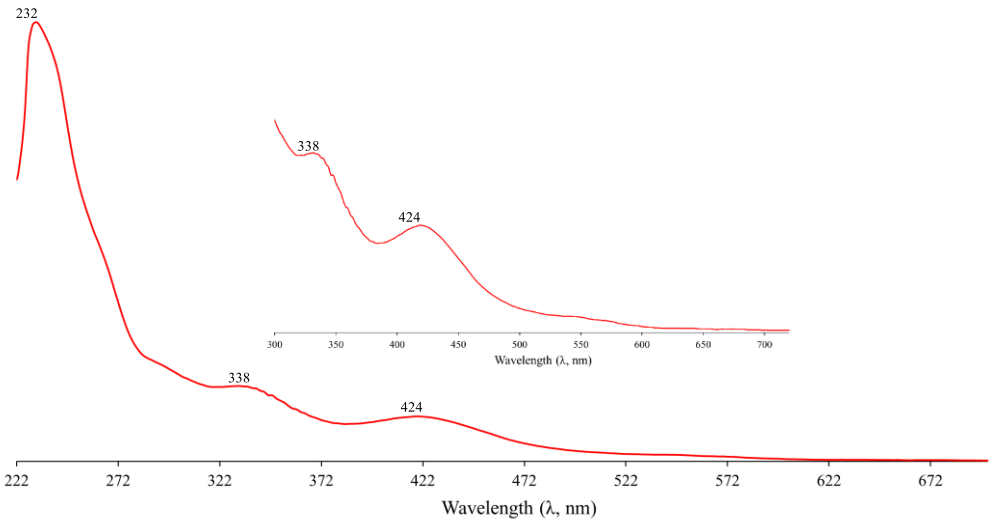

Figure 6.54 Ultraviolet-visible spectrum of the precursor complex, $[Ru_2(O_2CCH_3)_4Cl]$ (5.0 x 10^{-4} M) in methanol, recorded at room temperature.

The $[Ru_2(O_2CCH_3)_4Cl]$ precursor was partially soluble in methanol and dichloromethane and insoluble in organic and polar solvents. The absorption bands observed in the UV-visible spectrum correspond well with those reported in published reports.[3,4,5,6,7,8] Thus, confirming the successful synthesis of the desired $[Ru_2(O_2CCH_3)_4Cl]$ precursor. The spectrum shows an intense band observed at higher energies (232 λ, nm), assigned to the σ(Cl) → σ*(Ru_2) axial ligand to metal charge transfer (LMCT) transitions while the weaker shoulder band observed in the visible region (338 λ, nm) is assigned to the π (Cl) → π* (Ru_2) electronic transitions. Furthermore, in the visible region (424 λ, nm), an intense strong broad band is observed and assigned to the π(Ru - O, Ru_2) → π* (Ru_2) transition. All absorption bands observed in the spectrum of the $[Ru_2(O_2CCH_3)_4Cl]$ precursor agree with the absorption band assignments of the $[Ru_2(O_2CCH_3)_4X]$ reported in published works, where X = halide anion.[9]

High-resolution (ESI) Mass Spectrometry

High-resolution mass spectrometry (HRMS) analysis of $[Ru_2(O_2CCH_3)_4Cl]$ precursor complex was reordered in the positive-ion (+ve) mode. In the recorded ESI-MS spectrum (Figure 6.53), an intense molecular base ion peak was detected at m/z = 438.8630. This base peak corresponds to the $[M - Cl]^+$ positively charged ion fragment, indicating a mass loss of the chloride ion initially coordinated axially to the diruthenium metal-centred cores. This actual base peak value was consistent with the calculated proposed molecular weight of the precursor complex $[Ru_2(O_2CCH_3)_4]^+$ ($[M - Cl]^+$: 438.3148 m/z), with the isotopic signals observed in the same

region agreeing with those of the simulated signal pattern of the $[Ru_2(O_2CCH_3)_4]^+$ precursor complexes reported in published materials.[3,10]

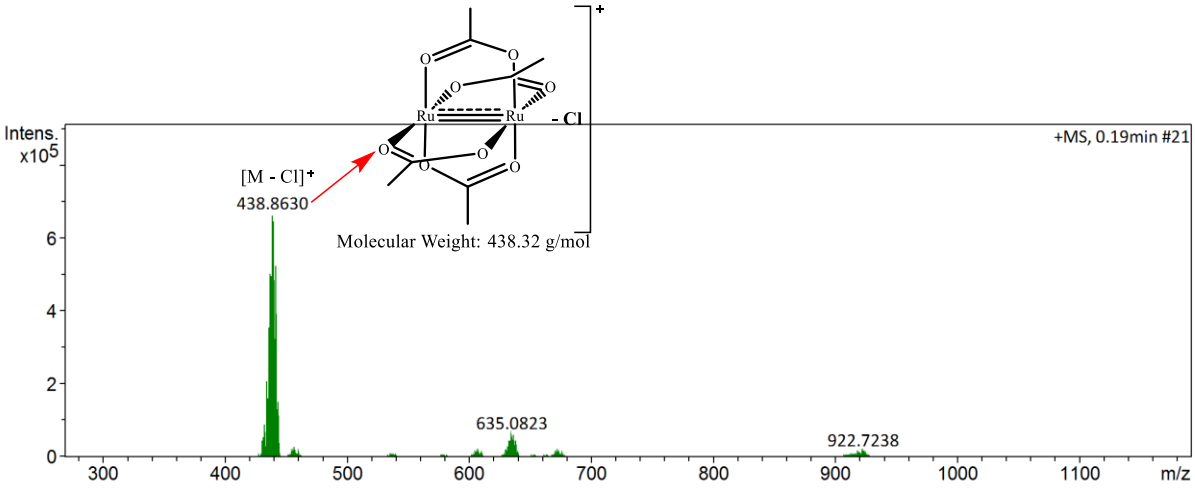

Figure 6.55 High resolution (ESI) mass spectrum of the assigned characteristics fragments of the $[Ru_2(O_2CCH_3)_4Cl]$ precursor complex, recorded in the positive-ion mode (+ve). The molecular ion base peak fragments were confirmed using the Molecular Weight Calculator Excel spreadsheet provided by Fiehn Lab, UC Davis Genome Center - Metabolomics.[2]

Elemental (CHNS) analysis of the ***[Ru$_2$(O$_2$CCH$_3$)$_4$Cl]*** *complex*

The predicted and obtained elemental % compositions of the $[Ru_2(O_2CCH_3)_4Cl]$ precursor are presented in Table 6.1, while the elemental analysis report is shown in Figure 6.54.

Table 6.1 Predicted and experimental elemental percentage composition of the precursor complex, $[Ru_2(O_2CCH_3)_4Cl]$.

Complex	**Predicted element % composition**		**Found element % composition**	
	C	**H**	**C**	**H**
[Ru$_2$(O$_2$CCH$_3$)$_4$Cl]	20.28	2.55	20.99	2.437

ICP-MS Laboratory
CAF Central Analytical Facilities STELLENBOSCH UNIVERSITY
Agilent Technologies

	Name	Weight (mg)	N [%]	C [%]	H [%]
QC value	Cert Ref Std sulfamethazine	10	20,13	51,78	5,07
	QC Analysed	2,093	20,56	52,09	4,832
		4,913	20,39	51,91	5,181
LOD			0,02	0,02	0,02
	Control Recovery %		102,1	100,6	95,3
	$[Ru_2(O_2CCH_3)_4Cl]$	5,24	0,09	20,99	2,437

Figure 6.56 The elemental analysis data sheet of the paddlewheel $[Ru_2(O_2CCH_3)_4Cl]$ precursor complex.

The % compositions of carbon and hydrogen are 20.99% and 2.437%, all in agreement with the theoretically predicted elemental % compositions of the precursor complex (Table 6.1). Thus, confirming the synthesized structural composition of the $[Ru_2(O_2CCH_3)_4Cl]$ precursor.

Characterization of $[Ru_2(O_2CCH_3)_3$(R-ap)Cl] complexes (C2, C4 - C7)

Single X-Ray Crystallographic CheckCIF file Reports for **C1**, **C3** and **C8**.

*Single X-Ray Crystallographic CheckCIF file Report for **C1**.*

checkCIF/PLATON report

Structure factors have been supplied for datablock(s) TM01

THIS REPORT IS FOR GUIDANCE ONLY. IF USED AS PART OF A REVIEW PROCEDURE FOR PUBLICATION, IT SHOULD NOT REPLACE THE EXPERTISE OF AN EXPERIENCED CRYSTALLOGRAPHIC REFEREE.

No syntax errors found. CIF dictionary Interpreting this report

Datablock: TM01

```
Bond precision:   C-C = 0.0035 A          Wavelength=0.71073

Cell:          a=8.5360(6)       b=10.6627(7)     c=12.6098(9)
               alpha=97.495(1)   beta=91.922(1)   gamma=108.613(1)
Temperature:   173 K
```

	Calculated	Reported
Volume	1074.93(13)	1074.92(13)
Space group	P -1	P -1
Hall group	-P 1	-P 1
Moiety formula	C17 H20 Cl N2 O7 Ru2, H2 O	C17 H20 Cl N2 O7 Ru2, H2 O
Sum formula	C17 H22 Cl N2 O8 Ru2	C17 H22 Cl N2 O8 Ru2
Mr	619.96	619.96
Dx,g cm-3	1.915	1.915
Z	2	2
Mu (mm-1)	1.575	1.575
F000	614.0	609.6
F000'	609.50	
h,k,lmax	11,14,16	11,14,16
Nref	5380	5363
Tmin,Tmax	0.719,0.815	0.890,1.000
Tmin'	0.617	

```
Correction method= # Reported T Limits: Tmin=0.890 Tmax=1.000
AbsCorr = MULTI-SCAN

Data completeness= 0.997          Theta(max)= 28.360

R(reflections)= 0.0229( 4654)                    wR2(reflections)=
                                                 0.0545( 5363)
S = 1.040                 Npar= 289
```

```
The following ALERTS were generated. Each ALERT has the format
      test-name_ALERT_alert-type_alert-level.
Click on the hyperlinks for more details of the test.
```

Alert level C

```
CRYSC01_ALERT_1_C No recognised colour has been given for crystal colour.
PLAT417_ALERT_2_C Short Inter D-H..H-D       H7B      ..H8B      .       2.13 Ang.
                                                    x,y,z  =      1_555 Check
```

Alert level G

```
PLAT002_ALERT_2_G Number of Distance or Angle Restraints on AtSite          6 Note
PLAT068_ALERT_1_G Reported F000 Differs from Calcd (or Missing)...     Please Check
PLAT154_ALERT_1_G The s.u.'s on the Cell Angles are Equal ..(Note)      0.001 Degree
PLAT172_ALERT_4_G The CIF-Embedded .res File Contains DFIX Records          2 Report
PLAT232_ALERT_2_G Hirshfeld Test Diff (M-X)  Ru1      --Cl1      .       12.7 s.u.
PLAT769_ALERT_4_G CIF Embedded Explicitly Supplied Scattering Data     Please Note
PLAT860_ALERT_3_G Number of Least-Squares Restraints .............          4 Note
PLAT883_ALERT_1_G No Info/Value for _atom_sites_solution_primary .     Please Do !
PLAT912_ALERT_4_G Missing # of FCF Reflections Above STh/L=  0.600         19 Note
PLAT960_ALERT_3_G Number of Intensities with I  <   - 2*sig(I) ...          3 Check
PLAT978_ALERT_2_G Number C-C Bonds with Positive Residual Density.          5 Info
PLAT982_ALERT_1_G The Ru-f'=   -1.2394 Deviates from  IT-value =     -1.2594 Check
PLAT983_ALERT_1_G The Cl-f"=    0.1603 Deviates from  IT-Value =      0.1585 Check
PLAT983_ALERT_1_G The Ru-f"=    0.8352 Deviates from  IT-Value =      0.8363 Check
```

```
  0 ALERT level A - Most likely a serious problem - resolve or explain
  0 ALERT level B - A potentially serious problem, consider carefully
  2 ALERT level C - Check. Ensure it is not caused by an omission or oversight
 14 ALERT level G - General information/check it is not something unexpected

  7 ALERT type 1 CIF construction/syntax error, inconsistent or missing data
  4 ALERT type 2 Indicator that the structure model may be wrong or deficient
  2 ALERT type 3 Indicator that the structure quality may be low
  3 ALERT type 4 Improvement, methodology, query or suggestion
  0 ALERT type 5 Informative message, check
```

Validation response form

Please find below a validation response form (VRF) that can be filled in and pasted into your CIF.

```
# start Validation Reply Form
_vrf_CRYSC01_TM01
;
PROBLEM: No recognised colour has been given for crystal colour.
RESPONSE: ...
;
_vrf_PLAT417_TM01
;
```

```
PROBLEM: Short Inter D-H..H-D       H7B      ..H8B      .       2.13 Ang.
RESPONSE: ...
;
# end Validation Reply Form
```

It is advisable to attempt to resolve as many as possible of the alerts in all categories. Often the minor alerts point to easily fixed oversights, errors and omissions in your CIF or refinement strategy, so attention to these fine details can be worthwhile. In order to resolve some of the more serious problems it may be necessary to carry out additional measurements or structure refinements. However, the purpose of your study may justify the reported deviations and the more serious of these should normally be commented upon in the discussion or experimental section of a paper or in the "special_details" fields of the CIF. checkCIF was carefully designed to identify outliers and unusual parameters, but every test has its limitations and alerts that are not important in a particular case may appear. Conversely, the absence of alerts does not guarantee there are no aspects of the results needing attention. It is up to the individual to critically assess their own results and, if necessary, seek expert advice.

Publication of your CIF in IUCr journals

A basic structural check has been run on your CIF. These basic checks will be run on all CIFs submitted for publication in IUCr journals (*Acta Crystallographica*, *Journal of Applied Crystallography*, *Journal of Synchrotron Radiation*); however, if you intend to submit to *Acta Crystallographica Section C* or *E* or *IUCrData*, you should make sure that full publication checks are run on the final version of your CIF prior to submission.

Publication of your CIF in other journals

Please refer to the *Notes for Authors* of the relevant journal for any special instructions relating to CIF submission.

PLATON version of 29/11/2023; check.def file version of 14/09/2023

Datablock TM01 - ellipsoid plot

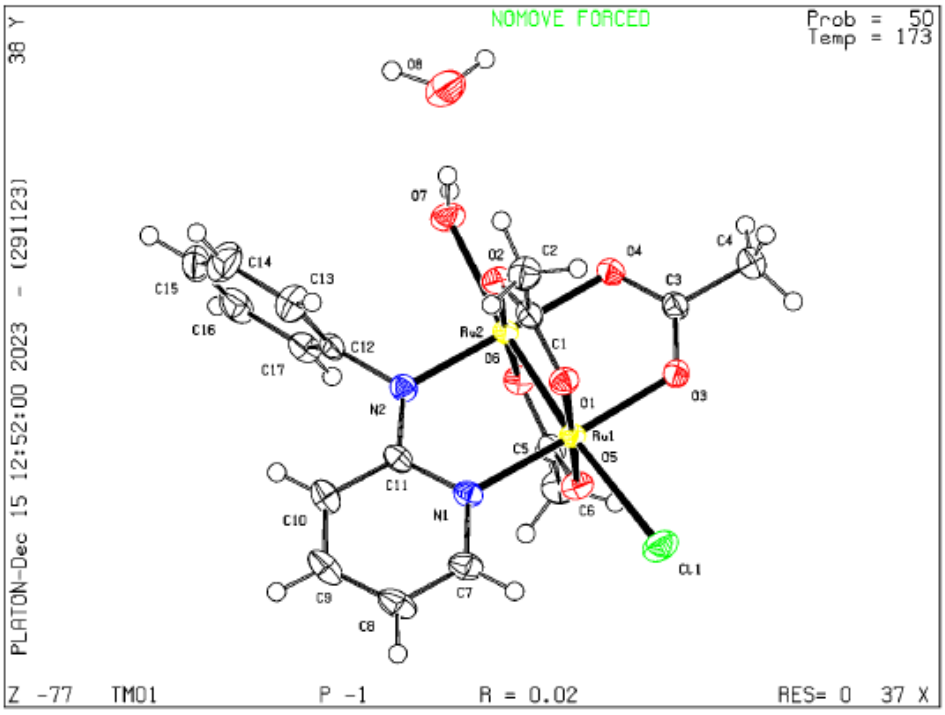

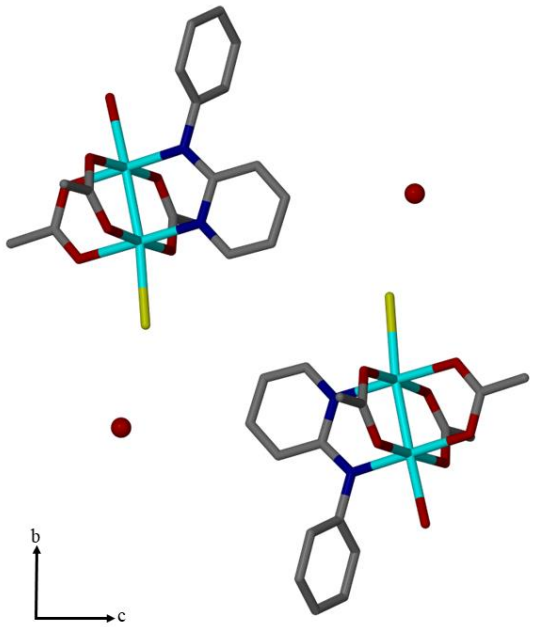

Figure 6.57 Single X-ray crystallographic packing diagram of **C1** around the a-axis.

*Single X-Ray Crystallographic CheckCIF file Report for **C3**.*

checkCIF/PLATON report

Structure factors have been supplied for datablock(s) TM02

THIS REPORT IS FOR GUIDANCE ONLY. IF USED AS PART OF A REVIEW PROCEDURE FOR PUBLICATION, IT SHOULD NOT REPLACE THE EXPERTISE OF AN EXPERIENCED CRYSTALLOGRAPHIC REFEREE.

No syntax errors found. CIF dictionary Interpreting this report

Datablock: TM02

Bond precision: C-C = 0.0063 A Wavelength=0.71073

Cell: a=10.5933(13) b=12.0749(16) c=14.8024(19)
alpha=92.817(3) beta=106.502(2) gamma=98.592(3)
Temperature: 173 K

	Calculated	Reported
Volume	1786.7(4)	1786.7(4)
Space group	P -1	P -1
Hall group	-P 1	-P 1
Moiety formula	C18 H22 Cl N2 O7 Ru2, 2(C Cl3), C H Cl3, H2 O	C18 H22 Cl N2 O7 Ru2, H2 O, 2(C Cl3), C H Cl3
Sum formula	C21 H25 Cl10 N2 O8 Ru2	C21 H25 Cl10 N2 O8 Ru2
Mr	990.07	990.10
Dx,g cm-3	1.840	1.840
Z	2	2
Mu (mm-1)	1.636	1.636
F000	974.0	972.3
F000'	972.21	
h,k,lmax	14,16,19	14,16,19
Nref	8902	8851
Tmin,Tmax	0.790,0.849	0.882,1.000
Tmin'	0.782	

Correction method= # Reported T Limits: Tmin=0.882 Tmax=1.000
AbsCorr = MULTI-SCAN

Data completeness= 0.994 Theta(max)= 28.330

R(reflections)= 0.0429(6417) wR2(reflections)= 0.1026(8851)

S = 1.002 Npar= 464

```
The following ALERTS were generated. Each ALERT has the format
      test-name_ALERT_alert-type_alert-level.
Click on the hyperlinks for more details of the test.
```

Alert level A

```
SHFSU01_ALERT_2_A  The absolute value of parameter shift to su ratio > 0.20
           Absolute value of the parameter shift to su ratio given   2.243
           Additional refinement cycles may be required.
PLAT080_ALERT_2_A Maximum Shift/Error ..........................       2.24 Why ?
```

Alert level C

```
CRYSC01_ALERT_1_C No recognised colour has been given for crystal colour.
PLAT042_ALERT_1_C Calc. and Reported MoietyFormula Strings  Differ     Please Check
             Calc: C18 H22 Cl N2 O7 Ru2, 2(C Cl3), C H Cl3, H2 O
             Rep.: C18 H22 Cl N2 O7 Ru2, H2 O, 2(C Cl3), C H Cl3
PLAT220_ALERT_2_C NonSolvent   Resd 1  C   Ueq(max)/Ueq(min) Range        3.7 Ratio
PLAT234_ALERT_4_C Large Hirshfeld Difference C15      --C18      .       0.16 Ang.
PLAT234_ALERT_4_C Large Hirshfeld Difference C15C     --C1C      .       0.16 Ang.
PLAT242_ALERT_2_C Low    'MainMol' Ueq as Compared to Neighbors of        C15 Check
PLAT244_ALERT_4_C Low    'Solvent' Ueq as Compared to Neighbors of        C1A Check
PLAT244_ALERT_4_C Low    'Solvent' Ueq as Compared to Neighbors of        C1C Check
PLAT244_ALERT_4_C Low    'Solvent' Ueq as Compared to Neighbors of        C1B Check
PLAT250_ALERT_2_C Large U3/U1 Ratio for Average U(i,j) Tensor ....        2.2 Note
PLAT336_ALERT_2_C Long Bond Distance for ..... C1C      -C15C          1.905 Ang.
PLAT911_ALERT_3_C Missing FCF Refl Between Thmin & STh/L=    0.600        13 Report
               1  0  0,  -1  1  0,   0 -1  1,   1 -2  2,  10 -5  3,  11 -5  3,
              10 -5  4,   9 -4  4,  10 -4  4,  10 -5  5,  10 -4  5,  10 -4  6,
              10 -3  6,
PLAT975_ALERT_2_C Check Calcd Resid. Dens.  0.86Ang From C1A     .       0.60 eA-3
```

Alert level G

```
PLAT002_ALERT_2_G Number of Distance or Angle Restraints on AtSite         20 Note
PLAT003_ALERT_2_G Number of Uiso or Uij Restrained non-H Atoms ...         14 Report
PLAT068_ALERT_1_G Reported F000 Differs from Calcd (or Missing)...     Please Check
PLAT172_ALERT_4_G The CIF-Embedded .res File Contains DFIX Records          4 Report
PLAT176_ALERT_4_G The CIF-Embedded .res File Contains SADI Records          2 Report
PLAT177_ALERT_4_G The CIF-Embedded .res File Contains DELU Records          2 Report
PLAT178_ALERT_4_G The CIF-Embedded .res File Contains SIMU Records          2 Report
PLAT302_ALERT_4_G Anion/Solvent/Minor-Residue Disorder (Resd  2  )         75% Note
PLAT302_ALERT_4_G Anion/Solvent/Minor-Residue Disorder (Resd  3  )         75% Note
PLAT432_ALERT_2_G Short Inter X...Y Contact  C12C     ..C18      .       3.12 Ang.
                                                -x,1-y,-z  =      2_565 Check
PLAT434_ALERT_2_G Short Inter HL..HL Contact C11B     ..C16C     .       3.30 Ang.
                                                x,y,z  =      1_555 Check
PLAT769_ALERT_4_G CIF Embedded Explicitly Supplied Scattering Data     Please Note
PLAT860_ALERT_3_G Number of Least-Squares Restraints .............        130 Note
PLAT912_ALERT_4_G Missing # of FCF Reflections Above STh/L=  0.600         39 Note
PLAT933_ALERT_2_G Number of HKL-OMIT Records in Embedded .res File          3 Note
               1 -2  2,   0 -1  1,  -1  1  0,
PLAT960_ALERT_3_G Number of Intensities with I  <   - 2*sig(I) ...          4 Check
PLAT978_ALERT_2_G Number C-C Bonds with Positive Residual Density.          1 Info
PLAT982_ALERT_1_G The Ru-f'=   -1.2394 Deviates from  IT-value =     -1.2594 Check
```

```
_vrf_CRYSC01_TM02
;
PROBLEM: No recognised colour has been given for crystal colour.
RESPONSE: ...
;
_vrf_PLAT080_TM02
;
PROBLEM: Maximum Shift/Error ..........................       2.24 Why ?
RESPONSE: ...
;
_vrf_PLAT042_TM02
;
PROBLEM: Calc. and Reported MoietyFormula Strings  Differ     Please Check
RESPONSE: ...
;
_vrf_PLAT220_TM02
;
PROBLEM: NonSolvent   Resd 1  C   Ueq(max)/Ueq(min) Range        3.7 Ratio
RESPONSE: ...
;
_vrf_PLAT234_TM02
;
PROBLEM: Large Hirshfeld Difference C15      --C18      .       0.16 Ang.
RESPONSE: ...
;
_vrf_PLAT242_TM02
;
PROBLEM: Low    'MainMol' Ueq as Compared to Neighbors of        C15 Check
RESPONSE: ...
;
_vrf_PLAT244_TM02
;
PROBLEM: Low    'Solvent' Ueq as Compared to Neighbors of        C1A Check
RESPONSE: ...
;
_vrf_PLAT250_TM02
;
PROBLEM: Large U3/U1 Ratio for Average U(i,j) Tensor ....        2.2 Note
RESPONSE: ...
;
_vrf_PLAT336_TM02
;
PROBLEM: Long Bond Distance for ..... C1C      -C15C          1.905 Ang.
RESPONSE: ...
;
_vrf_PLAT911_TM02
;
PROBLEM: Missing FCF Refl Between Thmin & STh/L=    0.600         13 Report
RESPONSE: ...
;
_vrf_PLAT975_TM02
;
PROBLEM: Check Calcd Resid. Dens.  0.86Ang From C1A     .       0.60 eA-3
RESPONSE: ...
;
# end Validation Reply Form
```

```
PLAT983_ALERT_1_G The Cl-f"=     0.1603 Deviates from  IT-Value =       0.1585 Check
PLAT983_ALERT_1_G The Ru-f"=     0.8352 Deviates from  IT-Value =       0.8363 Check

   2 ALERT level A = Most likely a serious problem - resolve or explain
   0 ALERT level B = A potentially serious problem, consider carefully
  13 ALERT level C = Check. Ensure it is not caused by an omission or oversight
  20 ALERT level G = General information/check it is not something unexpected

   6 ALERT type 1 CIF construction/syntax error, inconsistent or missing data
  13 ALERT type 2 Indicator that the structure model may be wrong or deficient
   3 ALERT type 3 Indicator that the structure quality may be low
  13 ALERT type 4 Improvement, methodology, query or suggestion
   0 ALERT type 5 Informative message, check
```

It is advisable to attempt to resolve as many as possible of the alerts in all categories. Often the minor alerts point to easily fixed oversights, errors and omissions in your CIF or refinement strategy, so attention to these fine details can be worthwhile. In order to resolve some of the more serious problems it may be necessary to carry out additional measurements or structure refinements. However, the purpose of your study may justify the reported deviations and the more serious of these should normally be commented upon in the discussion or experimental section of a paper or in the "special_details" fields of the CIF. checkCIF was carefully designed to identify outliers and unusual parameters, but every test has its limitations and alerts that are not important in a particular case may appear. Conversely, the absence of alerts does not guarantee there are no aspects of the results needing attention. It is up to the individual to critically assess their own results and, if necessary, seek expert advice.

Publication of your CIF in IUCr journals

A basic structural check has been run on your CIF. These basic checks will be run on all CIFs submitted for publication in IUCr journals (*Acta Crystallographica*, *Journal of Applied Crystallography*, *Journal of Synchrotron Radiation*); however, if you intend to submit to *Acta Crystallographica Section C* or *E* or *IUCrData*, you should make sure that full publication checks are run on the final version of your CIF prior to submission.

Publication of your CIF in other journals

Please refer to the *Notes for Authors* of the relevant journal for any special instructions relating to CIF submission.

Validation response form

Please find below a validation response form (VRF) that can be filled in and pasted into your CIF.

```
# start Validation Reply Form
_vrf_SHFSU01_TM02
;
PROBLEM: The absolute value of parameter shift to su ratio > 0.20
RESPONSE: ...
;
```

PLATON version of 29/11/2023; check.def file version of 14/09/2023

Datablock TM02 - ellipsoid plot

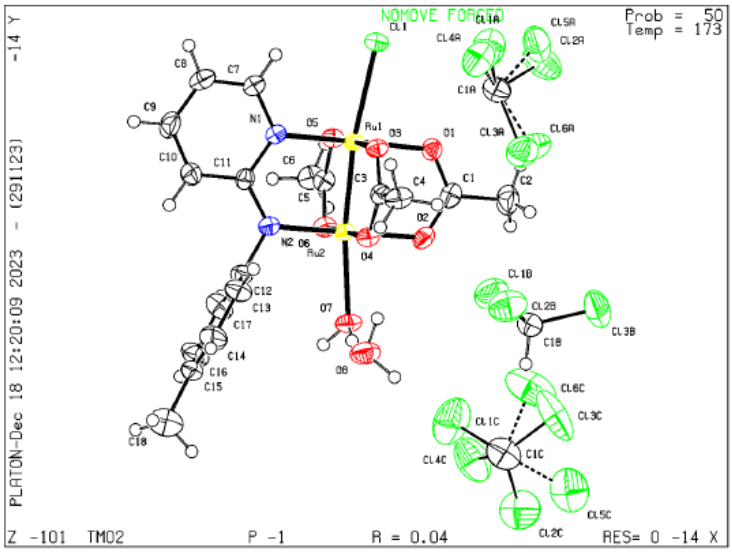

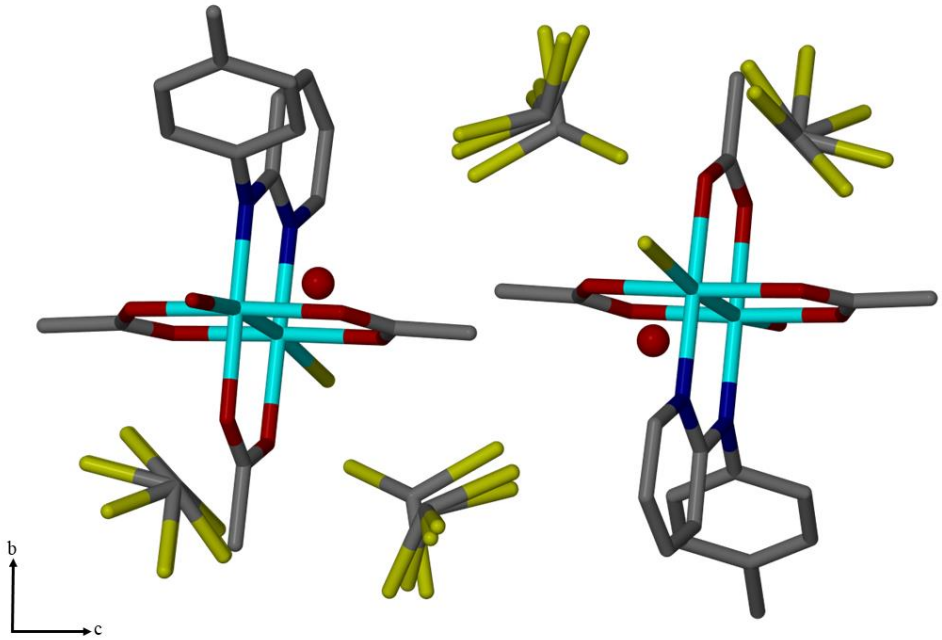

Figure 6.58 Single X-ray crystallographic packing diagram of **C3** around the a-axis.

*Single X-Ray Crystallographic CheckCIF file Report for **C8**.*

checkCIF/PLATON report

Structure factors have been supplied for datablock(s) TM08

THIS REPORT IS FOR GUIDANCE ONLY. IF USED AS PART OF A REVIEW PROCEDURE FOR PUBLICATION, IT SHOULD NOT REPLACE THE EXPERTISE OF AN EXPERIENCED CRYSTALLOGRAPHIC REFEREE.

No syntax errors found. CIF dictionary Interpreting this report

Datablock: TM08

Bond precision: C-C = 0.0062 A Wavelength=0.71073

Cell: a=10.4643(6) b=12.6964(8) c=14.7321(9)
alpha=78.130(2) beta=73.415(2) gamma=71.978(2)
Temperature: 173 K

	Calculated	Reported
Volume	1768.97(19)	1768.97(19)
Space group	P -1	P -1
Hall group	-P 1	-P 1
Moiety formula	C17 H19 Cl F N2 O7 Ru2, 3(C H Cl3), H2 O	?
Sum formula	C20 H24 Cl10 F N2 O8 Ru2	C20 H24 Cl10 F N2 O8 Ru2
Mr	996.05	996.05
Dx,g cm-3	1.870	1.870
Z	2	2
Mu (mm-1)	1.657	1.657
F000	978.0	978.0
F000'	976.24	
h,k,lmax	13,16,19	13,16,19
Nref	8831	8793
Tmin,Tmax	0.820,0.876	0.913,1.000
Tmin'	0.806	

Correction method= # Reported T Limits: Tmin=0.913 Tmax=1.000
AbsCorr = MULTI-SCAN

Data completeness= 0.996 Theta(max)= 28.346

R(reflections)= 0.0413(6355) wR2(reflections)= 0.0920(8793)

S = 1.021 Npar= 407

The following ALERTS were generated. Each ALERT has the format
test-name_ALERT_alert-type_alert-level.
Click on the hyperlinks for more details of the test.

Alert level B

```
PLAT417_ALERT_2_B Short Inter D-H..H-D       H7B      ..H8B      .       2.03 Ang.
                                                      x,y,z  =      1_555 Check
```

Alert level C

```
PLAT048_ALERT_1_C MoietyFormula Not Given (or Incomplete) ........     Please Check
PLAT244_ALERT_4_C Low    'Solvent' Ueq as Compared to Neighbors of       C1A Check
PLAT244_ALERT_4_C Low    'Solvent' Ueq as Compared to Neighbors of       C1B Check
PLAT244_ALERT_4_C Low    'Solvent' Ueq as Compared to Neighbors of       C1C Check
PLAT761_ALERT_1_C CIF Contains no X-H Bonds .......................     Please Check
PLAT762_ALERT_1_C CIF Contains no X-Y-H or H-Y-H Angles ..........     Please Check
PLAT975_ALERT_2_C Check Calcd Resid. Dens.  0.68Ang From O7      .       0.44 eA-3
```

Alert level G

```
PLAT002_ALERT_2_G Number of Distance or Angle Restraints on AtSite         6 Note
PLAT083_ALERT_2_G SHELXL Second Parameter in WGHT  Unusually Large      6.44 Why ?
PLAT154_ALERT_1_G The s.u.'s on the Cell Angles are Equal ..(Note)     0.002 Degree
PLAT172_ALERT_4_G The CIF-Embedded .res File Contains DFIX Records         5 Report
PLAT232_ALERT_2_G Hirshfeld Test Diff (M-X)  Ru2      --Cl1      .       5.2 s.u.
PLAT434_ALERT_2_G Short Inter HL..HL Contact C13A     ..F1       .      3.09 Ang.
                                                 1+x,-1+y,z  =     1_645 Check
PLAT790_ALERT_4_G Centre of Gravity not Within Unit Cell: Resd.  #         5 Note
            H2 O
PLAT860_ALERT_3_G Number of Least-Squares Restraints .............         5 Note
PLAT899_ALERT_4_G SHELXL2018 is Deprecated and Succeeded by SHELXL    2019/3 Note
PLAT910_ALERT_3_G Missing # of FCF Reflection(s) Below Theta(Min).         3 Note
              0  1  0,   0  0  1,   0  1  1,
PLAT912_ALERT_4_G Missing # of FCF Reflections Above STh/L=  0.600        34 Note
PLAT933_ALERT_2_G Number of HKL-OMIT Records in Embedded .res File         1 Note
              0  1  2,
PLAT978_ALERT_2_G Number C-C Bonds with Positive Residual Density.         0 Info
```

```
  0 ALERT level A - Most likely a serious problem - resolve or explain
  1 ALERT level B - A potentially serious problem, consider carefully
  7 ALERT level C - Check. Ensure it is not caused by an omission or oversight
 13 ALERT level G - General information/check it is not something unexpected

  4 ALERT type 1 CIF construction/syntax error, inconsistent or missing data
  8 ALERT type 2 Indicator that the structure model may be wrong or deficient
  2 ALERT type 3 Indicator that the structure quality may be low
  7 ALERT type 4 Improvement, methodology, query or suggestion
  0 ALERT type 5 Informative message, check
```

checkCIF publication errors

Alert level A

```
PUBL004_ALERT_1_A  The contact author's name and address are missing,
           _publ_contact_author_name and _publ_contact_author_address.
PUBL005_ALERT_1_A  _publ_contact_author_email, _publ_contact_author_fax and
           _publ_contact_author_phone are all missing.
           At least one of these should be present.
PUBL006_ALERT_1_A  _publ_requested_journal is missing
           e.g. 'Acta Crystallographica Section C'
PUBL008_ALERT_1_A  _publ_section_title is missing. Title of paper.
PUBL009_ALERT_1_A  _publ_author_name is missing. List of author(s) name(s).
PUBL010_ALERT_1_A  _publ_author_address is missing. Author(s) address(es).
PUBL012_ALERT_1_A  _publ_section_abstract is missing.
           Abstract of paper in English.
```

Alert level G

```
PUBL017_ALERT_1_G The _publ_section_references section is missing or
           empty.
```

```
  7 ALERT level A - Data missing that is essential or data in wrong format
  1 ALERT level G - General alerts. Data that may be required is missing
```

Publication of your CIF

You should attempt to resolve as many as possible of the alerts in all categories. Often the minor alerts point to easily fixed oversights, errors and omissions in your CIF or refinement strategy, so attention to these fine details can be worthwhile. In order to resolve some of the more serious problems it may be necessary to carry out additional measurements or structure refinements. However, the nature of your study may justify the reported deviations from journal submission requirements and the more serious of these should be commented upon in the discussion or experimental section of a paper or in the "special_details" fields of the CIF. *checkCIF* was carefully designed to identify outliers and unusual parameters, but every test has its limitations and alerts that are not important in a particular case may appear. Conversely, the absence of alerts does not guarantee there are no aspects of the results needing attention. It is up to the individual to critically assess their own results and, if necessary, seek expert advice.

If level A alerts remain, which you believe to be justified deviations, and you intend to submit this CIF for publication in a journal, you should additionally insert an explanation in your CIF using the Validation Reply Form (VRF) below. This will allow your explanation to be considered as part of the review process.

Validation response form

Please find below a validation response form (VRF) that can be filled in and pasted into your CIF.

```
# start Validation Reply Form
_vrf_PUBL004_GLOBAL
;
PROBLEM: The contact author's name and address are missing,
RESPONSE: ...
;
_vrf_PUBL005_GLOBAL
;
PROBLEM: _publ_contact_author_email, _publ_contact_author_fax and
RESPONSE: ...
;
_vrf_PUBL006_GLOBAL
;
PROBLEM: _publ_requested_journal is missing
RESPONSE: ...
;
_vrf_PUBL008_GLOBAL
;
PROBLEM: _publ_section_title is missing. Title of paper.
RESPONSE: ...
;
_vrf_PUBL009_GLOBAL
;
PROBLEM: _publ_author_name is missing. List of author(s) name(s).
RESPONSE: ...
;
_vrf_PUBL010_GLOBAL
;
PROBLEM: _publ_author_address is missing. Author(s) address(es).
RESPONSE: ...
;
_vrf_PUBL012_GLOBAL
;
PROBLEM: _publ_section_abstract is missing.
RESPONSE: ...
;
_vrf_PLAT417_TM08
;
PROBLEM: Short Inter D-H..H-D       H7B      ..H8B      .       2.03 Ang.
RESPONSE: ...
;
# end Validation Reply Form
```

If you wish to submit your CIF for publication in Acta Crystallographica Section C or E, you should upload your CIF via the web. If you wish to submit your CIF for publication in IUCrData you should upload your CIF via the web. If your CIF is to form part of a submission to another IUCr journal, you will be asked, either during electronic submission or by the Co-editor handling your paper, to upload your CIF via our web site.

PLATON version of 29/11/2023; check.def file version of 14/09/2023

Datablock TM08 - ellipsoid plot

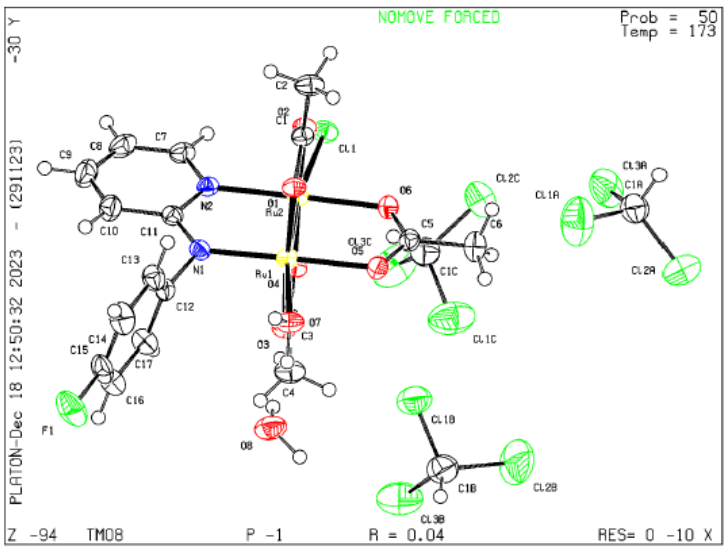

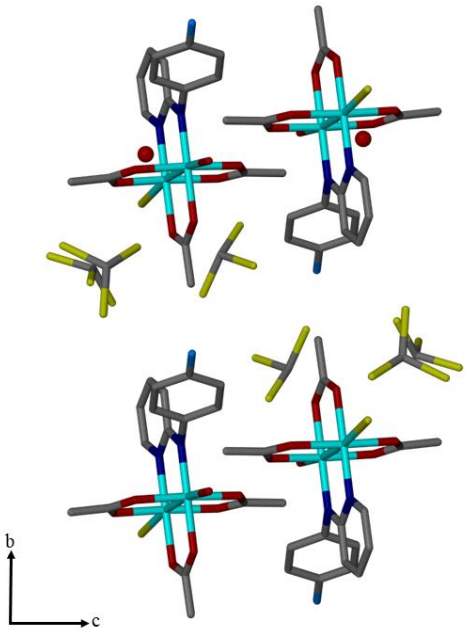

Figure 6.59 Single X-ray crystallographic packing diagram of **C8** around the a-axis.

Infrared spectra of $[Ru_2(O_2CCH_3)_3(R\text{-ap})]$ (**C2**, **C4** - **C7**)

*Infrared (IR-ATR) spectrum of **C2***

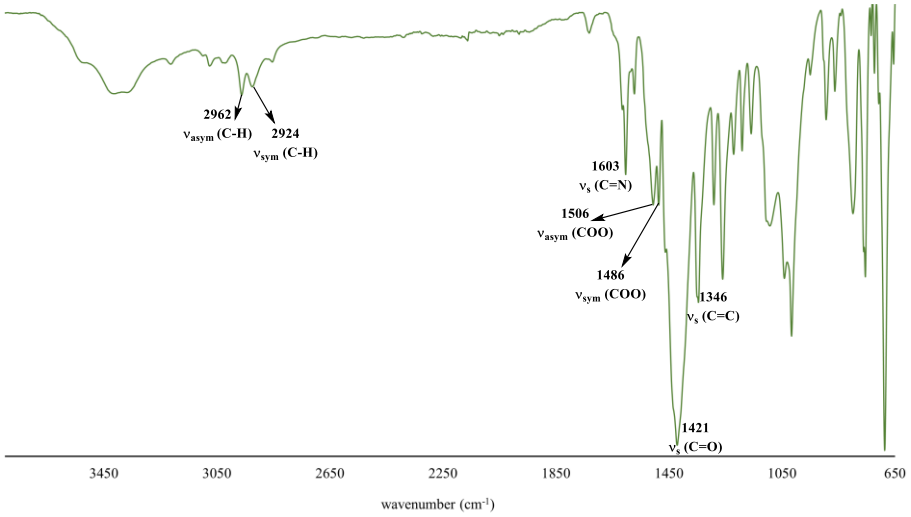

Figure 6.60 Infrared (IR-ATR) spectrum of **C2**.

*Infrared (IR-ATR) spectrum of **C4***

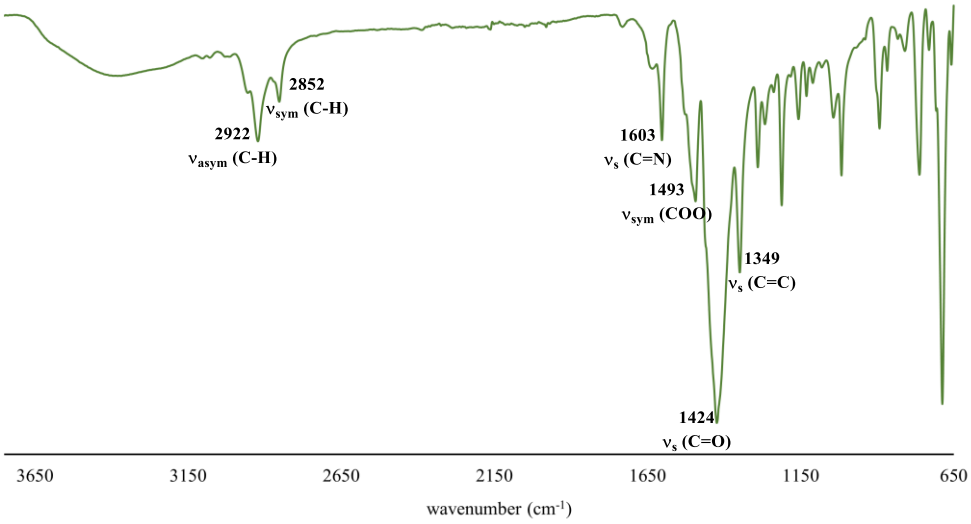

Figure 6.61 Infrared (IR-ATR) spectrum of **C4**.

*Infrared spectrum of **C5***

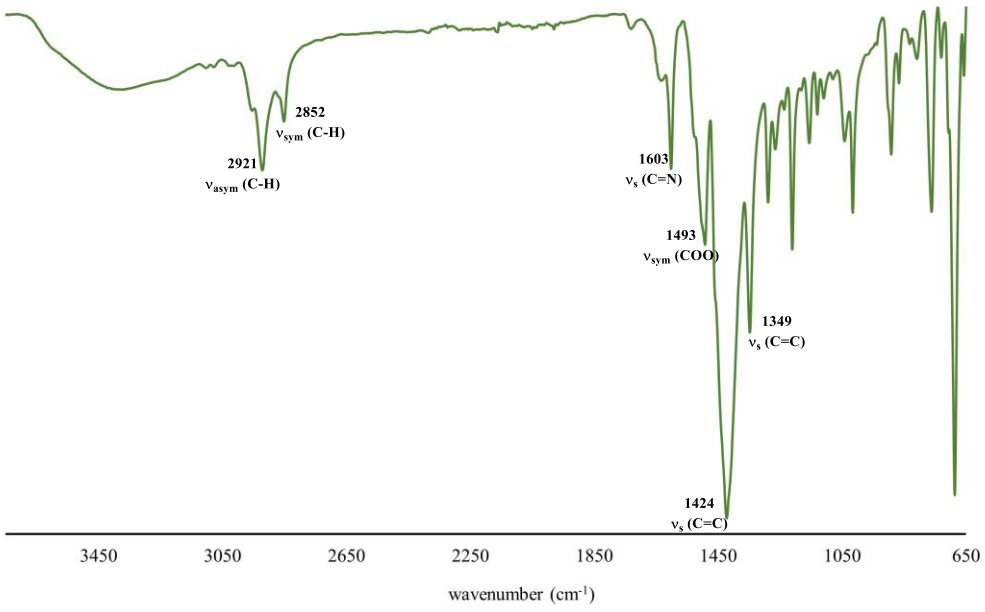

Figure 6.62 Infrared (IR-ATR) spectrum of **C5**.

*Infrared spectrum of **C6***

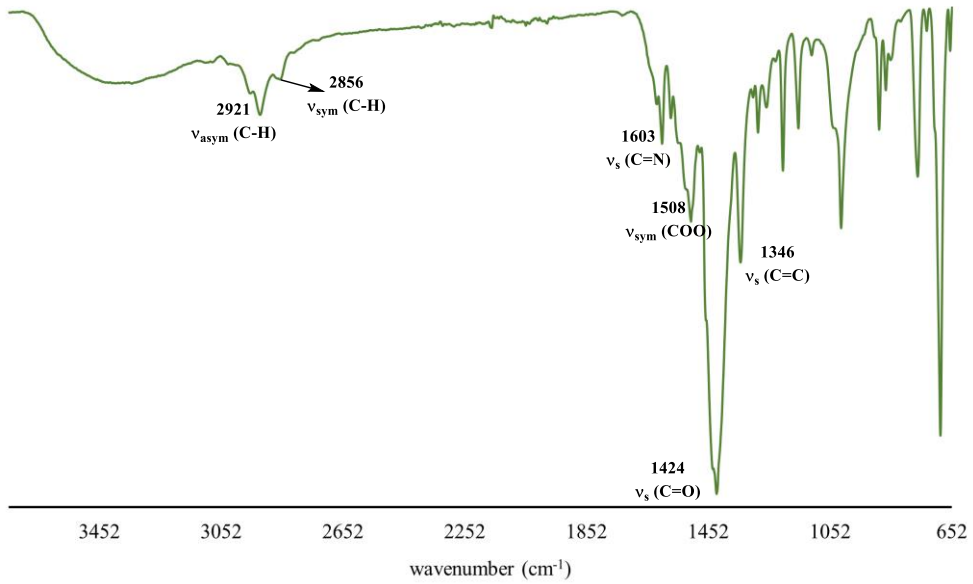

Figure 6.63 Infrared (IR-ATR) spectrum of **C6.**

*Infrared spectrum of **C7***

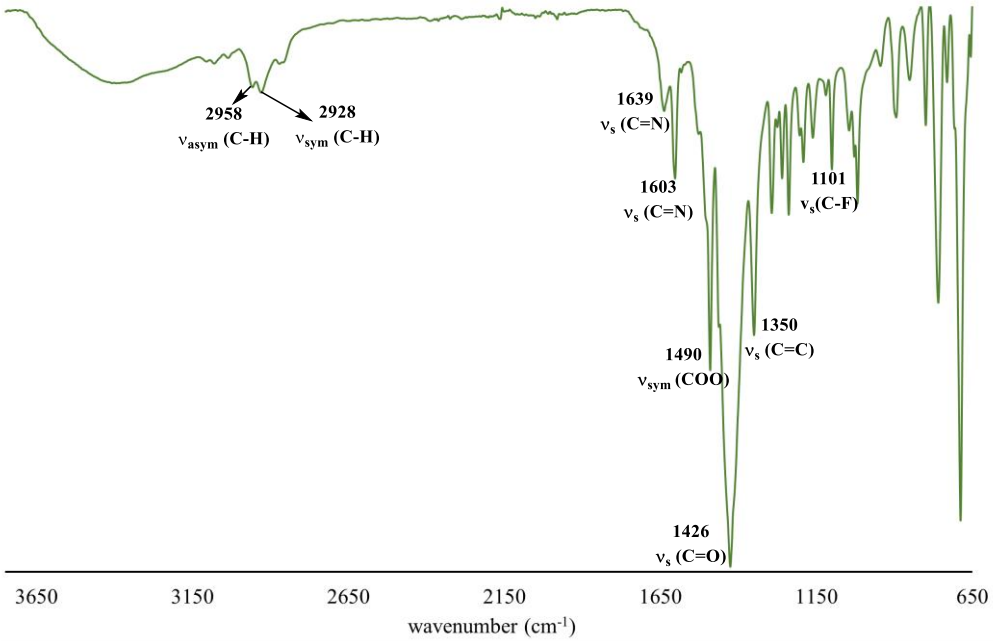

Figure 6.64 Infrared (IR-ATR) spectrum of **C7**.

Magnetic susceptibility of $[Ru_2(O_2CCH_3)_3(R\text{-}ap)Cl]$ (**C4** - **C7**) complexes

*Paramagnetic susceptibility ^{1}H-NMR spectrum of **C4***

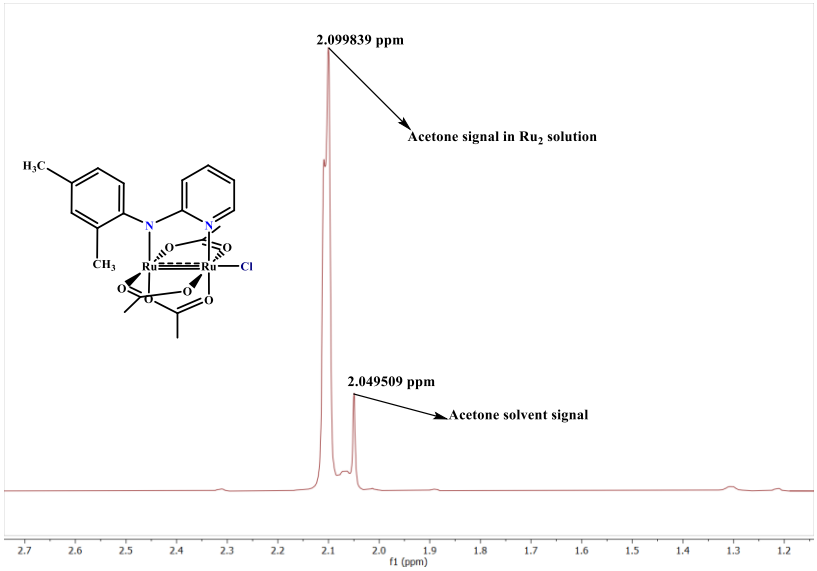

Figure 6.65 The paramagnetic susceptibility ^{1}H-NMR spectrum of **C4** in 50:1 (v/v) $(CD_3)_2CO$ and $(CH_3)_2CO$ solvent, recorded at room temperature (298K) using NMR (300 Hz) spectrometer.

*Paramagnetic susceptibility ^{1}H-NMR spectrum of **C5***

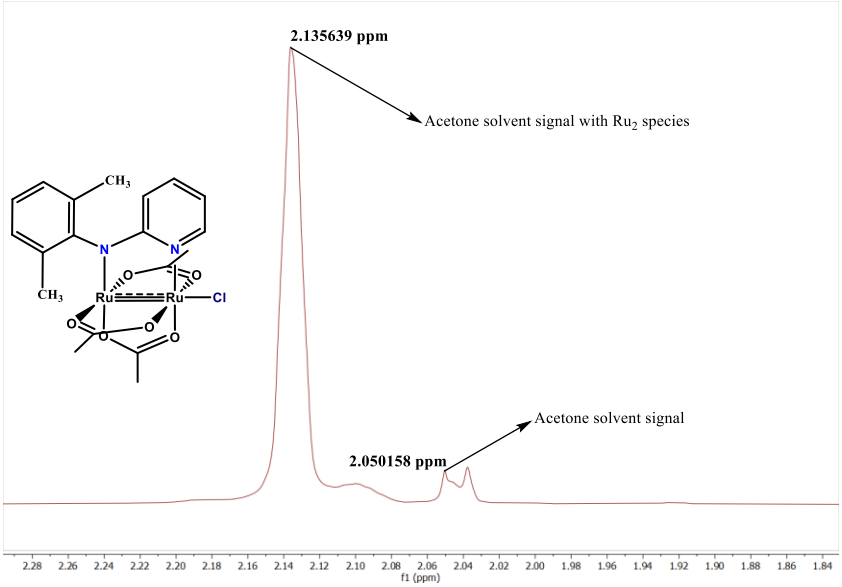

Figure 6.66 The paramagnetic susceptibility ^{1}H-NMR spectrum of **C5** in 50:1 (v/v) $(CD_3)_2CO$ and $(CH_3)_2CO$ solvent, recorded at room temperature (298K) using NMR (300 Hz) spectrometer.

*Paramagnetic susceptibility ^{1}H-NMR spectrum of **C6***

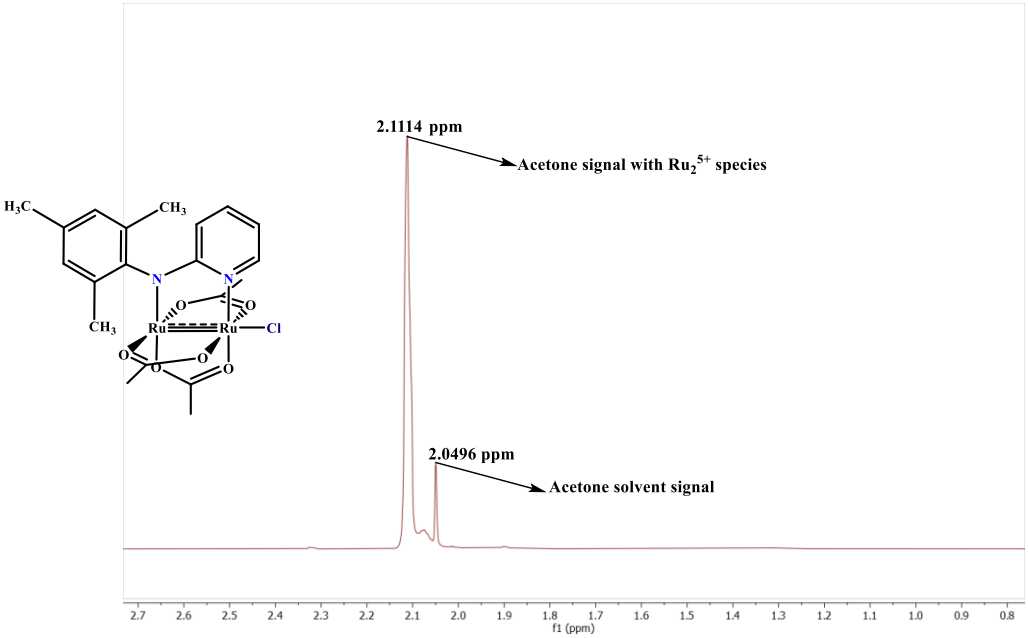

Figure 6.67 The paramagnetic susceptibility ^{1}H-NMR spectrum of **C6** in 50:1 (v/v) $(CD_3)_2CO$ and $(CH_3)_2CO$ solvent, recorded at room temperature (298K) using NMR (300 Hz) spectrometer.

*The paramagnetic susceptibility ^{1}H-NMR spectrum of **C7***

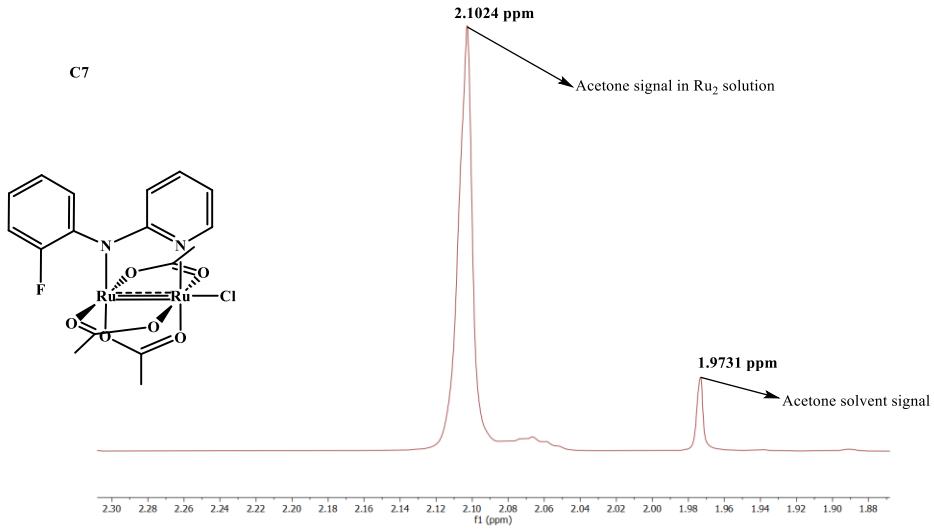

Figure 6.68 The paramagnetic susceptibility ^{1}H NMR spectrum of **C7** in 50:1 (v/v) $(CD_3)_2CO$ and $(CH_3)_2CO$ solvent, recorded at room temperature (298K) using NMR (300 Hz) spectrometer.

High-resolution (ESI) mass spectrometric spectra of **C2**, **C4** - **C7**.

*High-resolution (ESI) mass spectrum of **C2**.*

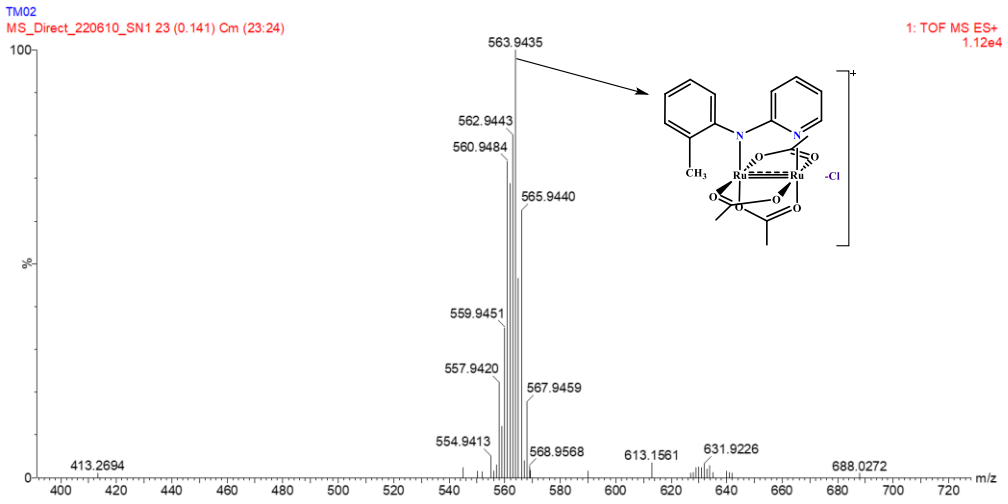

Figure 6.69 High resolution (ESI) mass spectrometry of complex, **C2**. The molecular ion base peak fragment was confirmed using the Molecular Weight Calculator Excel spreadsheet provided by Fiehn Lab, UC Davis Genome Centre - Metabolomics.[2]

*High-resolution (ESI) mass spectrum of **C4**.*

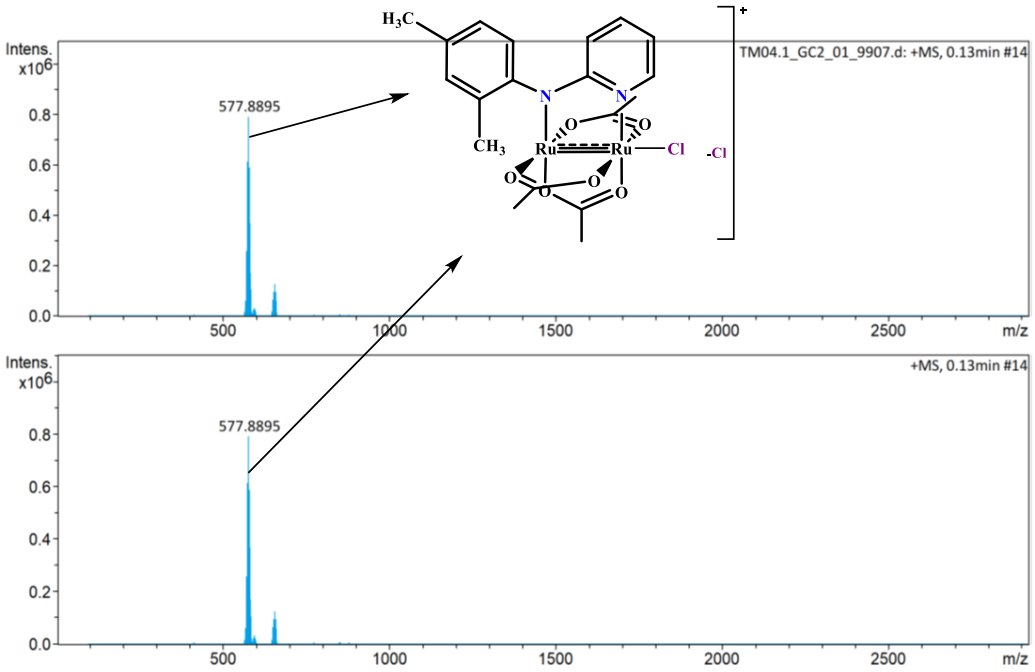

Figure 6.70 High resolution (ESI) mass spectrometry of complex, **C4**. The molecular ion base peak fragment was confirmed using the Molecular Weight Calculator Excel spreadsheet provided by Fiehn Lab, UC Davis Genome Centre - Metabolomics.[2]

*High-resolution (ESI) mass spectrum of **C5**.*

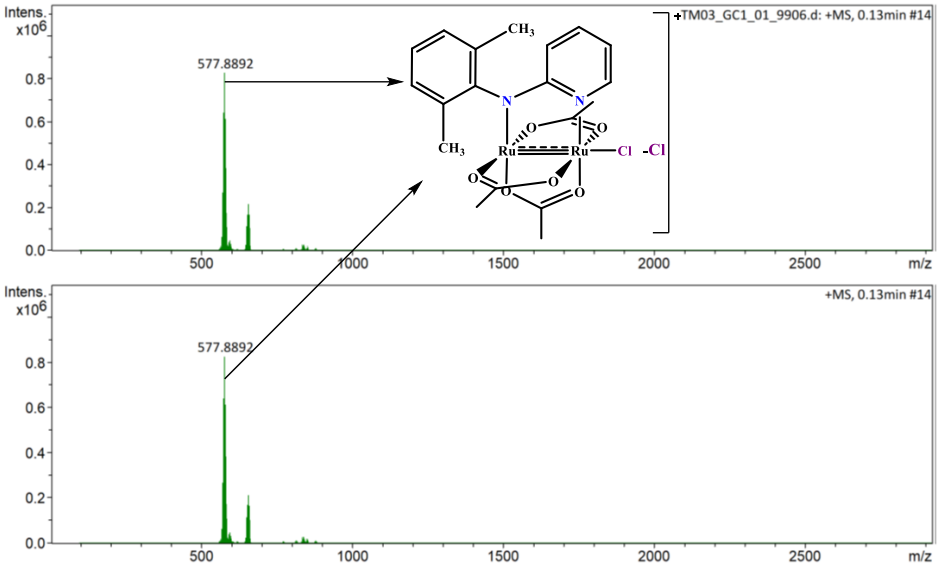

Figure 6.71 High Resolution (ESI) Mass Spectrometry of complex, **C5**. The molecular ion base peak fragment was confirmed using the Molecular Weight Calculator Excel spreadsheet provided by Fiehn Lab, UC Davis Genome Centre - Metabolomics.[2]

*High-resolution (ESI) mass spectrum of **C6**.*

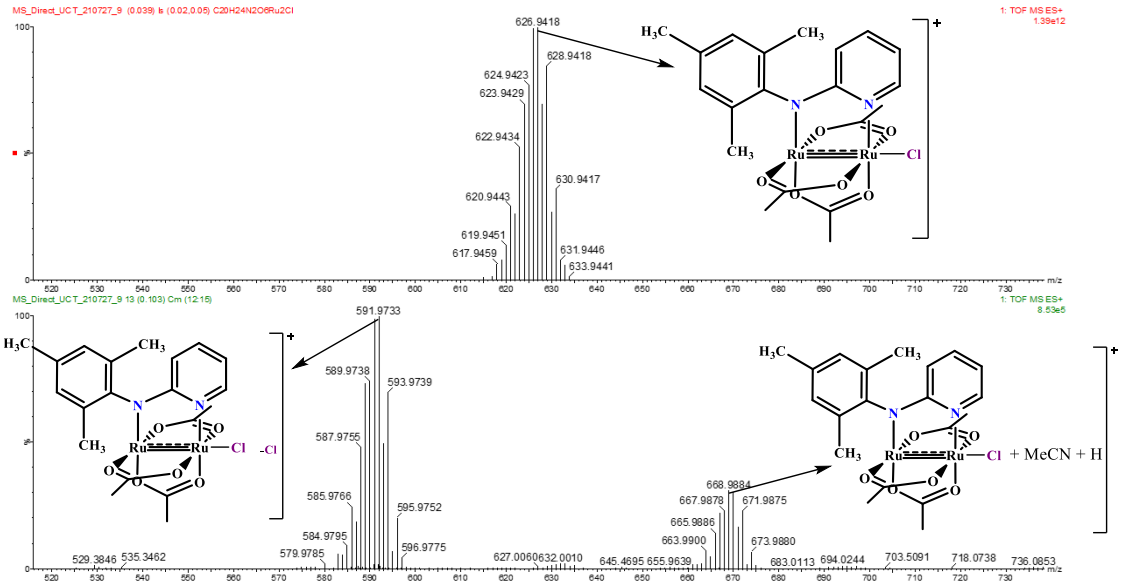

Figure 6.72 High resolution (ESI) mass spectrometry of complex, **C6**. The molecular ion base peak fragment was confirmed using the Molecular Weight Calculator Excel spreadsheet provided by Fiehn Lab, UC Davis Genome Centre - Metabolomics.[2]

*High-resolution (ESI) mass spectrum of **C7**.*

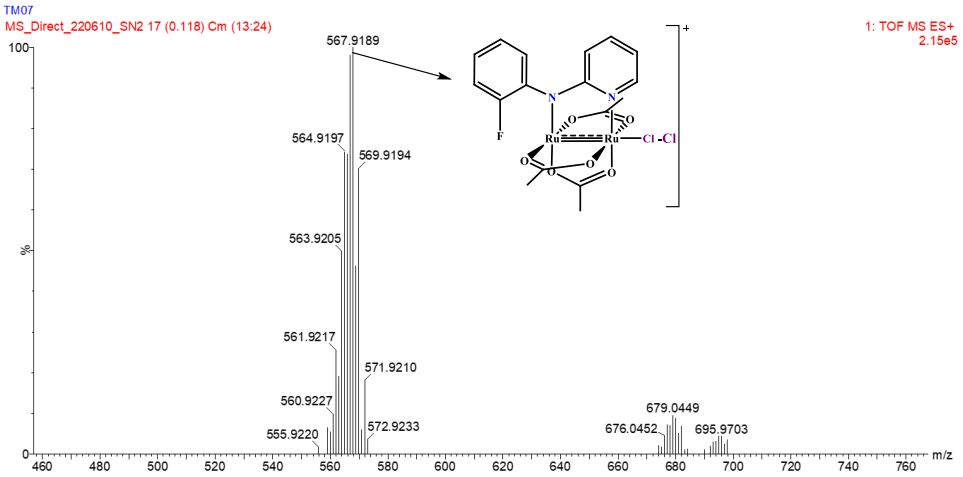

Figure 6.73 High resolution (ESI) mass spectrometry of complex, **C7**. The molecular ion base peak fragment was confirmed using the Molecular Weight Calculator Excel spreadsheet provided by Fiehn Lab, UC Davis Genome Centre - Metabolomics.[2]

UV-visible spectra of $[Ru_2(O_2CCH_3)_3(R\text{-ap})Cl]$ (**C1** - **C8**).

*UV-visible spectrum of **C1**.*

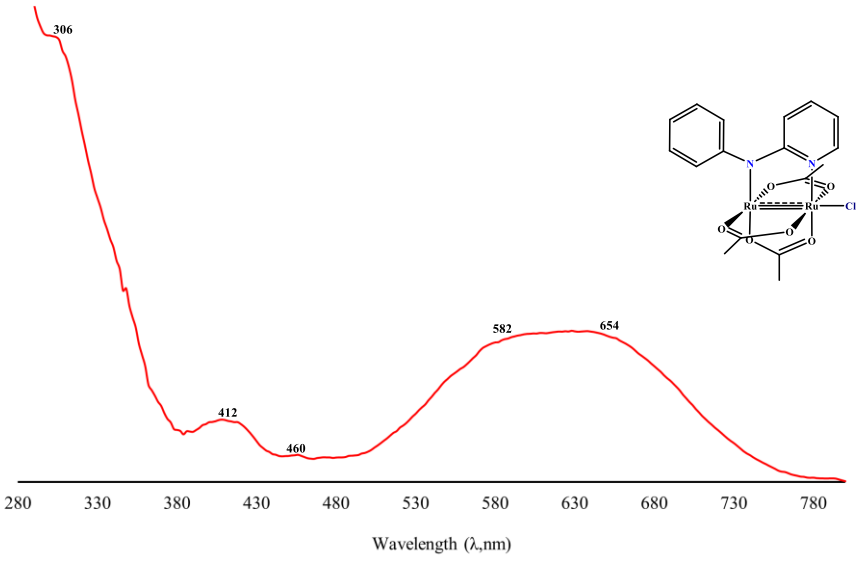

Figure 6.74 UV-visible spectrum of **C1** (5 x 10^{-4}M) in DCM, recorded at room temperature.

*UV-visible spectrum of **C2**.*

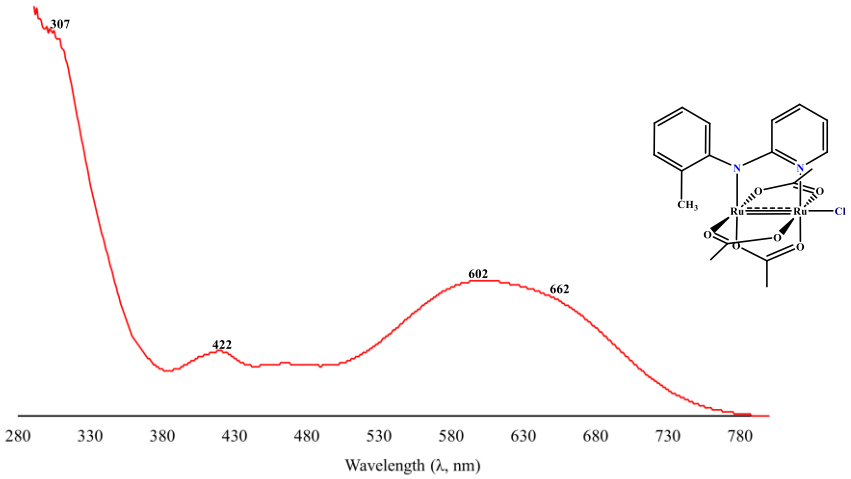

Figure 6.75 UV-visible spectrum of **C2** (5 x 10^{-4}M) in DCM, recorded at room temperature.

*UV-visible spectrum of **C3**.*

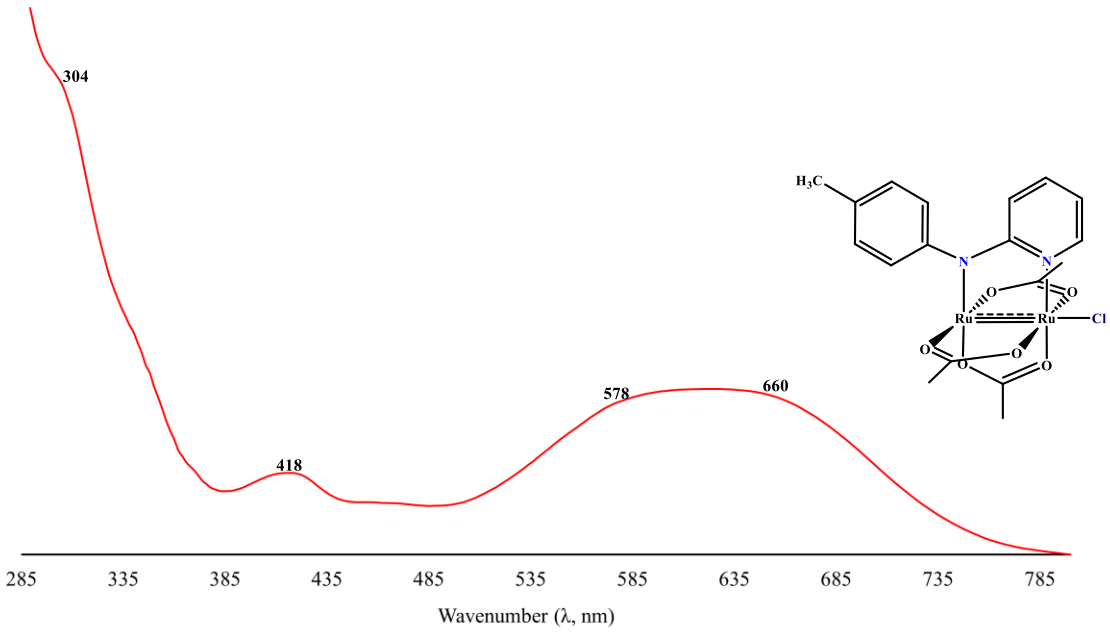

Figure 6.76 UV-visible spectrum of **C3** (5 x 10^{-4} M) in DCM, recorded at room temperature.

*UV-visible spectrum of **C4**.*

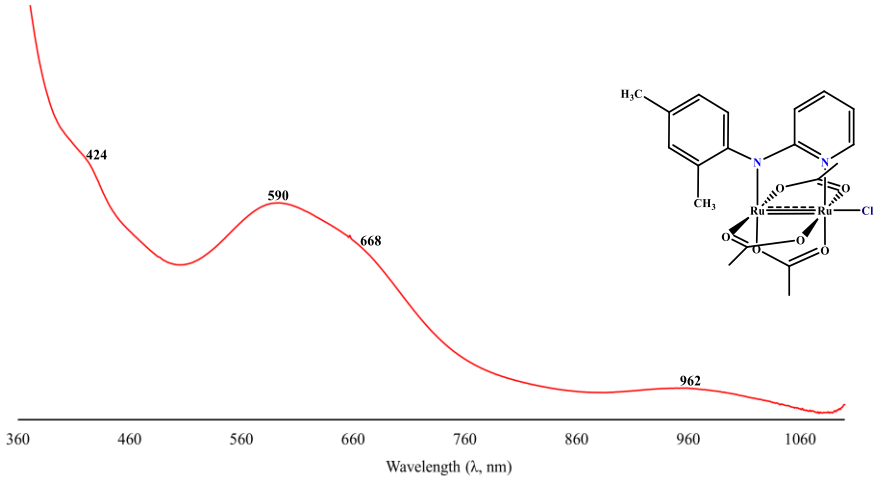

Figure 6.77 UV-visible spectrum of **C4** (5 x 10^{-4} M) in DCM, recorded at room temperature.

*UV-visible spectrum of **C5**.*

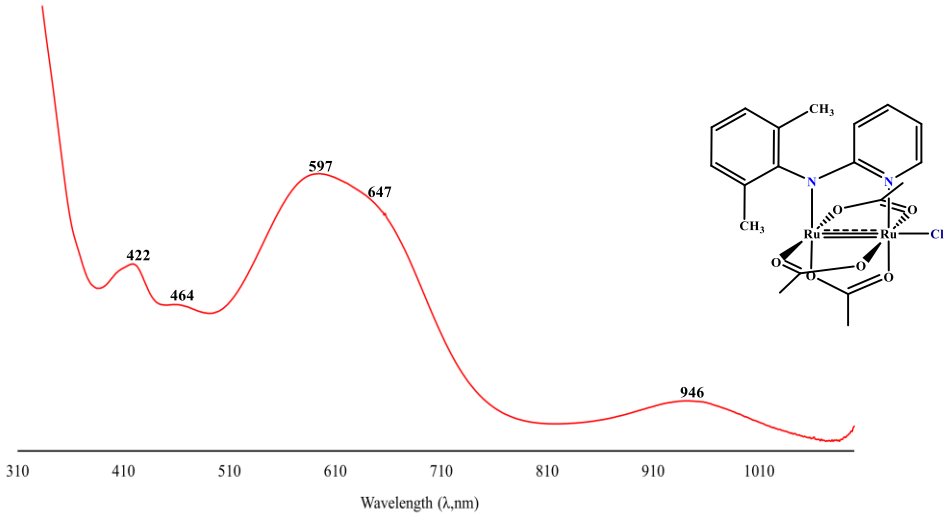

Figure 6.78 UV-visible spectrum of **C5** (5 x 10^{-4} M) in DCM, recorded at room temperature.

*UV-visible spectrum of **C6**.*

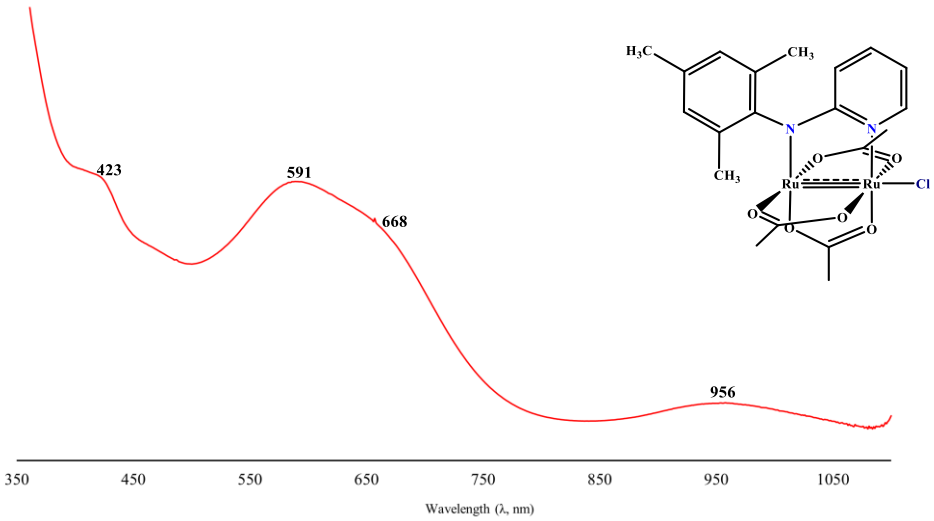

Figure 6.79 UV-visible spectrum of **C6** (5 x 10^{-4} M) in DCM, recorded at room temperature.

*UV-visible spectrum of **C7**.*

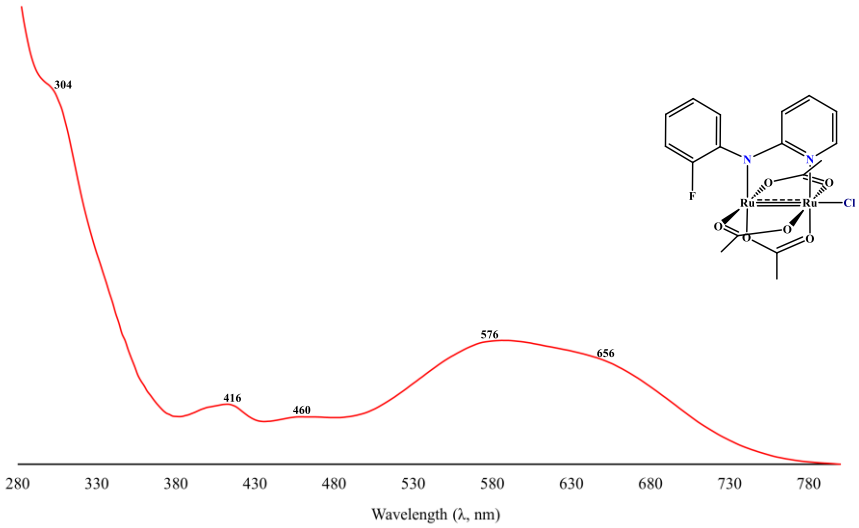

Figure 6.80 UV-visible spectrum of **C7** (5 x 10^{-4} M) in DCM, recorded at room temperature.

*UV-visible spectrum of **C8**.*

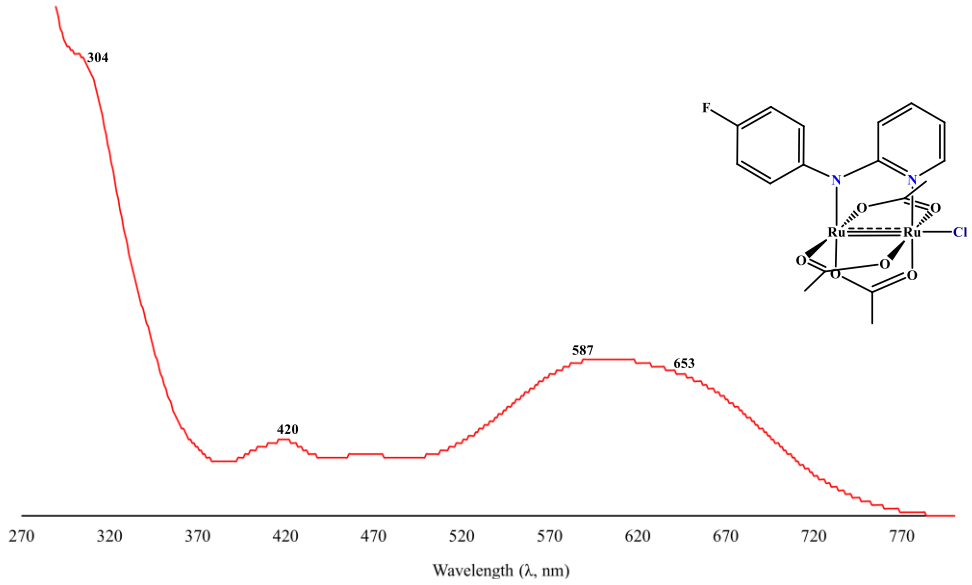

Figure 6.81 UV-visible spectrum of **C8** (5.00 x 10^{-4} M) in DCM, recorded at room temperature.

Cyclic Voltammetry Electrochemical measurements of $[Ru_2(O_2CCH_3)_3(R\text{-}ap)Cl]$ complexes.

*Cyclic voltammogram of **C4**.*

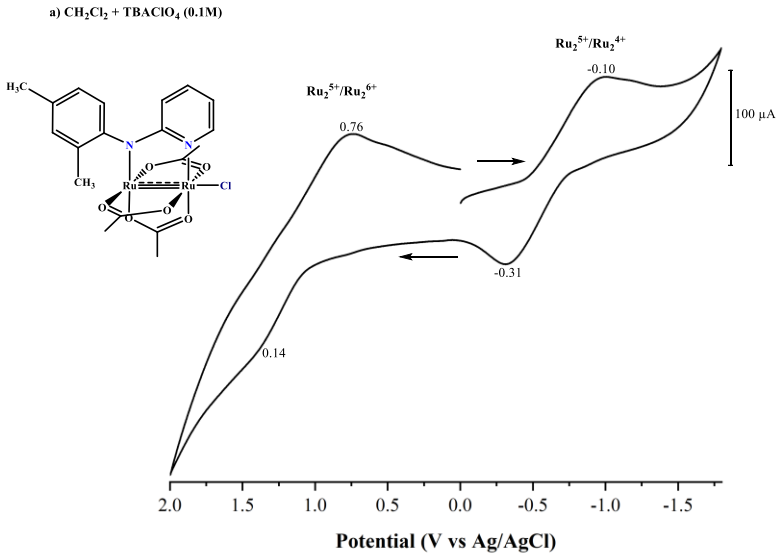

Figure 6.82 Cyclic voltammogram of **C4** (5.00 x 10^{-3} M) in CH_2Cl_2 recorded at room temperature. 0.1M $TBAClO_4^-$ was used as the supporting electrolyte. The CV shows two reductive one-electron $Ru_2^{5+/}Ru_2^{4+}$ couple and one oxidative Ru_2^{5+}/Ru_2^{6+} chemical process. Scan rate = 0.100 mV/s.

*Cyclic voltammogram of **C5**.*

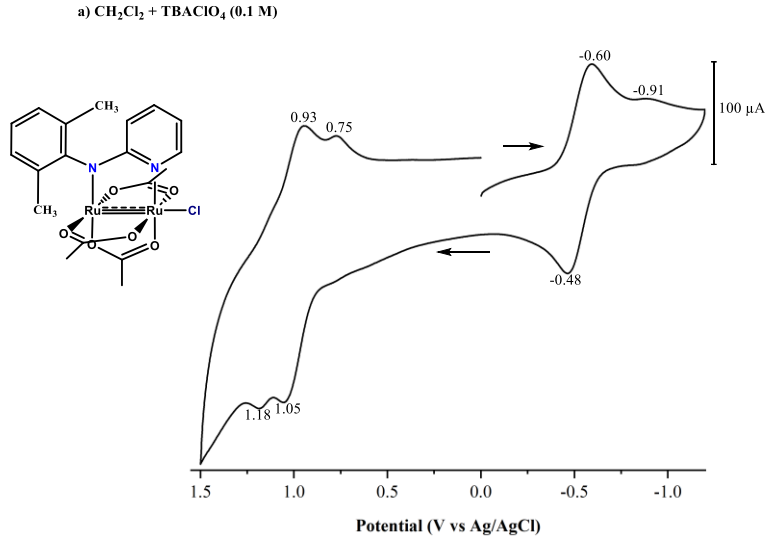

Figure 6.83 Cyclic voltammogram of **C5** (5.00 x 10^{-3} M) in CH_2Cl_2 recorded at room temperature. 0.1M $TBAClO_4^-$ was used as the supporting electrolyte. The CV shows two reductive one-electron $Ru_2^{5+/}Ru_2^{4+}$ couple and one oxidative Ru_2^{5+}/Ru_2^{6+} chemical process. Scan rate = 0.100 mV/s.

*Cyclic voltammogram of **C7**.*

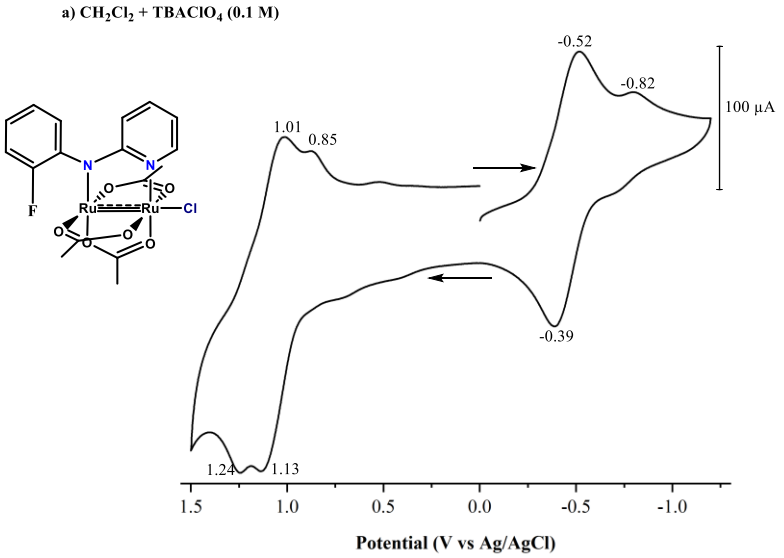

Figure 6.84 Cyclic voltammogram of **C7** (5.00 x 10^{-3} M) in CH_2Cl_2 recorded at room temperature. 0.1M $TBAClO_4^-$ was used as the supporting electrolyte. The CV shows two reductive one-electron $Ru_2^{5+/}Ru_2^{4+}$ couple and one oxidative Ru_2^{5+}/Ru_2^{6+} chemical process. Scan rate = 0.100 mV/s.

*Cyclic voltammogram of **C4**.*

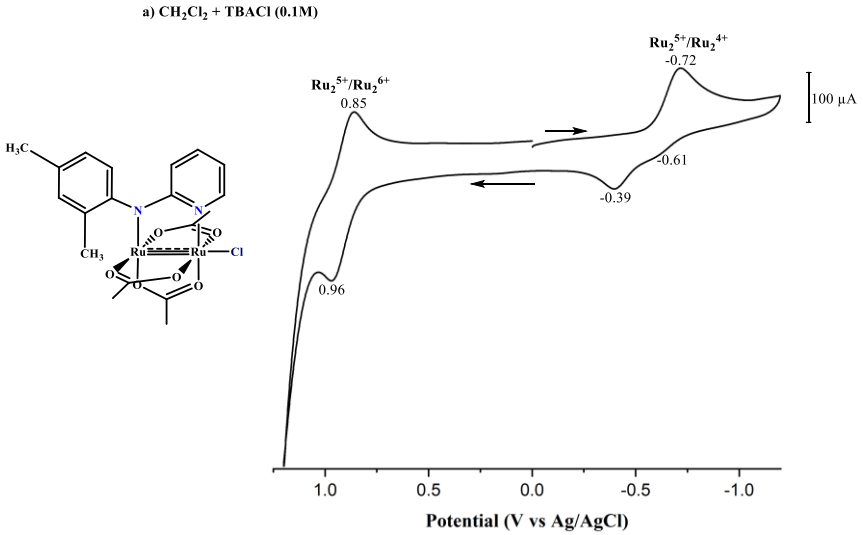

Figure 6.85 Cyclic voltammogram of **C4** (5.00 x 10^{-3} M) in CH_2Cl_2 recorded at room temperature. 0.1M TBACl was used as the supporting electrolyte. The CV shows a single one-electron $Ru_2^{5+/}Ru_2^{4+}$ reduction redox couple process. Scan rate = 0.100 mV/s.

*Cyclic voltammogram of **C7**.*

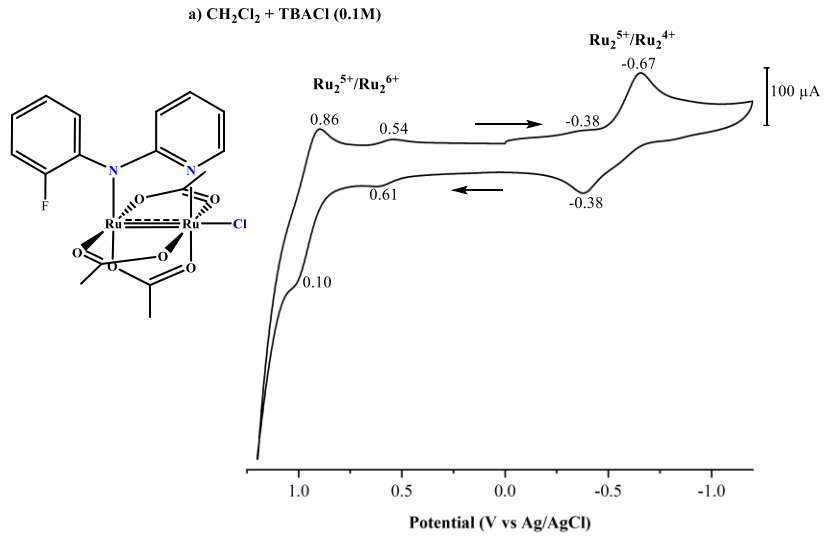

Figure 6.86 Cyclic voltammogram of **C7** (5.00 x 10^{-3} M) in CH_2Cl_2 recorded at room temperature. 0.1M TBACl was used as the supporting electrolyte. The CV shows a single one-electron $Ru_2^{5+/}Ru_2^{4+}$ reduction redox couple process. Scan rate = 0.100 mV/s.

Dose-response curves of complexes **C1 - C8, CDDP** tested against human breast MCF-7, MDA-MB-231 cancer and mammary non-malignant MCF12A epithelial cell lines after 72 hours of drug exposure.

*Dose-response curves of complexes **C1 - C8, CDDP** tested against human breast MCF-7 cancer cell line.*

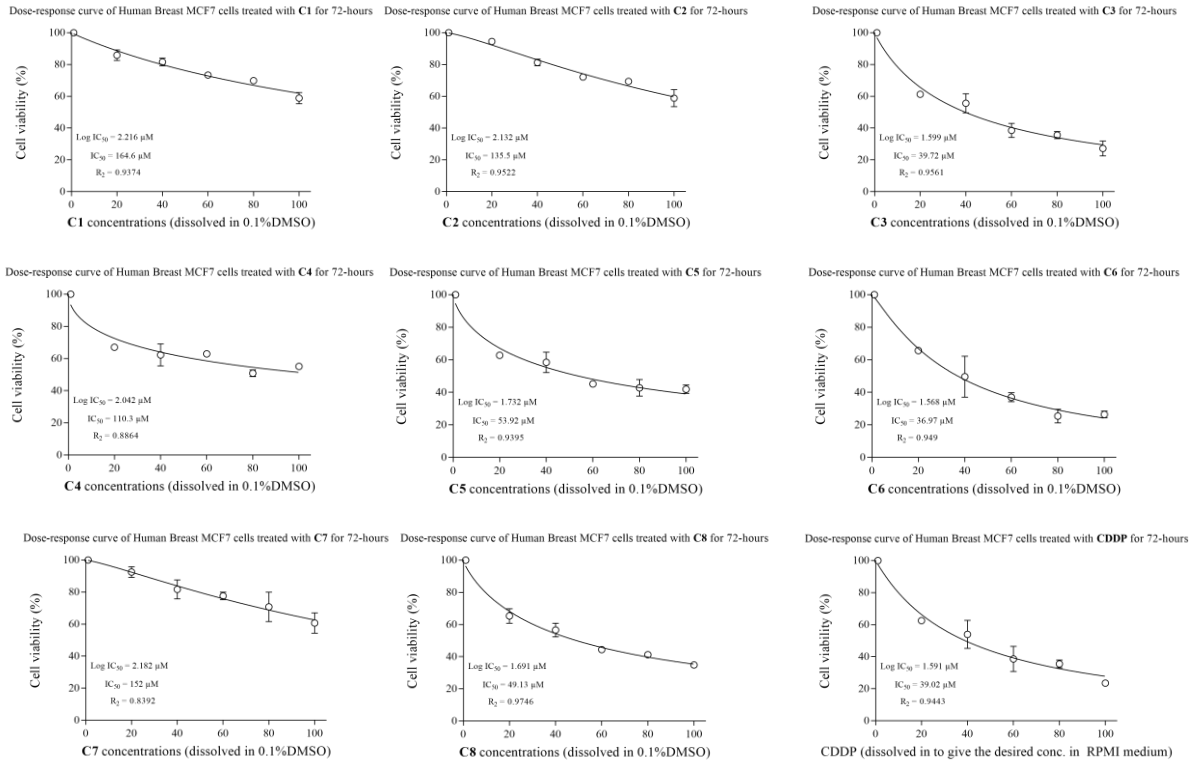

Figure 6. 87 Dose-response curves of **C1 - C8**, **CDDP** tested against human breast MCF-7 adenocarcinoma cell after 72 hours of drug exposure. Dose-response curves were drawn using GraphPad Prism v7.0 software, with IC_{50} values determined using the software and extrapolated from the curves.

*Dose-response curves of complexes **C1 - C8, CDDP** tested against human breast MDA-MB-231 cell line.*

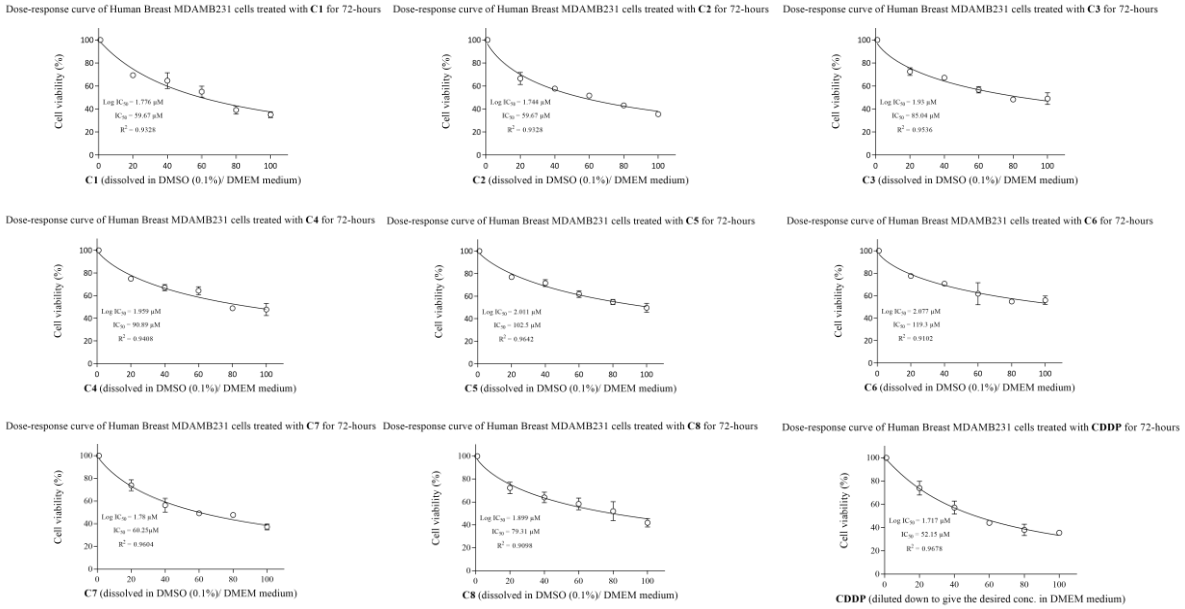

Figure 6.88 Dose-response curves of **C1 - C8**, **CDDP** tested against human breast MDAMB231 adenocarcinoma cell after 72 - hours of drug exposure. Dose-response curves were drawn using GraphPad Prism v7.0 software, with IC_{50} values determined using the software and extrapolated from the curves.

*Dose-response curves of complexes **C1 - C8, CDDP** tested against human breast mammary non-malignant MCF-12A epithelial cell line.*

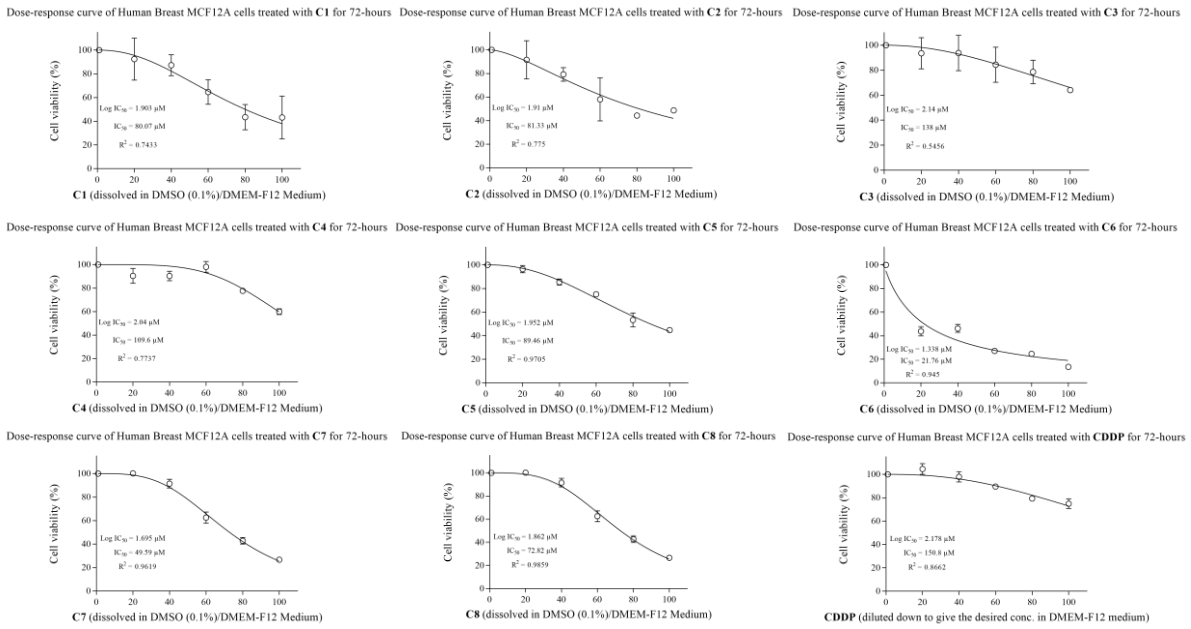

Figure 6.89 Dose-response curves of **C1 - C8**, **CDDP** tested against human breast MCF-12A adenocarcinoma cell after 72 - hours of drug exposure. Dose-response curves were drawn using GraphPad Prism v7.0 software, with IC_{50} values determined using the software and extrapolated from the curves.

Western Blotting analysis

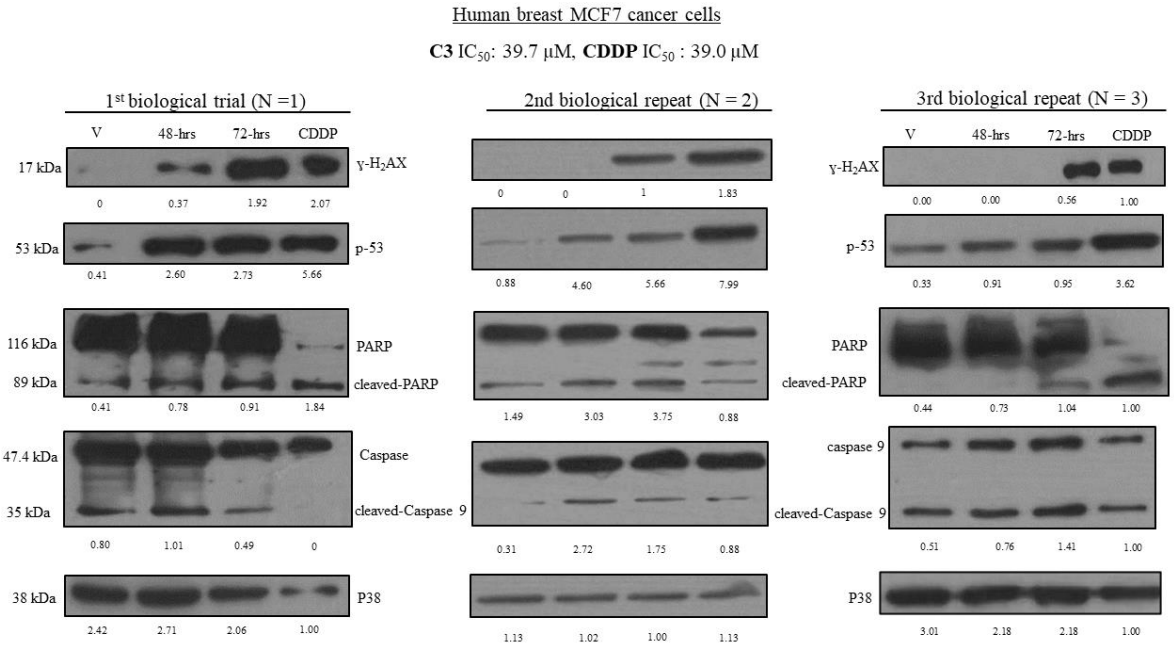

Figure 6.90 Western blot analysis of **C3** to probe for molecular intrinsic and extrinsic apoptotic markers (p53, Caspase 9 and Parp) and double-stranded DNA breaks (ɣ-H2AX). In all experiments, cisplatin (CDDP) was used as a positive control and cells were subjected to 72-hour treatment. Western blotting analysis with antibodies to ɣ-H2AX and p53 show that **C3**-treated MCF-7 cells induce double-stranded DNA damage response and expression of cell stress. Antibodies to caspase 9 and parp show that **C3**-treated MCF-7 cells induce cleavage of these proteins. Total p38 was used as a loading control. The expression of each protein was quantified as the densitometry value analysed by ImageJ software and is normalised to p38 levels.

Preparation of MTT reagent

MTT (5 mg/mL) was prepared in a sterile filtered 1x PBS solution as described by the manufacturer. Briefly, MTT (100 mg) was dissolved in 1x PBS (20 mL). The solution was incubated at 37°C for 15 minutes and filtered through a 0.2 µM filter. The solution was wrapped in foil and was refrigerated at 4°C.

Preparation of the solubilization buffer reagent

To prepare non-sterilized 10 % SDS (0.01M) in deionized water, SDS (25 g) was dissolved in deionized water (dH_2O, 250 ml). Concentrated hydrochloric acid (32.1%, 76.6 µl) was added to the solution.

Preparation of the mycoplasma staining reagent (mounting fluid)

To prepare mounting fluid, citric acid (20 mM) was added to a beaker containing $Na_2HPO_4 \cdot 2H_2O$ (55 mM). The pH of the acidic solution was adjusted to 5.5 pH reading with glycerol (50%). The solution was stored at 4°C before usage.

Preparation of 10x phosphate buffered saline (PBS) solution

To prepare phosphate buffer saline solution (10x, 2 L), NaCl (160 g) and KCl (4 g) were placed in a beaker. Distilled water (2 L) was added to the beaker and stirred. Na_2HPO_4 (28.8 g) and KH_2PO_4 (4 g) were added to the solution and the pH of the solution adjusted to 7.4. The solution was further transferred and diluted down to 1x concentration into a glass bottle (100 mL of 10x PBS + 900 mL distilled water).

Clonogenic assay

Preparation of crystal violet staining (0.5%, 100 mL) solution.

Crystal violet (0.5 g) was dissolved in 100 % methanol (50 mL). Citric acid (20 mM), $Na_2HPO_4 \cdot 2H_2O$ (55 mM), and glycerol (50 %) were added to the solution and the 50 mL centrifuge tube covered with tin foil to avoid exposure to direct sunlight.

Western blotting apparatus, chemicals, and reagents

Preparation of complete RIPA buffer

NaCl (150 mM)

Triton X-100 (1%)

SDS (0.1%)

Tris (20 mM, pH = 7.5)

Deoxycholate (1%)

Protease inhibitors added prior to harvesting

1x complete protease inhibitor tablets (Roche, Germany), aprotinin (1 µg/mL), pepstatin (1 µg/mL), phenylmethanesulphonyl fluoride (PMSF, 0.5 mM)

2x Protein loading dye:

Tris-HCl, pH = 6.5

0.4% SDS

10% β-mercaptoethanol

20% glycerol

5x Protein loading dye:

10% glycerol

1% SDS

0.25 Tris-HCl, pH = 6.8

3 mg Bromophenol blue

Sodium Dodecyl Sulphate (SDS)-polyacrylamide gels:

Resolving gel:

- Acryl-bisacryl-amide mix (30:8) (percentage dependent on the size of the protein of interest)
- 0.375M Tris (pH =8.8)
- 0.1% SDS
- 0.01% TEMED
- 0.1% Ammonium persulphate

Stacking gel:

- 5% Acryl-bisacryl-amide mix (30:08)
- 0.192M Tris (pH = 6.8)
- 0.1% SDS
- 0.01% TEMED
- 0.1% Ammonium persulphate

Preparation of the running buffer:

- 1g SDS
- 3.03g Tris
- 14.41g glycine
- Makeup to 1L

Preparation of the transfer buffer:

- 2.9g glycine
- 5.8g Tris
- 0.37g SDS

- 200 mL isopropanol
- Make up to 1L and store at 4°C

Phosphate buffered solution/Tween 20:

- 10x PBS
- 8g NaCl
- 1.45 $Na_2HPO_4 \cdot 12H_2O$
- 0.2g KCl
- 0.2g KH_2PO_4
- Make up to 1L, pH = 7.4

PBS/Tween:

- Membranes were washed with Tween (0.1%) to 1x PBS solution

REFERENCES

1 B. Lastra-Barreira, J. Díez and P. Crochet, *Green Chem.*, 2009, **11**, 1681.

2 N. Huang, M. M. Siegel, G. H. Kruppa and F. H. Laukien, *J. Am. Soc. Mass Spectrom.*, 1999, **10**, 1166–1173.

3 T. A. Stephenson and G. Wilkinson, *J. Inorg. Nucl. Chem.*, 1966, **28**, 2285–2291.

4 M. A. S. Aquino, *Coord. Chem. Rev.*, 2004, **248**, 1025–1045.

5 M. Mukaida, T. Nomura and T. Ishimori, *Bull. Chem. Soc. Jpn.*, 1972, **45**, 2143–2147.

6 M. A. S. Aquino, *Coord. Chem. Rev.*, 1998, **170**, 141–202.

7 V. M. Miskowski and H. B. Gray, *Inorg. Chem.*, 1988, **27**, 2501–2506.

8 C. R. Wilson and H. Taube, *Inorg. Chem.*, 1975, **14**, 2276–2279.

9 M. C. Barral, R. Jiménez-Aparicio, C. Rial, E. Royer, M. J. Saucedo and F. A. Urbanos, *Polyhedron*, 1990, **9**, 1723–1728.

10 R. W. Mitchell, A. Spencer and G. Wilkinson, *J. Chem. Soc. Dalt. Trans.*, 1973, 846–854.

	**Stellenbosch University** **Chemistry and Polymer Science** **Organometallic Research Group**	**SOP #**	1
		Revision #	2
		Implementation Date	Dec 2014
Page	1 of 2	**Last Reviewed/Update Date**	Jul, 2018
A.van Niekerk	16011988@sun.ac.za	**Approval**	

Tris-HCl buffer preparation (pH 7.2)

1. CHEMICALS, REAGENTS AND EQUIPMENT

The reagents required are listed below:

- Tris
- NaCl
- HCl
- Distilled water
- pH Meter
- Water bath

2. METHODS

- Rinse a clean volumetric flask (250/500 mL) with ethanol and place it in an oven to dry overnight.
- Switched on the water bath and set the temperature to 25°C.
- Weigh out Tris (0.121/0.242 g) and NaCl (0.584/1.168 g) and transfer these to the volumetric flask. Rinse the remaining excess reagents with distilled water.
- Transfer the remaining distilled water to the volumetric flask (180/360 mL) and fill it up to the meniscus mark.
- Place the volumetric flask in the water bath and allow 30 minutes of thermal equilibration time
- Calibrate the pH meter with pH buffers 4 and 7
- Dilute 37% HCl with water (1:9) – adding acid to water
- Adjust the pH to 7.2, using the diluted HCl
- Add the remaining 10% distilled water (20/40 mL) to obtain the final buffer solution
- Store in the fridge and use within 2 weeks

	**Stellenbosch University** **Chemistry and Polymer Science** **Organometallic Research Group**	**SOP #**	1
		Revision #	2
		Implementation Date	Dec 2014
Page	2 of 2	**Last Reviewed/Update Date**	Jul, 2018
A.van Niekerk	16011988@sun.ac.za	**Approval**	

3. REFERENCES

McB lab protocols (2018) http://mcblabprotocols.com/stock-solution-preparation/preparation-1-m-tris-cl-ph-7-2. Last visited on 10 July 10, 2018.

	**Stellenbosch University** **Chemistry and Polymer Science** **Organometallic Research Group**	**SOP #**	5
		Revision #	2
		Implementation Date	Apr 2015
Page	1 of 4	**Last Reviewed/Update Date**	Apr 2015
A. Blanckenberg	15288013@sun.ac.za	**Approval**	
A. van Niekerk	16011988@sun.ac.za		

DNA-Metal binding study probed using Agarose Gel Electrophoresis (Binding type/Concentration series)

1. CHEMICALS, REAGENTS AND EQUIPMENT

The following SOPs are required to complete this SOP:

- Electrophoresis buffer preparations
- Distilled water
- pBlueskript bacteria
- Plasmid DNA (Zyppy plasmid isolation kit and protocol)
- Agarose
- Ethidium bromide stain (10mg/mL)
- Gel electrophoresis apparatus

2. METHODS

Sample preparation:

- Prepare Loading buffer (10x) and TBE buffer (10x) using methods outlined in SOP 1. *N.B: Shelf life indefinite when stored in the refrigerator
- Dissolve TBE buffer (10x) to TBE buffer (1x) by a 1:9 dilution with distilled water
- Isolate plasmid, using Zyppy kit and protocol* (Check dilution of buffers with ethanol etc., as per protocol from supplier)
- Prepare (defrost) plasmid DNA master stock solution (as obtained from plasmid isolation kit)*
- Dilute master stock to required DNA concentrations with TBE buffer (1x) (min. 40 µg/mL)

	**Stellenbosch University** **Chemistry and Polymer Science** **Organometallic Research Group**	**SOP #**	5
		Revision #	2
		Implementation Date	Apr 2015
Page	2 of 4	**Last Reviewed/Update Date**	Apr 2015
A. Blanckenberg	15288013@sun.ac.za	**Approval**	
A. van Niekerk	16011988@sun.ac.za		

Preparation of a metal complex stock solution:

- By using distilled water or DMSO (In rare cases, where the complex is not water- or DMSO-soluble, acetone may be used), dissolve the complex with the necessary solvent.
- The concentration of the stock solution is determined by the concentration range (34, 340 and 680 µM for 10 – 200 µM range)

Preparation of samples:

- A total volume of 15 µL (excluding loading buffer)
- Constant solvent volume (10% or 25% water/ DMSO/ acetone)
- Final DNA conc. of min. 0.4 ug per well
- Final M conc. 10-200 µM

*Note: Buffer preparation, plasmid isolation and preparation of DNA master stock can be carried out as needed.

**After preparation, allow 24 hours for binding to occur- keep the sample at 25°C in the water bath to maintain temperature. (Due to the denaturation of DNA being observed at 37°C, samples are incubated at 25°C, rather than the more common 37°C).

Preparation and gel transfer:

- Transfer agarose (0.8 g) and TBE buffer (100 mL) to a volumetric flask. The solvent level should be marked on the flask and closed loosely with a cap.
- Mark the solvent meniscus level on the flask.
- Heat until all agarose has dissolved and aliquot excess buffer if any has evaporated
- Transfer to a beaker and add ethidium bromide stain (5 µL)
- Allow the gel to cool

	**Stellenbosch University** **Chemistry and Polymer Science** **Organometallic Research Group**	**SOP #**	5
		Revision #	2
		Implementation Date	Apr 2015
Page	3 of 4	**Last Reviewed/Update Date**	Apr 2015
A. Blanckenberg	15288013@sun.ac.za	**Approval**	
A. van Niekerk	16011988@sun.ac.za		

- Set up casting clamp with the comb of choice (14/20 tooth)
- Transfer gel, ensuring that there are no bubbles or bits of dust etc. (Use a pipette tip to draw to the side of the gel). Allow 30 min for the gel to set
- If the gel cannot be run immediately, place the gel with casting cassettes and place it in an air-tight container with a buffer. Store in the fridge

Loading the gel:

- Gently remove the comb from the gel. Place the gel into the tank and fill the tank with TBE buffer (1x)
- Prepare samples for loading (15 µL max.) by adding loading buffer (2 µL) and mixing gently with a micropipette
- Load a ready-to-use Lambda marker (6 µL) and the samples subsequently.

Running the gel:

- Place the lid on the gel tank, ensuring that electrodes are connected securely as indicated in the figure below (Figure 6.83):

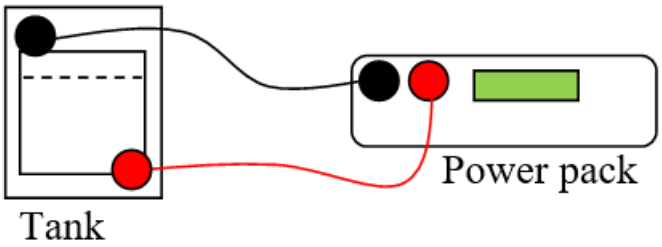

Figure 6.91 Diagram showing the setup instrumentation of the horizontal gel electrophoresis tank.

- Set the voltage to 80 V

	**Stellenbosch University** **Chemistry and Polymer Science** **Organometallic Research Group**	**SOP #**	5
		Revision #	2
		Implementation Date	Apr 2015
Page	4 of 4	**Last Reviewed/Update Date**	Apr 2015
A. Blanckenberg	15288013@sun.ac.za	**Approval**	
A. van Niekerk	16011988@sun.ac.za		

- Run the gel for approximately 2 hours or until loading buffer bands are at least halfway down the gel
- Once complete, remove the gel (keeping it in the tray) from the tank and place it on paper to absorb most of the buffer
- Keep the gel in the tray (UV transparent tray) and place it on black paper to visualise the gel in the UV box
- Photos can be taken in a dark room, using the UV light and a camera

*Note that this study should be repeated at least once to confirm the data. Due to slight differences in DNA stock solutions (due to denaturation), the results may not be identical, but the trends should remain the same.

4. REFERENCES

1. M. Frik *et al.*, *Inorg. Chem. Front.*, 2014, **1**, 231-241.
2. J. Albert *et al.*, *Organometallics*, 2014, **33**, 2862-2873.

	**Stellenbosch University** **Chemistry and Polymer Science** **Organometallic Research Group**	**SOP #**	9
		Revision #	1
		Implementation Date	Oct 2018
Page	1 of 2	**Last Reviewed/Update Date**	Oct 2018
A. van Niekerk	16011988@sun.ac.za	**Approval**	

10x TBE buffer preparation for Horizontal Gel Electrophoresis

1. PURPOSE

This SOP serves to ensure the correct formulation of TBE buffer for horizontal gel electrophoresis-DNA binding.

TBE and TAE buffers are often used in procedures and techniques involving nucleic acids, the most common being electrophoresis. Tris-acid solutions are effective buffers for slightly basic conditions, which keep DNA deprotonated and soluble in water. EDTA is a chelator of divalent cations, particularly of magnesium (Mg^{2+}). As these ions are necessary co-factors for many enzymes, including contaminant nucleases, the role of the EDTA is to protect the nucleic acids against enzymatic degradation. But since Mg^{2+} is also a co-factor for many useful DNA-modifying enzymes such as restriction enzymes and DNA polymerases, its concentration in TBE or TAE buffers is generally kept low (typically at around 1 mM).[1]

2. PREREQUISITES

All reagents and necessary equipment required to conduct the assay are as follows:

Chemicals and Reagents:

- EDTA
- Sodium Hydroxide
- Boric Acid
- Tris Base
- Distilled water

Equipment:

- Schott bottle (1 L)
- Magnetic stirrer bar
- Beaker

	**Stellenbosch University** **Chemistry and Polymer Science** **Organometallic Research Group**	**SOP #**	9
		Revision #	1
		Implementation Date	Oct 2018
Page	2 of 2	**Last Reviewed/Update Date**	Oct 2018
A. van Niekerk	16011988@sun.ac.za	**Approval**	

- pH meter
- Stirrer plate
- Water bath
- Spatula (large)

3. METHOD

- Rinse a volumetric flask (1 L) with ethanol and place it in an oven for drying overnight
- Switch on the water bath and set the temperature to 25°C, allow at least 1 hour for stabilization
- Weigh out Tris (108 g) and boric acid (55 g) and transfer them to the volumetric flask with distilled water (900 mL)
- Add EDTA (9.3 g) to distilled water (40 mL) in a beaker and adjust the pH to 8.0.
  *NB: EDTA will not dissolve fully until the pH reaches 8.0.
- Add the EDTA solution to the volumetric flask.
- Add the remainder of the distilled water to the flask (60 mL)
- Place the sealed flask in the water bath and allow 30 min thermal equilibration time
- Stored at room temperature indefinitely but should be discarded if a precipitate is formed.
- Before use: dilute 1:9 for a 1x TBE buffer

4. REFERENCES

1. https://openwetware.org/wiki/TBE
2. Qiagen. (2001). *Qiagen Bench Guide*.

	**Stellenbosch University** **Chemistry and Polymer Science** **Organometallic Research Group**	**SOP #**	10
		Revision #	1
		Implementation Date	Oct, 2018
Page	1 of 2	**Last Reviewed/Update Date**	Oct, 2018
A. van Niekerk	16011988@sun.ac.za	**Approval**	

Bromophenol blue preparation for Horizontal Gel Electrophoresis

1. PURPOSE

This SOP serves to guide the correct formulation of bromophenol blue loading dye for horizontal gel electrophoresis.

Loading dye is required to track samples through the gel to ensure that the gel is not overrun. The dye also contains glycerol to make the loaded samples denser so that they settle into the bottom of the wells.

2. CHEMICALS, REAGENTS AND EQUIPMENT

All chemicals, reagents and equipment required for the completion of this assay are listed below:

Chemicals and Reagents:

30% Glycerol

Bromophenol blue

1x TBE Buffer

Equipment:

Spatula

Microcentrifuge tubes (15 x 1.5 mL)

Pasteur pipette

Centrifuge tube (15 mL)

4. METHOD

- Add 30 % glycerol (4 g) to a centrifuge tube (15 mL).
- Add bromophenol blue (25 mg) and top up with TBE buffer to a total volume of 10 mL. Mix by inverting the centrifuge tube.

	**Stellenbosch University** **Chemistry and Polymer Science** **Organometallic Research Group**	**SOP #**	9
		Revision #	1
		Implementation Date	Oct 2018
Page	2 of 2	**Last Reviewed/Update Date**	Oct 2018
A. van Niekerk	16011988@sun.ac.za	**Approval**	

**Note: Remove solid particles by centrifuging the mixture at 4000 rpm for 10 minutes.

- Aliquot 1 mL x 15 into micro-centrifuge tubes.
- Can be stored at 4 °C indefinitely.

3. REFERENCES

1. http://mcblabprotocols.com/protocols/preparation-6x-dna-loading-dye-bromophenol-blue-xylene-cyanol-ff-ficoll/

2. Qiagen. (2001). *Qiagen Bench Guide*.